

ABSTRACT

Title of dissertation: MIXED-SPECIES ION CHAINS
FOR QUANTUM NETWORKS

Ksenia Sosnova
Doctor of Philosophy, 2020

Dissertation directed by: Professor Christopher Monroe
Joint Quantum Institute,
University of Maryland Department of Physics

Quantum computing promises solutions to some of the world’s most important problems that classical computers have failed to address. The trapped-ion-based quantum computing platform has a lot of advantages for doing so: ions are perfectly identical and near-perfectly isolated, feature long coherent times, and allow high-fidelity individual laser-controlled operations. One of the greatest remaining obstacles in trapped-ion-based quantum computing is the issue of scalability. The approach that we take to address this issue is a modular architecture: separate ion traps, each with a manageable number of ions, are interconnected via photonic links. To avoid photon-generated crosstalk between qubits and utilize advantages of different kinds of ions for each role, we use two distinct species – $^{171}\text{Yb}^+$ as memory qubits and $^{138}\text{Ba}^+$ as communication qubits. The qubits based on $^{171}\text{Yb}^+$ are defined within the hyperfine “clock” states characterized by a very long coherence time while $^{138}\text{Ba}^+$ ions feature visible-range wavelength emission lines. Current optical and fiber technologies are more efficient in this range than at shorter wavelengths.

We present a theoretical description and experimental demonstration of the key elements of a quantum network based on the mixed-species paradigm. The first one is entanglement between an atomic qubit and the polarization degree of freedom of a pure single photon. We observe a value of the second-order correlation function $g^{(2)}(0) = (8.1 \pm 2.3) \times 10^{-5}$ without background subtraction, which is consistent with the lowest reported value in any system. Next, we show mixed-species entangling gates with two ions using the Mølmer-Sørensen and Cirac-Zoller protocols. Finally, we theoretically generalize mixed-species entangling gates to long ion chains and characterize the roles of normal modes there. In addition, we explore sympathetic cooling efficiency in such mixed-species crystals. Besides these developments, we demonstrate new techniques for manipulating states within the $D_{3/2}$ -manifold of zero-nuclear-spin ions – a part of a protected qubit scheme promising seconds-long coherence times proposed by Aharon et al. in 2013. As a next step, we provide a detailed description of the protocols for three- and four-node networks with mixed species, along with a novel design for the third trap with in-vacuum optics to optimize light collection.

MIXED-SPECIES ION CHAINS FOR QUANTUM NETWORKS

by

Ksenia Sosnova

Dissertation submitted to the Faculty of the Graduate School of the
University of Maryland, College Park in partial fulfillment
of the requirements for the degree of
Doctor of Philosophy
2020

Advisory Committee:

Professor Christopher Monroe, Chair/Advisor

Professor Christopher Jarzynski

Professor Gretchen Campbell

Professor James Williams

Professor Norbert Linke

© Copyright by
Ksenia Sosnova
2020

*I shall be telling this with a sigh
Somewhere ages and ages hence:
Two roads diverged in a wood, and I –
I took the one less traveled by,
And that has made all the difference.*

Robert Frost. The Road not Taken

Dedication

To Efim

Acknowledgments

First and foremost, I would like to thank my advisor, Chris Monroe. I came to the U.S. from Russia, where I was trained purely as a theorist, and when I started grad school, I had no experience working in an experimental lab. Nevertheless, Chris believed in me and accepted me into his group. I am deeply thankful to him for that great chance he gave me. He has provided critical help and guidance throughout this time.

In our group, I was fortunate to work side by side with many talented and knowledgeable physicists, including Dave Hucul, Grahame Vittorini, Volkan Inlek, Clay Crocker, Marty Lichtman, Allison Carter, Jameson O'Reilly, and George Toh. Even though I overlapped just briefly with Dave Hucul and Grahame Vittorini, they were very helpful in teaching me some of the fundamentals of the experiment. Volkan Inlek was a great teacher, and I learnt a lot from him. He was always patient in answering my countless questions and in explaining all the physics related to the experiment, as well as the basics of the experimental work in general. I am most grateful to Volkan, as it was thanks to him that my learning was fast and engaging. When we moved and started to build the new lab in PSC, I worked closely with Clay Crocker and continued learning and improving. It was a lot of work, but also a lot of fun building a new lab from the ground up and collecting the data for our single-photon paper together. Marty Lichtman was our postdoc who was one of the main forces in the lab building process. He was always positive and creative in problem solving and had many exciting ideas on the future of quantum networks. He was a

supportive and enthusiastic mentor for graduate and undergraduate students. Closer to the end of my grad school, I worked a lot with Allison Carter, who was a junior graduate student at that point. She rapidly progressed in multiple aspects of the experiment, and it is great to see her now as an independent, talented, and successful scientist. A new grad student, Jameson O'Reilly, and a new postdoc, George Toh, have joined our group during my last semester in grad school. Unfortunately, I did not have a lot of time to work with them closer, but looking at their progress right now, I can see that they will have a bright future in the Ion-Photon lab.

Finally, I want to thank my husband, Efim, for his endless love, support and help. None of it would be possible without you. Moving to the U.S. was hard to me and to you, and I am so happy that we did it together, that we had each other and could always support and take care of each other. And I cannot be thankful enough to you for being with me during all these years. All the difficulties and problems can be easily overcome if you are with me. I love you so much!

Table of Contents

Dedication	ii
Acknowledgements	iii
Table of Contents	v
List of Tables	viii
List of Figures	ix
List of Abbreviations	xvii
1 Introduction	1
1.1 Classical and Quantum Computing	1
1.2 Quantum Computing with Ions	3
1.3 Quantum Networks with Mixed Species	6
1.4 Thesis outline	9
2 Ytterbium and Barium Atomic Ions	11
2.1 Optical Bloch Equations	11
2.1.1 Four-level system. $^{171}\text{Yb}^+$	14
2.1.2 Four-level system. $^{174}\text{Yb}^+$	22
2.1.3 Eight-level system. $^{138}\text{Ba}^+$	28
2.2 Ytterbium operations	35
2.2.1 State initialization and readout	35
2.2.2 Single qubit rotations	38
2.3 Barium operations	40
2.3.1 S-manifold operations	40
2.3.1.1 State initialization and readout	41
2.3.1.2 Single qubit rotations	43
2.3.2 D-manifold operations	43
2.3.2.1 Sate initialization and readout	46
2.3.2.2 Coherent operations with 532 nm light	50
2.3.2.3 Protected qubit subspace	55

3	Mixed-Species Gates	68
3.1	Two-Species Entangling Gates	70
3.1.1	Normal mode participation	70
3.1.2	Mølmer-Sørensen interaction	71
3.1.3	Experimental demonstration of entangling gates	78
3.1.3.1	Cirac-Zoller SWAP operations	78
3.1.3.2	Mølmer-Sørensen gates	81
3.2	Long ion chains	83
3.2.1	Role of normal modes in MS gates	85
3.2.2	AM gates	89
3.2.3	AM-FM gates	96
3.2.4	Sympathetic cooling	99
3.2.4.1	Cooling rate calculations	99
3.2.4.2	Re-ordering ions of different masses	105
3.2.5	Summary	107
4	Barium ions as communication qubits	109
4.1	Pure single photon generation	109
4.1.1	Autocorrelation function $g^{(2)}$	110
4.1.2	650 nm excitation	115
4.1.3	Pure single photons	119
4.1.4	Double excitations	121
4.2	Ion-photon entanglement	127
4.2.1	Experimental demonstration of ion-photon entanglement	127
4.2.2	Polarization mixing	130
4.2.3	Photon collection into a single-mode fiber	133
5	Outlook	136
5.1	Quantum network with several nodes	136
5.1.1	Three-node network	137
5.1.2	Four-node network	140
5.1.3	New trap design	144
5.2	$^{133}\text{Ba}^+$ as a memory qubit	147
5.2.1	Crosstalk during single photon generation	148
5.2.2	Crosstalk during optical pumping	152
5.2.3	Sympathetic cooling	155
A	Remote entanglement	156
A.1	Hong-Ou-Mandel effect	156
A.2	Entanglement of remote qubits	158
B	355nm/532nm Optical-Frequency Combs Shifted in Time	162
B.1	Infinite-pulse trains	162
B.2	Finite N-pulse trains	165

C	Coherent operations with 532 nm light	170
C.1	The Rabi Frequencies	170
C.2	Differential Stark Shifts	173
	Bibliography	175

List of Tables

2.1	Detection of the $ D_{3/2}, m_j = 3/2\rangle$ state. The left hand side shows the raw data from the $D_{3/2}$ state detection when five different polarization combinations are applied. The right hand side presents the corresponding solution of the over-constrained problem (2.53) – the populations of all four states in the $D_{3/2}$ manifold.	50
3.1	Peak Rabi frequencies Ω_{peak} and average fidelities F of five-segment AM entangling gates between different $^{171}\text{Yb}^+ - ^{138}\text{Ba}^+$ pairs in a five-ion chain based on axial and radial modes. The $^{138}\text{Ba}^+$ ion is located at the position 5.	92
4.1	Fidelity loss in % calculated for various pulse shapes with different pulse durations ranging between 1 ns and ∞	124
4.2	Ion-photon entanglement fidelities obtained by spatial filtering of ion light: simulation and experimental results for various apertures. . . .	133
C.1	Atomic parameters such as the natural linewidth and detuning from the excited states $P_{1/2}$ and $P_{3/2}$ as well as the calculated Rabi frequency for different manifolds.	172

List of Figures

1.1	Modular architecture of large-scale quantum information processing systems. Each module represented as a red block has a manageable number of trapped ions in it. In this architecture, within one module ions interact locally via phonons, while different ion-trap modules are connected via photonic buses shown in yellow. The $N \times N$ optical cross-connect switch supports a pairwise connectivity between arbitrary modules. Single photons emitted from communication qubits in different modules are sent into a photonic Bell state analyzer, which consists of beamsplitters and photon detectors.	6
2.1	Energy level diagram for $^{171}\text{Yb}^+$. The qubit is defined in the $S_{1/2}$ ground state hyperfine “clock” levels denoted $ 0\rangle$ and $ 1\rangle$. The main transition at 369 nm shown in purple, between $S_{1/2}$ and $P_{1/2}$, is nearly a cycling transition. When the ion decays to $D_{3/2}$ manifold (0.5% of the time), it is repumped by 935 nm laser to the $^3[3/2]_{1/2}$ state, which quickly decays back to the $S_{1/2}$ manifold.	15
2.2	Hyperfine structure level scheme of $^{171}\text{Yb}^+$ with Zeeman splitting relevant for calculations.	16
2.3	Excitation spectrum of a four-level $^{171}\text{Yb}^+$. Parameters: $\Gamma_{\text{las}} = 0$, $u = 11.35$ MHz, $\alpha = \arccos(1/\sqrt{3})$, saturation parameter $s = \Omega/\Gamma = 1$. Red dots represent our solutions of the optical Bloch equations for a four-level model of $^{171}\text{Yb}^+$; black solid curve is obtained from Eq. (2.29).	21
2.4	Fine structure level scheme of $^{174}\text{Yb}^+$ with Zeeman splitting.	23
2.5	Excitation spectrum of $^{174}\text{Yb}^+$. Parameters: $\Gamma_{\text{las}} = 0$, $u = 0$, $\alpha = 0$, saturation parameter $s = \Omega/\Gamma = 1$. Red dots represent our calculations of the Bloch equations for a four-level model of $^{174}\text{Yb}^+$; black solid curve describes a two-level model solution, which is identical to the four-level one at zero magnetic field.	27
2.6	Fine structure level scheme of $^{138}\text{Ba}^+$ with Zeeman splitting.	28

2.7	Excitation spectrum of an eight-level model of $^{138}\text{Ba}^+$ as a function of 493 nm laser frequency. Parameters: $\omega_r = 461.311845$ THz, $u = 11.35$ MHz, $\alpha = 15^\circ$, saturation parameters $s_g = \Omega_g/\Gamma = 1$ and $s_r = \Omega_r/\Gamma = 3.8$. The experimental data is presented in black dots; the solid black curve represents our solution of the optical Bloch equations fitted to the data over the saturation parameters s_g and s_r and the angle α	33
2.8	Excitation spectrum of an eight-level model of $^{138}\text{Ba}^+$ as a function of 650 nm laser frequency. Parameters: $\omega_g = 607.42614$ THz, $u = 11.35$ MHz, $\alpha = 80^\circ$, saturation parameters $s_g = \Omega_g/\Gamma = 1.6$ and $s_r = \Omega_r/\Gamma = 1.4$. The experimental data is presented in solid black dots; the solid black curve represents our solution of the optical Bloch equations fitted to the data over the saturation parameters s_g and s_r and the angle α	34
2.9	$^{171}\text{Yb}^+$ processes when 369 nm laser light is applied. (a) Doppler cooling with 369 nm laser beam detuned from the resonance by 10 MHz. Since due to off-resonant coupling to the $P_{1/2} F = 1\rangle$ manifold, the ion can decay to the state $ 0\rangle$, 14.7 GHz sidebands are applied to return the ion in the main cooling cycle. (b) Optical pumping. We add 2.1 GHz sidebands to the resonant beam to excite the ion from the state $S_{1/2} F = 1\rangle$ to $P_{1/2} F = 1\rangle$. Then, with a probability 1/3 the ion decays to the $ 0\rangle$ state, where it is trapped. (c) Qubit state detection. The 369 nm light resonant to $S_{1/2} F = 1\rangle \leftrightarrow P_{1/2} F = 0\rangle$ transition is applied. The ion prepared in the state $ 1\rangle$ emits a lot of photons, while in the state $ 0\rangle$, it does not, because the laser is detuned by 14.7 GHz from the closest allowed transition.	37
2.10	Microwave rotations between the states $ 0\rangle$ and $ 1\rangle$ in $^{171}\text{Yb}^+$. In the beginning of the experiment, the system is initialized in the $ 0\rangle$ state, then the microwave radiation is applied for a varied time.	38
2.11	(a) Initialization and detection scheme for $S_{1/2}$ -manifold states in $^{138}\text{Ba}^+$. (b) Population of the $ \uparrow\rangle$ state during coherent rotations in the $S_{1/2}$ manifold which were performed via a pair of 532 nm Raman beams with all polarizations.	44
2.12	Barium level structure: (a) in the absence of magnetic field; (b) in presence of magnetic field. A few representative transitions are shown for clarity.	45
2.13	Off-resonant coupling of 532 nm laser beams – represented by the green arrows – to $P_{1/2}$ and $P_{3/2}$ manifolds in $^{138}\text{Ba}^+$. Short black arrows represent $\Delta m_j = \pm 1$ rotations between all four $D_{3/2}$ states; for these, 532 nm Raman beams have to have σ^\pm and π polarizations. Long black arrows represent $\Delta m_j = \pm 2$ rotations between the two possible pairs of states; for these, 532 nm Raman beams only need to have σ^+ and σ^- polarizations. However, in order to minimize the two-photon AC Stark shifts, we keep the π polarization component on for these operations, too.	51

- 2.14 State populations during coherent rotations with $\Delta m_j = \pm 1$ in the $D_{3/2}$ manifold. In the presence of the pair of 532 nm Raman beams with all polarizations, all four states are involved in the time evolution. The markers show the experimental data. Yellow circles: $|d_0\rangle$ state ($m_j = -3/2$); green diamonds: $|d_1\rangle$ state ($m_j = -1/2$); red squares: $|d_2\rangle$ state ($m_j = 1/2$); and blue crosses: $|d_3\rangle$ state ($m_j = 3/2$). Solid lines of the corresponding colors show the QuTiP simulations for a four-level system initialized with all the population in the $|d_3\rangle$ state ($m_j = 3/2$) with the effective microwave rotations between the $D_{3/2}$ states. We fit the QuTiP simulations to the experimental data over the Rabi frequency Ω and the decay time τ 52
- 2.15 State populations during coherent rotations with $\Delta m_j = \pm 2$ in the $D_{3/2}$ manifold. In the presence of a pair of 532 nm Raman beams with σ^+ and σ^- polarizations, only two states are evolving while the other two are unaffected. The markers show the experimental data. Yellow circles: $|d_0\rangle$ state ($m_j = -3/2$); green diamonds: $|d_1\rangle$ state ($m_j = -1/2$); red squares: $|d_2\rangle$ state ($m_j = 1/2$); and blue crosses: $|d_3\rangle$ state ($m_j = 3/2$). Solid lines of the corresponding colors show the QuTiP simulations for a four-level system initialized with all the population in the $|d_3\rangle$ state ($m_j = 3/2$) with the effective microwave rotations between the $D_{3/2}$ states. We fit the QuTiP simulations to the experimental data over the Rabi frequency Ω and the decay time τ . 54
- 2.16 Coherent $\Delta m_j = \pm 1$ rotations between the $|D_1\rangle$ and $|D_2\rangle$ states. In the presence of a pair of 532 nm Raman beams, all four $D_{3/2}$ -manifold states are involved in the time evolution. **(a)** The markers show the experimental data. Yellow circles: $|d_0\rangle$ state ($m_j = -3/2$); green diamonds: $|d_1\rangle$ state ($m_j = -1/2$); red squares: $|d_2\rangle$ state ($m_j = 1/2$); and blue crosses: $|d_3\rangle$ state ($m_j = 3/2$). Solid lines of the corresponding colors show the QuTiP simulations for a four-level system starting with the $|D_1\rangle$ state and performing the effective microwave rotations between the $D_{3/2}$ -manifold states. We fit the QuTiP simulations to the experimental data over the Rabi frequency Ω and the decay time τ . **(b)** The synthetic qubit state populations. The markers show the experimental data. Magenta up-pointing triangles: $|D_1\rangle$ state; black down-pointing triangles: $|D_2\rangle$ state. Solid lines of the corresponding colors represent the corresponding QuTiP simulations. 57
- 2.17 Construction of the protected qubit subspace. Two Λ configurations of resonant σ^+ and σ^- 650 nm beams with equal intensities are applied, so that the system is constantly reprojected into the protected subspace \mathcal{H}_D 59
- 2.18 Decoupling of a protected qubit state. Effectively, only the state $|B_1\rangle$ is coupled to the excited state $|p_1\rangle$, and the state $|D_1\rangle$ is dark. 60
- 2.19 Creation of the dark state by applying only σ^+ and σ^- 650 nm beams with the frequency difference δ equal to the frequency difference between the states $|d_1\rangle$ and $|d_3\rangle$ in the $D_{3/2}$ manifold. 61

2.20	System reprojection to the protected qubit subspace by having the driving 650 nm laser fields on during all the Raman operations with 532 nm light.	62
2.21	Coherent $\Delta m_j = \pm 1$ rotations between the $ D_1\rangle$ and $ D_2\rangle$ states performed by a pair of Raman 532 nm beams in the presence of σ^+ and σ^- 650 nm driving (reprojecting) laser fields.	63
2.22	Schematic of RF circuitry used for driving coherent operations with 532 nm light in the $D_{3/2}$ manifold and for creating a driving Hamiltonian H_d based on σ^+ and σ^- 650 nm laser fields. Only two AWG channels are used in the experiment to produce three RF signals. . .	64
2.23	Beatnote signal between 650 nm σ^+ and σ^- laser beams on the fast photo diode.	65
2.24	Schematic of RF circuitry used for the phase control between σ^+ and σ^- 650 nm laser fields that create a driving Hamiltonian H_d . By implementing beatnote lock, we improve the phase stability. The red line represents the optical 650 nm signal going to the photo diode. . .	66
2.25	Improvement of the phase stability. In the “step-in-place” experiment where the rotation to $ D_1\rangle$ is performed with the driving H_d turned on, (a) before the implementation of the phase lock, the state flip starts around $t = 5$ arb. units and completes at $t = 50$ arb. units; (b) after the implementation of the phase lock, the state flip does not start until $t = 200$ arb. units and only completes at $t = 500$ arb. units.	67
3.1	(a) Experimental sequence of Cirac-Zoller (CZ) entangling gate. (b) Rabi flopping performed on the $^{138}\text{Ba}^+$ ion and then read from the $^{171}\text{Yb}^+$ ion after the state mapping. The low mapping efficiency of 0.75 is due to imperfect cooling with the average number of quanta equal $\bar{n} \approx 0.1$	80
3.2	The Raman beam configuration for MS interaction between $^{171}\text{Yb}^+$ and $^{138}\text{Ba}^+$ ions. MS interaction is induced by simultaneous excitation of the off-resonant red and blue sideband transitions. The resulting $\Delta \mathbf{k}$ is along the trap axis, so that we address axial modes of motion.	81
3.3	The experimental data for the MS entangling gate between $^{171}\text{Yb}^+$ and $^{138}\text{Ba}^+$ ions. (a) The correlations between $^{171}\text{Yb}^+$ and $^{138}\text{Ba}^+$ spin states measured in the z -basis. (b) The correlations between $^{171}\text{Yb}^+$ and $^{138}\text{Ba}^+$ spin states measured in the x -basis. After the MS interaction, we apply $\frac{\pi}{2}$ pulses on both qubits. $^{171}\text{Yb}^+$ $\frac{\pi}{2}$ rotation phase is scanned to achieve maximum contrast points, while $^{138}\text{Ba}^+$ $\frac{\pi}{2}$ rotation phase is fixed.	83
3.4	(a) Axial normal modes and their frequencies for a five-ion chain – four $^{171}\text{Yb}^+$ ions (blue) and one $^{138}\text{Ba}^+$ ion (red) located at the edge of the ion chain. (b) The same for the radial normal modes.	87

3.5	Amplitude-modulated pulses of the driving field for a radial AM entangling gate between $^{171}\text{Yb}^+$ and $^{138}\text{Ba}^+$ ions in a five-ion chain for the ion pair (1 – 5). (a) Five-segment pulse with the peak Rabi frequency $\Omega_{\text{peak}} = 400$ kHz; (b) ten-segment pulse with the peak Rabi frequency $\Omega_{\text{peak}} = 900$ kHz. In both cases, the pulse duration $\tau = 200$ μs	93
3.6	Dual five-segment amplitude modulation of the driving fields for an entangling radial gate between $^{171}\text{Yb}^+$ and $^{138}\text{Ba}^+$ ions in a five-ion chain, ion pair (1–5). 355 nm AM pulse shape and the corresponding vertical axis on the left side are shown in blue; 532 nm pulse and the corresponding vertical axis on the right side are in red. The pulse duration $\tau = 200$ μs	94
3.7	Amplitude and frequency modulation of the driving fields for an AM-FM entangling gate between $^{171}\text{Yb}^+$ and $^{138}\text{Ba}^+$ ions in a five-ion chain – ion pair (1 – 5). (a) Fixed amplitude modulation consists of three plateaus connected with cosine ramps. (b) Optimized frequency modulation has a set of turning points (blue dots) connected via cosine curves. Note that the pulse is set to be symmetric in time. The gate duration $\tau = 200$ μs	98
3.8	Frequencies and radial normal modes for a 13-ion-long chain - nine $^{171}\text{Yb}^+$ ions (blue) and four $^{138}\text{Ba}^+$ ion (red) placed periodically in the ion chain. The mode with the highest frequency is the center-of-mass (CM) mode.	101
3.9	Cooling rates for the axial modes in a mixed-species chain with four periodically set “coolant” $^{138}\text{Ba}^+$ ions. The cooling rates are plotted as functions of the total number of ions in the chain. $^{138}\text{Ba}^+$ ions are represented as red circles, the rest of the ions – black circles – are $^{171}\text{Yb}^+$	102
3.10	Cooling rates for the axial modes. Solid lines represent cooling rates in a mixed-species chain with four periodically set “coolant” $^{138}\text{Ba}^+$ ions (as in Fig. 3.9); dashed lines represent cooling rates in a pure $^{171}\text{Yb}^+$ ion chain with four of the $^{171}\text{Yb}^+$ ions in the respective positions used as “coolant” ions. The cooling rates are plotted as functions of the total number of ions in the chain.	103
3.11	Cooling rates for the radial modes in a mixed-species chain with four periodically set “coolant” $^{138}\text{Ba}^+$ ions. The cooling rates are plotted as functions of the total number of ions in the chain.	104
3.12	(a)-(d) Successive stages of re-ordering within the novel technique discussed in the text. Black circles represent heavier ions, and red circles represent lighter ions.	107
4.1	Experimental Hanbury Brown – Twiss setup to investigate the purity of single 493 nm photons emitted by $^{138}\text{Ba}^+$ ion.	110

4.2	The second-order correlation function $g^{(2)}(\tau)$ that demonstrates photon antibunching at $\tau = 0$. Photons are generated with 493 nm excitation line shown in Fig. 4.4(a). Experimental data is shown in blue with 493 nm laser power of $32 \mu\text{W}$. Theoretical calculations based on the solutions of the optical Bloch equations for an 8-level model of $^{138}\text{Ba}^+$ are shown in red. The inset shows the same data as the main plot, but zoomed in at short times. A 5 ns delay is present due to the difference in optical path lengths and in the cable lengths, so the horizontal axes show $\tau + 5$ ns. Fitting parameters are: intensities of 493 nm and 650 nm laser beams, I_g and I_r ; detunings Δ_g and Δ_r ; and magnetic field B	113
4.3	The second-order correlation function $g^{(2)}(\tau)$ that demonstrates photon antibunching at $\tau = 0$. Photons are generated with 493 nm excitation line shown in Fig. 4.4(a). Experimental data is shown in blue with 493 nm laser power of $85 \mu\text{W}$. Theoretical calculations based on the solutions of the optical Bloch equations for an 8-level model of $^{138}\text{Ba}^+$ are shown in red. The inset shows the same data as the main plot, but zoomed in at short times. A 5 ns delay is present due to the difference in optical path lengths and in the cable lengths, so the horizontal axes show $\tau + 5$ ns. Fitting parameters are: intensities of 493 nm and 650 nm laser beams, I_g and I_r ; detunings Δ_g and Δ_r ; and magnetic field B	114
4.4	Excitation schemes for a $^{138}\text{Ba}^+$ ion. (a) Fast excitation using 493 nm line with σ^+ polarization. (b) Fast excitation using 650 nm line with σ^- polarization. As a result of each of these schemes, all the population is transferred to the excited state $6P_{1/2} m_J = +1/2\rangle$, from where it spontaneously decays, and 493 nm photons are collected. . .	115
4.5	650 nm optical pulse with pulse time of 10 ns. The optical 650 nm pulse is created by a fast AOM and measured on a fast photodiode. The experimental data is fitted to a Gaussian.	116
4.6	Single 493 nm photon temporal profiles. First, we drive the π rotation with a 10 ns 650 nm pulse, so that all the population is excited to the $6^2P_{1/2}$ manifold. The resulting single-photon temporal profile is shown by the blue curve. Next, we apply longer 650 nm pulses with 20 ns and 30 ns lengths, and the resulting temporal profiles are shown by the red and green curves, respectively.	117
4.7	Single 493 nm photon temporal profiles. The intensity of 650 nm pulse is reduced by half in comparison to Fig. 4.6. In this case, the π rotation corresponds to a 15 ns 650 nm pulse. We show single-photon temporal profiles at the same pulse lengths as in Fig. 4.6.	118

4.8	(a) Normalized second-order autocorrelation function in a semi-log scale. Side peaks are located $26.8 \mu\text{s}$ apart, which corresponds to the repetition rate of the experiment. The strong dip at $\tau = 0$ demonstrates the high purity of single photon source. (b) Autocorrelation $g^{(2)}(0)$ as a function of the fraction of light collected if we consider shorter times for integration around the center of the peak. The experimental data is shown in blue; 1σ error bars for this data are shown in yellow. The detector dark-count limited $g^{(2)}(0)$ is shown in green; the fitted effective dark-count limited $g^{(2)}(0)$ is shown in red.	120
4.9	$^{138}\text{Ba}^+$ subject to square-shaped 650nm excitation pulse. Fidelity loss as a function of pulse time.	122
4.10	Population transfer in $^{138}\text{Ba}^+$ subject to a 1 ns-long 650 nm excitation pulse. Black curve and left vertical axis: $S_{1/2}$ manifold population. Red curve and right vertical axis: fidelity loss. Both are plotted as functions of the normalized Rabi frequency Ω/Ω_0	125
4.11	Population transfer in $^{138}\text{Ba}^+$ subject to a 5 ns-long 650 nm excitation pulse. Black curve and left vertical axis: $S_{1/2}$ manifold population. Red curve and right vertical axis: fidelity loss. Both are plotted as functions of the normalized Rabi frequency Ω/Ω_0	126
4.12	Population transfer in $^{138}\text{Ba}^+$ subject to a 10 ns-long 650 nm excitation pulse. Black curve and left vertical axis: $S_{1/2}$ manifold population. Red curve and right vertical axis: fidelity loss. Both are plotted as functions of the normalized Rabi frequency Ω/Ω_0	126
4.13	Population transfer in $^{138}\text{Ba}^+$ subject to a 50 ns-long 650 nm excitation pulse. Black curve and left vertical axis: $S_{1/2}$ manifold population. Red curve and right vertical axis: fidelity loss. Both are plotted as functions of the normalized Rabi frequency Ω/Ω_0	127
4.14	Experimental setup for showing entanglement between the state of a $^{138}\text{Ba}^+$ ion and the polarization of the emitted 493 nm photon.	128
4.15	(a) Ion-photon correlations as a function of the wave-plate rotation angle. The red (blue) curve shows the probability of finding the ion in the $ \uparrow\rangle$ state when the photon is detected on APD ₁ (APD ₂). No stops are implemented for this experiment (see Section 4.2.2). (b) Ion-photon coherences (correlations measured in the x -basis) as a function of the phase of the $\pi/2$ rotation performed on the ion qubit. No stops are implemented for this experiment, as well. Amplitudes represent the corresponding entanglement fidelity $F = 0.884(4)$	130
4.16	(a) Radiation pattern of a σ -polarized (blue surface) and π -polarized (yellow surface) light emitted along the z quantization axis; (b) Radiation patterns for the decomposition of the σ -polarized light [the blue surface in the panel (a)] into the H (blue surface) and V (yellow surface) linear polarization components; (c) Two types of apertures used in the experiment to reduce the V-polarized light collection angle thereby improving the ion-photon entanglement fidelity.	131

5.1	Three-node network. Red circles represent separate ion traps with one $^{171}\text{Yb}^+$ ion and one $^{138}\text{Ba}^+$ ion; blue lines represent photonic interconnections between ion traps.	138
5.2	Four-node network. Red circles represent separate ion traps with one $^{171}\text{Yb}^+$ ion and one $^{138}\text{Ba}^+$ ion; blue lines represent photonic interconnections between the ion traps.	140
5.3	Three-trap network. Alice and Bob are currently on the optical table, and have free-space 0.6 NA objectives for 493 nm light collection and its coupling into an SM fiber. A new node will support 493 nm light collection from both sides with the help of 0.8 NA in-vacuum optics. .	144
5.4	Design of a new vacuum chamber. (a) $^{171}\text{Yb}^+$ and $^{138}\text{Ba}^+$ ions are trapped in a four-rod trap with an enhanced 493 nm light collection with the help of two 0.8 NA in-vacuum custom aspheres that collimate $^{138}\text{Ba}^+$ light. Two three-axis piezo stages are used for fine linear adjustment of the in-vacuum aspheres. Outside of the vacuum chamber, two 0.1 NA custom aspheres are utilized for the fiber coupling. (b) The four-rod trap and in-vacuum aspheres are shown in a zoomed-in view.	146
5.5	Designs of a four-rod trap. (a) Square aspect-ratio trap design used in Alice and Bob. When collecting 493 nm light with free-space 0.6 NA objective, rods are clipping about 20% of the light. (b) High optical access trap design intended to collect 493 nm light with 0.8 NA in-vacuum aspheres on two sides.	147
5.6	Representation of crosstalk between a memory qubit and a photonic communication qubit located a distance r away from its neighbor in an ion-trap node. The resonant absorption cross section σ is described by the angle $2\theta(r)$	149
5.7	Energy level diagram for $^{133}\text{Ba}^+$. The qubit is defined within the hyperfine sublevels of the $S_{1/2}$ manifold, with the qubit splitting $\Delta_q = 9.93$ GHz. The hyperfine splittings in the $P_{1/2}$ and $D_{3/2}$ manifolds are $\Delta_1 = 1.84$ GHz and $\Delta_2 = 0.94$ GHz, respectively. The other relevant frequencies are $\nu_0^b = \nu_{138}^b + 4.22$ GHz, and $\nu_1^b = \nu_{138}^b - 7.53$ GHz, where $\nu_{138}^b = 607.4263$ THz is the resonant frequency of the $S_{1/2} \leftrightarrow P_{1/2}$ transition in $^{138}\text{Ba}^+$	150
5.8	Crosstalk probability as a function of beam waist. The red solid curve represents the crosstalk probability in the case where the $^{133}\text{Ba}^+$ qubit has population in the $S_{1/2} F = 0\rangle$ state; the blue dashed line represents the crosstalk probability in the case where the $^{133}\text{Ba}^+$ qubit has population in the $S_{1/2} F = 1\rangle$ state.	154
C.1	Off-resonant coupling of 532 nm laser beams – represented by the green arrows – to $P_{1/2}$ and $P_{3/2}$ manifolds in $^{138}\text{Ba}^+$ in the case of the $\Delta m_j = \pm 2$ rotations between the states $ 1\rangle$ and $ 2\rangle$	171

List of Abbreviations

AC	Alternating Current
AOM	Acousto-Optic Modulator
APD	Avalanche Photo Diode
AWG	Arbitrary Waveform Generator
BCH	Baker-Campbell-Hausdorff
CM	Center-of-Mass
CW	Continuous Wave
CZ	Cirac-Zoller
EIT	Electromagnetically Induced Transparency
ELU	Elementary Logical Unit
EOM	Electro-Optic Modulator
FWHM	Full Width at Half Maximum
GHZ	Greenberger-Horne-Zeilinger
HF	Hyperfine
HOM	Hong-Ou-Mandel
HWP	Half Waveplate
ITO	Indium Tin Oxide
MS	Mølmer-Sørensen
NA	Numerical Aperture
NV	Nitrogen-Vacancy
PBS	Polarizing Beamsplitter
PMT	Photo Multiplier Tube
QCCD	Quantum Charge-Coupled Device
QWP	Quarter Waveplate
RSB	Red Sideband
RWA	Rotating Wave Approximation

SM Single-Mode

UHV Ultra-High Vacuum

Chapter 1: Introduction

1.1 Classical and Quantum Computing

The impact of digital computing on practically all areas of our lives is enormous. However, despite the immense success of classical computing, some problems remain very difficult or impossible to solve this way, despite the steady Moore's law exponential growth of computing power. Some important problems in cryptography, optimization, quantum chemistry, biochemistry, and many other areas scale too quickly for any classical computer to tackle in a reasonable time.

With the enormous complexity that even tiny quantum systems of a few hundred constituents possess, it quickly becomes impossible to describe them with the help of classical computers [1]. However, one could instead leverage this complexity in a controlled way to solve some very hard problems starting with quantum simulations and going forward to more general kinds of complex problems [2, 3]. This was the revolutionary idea that Yuri Manin [4], and then Paul Benioff [5], Richard Feynman [6], and others suggested in the early 1980s. Shortly after, David Deutsch [7] described a universal quantum computer. A few years later, David Deutsch and Richard Jozsa [8] proposed the first example of a problem that could be solved efficiently with a deterministic quantum algorithm, but for which no deterministic

classical algorithm existed. Then, Peter Shor [9] developed one of the most famous algorithms that directly employ the advantage of quantum computers – quantum superpositions and entanglement – to solve the large integer factorization problem in polynomial time. Very soon after, a method for experimental realization of a controlled-NOT quantum gate in trapped ions was suggested by Ignacio Cirac and Peter Zoller [10] and implemented by Christopher Monroe and David Wineland [11]. The same year Peter Shor [12] and Andrew Steane [13] simultaneously proposed quantum error correction, and Lov Grover developed the most efficient database search algorithm [14].

These early developments paved the way for the modern quantum-computing boom that is growing by the day and is promising to revolutionize the world again, just as its classical predecessor have. Some of the most important problems that that may be solved with the help of quantum computers are novel drug development, control and general optimization (starting with transportation and logistics), secure communications and finance, and, of course, further fundamental research in many scientific disciplines. But as much as quantum computers can be powerful, they are also difficult to build and operate, and a multitude of discoveries and engineering solutions have already contributed and will need to be developed before a full-scale universal quantum computer becomes available. Many different physical platforms are being explored, but they all have their strengths and weaknesses.

1.2 Quantum Computing with Ions

Tremendous progress has been made towards building a quantum computer based both on atomic systems (such as ions [15] and neutral atoms [16]) and on solid-state systems (such as NV centers [17], superconductors [18], and quantum dots [19]).

There are set requirements for a system to be a quantum computer. In 2000, DiVincenzo listed five key criteria for a quantum information processor [20] which are:

1. A scalable physical system with well characterized qubits;
2. The ability to initialize the state of the qubits to a simple fiducial state, such as $|000\dots\rangle$;
3. Long relevant decoherence times, much longer than the gate operation time;
4. A “universal” set of quantum gates;
5. A qubit-specific measurement capability.

Trapped ions are an extremely promising system that fulfills all of the DiVincenzo’s original criteria with high fidelity. In the case of trapped ions, internal electronic states of the ion can be used to encode the qubit states $|0\rangle$ and $|1\rangle$. Since all ions of a given species and isotope are fundamentally identical and well isolated from the environment, the microwave or laser frequency used to manipulate each ion will be the same, and each ion will have the same coherence time given the same

electromagnetic conditions. That is not the case for many other candidates, such as NV centers, quantum dots, or superconducting qubits, due to the presence of a solid-state medium [21, 22, 23].

One way to hold ions is to trap them in RF Paul traps [24] inside a vacuum chamber, and thus they are well isolated from the environment, which leads to very long coherence times [25, 26]. Typically, the limitation on the coherence time comes from magnetic field fluctuations. With the help of dynamical decoupling, coherence times in trapped ions have been extended up to 10 minutes [27]. Since a typical two-qubit gate takes $1\ \mu\text{s}$ [28] to $200\ \mu\text{s}$, the ratio of the coherence time to gate time is about $\sim 10^6$. This is a much higher ratio than the one achieved in superconducting qubits [29], NV centers [30, 31], or Rydberg atom qubits [32].

Also, ions can be trapped in an ion trap for many hours, or even days and months (in the case of heavy ions in deep traps). The achieved lifetimes are much longer than other candidates have, including Rydberg atoms in optical lattices.

Moreover, trapped ions feature near perfect state initialization and detection [33, 34]. A readout fidelity higher than 99.99% was achieved [35] in trapped ions in less than $150\ \mu\text{s}$ detection time. With a shorter detection time of $11\ \mu\text{s}$, a readout fidelity of 99.93% was recorded [36]. The achieved initialization and readout fidelities in trapped ions are higher than in any other quantum platform [37, 38, 39].

Finally, one of the most important features of trapped-ion systems is the ability to achieve high-fidelity gates. Single-qubit gate fidelities of 99.9999% [33] were demonstrated with microwave-based operations, which exceeds fidelities in any other platform [40, 41, 42]. Two-qubit gates with fidelities as high as 99.9% have been

performed [43, 44].

Currently, the most challenging task in trapped-ion-based quantum computing is to satisfy the first of DiVincenzo’s criteria – the scalability of the system. As the number of ions in an ion chain increases, spectral crowding of the motional-mode structure leads to an increase in stray excitations and the decrease of the fidelity of entangling operations. In addition, with the increasing number of ions in a chain, the resulting decrease in inter-ion spacing leads to crosstalk during individual addressing [45]. Additionally, with a large number of ions N , the motional coupling parameter (Lamb-Dicke parameter) $\eta \propto \frac{1}{\sqrt{N}}$ decreases, leading to longer gate times.

Two approaches are mainly used to address this scalability problem with trapped ions. One possible solution is to design a system in a quantum charge-coupled device (QCCD) architecture [46], using ion traps which consist of many trapping regions, and groups of ions can be shuttled to different interaction zones using dynamic control voltages [47, 48, 49]. In this approach, the main difficulty comes from heating – or motional excitations – of the ions while they are being transported, which leads to decreased fidelities of coherent operations. A different way to scale the system up is via a modular architecture [50, 51], where single traps can be considered as elementary logical units (ELU) or modules. These modules are connected by photonic links, which are routed by an $N \times N$ optical cross-connect switch [52] as shown in Fig. 1.1. Information is stored and manipulated using coherent interactions within each module, each of which has a manageable number of qubits.

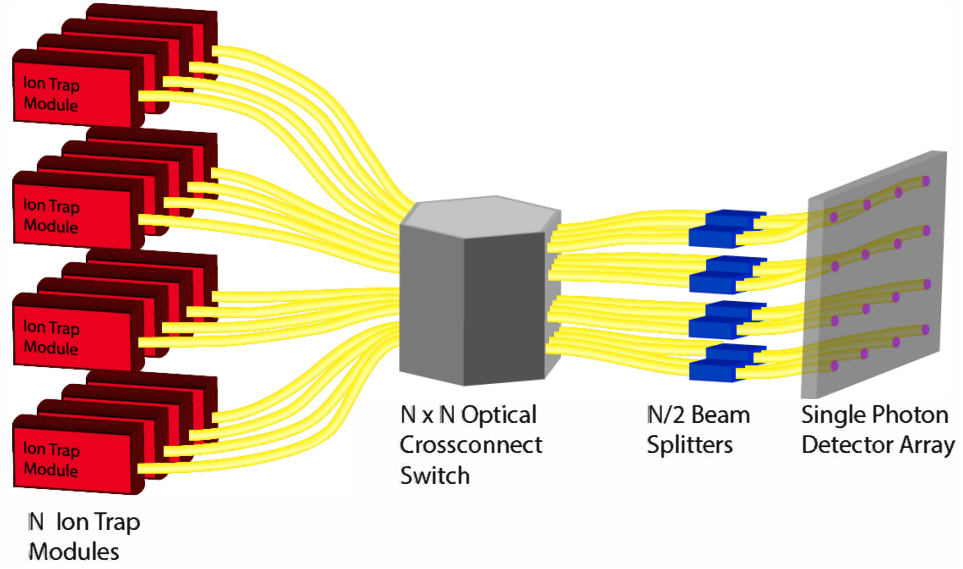


Figure 1.1: Modular architecture of large-scale quantum information processing systems. Each module represented as a red block has a manageable number of trapped ions in it. In this architecture, within one module ions interact locally via phonons, while different ion-trap modules are connected via photonic buses shown in yellow. The $N \times N$ optical cross-connect switch supports a pairwise connectivity between arbitrary modules. Single photons emitted from communication qubits in different modules are sent into a photonic Bell state analyzer, which consists of beamsplitters and photon detectors.

1.3 Quantum Networks with Mixed Species

In the previous section, we discussed approaches to scaling up ion-based quantum information processing systems. In our work, we focus on the modular architecture approach, where ion-trap modules are connected via photonic buses. Such systems can also be used for quantum networks [53, 54, 55], quantum repeaters [56, 57, 58, 59], secure quantum key distribution [60, 61, 62], quantum random number generation [63, 64, 65], cluster state computation [66, 67], and other applications of quantum information processing and communication. All of these applications require high fidelity ion-photon entanglement operations and high pu-

rity of single photons.

Optical photons are chosen as natural carriers of quantum information, since they can traverse large distances in room-temperature optical fibers [68, 69, 70] and through the atmosphere [71, 72]. A parent qubit can be entangled with various degrees of freedom of an emitted photon, such as photon number, frequency, or polarization [73]. Moreover, polarization qubits can be converted to time-bin qubits [74] that can be advantageous for long distance networks. Entanglement between parent qubits and the corresponding emitted photons has been demonstrated in quantum computing systems based on trapped ions [75], neutral atoms [76], quantum dots [77], and NV centers [78]. This crucial feature of modular quantum computers led to the demonstration of teleportation of quantum information between qubits at a distance in various platforms such as trapped ions [55, 79], neutral atoms [80], NV centers [30], and superconducting qubits [81].

Note that for a successful implementation of a modular quantum computer, remote entanglement generation time has to be much shorter than the qubit coherence time. Trapped ions then become an especially attractive candidate for quantum networks, since they satisfy this requirement much better than any other platform does [82, 83]. Moreover, identical atomic qubits guarantee indistinguishability of emitted photons – a critical requirement for quantum computing applications.

To create remote entanglement between separate quantum nodes, we excite ions in both traps simultaneously, collect the emitted photons into single-mode fibers, and send them into a photonic Bell state analyzer. The details of the remote entanglement process are given in Appendix A. Since all the processes that

are relevant to the remote entanglement (photon emission into the correct mode, photon collection, photon detection) are probabilistic, the success rate of this whole procedure is low, and we have to initiate excitation events at a high rate. Resonant light from a photonic entanglement process can destroy the information stored in the nearby memory qubits. We resolve this crosstalk issue by using two distinct atomic species.

It is advantageous to use specific properties of each species for certain corresponding tasks. In our experiments, we use $^{171}\text{Yb}^+$ as quantum memory and processing qubits because they are insensitive to magnetic field and have long coherence times [26, 27], while $^{138}\text{Ba}^+$ ions are used as communication qubits since their visible photon-emission lines at 493 nm are more efficient with current fiber-optics and detector technologies [84, 85, 86, 87].

In addition to network interconnections, a multi-species setup has another advantage – the communication ions can also serve for sympathetic cooling of the memory qubits in the long ion chains [88, 89, 90, 91, 92]. Usually, ions experience heating caused by fluctuations in the electric potential at the ion positions [93, 94], or by the shuttling, separation, and recombination of ion strings [95, 96]. The ability to cool down memory qubits efficiently allows for longer computational times and for operations with higher fidelity, leading to a wider range of applications for quantum information processing.

Moreover, a combination of two different ion species can be necessary for quantum logic spectroscopy [97]. Some atomic and molecular ions lack suitable transitions for efficient laser cooling, internal state preparation, and detection. An

auxiliary “logic” ion can allow not just sympathetic laser cooling, but also state initialization and detection for a simultaneously trapped “spectroscopy” ion.

1.4 Thesis outline

In this thesis, we present a theoretical description and experimental demonstration of the key elements of a quantum network based on mixed-species ion-trap nodes: (i) entanglement between an atomic qubit and a polarization degree of freedom of a pure single photon; (ii) mixed-species entangling gates with two ions; and (iii) generalization of mixed-species entangling gates to long ion chains.

- Chapter 2 gives a description of the atomic ions that we use in the experiments: $^{171}\text{Yb}^+$ memory/processing ions and $^{138}\text{Ba}^+$ communication ions. We start this discussion with solving the optical Bloch equations for both systems of interest and then describe the basic operations with $^{171}\text{Yb}^+$ ions. Next, we show the basic $S_{1/2}$ -manifold qubit manipulation in $^{138}\text{Ba}^+$ and its generalization to the $D_{3/2}$ manifold. We provide a scheme to create a protected qubit defined in the $D_{3/2}$ manifold with long coherence times and present our experimental progress in this direction.
- Chapter 3 discusses mixed-species entangling gates – gates between $^{171}\text{Yb}^+$ and $^{138}\text{Ba}^+$ ions. We start with entangling gates in two-ion chains and show the experimental results for Mølmer-Sørensen and Cirac-Zoller operations. Next, we characterize the role of normal modes in long ion chains and carry out simulations of the entangling gates in long ion crystals. We finish this chapter

with discussion of sympathetic cooling and re-ordering techniques.

- Chapter 4 gives an overview of network experiments with $^{138}\text{Ba}^+$ ions. We begin with pure single photon generation and the corresponding experimental results on the second-order correlation function $g^{(2)}(0)$. Then we demonstrate entanglement between the state of a $^{138}\text{Ba}^+$ ion and a polarization of its emitted photon.
- Chapter 5 concludes this thesis with outlook and future directions. We provide a detailed description of the protocols for three- and four-node networks with mixed species, along with a novel design for the third trap. In addition, we discuss a possibility of using $^{133}\text{Ba}^+$ as memory ions and potential crosstalk channels.

Chapter 2: Ytterbium and Barium Atomic Ions

Trapped ions are a leading platform for quantum computing and quantum communication networks, featuring long coherence times and high-fidelity operations [98, 99, 100, 101]. To address the challenges of scaling up such systems, we utilize a modular architecture consisting of separate traps with memory/processing qubits and communication qubits that support photonic links for remote entanglement [51, 102]. In our experiments, $^{171}\text{Yb}^+$ ions are used for quantum memory and processing, while $^{138}\text{Ba}^+$ ions are used as communication qubits.

2.1 Optical Bloch Equations

In this section, we discuss, model and characterize the laser-matter interaction for the systems of our interest – $^{171}\text{Yb}^+$ and $^{138}\text{Ba}^+$ ions. The evolution of these systems under laser excitation is described by optical Bloch equations. We show how to construct the optical Bloch equations and solve them for time evolution of the system subject to arbitrary interaction, as well as for excitation spectrum with the corresponding dark resonances.

First, in this subsection, we write optical Bloch equations for an atomic system described by Hamiltonian $H = H_{\text{atom}} + H_{\text{int}}$, where H_{atom} is the atomic Hamiltonian

and H_{int} is the laser-matter interaction Hamiltonian. We also take into account damping terms L_{damp} due to spontaneous emission and the finite laser linewidth. As a result, the system is no longer in a pure state and is described by a density operator $\hat{\rho}$.

In the basis $\{|i\rangle\}$ of the eigenstates $|i\rangle$ of H_{atom} , the density operator $\hat{\rho}$ is conventionally written down as:

$$\hat{\rho} = \sum_{i,j} \rho_{ij} |i\rangle\langle j|. \quad (2.1)$$

The time evolution of the density operator is described by the optical Bloch equations:

$$\frac{d\hat{\rho}}{dt} = -\frac{i}{\hbar} [\hat{H}, \hat{\rho}] + L_{\text{damp}}(\hat{\rho}), \quad (2.2)$$

where \hat{H} is the Hamiltonian of the system including interaction, and L_{damp} describes the damping terms:

$$L_{\text{damp}}(\hat{\rho}) = -\frac{1}{2} \sum_k \left(\hat{C}_k^\dagger \hat{C}_k \hat{\rho} + \hat{\rho} \hat{C}_k^\dagger \hat{C}_k - 2\hat{C}_k \hat{\rho} \hat{C}_k^\dagger \right). \quad (2.3)$$

Here, the operators \hat{C}_k govern various dissipative processes, and k enumerates them. The processes of decay from a level i to a level j with the corresponding decay rate Γ_{ij} are described as:

$$\hat{C}_k = \sqrt{\Gamma_{ij}} |j\rangle\langle i|. \quad (2.4)$$

The dissipation due to the finite laser linewidths Γ_{las} is accounted for via the

operators in the form:

$$\hat{C}_k = \sqrt{2\Gamma_{\text{las}}}|i\rangle\langle i|. \quad (2.5)$$

We can rewrite Eq. (2.2) as:

$$\begin{aligned} \frac{d\hat{\rho}}{dt} &= -\frac{i}{\hbar} \left[\left(\hat{H} - \frac{i\hbar}{2} \sum_k \hat{C}_k^\dagger \hat{C}_k \right) \hat{\rho} - \hat{\rho} \left(\hat{H} + \frac{i\hbar}{2} \sum_k \hat{C}_k^\dagger \hat{C}_k \right) \right] + \sum_k \hat{C}_k \hat{\rho} \hat{C}_k^\dagger \\ &= -\frac{i}{\hbar} \left[\tilde{H} \hat{\rho} - \hat{\rho} \tilde{H}^\dagger \right] + \sum_k \hat{C}_k \hat{\rho} \hat{C}_k^\dagger, \end{aligned} \quad (2.6)$$

where

$$\tilde{H} = \hat{H} - \frac{i\hbar}{2} \sum_k \hat{C}_k^\dagger \hat{C}_k. \quad (2.7)$$

Also we take into account the normalization condition:

$$\sum_i \rho_{ii} = 1. \quad (2.8)$$

The Bloch equation in components has the following form:

$$\begin{aligned} \frac{d\rho_{rs}}{dt} &= -\frac{i}{\hbar} \left\langle r \left| \left[\tilde{H} \rho - \rho \tilde{H}^\dagger \right] \right| s \right\rangle + \left\langle r \left| \sum_k \hat{C}_k \rho \hat{C}_k^\dagger \right| s \right\rangle \\ &= \sum_{mj} L_{rs,mj} \rho_{mj}, \end{aligned} \quad (2.9)$$

where

$$L_{rs,mj} = -\frac{i}{\hbar} \left[\tilde{H}_{rm} \delta_{js} - \tilde{H}_{js}^\dagger \delta_{rm} \right] + \sum_k \hat{C}_{krm} \hat{C}_{kjs}^\dagger. \quad (2.10)$$

Now we apply the optical Bloch equations for various atomic systems such as $^{171}\text{Yb}^+$ (a memory ion) and $^{138}\text{Ba}^+$ (a communication ion), to find excitation spectra with

the corresponding dark resonances. Also we consider $^{174}\text{Yb}^+$ system, since $^{174}\text{Yb}^+$ isotope was explored in our group before [103, 104], and it might turn out to be useful in the future experiments. For example, in Section 3.2.4, we will discuss a possibility of using $^{174}\text{Yb}^+$ ions to sympathetically cool $^{171}\text{Yb}^+$ ones.

2.1.1 Four-level system. $^{171}\text{Yb}^+$

a. Atomic Hamiltonian

$^{171}\text{Yb}^+$ has non-zero nuclear spin ($S_n = \frac{1}{2}$), and in a magnetic field, the splitting of the energy levels is given by:

$$\Delta E = m_F g_F \mu_B \left| \vec{B} \right| = m_F g_F u, \quad (2.11)$$

where $u = \mu_B \left| \vec{B} \right|$, μ_B is the Bohr magneton, \vec{B} is the magnetic field, and m_F is the projection of the full angular momentum $\vec{F} = \vec{J} + \vec{S}_n$. In the case of non-zero nuclear spin, the Lande factors [105] are given by the following formula:

$$g_F = g_J \frac{F(F+1) + J(J+1) - S_n(S_n+1)}{2F(F+1)}, \quad (2.12)$$

where

$$g_J = 1 + \frac{J(J+1) - L(L+1) + S(S+1)}{2J(J+1)}, \quad (2.13)$$

with the total angular momentum $\vec{J} = \vec{L} + \vec{S}$.

In Fig. 2.1, the diagram of $^{171}\text{Yb}^+$ energy levels is shown. The main transition at 369 nm, between the $S_{1/2}$ and $P_{1/2}$ states, is utilized to perform Doppler cooling,

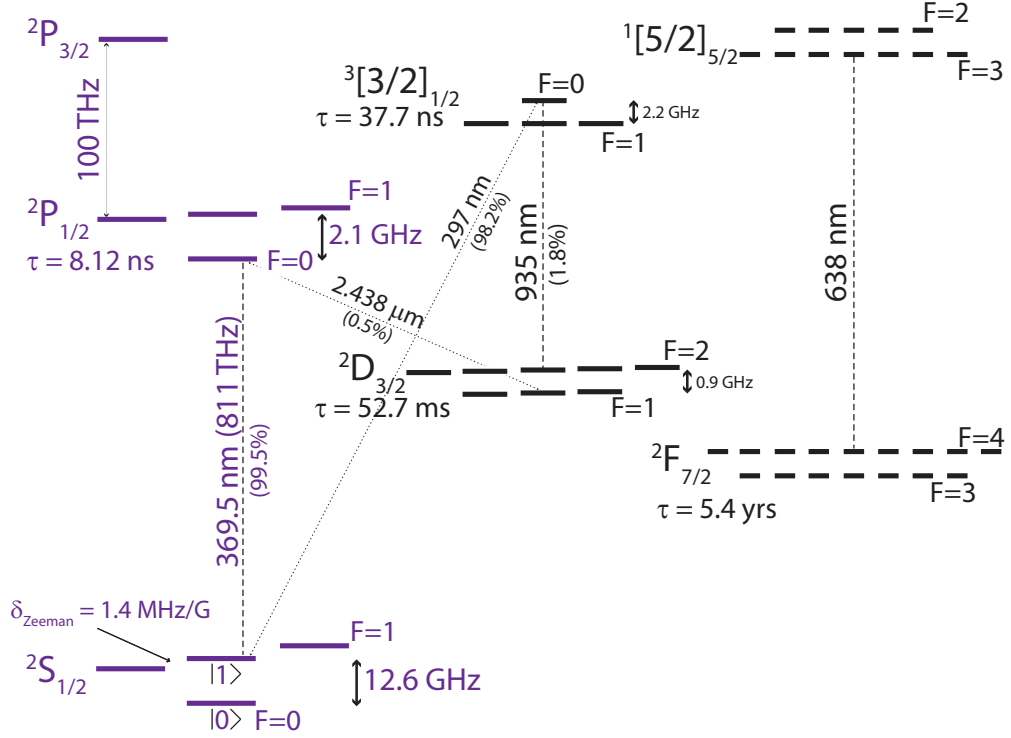


Figure 2.1: Energy level diagram for $^{171}\text{Yb}^+$. The qubit is defined in the $S_{1/2}$ ground state hyperfine “clock” levels denoted $|0\rangle$ and $|1\rangle$. The main transition at 369 nm shown in purple, between $S_{1/2}$ and $P_{1/2}$, is nearly a cycling transition. When the ion decays to $D_{3/2}$ manifold (0.5% of the time), it is repumped by 935 nm laser to the $^3[3/2]_{1/2}$ state, which quickly decays back to the $S_{1/2}$ manifold.

state initialization, and state readout using state-dependent fluorescence technique that we will discuss in Section 2.2.

The scheme of the $^{171}\text{Yb}^+$ levels relevant for these calculations – these levels nearly form a cycling transition – is presented in Fig. 2.2. According to this scheme,

$$g_F = 1.$$

Then $g_F \cdot m_F(|1\rangle) = -1$, $g_F \cdot m_F(|2\rangle) = 0$, and $g_F \cdot m_F(|3\rangle) = 1$.

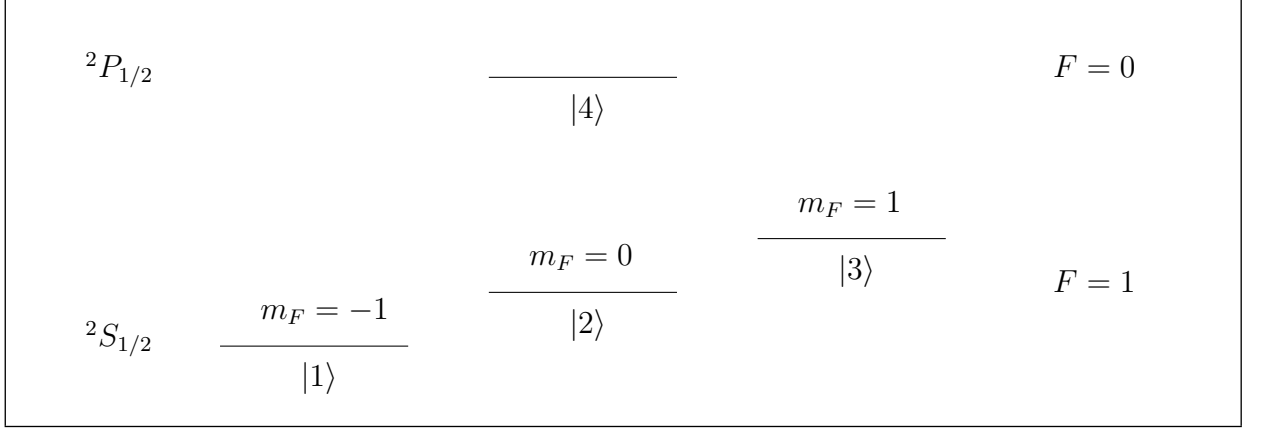


Figure 2.2: Hyperfine structure level scheme of $^{171}\text{Yb}^+$ with Zeeman splitting relevant for calculations.

The atomic Hamiltonian is given by:

$$\begin{aligned}
 \hat{H}_{\text{atom}} &= \sum_{a=1}^4 \hbar\omega_a |a\rangle\langle a| \\
 &= \hbar(\omega_s - \omega_p - u)|1\rangle\langle 1| + \hbar(\omega_s - \omega_p)|2\rangle\langle 2| + \hbar(\omega_s - \omega_p + u)|3\rangle\langle 3|, \quad (2.14)
 \end{aligned}$$

where $\hbar\omega_s$ and $\hbar\omega_p$ represent energy levels of the $S_{1/2}$ and $P_{1/2}$ states. Here we assign zero energy to the state $|4\rangle$.

b. Interaction Hamiltonian

Let us choose the z -axis to be along the magnetic field, and the y -axis to be along the light propagation direction. Then the polarization vector lies in the $(x-z)$ -plane:

$$\vec{\epsilon} = \begin{pmatrix} \sin(\alpha) \\ 0 \\ \cos(\alpha) \end{pmatrix}. \quad (2.15)$$

The dipole moment operator is written as:

$$\begin{aligned}\hat{\vec{D}} &= \vec{D}_{14}|1\rangle\langle 4| + \vec{D}_{24}|2\rangle\langle 4| + \vec{D}_{34}|3\rangle\langle 4| + \text{H.c.}, \\ \vec{D}_{ab} &= \langle a|e\vec{r}|b\rangle.\end{aligned}\tag{2.16}$$

We express the position operator in terms of the spherical harmonics:

$$\vec{r} = \begin{pmatrix} x \\ y \\ z \end{pmatrix} = \begin{pmatrix} \frac{1}{\sqrt{2}} (Q_1^{-1} - Q_1^1) \\ \frac{i}{\sqrt{2}} (Q_1^{-1} + Q_1^1) \\ Q_1^0 \end{pmatrix},\tag{2.17}$$

where

$$Q_l^m = \sqrt{\frac{4\pi}{2l+1}} r^l Y_l^m(\theta, \phi).\tag{2.18}$$

The corresponding matrix element is given by:

$$\langle a|Q_1^m|b\rangle = \langle n_a L_a S_a S_{n_a} F_a m_{F_a} | Q_1^m | n_b L_b S_b S_{n_b} F_b m_{F_b} \rangle.\tag{2.19}$$

First, we consider the coupling between the orbital momentum \vec{L} and electron spin \vec{S} that is described by a Clebsch-Gordan coefficient $C_{l m_l s m_s}^{j m_j}$, and after that the coupling between the total momentum \vec{J} and the nuclear spin \vec{S}_n described by

$$C_{jm_j s_n m_{s_n}}^{Fm_F} \text{ [106].}$$

$$\begin{aligned} \langle a | Q_1^m | b \rangle &= \sum_{m_{l_a} m_{s_a} m_{s_{n_a}}} \sum_{m_{l_b} m_{s_b} m_{s_{n_b}}} C_{j_a m_{j_a} s_{n_a} m_{s_{n_a}}}^{F_a m_{F_a}} C_{l_a m_{l_a} s_a m_{s_a}}^{j_a m_{j_a}} C_{j_b m_{j_b} s_{n_b} m_{s_{n_b}}}^{F_b m_{F_b}} C_{l_b m_{l_b} s_b m_{s_b}}^{j_b m_{j_b}} \\ &\times \langle L_a m_{l_a} | Q_1^m | L_b m_{l_b} \rangle \delta_{m_{s_a} m_{s_b}} \delta_{m_{s_{n_a}} m_{s_{n_b}}}. \end{aligned} \quad (2.20)$$

According to the Eckart-Wigner theorem,

$$\langle L_a m_{l_a} | Q_1^m | L_b m_{l_b} \rangle = \frac{1}{\sqrt{2L_a + 1}} C_{l_b m_{l_b} 1 m}^{l_a m_{l_a}} \langle n_a L_a || Q_1 || n_b L_b \rangle, \quad (2.21)$$

where $\langle n_a L_a || Q_1 || n_b L_b \rangle = d$ is the reduced matrix element that does not depend on m_F . Calculating the matrix elements using the Clebsch-Gordan coefficients, we get:

$$\vec{D}_{41} = d \begin{pmatrix} -\frac{1}{\sqrt{6}} \\ \frac{1}{\sqrt{6}} \\ 0 \end{pmatrix}, \quad \vec{D}_{42} = d \begin{pmatrix} 0 \\ 0 \\ -\frac{1}{\sqrt{3}} \end{pmatrix}, \quad \vec{D}_{43} = d \begin{pmatrix} \frac{1}{\sqrt{6}} \\ \frac{1}{\sqrt{6}} \\ 0 \end{pmatrix}. \quad (2.22)$$

Since the interaction Hamiltonian

$$\hat{H}_{\text{int}} \sim -\hat{\vec{D}} \cdot \vec{\epsilon}, \quad (2.23)$$

then

$$\begin{aligned}
(H_{\text{int}})_{14} &= -\Omega \frac{1}{\sqrt{6}} \sin \alpha e^{i\omega t}, \\
(H_{\text{int}})_{24} &= -\Omega \frac{1}{\sqrt{3}} \cos \alpha e^{i\omega t}, \\
(H_{\text{int}})_{34} &= \Omega \frac{1}{\sqrt{6}} \sin \alpha e^{i\omega t},
\end{aligned} \tag{2.24}$$

where Ω is a Rabi frequency, and ω is a frequency of the laser field.

The total Hamiltonian has the following form:

$$H = \begin{pmatrix} \omega_s - \omega_p - u & 0 & 0 & -\Omega \frac{1}{\sqrt{6}} \sin \alpha e^{i\omega t} \\ 0 & \omega_s - \omega_p & 0 & -\Omega \frac{1}{\sqrt{3}} \cos \alpha e^{i\omega t} \\ 0 & 0 & \omega_s - \omega_p + u & \Omega \frac{1}{\sqrt{6}} \sin \alpha e^{i\omega t} \\ -\Omega \frac{1}{\sqrt{6}} \sin \alpha e^{-i\omega t} & -\Omega \frac{1}{\sqrt{3}} \cos \alpha e^{-i\omega t} & \Omega \frac{1}{\sqrt{6}} \sin \alpha e^{-i\omega t} & 0 \end{pmatrix}. \tag{2.25}$$

Going to the rotating frame and applying the rotating wave approximation (RWA),

we get

$$H = \begin{pmatrix} \Delta - u & 0 & 0 & -\Omega \frac{1}{\sqrt{6}} \sin \alpha \\ 0 & \Delta & 0 & -\Omega \frac{1}{\sqrt{3}} \cos \alpha \\ 0 & 0 & \Delta + u & \Omega \frac{1}{\sqrt{6}} \sin \alpha \\ -\Omega \frac{1}{\sqrt{6}} \sin \alpha & -\Omega \frac{1}{\sqrt{3}} \cos \alpha & \Omega \frac{1}{\sqrt{6}} \sin \alpha & 0 \end{pmatrix}, \tag{2.26}$$

where $\Delta = \omega - \omega_s + \omega_p$ is the laser detuning.

c. Damping terms

Now, let us consider the dissipative processes.

If the total decay rate from the state $|4\rangle$ is equal to Γ , then using Eq. (2.22), we find

$$\Gamma_{14} = \Gamma_{24} = \Gamma_{34} = \frac{1}{3}\Gamma. \quad (2.27)$$

Consequently, the corresponding operators have the following form:

$$\begin{aligned} C_1 &= \sqrt{\frac{\Gamma}{3}}|1\rangle\langle 4|, \\ C_2 &= \sqrt{\frac{\Gamma}{3}}|2\rangle\langle 4|, \\ C_3 &= \sqrt{\frac{\Gamma}{3}}|3\rangle\langle 4|, \\ C_4 &= \sqrt{2\Gamma_{\text{las}}}(|1\rangle\langle 1| + |2\rangle\langle 2| + |3\rangle\langle 3|). \end{aligned} \quad (2.28)$$

d. Results

In order to verify the calculation results, we compare the excited-state population ρ_{44} with the analytic steady-state solution (assuming the laser linewidth is equal to zero) from Ref. [107]:

$$\rho_{44} = \frac{3}{4} \frac{\Omega^2 \cos^2 \alpha \sin^2 \alpha}{1 + 3 \cos^2 \alpha} \frac{1}{(\gamma'/2)^2 + \Delta^2}, \quad (2.29)$$

where

$$\left(\frac{\gamma'}{2}\right)^2 = \left(\frac{\Gamma}{2}\right)^2 + \Omega^2 \cos^2 \alpha \frac{1 - 3 \cos^2 \alpha}{1 + 3 \cos^2 \alpha} + \frac{\cos^2 \alpha}{1 + 3 \cos^2 \alpha} \left(\frac{\Omega^4}{4u^2} + 4u^2\right). \quad (2.30)$$

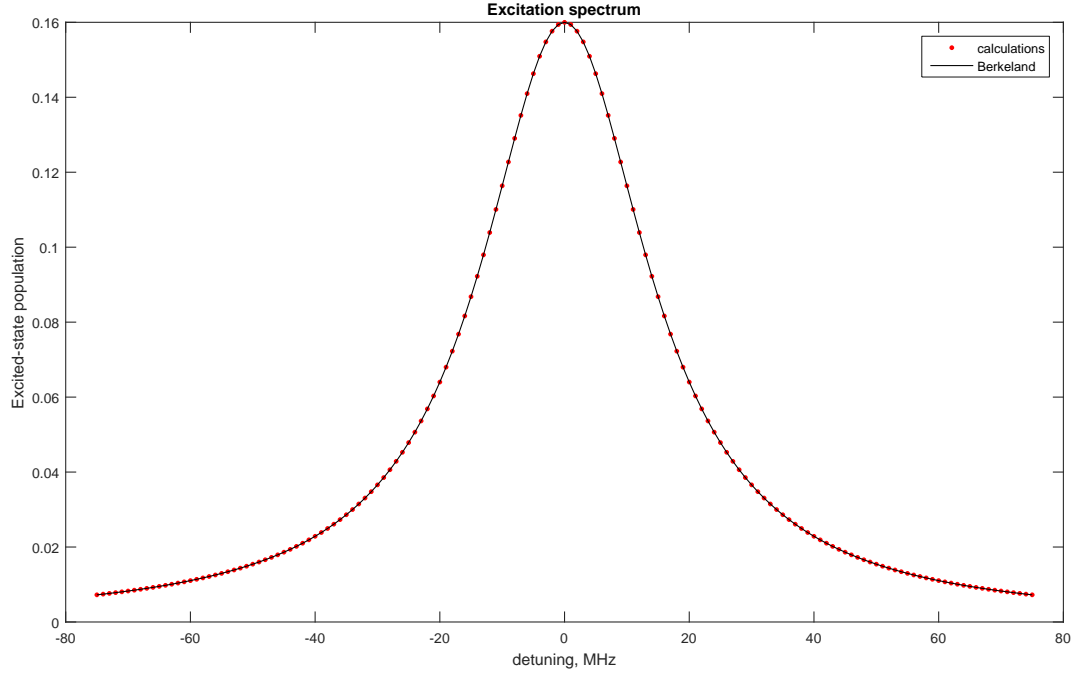


Figure 2.3: Excitation spectrum of a four-level $^{171}\text{Yb}^+$. Parameters: $\Gamma_{\text{las}} = 0$, $u = 11.35$ MHz, $\alpha = \arccos(1/\sqrt{3})$, saturation parameter $s = \Omega/\Gamma = 1$. Red dots represent our solutions of the optical Bloch equations for a four-level model of $^{171}\text{Yb}^+$; black solid curve is obtained from Eq. (2.29).

In Fig. 2.3, we demonstrate a comparison between our solutions of the optical Bloch equations for a four-level model of $^{171}\text{Yb}^+$ – shown by red dots – and the analytic steady-state solution given by Eq. (2.29) – shown by black curve. We find a perfect agreement between the two. The parameters of the magnetic field u and

the laser-polarization angle α are chosen to maximize the excited-state population $\rho_e = \rho_{44}$, or in other words, the scattering rate S , since $S = \gamma\rho_e$. To maximize ρ_{44} , we need to minimize $(\gamma'/2)^2$ from Eqs. (2.29) and (2.30), and that means that for a given Rabi frequency Ω the magnetic-field strength u is chosen to be $u = \Omega/2$ and the angle is $\alpha = \arccos(1/\sqrt{3})$. This particular laser-polarization angle makes the three transition Rabi frequencies equal.

Moreover, when we choose $\alpha = 0$, in our calculations we achieve zero scattering rate, which matches with Eq. (2.29) and $\rho_{44} = 0$. In this case, the laser light has only π polarization, and the ion quickly decays to a dark state – a combination of the edge states $|1\rangle$ and $|3\rangle$ from Fig. 2.2. Similarly, when $\alpha = \pi/2$, our calculations and Eq. (2.29) give us $\rho_{44} = 0$. Here, the laser light has only σ polarization, and the ion quickly decays to a dark state $|2\rangle$.

Furthermore, when the magnetic field $B = 0$, in $^{171}\text{Yb}^+$ level configuration, there are always two dark states for any laser polarization according to Ref. [107], and the ion does not fluoresce at all. In our calculations, zero excited-state population was obtained in accordance with this analytic finding.

2.1.2 Four-level system. $^{174}\text{Yb}^+$

a. Atomic Hamiltonian

$^{174}\text{Yb}^+$ has zero nuclear spin, and in a magnetic field, the splitting of the energy levels is given by:

$$\Delta E = m_J g_J \mu_B \left| \vec{B} \right| = m_J g_J u. \quad (2.31)$$

Fine structure level scheme of $^{174}\text{Yb}^+$ is presented in Fig. 2.4.

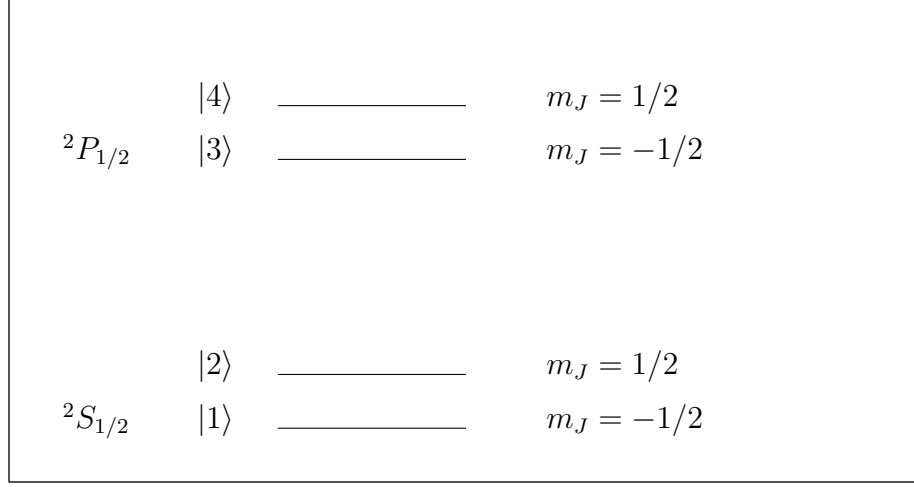


Figure 2.4: Fine structure level scheme of $^{174}\text{Yb}^+$ with Zeeman splitting.

According to this scheme, $g_J(^2S_{1/2}) = 2$ and $g_J(^2P_{1/2}) = 2/3$, thus we get $g_J \cdot m_J(|1\rangle) = -1$, $g_J \cdot m_J(|2\rangle) = 1$, $g_J \cdot m_J(|3\rangle) = -1/3$, and $g_J \cdot m_J(|4\rangle) = 1/3$.

The atomic Hamiltonian is given by:

$$\begin{aligned} \hat{H}_{\text{atom}} &= \sum_{a=1}^4 \hbar\omega_a |a\rangle\langle a| \\ &= \hbar(\omega_s - \omega_p - u)|1\rangle\langle 1| + \hbar(\omega_s - \omega_p + u)|2\rangle\langle 2| - \frac{1}{3}\hbar u|3\rangle\langle 3| + \frac{1}{3}\hbar u|4\rangle\langle 4|, \end{aligned} \quad (2.32)$$

here we assign zero energy to the middle between the states $|3\rangle$ and $|4\rangle$.

b. Interaction Hamiltonian

Similar to the case of $^{171}\text{Yb}^+$, we choose z -axis along the magnetic field, and y -axis along the light propagation direction, so that the polarization vector lies in the

x - z -plane:

$$\vec{\epsilon} = \begin{pmatrix} \sin(\alpha) \\ 0 \\ \cos(\alpha) \end{pmatrix}, \quad (2.33)$$

The dipole moment operator is:

$$\hat{\vec{D}} = \vec{D}_{13}|1\rangle\langle 3| + \vec{D}_{14}|1\rangle\langle 4| + \vec{D}_{23}|2\rangle\langle 3| + \vec{D}_{24}|2\rangle\langle 4| + \text{H.c.}, \quad (2.34)$$

$$\vec{D}_{ab} = \langle a | e\vec{r} | b \rangle.$$

$^{174}\text{Yb}^+$ has zero nuclear spin. Therefore, in contrast to Eq. (2.20), the corresponding matrix elements are given by:

$$\langle a | Q_1^m | b \rangle = \sum_{m_{l_a} m_{s_a}} \sum_{m_{l_b} m_{s_b}} C_{l_a m_{l_a} s_a m_{s_a}}^{j_a m_{j_a}} C_{l_b m_{l_b} s_b m_{s_b}}^{j_b m_{j_b}} \langle L_a m_{l_a} | Q_1^m | L_b m_{l_b} \rangle \delta_{m_{s_a} m_{s_b}}. \quad (2.35)$$

According to the Eckhart-Wigner theorem,

$$\langle L_a m_{l_a} | Q_1^m | L_b m_{l_b} \rangle = \frac{1}{\sqrt{2L_a + 1}} C_{l_b m_{l_b} 1 m}^{l_a m_{l_a}} \langle n_a L_a || Q_1 || n_b L_b \rangle, \quad (2.36)$$

where $\langle n_a L_a || Q_1 || n_b L_b \rangle = d$ is the reduced matrix element that does not depend on m_J .

Performing the calculations with the Clebsch-Gordan coefficients, we get:

$$\vec{D}_{31} = d \begin{pmatrix} 0 \\ 0 \\ \frac{1}{\sqrt{3}} \end{pmatrix}, \quad \vec{D}_{41} = d \begin{pmatrix} -\frac{1}{\sqrt{3}} \\ \frac{i}{\sqrt{3}} \\ 0 \end{pmatrix}, \quad \vec{D}_{32} = d \begin{pmatrix} -\frac{1}{\sqrt{3}} \\ -\frac{i}{\sqrt{3}} \\ 0 \end{pmatrix}, \quad \vec{D}_{42} = d \begin{pmatrix} 0 \\ 0 \\ -\frac{1}{\sqrt{3}} \end{pmatrix}. \quad (2.37)$$

And the total Hamiltonian in the rotating wave approximation is:

$$H = \begin{pmatrix} \Delta - u & 0 & \Omega \frac{1}{\sqrt{3}} \cos \alpha & -\Omega \frac{1}{\sqrt{3}} \sin \alpha \\ 0 & \Delta + u & -\Omega \frac{1}{\sqrt{3}} \sin \alpha & -\Omega \frac{1}{\sqrt{3}} \cos \alpha \\ \Omega \frac{1}{\sqrt{3}} \cos \alpha & -\Omega \frac{1}{\sqrt{3}} \sin \alpha & -\frac{1}{3}u & 0 \\ -\Omega \frac{1}{\sqrt{3}} \sin \alpha & -\Omega \frac{1}{\sqrt{3}} \cos \alpha & 0 & \frac{1}{3}u \end{pmatrix}, \quad (2.38)$$

where $\Delta = \omega - \omega_s + \omega_p$ is the laser detuning.

c. Damping terms

Now, let us consider the dissipative processes.

If the total decay rate from the state $|3\rangle$ is equal to Γ , and similarly the total decay rate from the state $|4\rangle$ is equal to Γ , then, using Eq. (2.37), we find

$$\Gamma_{13} = \Gamma_{24} = \frac{1}{3}\Gamma, \quad \Gamma_{23} = \Gamma_{14} = \frac{2}{3}\Gamma. \quad (2.39)$$

Consequently, the corresponding operators are:

$$\begin{aligned}
C_1 &= \sqrt{\frac{2\Gamma}{3}}|1\rangle\langle 4|, \\
C_2 &= \sqrt{\frac{2\Gamma}{3}}|2\rangle\langle 3|, \\
C_3 &= \sqrt{\frac{\Gamma}{3}}(|1\rangle\langle 3| - |2\rangle\langle 4|), \\
C_4 &= \sqrt{2\Gamma_{\text{las}}}(|1\rangle\langle 1| + |2\rangle\langle 2|).
\end{aligned} \tag{2.40}$$

d. Results

The results of this calculation are given in Fig. 2.5. In order to verify them, we compare the excited-state population as a solution to the optical Bloch equations with the analytic steady-state solution (assuming the laser linewidth is equal to zero) in a zero magnetic field. In this case, the ion is described as a two-level system:

$$\rho_{\text{exc}} = \frac{\frac{1}{2} \cdot \frac{I}{I_{\text{sat}}}}{1 + \frac{I}{I_{\text{sat}}} + 4 \left(\frac{\Delta}{\Gamma} \right)^2}. \tag{2.41}$$

The calculations that we perform and the analytical solution are again in a perfect agreement with each other.

The maximum possible scattering rate can be achieved with the laser intensities much higher than the saturation intensity I_{sat} . Thus, with $\frac{I}{I_{\text{sat}}} \gg 1$, we get $S = \frac{\Gamma}{2}$, and our calculations match this result. Additionally, for $I = I_{\text{sat}}$, and $S = \Gamma/4$, our calculations again agree with the analytical result.

At this point we have only discussed the case of zero magnetic field $B = 0$ for a four-level model of $^{174}\text{Yb}^+$. When the magnetic field is non-zero, $B \neq 0$, the highest

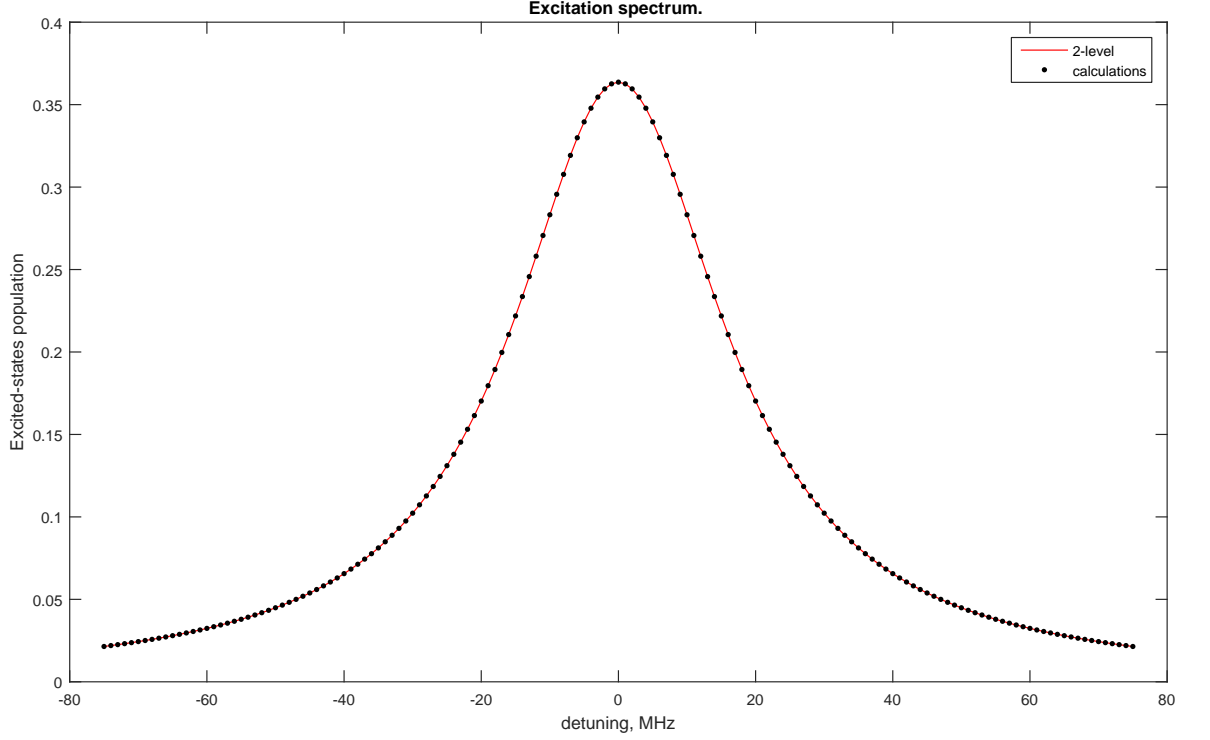


Figure 2.5: Excitation spectrum of $^{174}\text{Yb}^+$. Parameters: $\Gamma_{\text{las}} = 0$, $u = 0$, $\alpha = 0$, saturation parameter $s = \Omega/\Gamma = 1$. Red dots represent our calculations of the Bloch equations for a four-level model of $^{174}\text{Yb}^+$; black solid curve describes a two-level model solution, which is identical to the four-level one at zero magnetic field.

scattering rate can be achieved with the laser-polarization angle $\alpha = 0$ according to our calculations. This angle α corresponds to the π polarization of the laser light. According to Ref. [107], when circularly polarized light is applied, there is always a dark state in the case of $^{174}\text{Yb}^+$ system. Therefore, this dark state decreases the brightness of the ion when the light is not perfectly π polarized.

2.1.3 Eight-level system. $^{138}\text{Ba}^+$

The following calculations are based in part on Refs. [108, 109].

a. Atomic Hamiltonian

$^{138}\text{Ba}^+$ also has zero nuclear spin, as well as $^{174}\text{Yb}^+$, and in a magnetic field, the splitting of the energy levels is given by:

$$\Delta E = m_J g_J \mu_B |\vec{B}| = m_J g_J u. \quad (2.42)$$

Fine structure level scheme of $^{138}\text{Ba}^+$ is presented in Fig. 2.6.

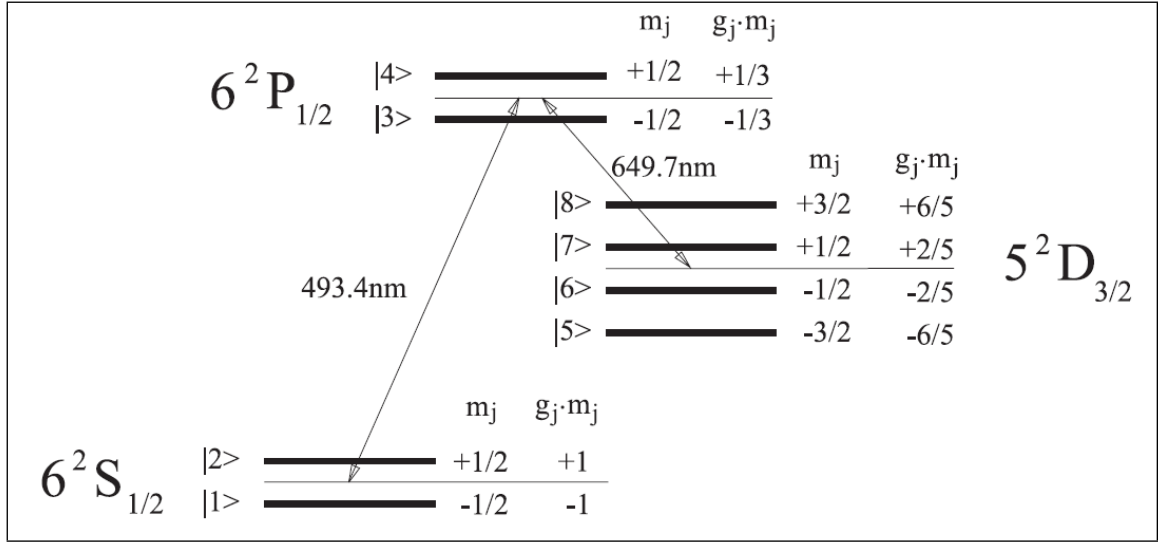


Figure 2.6: Fine structure level scheme of $^{138}\text{Ba}^+$ with Zeeman splitting.

The atomic Hamiltonian has the following form:

$$\begin{aligned}
\hat{H}_{\text{atom}} &= \sum_{a=1}^8 \hbar \omega_a |a\rangle \langle a| = \hbar(\omega_s - \omega_p - u) |1\rangle \langle 1| + \hbar(\omega_s - \omega_p + u) |2\rangle \langle 2| \\
&- \frac{1}{3} \hbar u |3\rangle \langle 3| + \frac{1}{3} \hbar u |4\rangle \langle 4| + \hbar(\omega_D - \omega_p - \frac{6}{5}u) |5\rangle \langle 5| + \hbar(\omega_D - \omega_p - \frac{2}{5}u) |6\rangle \langle 6| \\
&+ \hbar(\omega_D - \omega_p + \frac{2}{5}u) |7\rangle \langle 7| + \hbar(\omega_D - \omega_p + \frac{6}{5}u) |8\rangle \langle 8|,
\end{aligned} \tag{2.43}$$

where we assign zero energy to the middle between the energies of the states $|3\rangle$ and $|4\rangle$.

b. Interaction Hamiltonian

Similar to the previous cases, the dipole moment operator is given by:

$$\begin{aligned}
\hat{\vec{D}} &= \vec{D}_{13} |1\rangle \langle 3| + \vec{D}_{14} |1\rangle \langle 4| + \vec{D}_{23} |2\rangle \langle 3| + \vec{D}_{24} |2\rangle \langle 4| + \vec{D}_{53} |5\rangle \langle 3| + \vec{D}_{54} |5\rangle \langle 4| \\
&+ \vec{D}_{63} |6\rangle \langle 3| + \vec{D}_{64} |6\rangle \langle 4| + \vec{D}_{73} |7\rangle \langle 3| + \vec{D}_{74} |7\rangle \langle 4| + \vec{D}_{83} |8\rangle \langle 3| + \vec{D}_{84} |8\rangle \langle 4| + \text{H.c.}, \\
\vec{D}_{ij} &= \langle a | e \vec{r} | b \rangle.
\end{aligned} \tag{2.44}$$

Performing the calculations with the Clebsch-Gordan coefficients, we get:

$$\begin{aligned}
\vec{D}_{31} &= d_g \begin{pmatrix} 0 \\ 0 \\ \frac{1}{\sqrt{3}} \end{pmatrix}, & \vec{D}_{41} &= d_g \begin{pmatrix} -\frac{1}{\sqrt{3}} \\ \frac{i}{\sqrt{3}} \\ 0 \end{pmatrix}, & \vec{D}_{32} &= d_g \begin{pmatrix} -\frac{1}{\sqrt{3}} \\ -\frac{i}{\sqrt{3}} \\ 0 \end{pmatrix}, & \vec{D}_{31} &= d_g \begin{pmatrix} 0 \\ 0 \\ -\frac{1}{\sqrt{3}} \end{pmatrix}, \\
\vec{D}_{35} &= d_r \begin{pmatrix} -\frac{1}{2} \\ -\frac{i}{2} \\ 0 \end{pmatrix}, & \vec{D}_{45} &= d_r \begin{pmatrix} 0 \\ 0 \\ 0 \end{pmatrix}, & \vec{D}_{36} &= d_r \begin{pmatrix} 0 \\ 0 \\ -\frac{1}{\sqrt{3}} \end{pmatrix}, & \vec{D}_{46} &= d_r \begin{pmatrix} -\frac{1}{2\sqrt{3}} \\ \frac{i}{2\sqrt{3}} \\ 0 \end{pmatrix}, \\
& & & & & (2.45) \\
\vec{D}_{37} &= d_r \begin{pmatrix} \frac{1}{2\sqrt{3}} \\ \frac{i}{2\sqrt{3}} \\ 0 \end{pmatrix}, & \vec{D}_{47} &= d_r \begin{pmatrix} 0 \\ 0 \\ -\frac{1}{\sqrt{3}} \end{pmatrix}, & \vec{D}_{38} &= d_r \begin{pmatrix} 0 \\ 0 \\ 0 \end{pmatrix}, & \vec{D}_{48} &= d_r \begin{pmatrix} -\frac{1}{2} \\ \frac{i}{2} \\ 0 \end{pmatrix}.
\end{aligned}$$

And the total Hamiltonian in the rotating wave approximation (RWA) is pre-

sented in the matrix form:

$$H = \begin{pmatrix} \Delta_g - u & 0 & \frac{\Omega_g}{\sqrt{3}} \cos \alpha & -\frac{\Omega_g}{\sqrt{3}} \sin \alpha & 0 & 0 & 0 & 0 \\ 0 & \Delta_g + u & -\frac{\Omega_g}{\sqrt{3}} \sin \alpha & -\frac{\Omega_g}{\sqrt{3}} \cos \alpha & 0 & 0 & 0 & 0 \\ \frac{\Omega_g}{\sqrt{3}} \cos \alpha & -\frac{\Omega_g}{\sqrt{3}} \sin \alpha & -\frac{1}{3}u & 0 & -\frac{\Omega_r}{2} \sin \alpha & -\frac{\Omega_r}{\sqrt{3}} \cos \alpha & \frac{\Omega_r}{2\sqrt{3}} \sin \alpha & 0 \\ -\frac{\Omega_g}{\sqrt{3}} \sin \alpha & -\frac{\Omega_g}{\sqrt{3}} \cos \alpha & 0 & \frac{1}{3}u & 0 & -\frac{\Omega_r}{2\sqrt{3}} \sin \alpha & -\frac{\Omega_r}{\sqrt{3}} \cos \alpha & \frac{\Omega_r}{2} \sin \alpha \\ 0 & 0 & -\frac{\Omega_r}{2} \sin \alpha & 0 & \Delta_r - \frac{6}{5}u & 0 & 0 & 0 \\ 0 & 0 & -\frac{\Omega_r}{\sqrt{3}} \cos \alpha & -\frac{\Omega_r}{2\sqrt{3}} \sin \alpha & 0 & \Delta_r - \frac{2}{5}u & 0 & 0 \\ 0 & 0 & \frac{\Omega_r}{2\sqrt{3}} \sin \alpha & -\frac{\Omega_r}{\sqrt{3}} \cos \alpha & 0 & 0 & \Delta_r + \frac{2}{5}u & 0 \\ 0 & 0 & 0 & \frac{\Omega_r}{2} \sin \alpha & 0 & 0 & 0 & \Delta_r + \frac{6}{5}u \end{pmatrix}, \quad (2.46)$$

where the corresponding detunings $\Delta_g = \omega_g - \omega_s + \omega_p$ and $\Delta_r = \omega_r - \omega_s + \omega_p$.

c. Damping terms

Now, let us consider the dissipative processes such as spontaneous emission and the finite laser linewidth.

In this case, there are two decay rates Γ_g and Γ_r . Using Eq. (2.45), we find

$$\begin{aligned}
\Gamma_{13} &= \Gamma_{24} = \frac{1}{3}\Gamma_g, & \Gamma_{23} &= \Gamma_{14} = \frac{2}{3}\Gamma_g, \\
\Gamma_{35} &= \Gamma_{48} = \frac{1}{2}\Gamma_r, & \Gamma_{36} &= \Gamma_{47} = \frac{1}{3}\Gamma_r, \\
\Gamma_{37} &= \Gamma_{46} = \frac{1}{6}\Gamma_r, & \Gamma_{38} &= \Gamma_{45} = 0.
\end{aligned} \tag{2.47}$$

Consequently, the corresponding operators are:

$$\begin{aligned}
C_1 &= \sqrt{\frac{2\Gamma_g}{3}}|1\rangle\langle 4|, \\
C_2 &= \sqrt{\frac{2\Gamma_g}{3}}|2\rangle\langle 3|, \\
C_3 &= \sqrt{\frac{\Gamma_g}{3}}(|1\rangle\langle 3| - |2\rangle\langle 4|), \\
C_4 &= \sqrt{\frac{\Gamma_r}{2}}|5\rangle\langle 3| + \sqrt{\frac{\Gamma_r}{6}}|6\rangle\langle 4|, \\
C_5 &= \sqrt{\frac{\Gamma_r}{2}}|8\rangle\langle 4| + \sqrt{\frac{\Gamma_r}{6}}|7\rangle\langle 3|, \\
C_6 &= \sqrt{\frac{\Gamma_r}{3}}(|6\rangle\langle 3| + |7\rangle\langle 4|), \\
C_7 &= \sqrt{2\Gamma_{las_g}}(|1\rangle\langle 1| + |2\rangle\langle 2|), \\
C_8 &= \sqrt{2\Gamma_{las_r}}(|5\rangle\langle 5| + |6\rangle\langle 6| + |7\rangle\langle 7| + |8\rangle\langle 8|),
\end{aligned} \tag{2.48}$$

d. Results

In Figs. 2.7 – 2.8, we show the excitation spectrum of an eight-level model of $^{138}\text{Ba}^+$ as a function of 493 nm and 650 nm laser frequencies (see Fig. 2.6), respectively. The experimental data shown in solid black dots is obtained by counting a photon number on a detector – on an APD in our case. The solid line is a fit to the experimental

data calculated with the eight-level Bloch equations. The disagreement between the fit and the experimental data can be caused by a frequency drift in the lock or larger laser linewidth than assumed.

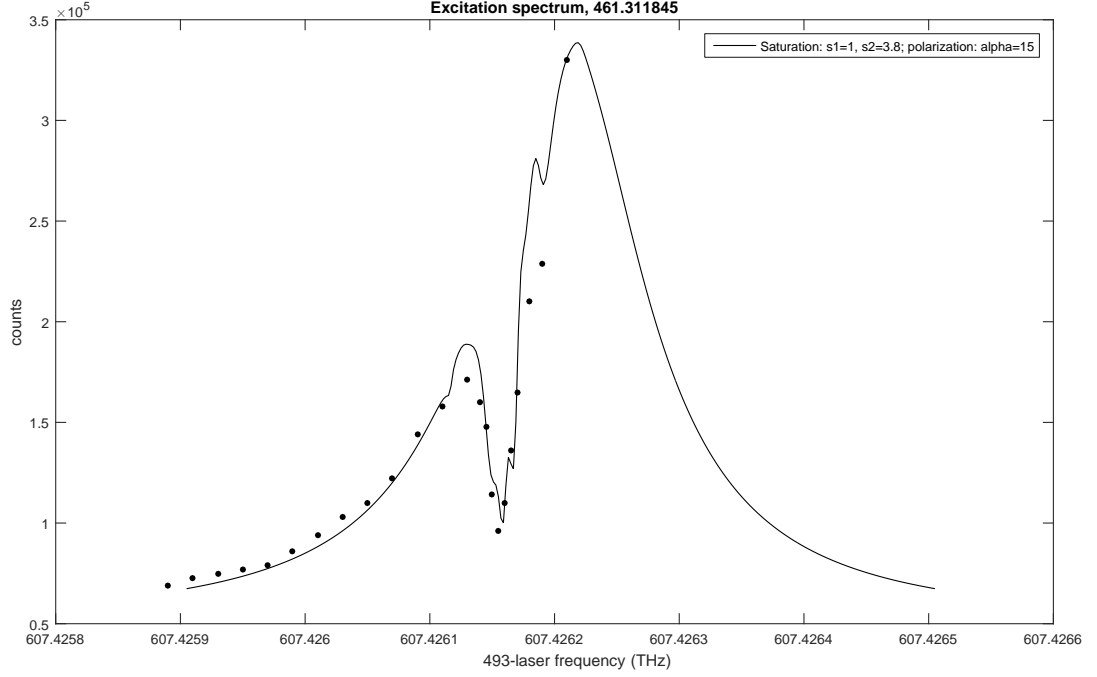


Figure 2.7: Excitation spectrum of an eight-level model of $^{138}\text{Ba}^+$ as a function of 493 nm laser frequency. Parameters: $\omega_r = 461.311845$ THz, $u = 11.35$ MHz, $\alpha = 15^\circ$, saturation parameters $s_g = \Omega_g/\Gamma = 1$ and $s_r = \Omega_r/\Gamma = 3.8$. The experimental data is presented in black dots; the solid black curve represents our solution of the optical Bloch equations fitted to the data over the saturation parameters s_g and s_r and the angle α .

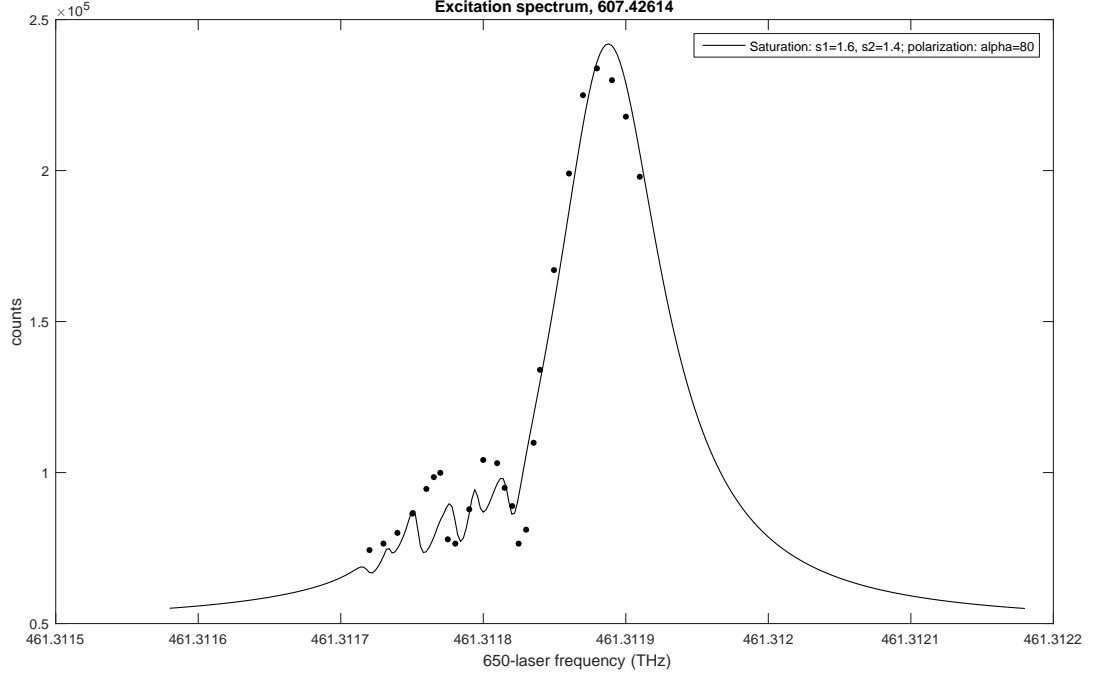


Figure 2.8: Excitation spectrum of an eight-level model of $^{138}\text{Ba}^+$ as a function of 650 nm laser frequency. Parameters: $\omega_g = 607.42614\text{THz}$, $u = 11.35\text{ MHz}$, $\alpha = 80^\circ$, saturation parameters $s_g = \Omega_g/\Gamma = 1.6$ and $s_r = \Omega_r/\Gamma = 1.4$. The experimental data is presented in solid black dots; the solid black curve represents our solution of the optical Bloch equations fitted to the data over the saturation parameters s_g and s_r and the angle α .

2.2 Ytterbium operations

In the network experiments, $^{171}\text{Yb}^+$ ions are used for quantum memory and processing. The qubits are based on the hyperfine “clock” sublevels of the $S_{1/2}$ ground manifold:

$$|F = 0, m_F = 0\rangle \equiv |0\rangle \text{ and } |F = 1, m_F = 0\rangle \equiv |1\rangle,$$

and they are insensitive to magnetic field fluctuations and hence have long coherence times [26, 27]. In reality, the qubit splitting is magnetically insensitive only to the second order and is given by: $12642812118.5 \text{ Hz} + \Delta$, where $\Delta = 310.8 B^2 \text{ Hz}$ with the magnetic field B in Gauss. In our experiments, $B \sim 5 \text{ G}$ making this sensitivity negligible.

In Fig. 2.1, the diagram of the most relevant $^{171}\text{Yb}^+$ energy levels is shown. The main transition at 369 nm, between the $S_{1/2}$ and $P_{1/2}$ states, is utilized to perform Doppler cooling, state initialization, and state readout using state-dependent fluorescence technique. 0.5% of the time the ion decays to $D_{3/2}$ manifold, and – by sending 935 nm light with 3.07 GHz sidebands produced by an electro-optic modulator (EOM) – we can repump the ion to the $^3[3/2]_{1/2}$ state, which then quickly decays back to the $S_{1/2}$ manifold [110, 111].

2.2.1 State initialization and readout

To perform Doppler cooling on $^{171}\text{Yb}^+$ ions, we apply a 369 nm laser light which is red-detuned [111, 112] from the $S_{1/2} |F = 1\rangle \leftrightarrow P_{1/2} |F = 0\rangle$ transition.

The most efficient cooling can be achieved when the laser is detuned by half of the 20 MHz transition linewidth away from the resonance. In order to cool motional modes in all three dimensions, the 369 nm laser beam should form an acute angle with the principal axes of the trap [113]. Due to off-resonant coupling to the $P_{1/2} |F = 1\rangle$ manifold, the ion might be trapped in the state $|0\rangle$. To avoid this issue, we add $14.7 \text{ GHz} = (12.6 + 2.1) \text{ GHz}$ sidebands that return the ion to the main cooling cycle via the $S_{1/2} |F = 0\rangle \leftrightarrow P_{1/2} |F = 1\rangle$ transition as shown in Fig. 2.9(a).

Optical pumping to the $|0\rangle$ state is an important step at the beginning of each experiment. In Fig. 2.9(b), the scheme of the qubit initialization is presented. By adding 2.1 GHz sidebands to the resonant 369 nm beam, we can excite the ion from the state $S_{1/2} |F = 1\rangle$ to $P_{1/2} |F = 1\rangle$. Then, with a probability $1/3$ the ion decays to the $|0\rangle$ state, where it is trapped within a few μs . Since the $P_{1/2}$ states also decay to the $D_{3/2}$ manifold, we keep the 935 nm repump laser beam on during the initialization step.

In the case of $^{171}\text{Yb}^+$, the qubit state detection is performed with the help of the standard ion fluorescence techniques [114, 115] as illustrated in Fig. 2.9(c). During the detection, we send 369 nm laser beam resonant with $S_{1/2} |F = 1\rangle \leftrightarrow P_{1/2} |F = 0\rangle$ transition. If the ion is prepared in the $|0\rangle$ state, then it will not scatter any light, since the laser is detuned by 14.7 GHz from the closest allowed transition. On the other hand, if the ion is prepared in the $|1\rangle$ state, then many scattered photons are observed, since the laser is nearly on resonance. High fidelity above 99.9% [36, 116] can be achieved with this detection scheme. Additionally, in contrast to the $^{138}\text{Ba}^+$ detection scheme discussed in Section 2.3.1.1, this detection is deterministic. We

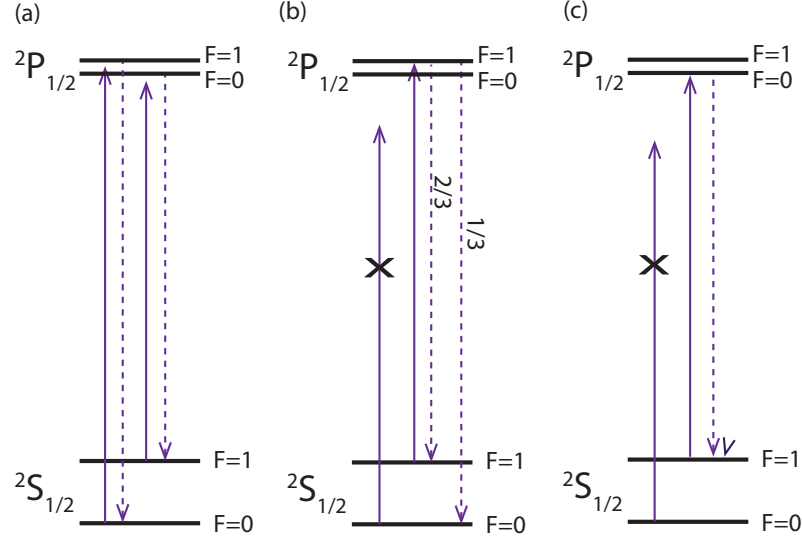


Figure 2.9: $^{171}\text{Yb}^+$ processes when 369 nm laser light is applied. (a) Doppler cooling with 369 nm laser beam detuned from the resonance by 10 MHz. Since due to off-resonant coupling to the $P_{1/2} |F = 1\rangle$ manifold, the ion can decay to the state $|0\rangle$, 14.7 GHz sidebands are applied to return the ion in the main cooling cycle. (b) Optical pumping. We add 2.1 GHz sidebands to the resonant beam to excite the ion from the state $S_{1/2} |F = 1\rangle$ to $P_{1/2} |F = 1\rangle$. Then, with a probability $1/3$ the ion decays to the $|0\rangle$ state, where it is trapped. (c) Qubit state detection. The 369 nm light resonant to $S_{1/2} |F = 1\rangle \leftrightarrow P_{1/2} |F = 0\rangle$ transition is applied. The ion prepared in the state $|1\rangle$ emits a lot of photons, while in the state $|0\rangle$, it does not, because the laser is detuned by 14.7 GHz from the closest allowed transition.

determine the state of the ion by the number of photons detected by the PMT or APD during the detection interval. The ion is defined to be in the state $|1\rangle$, if we observe more than one photon during detection, and in the state $|0\rangle$, if we observe one or zero photons. The main error source is due to off-resonant excitation to the $P_{1/2} |F = 1\rangle$ state if the ion being detected is in the state $|1\rangle$ [26, 117], because from the excited $P_{1/2} |F = 1\rangle$ state, the electron can decay to the ground $S_{1/2} |F = 0\rangle$ state and remains there.

2.2.2 Single qubit rotations

One simple way to drive rotations between $^{171}\text{Yb}^+$ qubit states is by applying microwaves resonant with the 12.6 GHz hyperfine splitting. In the experiment, we use a microwave horn directed towards the center of the trap with about 1 W of microwave power. To make rotations faster, we can change the direction of the horn and the polarizations by physically moving or rotating the horn. The derivation of the coupling between the microwaves and qubit is given in Ref. [118] in detail. A typical Rabi flopping driven by microwaves is presented in Fig. 2.10.

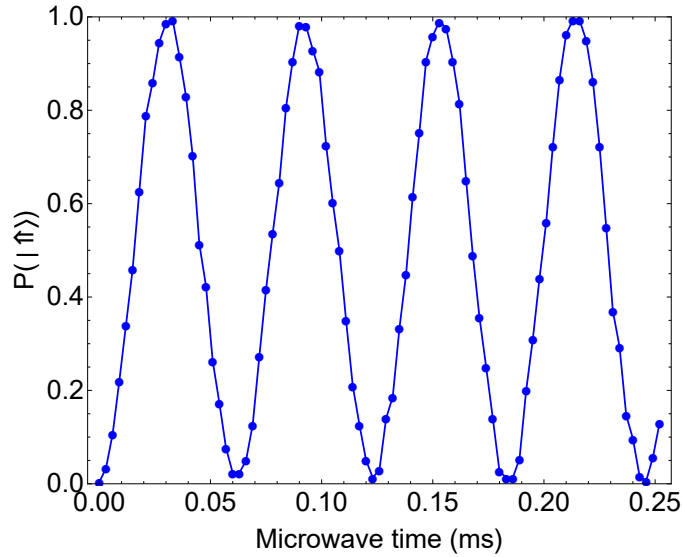


Figure 2.10: Microwave rotations between the states $|0\rangle$ and $|1\rangle$ in $^{171}\text{Yb}^+$. In the beginning of the experiment, the system is initialized in the $|0\rangle$ state, then the microwave radiation is applied for a varied time.

Although microwaves are useful as a tool for detection characterization, diagnostics, and Ramsey-type experiments, they do not resolve the collective motion of the ions. As a result, microwaves cannot be used for two-qubit entanglement operations. Instead, for this purpose, we apply a pair of Raman beams which couple the

ground manifold substates through a virtual excited state.

Coherent qubit operations in $^{171}\text{Yb}^+$ are performed by a pair of Raman beams coming from the Spectra Physics Vanguard pulsed laser at 355 nm wavelength which is the third harmonic of its 1064 nm Nd:YVO4 source. In frequency space, each beam can be represented by a pulse train [119] with comb teeth separated by the repetition rate of the laser, $\nu_r \approx 80$ MHz. A pair of comb teeth separated in frequency space can be chosen such that $n\nu_r = \nu_{HF} - \delta$, where $\nu_{HF} = 12.6$ GHz is the qubit splitting. $n = 158$ in our experiment, and the difference $\delta \sim 10$ MHz can be compensated for using an AOM. We observe that the laser repetition rate is unstable, therefore the beatnote stabilization of mode-locked laser is necessary. It can be accomplished via an AOM beatnote lock [120, 121].

Even though 355 nm laser used in the experiments is pulsed, it can be demonstrated that these optical fields can be treated as continuous waves (CW) [122] without loss of generality. Raman beams off-resonantly couple the ground states, $|0\rangle$ and $|1\rangle$, to an excited state $|e\rangle$ forming a Λ -system. Then, the two-photon Rabi frequency can be derived [103]:

$$\Omega = \frac{g_{0,e}^* g_{1,e}}{2\Delta_e}, \quad (2.49)$$

where $g_{0,e}$ and $g_{1,e}$ are single-photon Rabi frequencies, and Δ_e is the detuning from the excited state $|e\rangle$. In the case of multiple excited states $|i\rangle$ involved in the stimulated Raman transitions, the two-photon Rabi frequency has the following

form:

$$\Omega = \sum_i \frac{g_{0,i}^* g_{1,i}}{2\Delta_i}. \quad (2.50)$$

In the case of $^{171}\text{Yb}^+$, the ground states are coupled to both $P_{1/2}$ and $P_{3/2}$ manifolds. The corresponding calculations are discussed in Appendix C in detail, where we compare $^{171}\text{Yb}^+$ and $^{138}\text{Ba}^+$ ions together.

2.3 Barium operations

In Section 2.1.3, we considered the relevant level structure of $^{138}\text{Ba}^+$ ion. The conventional $^{138}\text{Ba}^+$ qubit is defined in the $S_{1/2}$ manifold. In this section, we show the basic $S_{1/2}$ -manifold qubit manipulation in $^{138}\text{Ba}^+$ and its generalization to the $D_{3/2}$ manifold, including a novel detection technique for all four states in the $D_{3/2}$ manifold and relevant coherent operations. In addition, we provide a scheme to create a protected qubit defined in the $D_{3/2}$ manifold with seconds-long coherence times and present our experimental progress in this direction.

2.3.1 S-manifold operations

In this section, we discuss the implementation of the state preparation, state detection, and qubit manipulations in the $S_{1/2}$ manifold of $^{138}\text{Ba}^+$. In the mixed-species network architecture, $^{138}\text{Ba}^+$ ions are used as communication qubits, and they provide a link between $^{171}\text{Yb}^+$ memory qubits. In the future network experiments, the $^{138}\text{Ba}^+$ state detection is not required, since the information stored in $^{138}\text{Ba}^+$ qubit can be swapped to $^{171}\text{Yb}^+$ qubit through Coulomb-based gates, but

the rotations of the $^{138}\text{Ba}^+$ qubit will always be needed in the experiments. However, $^{138}\text{Ba}^+$ qubit state operations, such as detection and rotations, are useful for calibration and diagnostics of the system.

2.3.1.1 State initialization and readout

Usually in $^{138}\text{Ba}^+$, the qubit is defined in the $6S_{1/2}$ ground-state manifold with the “spin states” $|\downarrow\rangle = |m_j = -1/2\rangle$ and $|\uparrow\rangle = |m_j = 1/2\rangle$. Since there is no closed cycling transition in $^{138}\text{Ba}^+$ ion, we introduced a probabilistic detection scheme for the states in the $S_{1/2}$ -manifold [123].

As shown in Fig. 2.11(a), $^{138}\text{Ba}^+$ ion can be initialized in $|\uparrow\rangle$ state by applying 493 nm σ^+ beam and 650 nm light with all the polarizations to repump population from $D_{3/2}$ manifold, and similarly, we can initialize the ion in $|\downarrow\rangle$ state by applying 493 nm σ^- beam and 650 nm light with all the polarizations.

Within the probabilistic detection approach, we apply 493 nm σ^+ and σ^- pulses (see Fig. 2.11(a)) and record the average number of 493 nm photons collected before the ion gets optically pumped into a dark state. For example, if the ion is in the $|\downarrow\rangle$ state, and we apply 493 nm σ^+ light only, on average the ion scatters 2.8 493 nm photons before getting optically pumped into the $|\uparrow\rangle$ state. On the contrary, the ion in the $|\uparrow\rangle$ state does not scatter any photons when the σ^+ light is applied. Generally speaking, we can extract some information about the qubit state by applying only one of the 493 nm σ beams, however, to reduce statistical effects on state detection accuracy, we alternate between 493 nm σ^+ and σ^- pulses.

Additionally, this method does not strongly depend on the intensity and frequency noise of the 493 nm laser.

The conventional detection method [124, 125] requires two additional lasers – one with a narrow line-width for shelving and another one for depopulating the long-lived state. Our technique does not require additional lasers.

From now on, we use the notations $|s_{1/2+m_i}\rangle \equiv |S_{1/2}; m_i\rangle$, where s_i , $i = 0, 1$, are the $S_{1/2}$ sub-level populations. These populations can be found by:

$$s_0 = \frac{n_-}{n_+ + n_-}, \quad s_1 = \frac{n_+}{n_+ + n_-}, \quad (2.51)$$

where n_{\pm} represents the average number of photons collected in a σ^{\pm} trial. In a matrix form, it would look the following way:

$$\begin{pmatrix} n_+ \\ n_- \end{pmatrix} = E_s M^s \begin{pmatrix} s_0 \\ s_1 \end{pmatrix} = E_s \begin{pmatrix} 2.8 & 0 \\ 0 & 2.8 \end{pmatrix} \begin{pmatrix} s_0 \\ s_1 \end{pmatrix}, \quad (2.52)$$

where E_s is the detection efficiency and the matrix element M_{ei}^s gives the average number of 493 nm photons scattered from an ion in the state $|i\rangle$ and a trial with polarization ϵ .

The solution of this matrix equation is trivial and is given in Eq. (2.51). However, the matrix approach will be useful for the detection method for the states in the $D_{3/2}$ manifold discussed in the next section.

To perform detection, we apply alternating 493 nm σ^+ or σ^- pulses for $\sim 1 \mu s$ after each experiment, and repeat this sequence many times. We use 0.6 NA micro-

scope objective for the ion light collection. APD¹ with a quantum efficiency of 71% at 493 nm and a dark-count rate of 10 s^{-1} is used as a detector. In Fig. 2.11(b), we demonstrate the coherent rotations in the $S_{1/2}$ manifold, and the detection fidelity of 98% is limited by a polarization purity of the 493 nm σ beams and background dark counts.

2.3.1.2 Single qubit rotations

The coherent operations in the $S_{1/2}$ manifold can be implemented by applying RF directly to the trap electrodes [126], or by using an inductive coil near the trap [127]. But in our experiment, we utilize a pair of copropagating Raman beams with both σ and π polarizations, and the frequency difference equal to the splitting between $S_{1/2}$ - manifold Zeeman levels, $2\delta_Z B$, where $\delta_Z \approx 1.4 \text{ MHz/G}$, and B is the magnetic field in Gauss. Conveniently, the second harmonic of the same 1064 nm Nd:YVO₄ source as we use for $^{171}\text{Yb}^+ - 532 \text{ nm}$ – can be used to drive rotations in the $S_{1/2}$ manifold in $^{138}\text{Ba}^+$. By applying a pair of copropagating 532 nm Raman beams, we perform Rabi flopping in the $S_{1/2}$ manifold shown in Fig. 2.11(b).

2.3.2 D-manifold operations

As we discussed in the previous section, the conventional $^{138}\text{Ba}^+$ qubit is a Zeeman qubit and defined in the $S_{1/2}$ manifold, thus the magnetic field sensitivity of that qubit leads to a significant decrease in coherence time. One way around this is to transfer any information from the communication qubits immediately to

¹Laser Components, COUNT BLUE Series

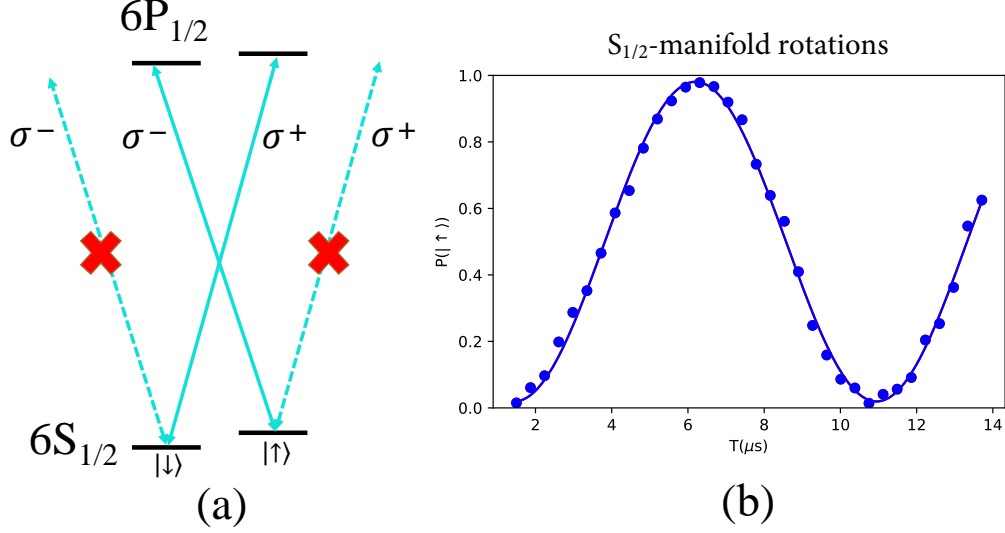


Figure 2.11: (a) Initialization and detection scheme for $S_{1/2}$ -manifold states in $^{138}\text{Ba}^+$. (b) Population of the $|\uparrow\rangle$ state during coherent rotations in the $S_{1/2}$ manifold which were performed via a pair of 532 nm Raman beams with all polarizations.

the neighboring memory qubits [128]. However, having a $^{138}\text{Ba}^+$ qubit with longer coherence times allows for implementation of more complex protocols. Magnetic-field stabilization alleviates this decoherence to a limited extent [129]. In the present work, we explore an alternative approach that has a much further-reaching potential using states in the $D_{3/2}$ manifold and the corresponding quantum operations. In $^{138}\text{Ba}^+$, the lifetime of the $D_{3/2}$ states is about 80 s [130], which is longer than any conceivable quantum operation could take. In addition, the branching ratio from the $P_{1/2}$ manifold to the $S_{1/2}$ and $D_{3/2}$ manifolds is moderate – 3:1, respectively, – ensuring fast rates of pumping into and exciting out of the $D_{3/2}$ states. Moreover, the 650 nm $P_{1/2} - D_{3/2}$ transition is spectrally distant from the 493 nm $S_{1/2} - P_{1/2}$ transition (see Fig. 2.12a), and the former is compatible with the efficient fiber technologies.

Detection of the $D_{3/2}$ -manifold states has not yet been widely used in quantum

computing. On the other hand, novel approaches [131, 132, 133] to create and operate protected atomic qubits rely on the ability to detect these states efficiently. To the best of our knowledge, no such detection schemes have been implemented to date.

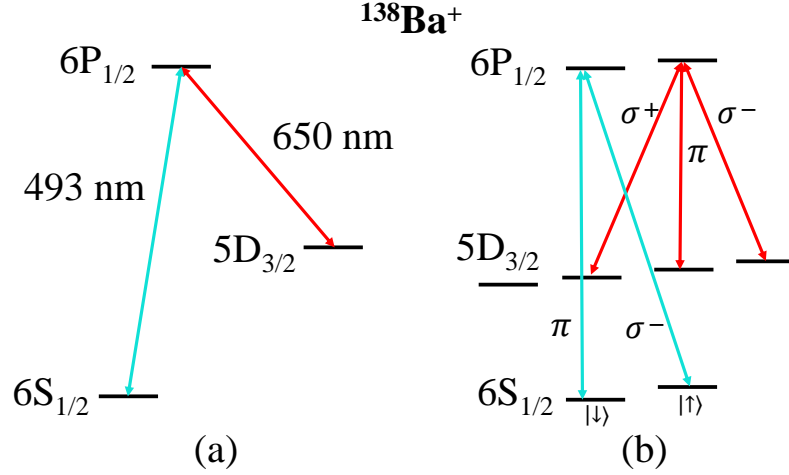


Figure 2.12: Barium level structure: (a) in the absence of magnetic field; (b) in presence of magnetic field. A few representative transitions are shown for clarity.

In this work, we introduce a novel detection technique for all four states in the $D_{3/2}$ manifold. We demonstrate this technique in $^{138}\text{Ba}^+$ ion, which is preferential due to the properties explained above, but our general scheme can also be applied to other ions with nuclear spin $I = 0$, such as $^{40}\text{Ca}^+$ [134, 135], and $^{88}\text{Sr}^+$ [136, 137]. We also demonstrate various coherent operations in the $D_{3/2}$ manifold including coherent $\Delta m_j = \pm 1$ and $\Delta m_j = \pm 2$ rotations within the manifold, using our detection scheme to verify the results. We obtain experimental data that agrees with theoretical simulations performed in Quantum Toolbox in Python (QuTiP). Using a pair of Raman beams or, alternatively, a STIRAP procedure using 650 nm light, we create a synthetic qubit insensitive to the magnetic field, and show improvement in the

coherence time T_2^* by the factor of 3 in comparison to a magnetically sensitive qubit. We discuss future steps in improving the coherence time by creating a protected subspace and applying a driving Hamiltonian that constantly reprojects the ion state into this subspace [131, 132, 133].

2.3.2.1 State initialization and readout

a. Problem Formulation

In this work, we generalize the probabilistic detection method to detect all four Zeeman states in the $D_{3/2}$ manifold. As before, we send pulses with varying polarizations – this time at 650 nm wavelength, which corresponds to the $P_{1/2}$ – $D_{3/2}$ transition, – while still collecting 493 nm-wavelength photons. During the detection procedure, the 493 nm light is turned on all the time to re-pump population out of the S manifold. However, as opposed to the case of the S -manifold state detection, we now require five different polarization combinations: σ^+ , σ^- , π , (σ^+ and π), and (σ^- and π).

We would like to emphasize that (σ^\pm and π) readout operations give equations linearly independent from the ones obtained by the readout operations with individual polarizations, σ^\pm and π . This can be shown by considering the number of stationary dark states in these cases. For $D_{3/2} \rightarrow P_{1/2}$ ($J = 3/2 \rightarrow J = 1/2$) transition, there are two dark states for any polarization of the applied light [107]. For an individual σ^+ , σ^- , or π polarization of the 650 nm light, both dark states are stationary even when a magnetic field is applied. But for combinations (σ^+ and π)

or (σ^- and π), only one dark state is stationary, while another one quickly evolves to a bright state, when π and σ^\pm beams have different detunings.

In addition to the five different polarization readouts, we have two further constraints: the unitarity condition $\sum_{i=0}^3 d_i = 1$, and $d_i \in [0; 1]$, $\forall i = 0, \dots, 3$, where d_i represent populations of the D -manifold levels.

We generalize Eq. (2.52) for the populations to the case of the $|d_i\rangle$ states in the $D_{3/2}$ manifold ($i = 0, \dots, 3$):

$$\begin{pmatrix} n_+ \\ n_- \\ n_\pi \\ n_{+\pi} \\ n_{-\pi} \end{pmatrix} = E_d M^d \begin{pmatrix} d_0 \\ d_1 \\ d_2 \\ d_3 \end{pmatrix}, \quad (2.53)$$

where E_d is a detection efficiency. n_ϵ represents the average number of 493 nm photons detected from a trial with the detection polarization:

$$\epsilon \in \{\sigma^+, \sigma^-, \pi, (\sigma^+ \text{ and } \pi), (\sigma^- \text{ and } \pi)\}.$$

We perform each experiment many times and apply one of the polarization configurations ϵ to build sufficient statistics for the values of n_ϵ . Similarly, a matrix element $M_{\epsilon i}^d$ gives the average number of 493 nm photons scattered from an ion in the particular state $|i\rangle$ in a trial with polarization ϵ .

To find matrix elements $M_{\epsilon i}^d$, we use the stochastic Markov chain approach. In particular, we perform simulation of the 8-level $^{138}\text{Ba}^+$ system and introduce the

9th state to keep track of the average number of scattered 493 nm photons [138].

Here, we assume that the intensities are the same for all the polarizations of 493 nm beams, and that 650 nm beams for each polarization also have the same intensities.

Under these assumptions, the resulting matrix M^d acquires the following form:

$$M^d = \begin{pmatrix} 6.6 & 5.4 & 0 & 0 \\ 0 & 0 & 5.4 & 6.6 \\ 0 & 6 & 6 & 0 \\ 13.3 & 12.6 & 11.4 & 0 \\ 0 & 11.4 & 12.6 & 13.3 \end{pmatrix}. \quad (2.54)$$

Additionally, we impose two constraints: (i) the unitarity condition: $\sum_{i=0}^3 d_i = 1$ and (ii) populations $d_i \in [0; 1]$, $i = 0, \dots, 3$. As a result, we construct an over-constrained problem with four unknown populations d_i , five equations, four bounds, and one constraint.

b. Problem Solution

Two different ways of solving this problem are discussed below, with the first one treating the efficiency E_d as an additional unknown, while the second one taking it as an independently determined constant.

In the first method of solution, in addition to $\{d_i\}$ and E_d , we introduce another unknown variable C_b – a static background count rate. That results in the total of six unknown variables and six equations: five ones from different polarization

configurations as in Eq. (2.53) and the unitarity condition. This method, however, does not account for the bounds $d_i \in [0; 1]$. The matrix form of the equation becomes:

$$\begin{pmatrix} n_+ \\ n_- \\ n_\pi \\ n_{+\pi} \\ n_{-\pi} \end{pmatrix} = E_d \begin{pmatrix} 6.6 & 5.4 & 0 & 0 & 1 \\ 0 & 0 & 5.4 & 6.6 & 1 \\ 0 & 6 & 6 & 0 & 1 \\ 13.3 & 12.6 & 11.4 & 0 & 1 \\ 0 & 11.4 & 12.6 & 13.3 & 1 \end{pmatrix} \begin{pmatrix} d_0 \\ d_1 \\ d_2 \\ d_3 \\ C_b \end{pmatrix}. \quad (2.55)$$

We solved this system directly in Ref. [138]. Since we did not impose the requirements $d_i \in [0; 1]$, $i = 0, \dots, 3$, some of the populations that we obtained that way fluctuated outside of this physical region due to the background noise and polarization imperfections.

The second method takes all the necessary conditions, including the bounds, into account, making the system over-constrained. We solve it using a constrained linear least-squares solver. The data shown in Section 2.3.2.2 is obtained with this method of analysis, but the two methods give very closely matching results. The corresponding error bars are obtained via the Hessian calculated at the solution point.

In order to illustrate how this $D_{3/2}$ state detection works, we present an example of the solution for all four state populations when the ion is pumped to the edge state $|D_{3/2}, m_j = 3/2\rangle$. In Table 2.1, the left hand side presents the raw data – the average number of the detected 493 nm photons from the $D_{3/2}$ state detection with five different laser polarization combinations. We performed 10000 repetitions

of each measurement with the detection window of $5 \mu s$ to get these numbers. After the comparison with the last column from Eq. (2.54), we can see the background noise and polarization imperfections. They are especially noticeable in the number of photons collected with the σ^+ and π polarization configuration, which should yield 0 collected photons in the ideal scenario. Then, we demonstrate a solution of the corresponding over-constrained problem in Eq. (2.53) in the right hand side of Table 2.1. The populations of all four states in the $D_{3/2}$ manifold indicate that the ion was prepared in the $|D_{3/2}, m_j = 3/2\rangle$ state.


Polarization	Collected photons		State in $D_{3/2}$ manifold	State population
σ^+	165		$m_j = -3/2$	0.00 ± 0.09
σ^-	2054		$m_j = -1/2$	0.04 ± 0.08
π	99		$m_j = 1/2$	0.02 ± 0.09
σ^+ and π	311		$m_j = 3/2$	0.94 ± 0.09
σ^- and π	4360			

Table 2.1: Detection of the $|D_{3/2}, m_j = 3/2\rangle$ state. The left hand side shows the raw data from the $D_{3/2}$ state detection when five different polarization combinations are applied. The right hand side presents the corresponding solution of the over-constrained problem (2.53) – the populations of all four states in the $D_{3/2}$ manifold.

2.3.2.2 Coherent operations with 532 nm light

In the $D_{3/2}$ manifold, we can perform two types of qubit rotations: (i) with the angular-momentum projection change $\Delta m_j = \pm 1$, and (ii) with that of $\Delta m_j = \pm 2$, as shown in Fig. 2.13.

The necessary splitting for the $\Delta m_j = \pm 1$ rotations is equal to the splitting between adjacent Zeeman levels, $\frac{4}{5}\delta_Z B$, where $\delta_Z \approx 1.4$ MHz/G, and B is the magnetic field in Gauss. Similarly, the frequency for $\Delta m_j = \pm 2$ operations has

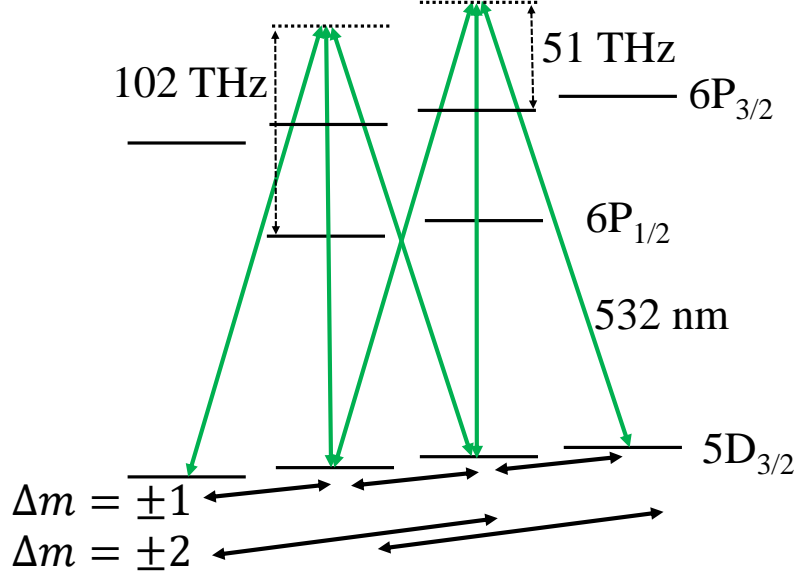


Figure 2.13: Off-resonant coupling of 532 nm laser beams – represented by the green arrows – to $P_{1/2}$ and $P_{3/2}$ manifolds in $^{138}\text{Ba}^+$. Short black arrows represent $\Delta m_j = \pm 1$ rotations between all four $D_{3/2}$ states; for these, 532 nm Raman beams have to have σ^\pm and π polarizations. Long black arrows represent $\Delta m_j = \pm 2$ rotations between the two possible pairs of states; for these, 532 nm Raman beams only need to have σ^+ and σ^- polarizations. However, in order to minimize the two-photon AC Stark shifts, we keep the π polarization component on for these operations, too.

to be tuned to $\frac{8}{5}\delta_Z B$. For all the experiments discussed in this section, we used the magnetic field $B = 2.2$ G, which makes the frequency between the adjacent levels equal 2.5 MHz. In order to perform not only $\Delta m_j = \pm 1$ rotations, but also $\Delta m_j = \pm 2$ ones, we utilize a pair of 532 nm Raman co-propagating beams which are off-resonantly coupled to the $6P_{1/2}$ and $6P_{3/2}$ states. From this point on, we will use the notations $|d_{3/2+m_i}\rangle \equiv |D_{3/2}; m_i\rangle$ and $|p_{1/2+m_i}\rangle \equiv |P_{1/2}; m_i\rangle$.

a. Rotations with $\Delta m = \pm 1$

We start with $\Delta m_j = \pm 1$ rotations in the $D_{3/2}$ manifold shown in Fig. 2.14. In order to minimize differential two-photon AC Stark shifts, we adjust the polarizations of

our 532 nm Raman beams so that the intensities of each polarization (σ^+ , σ^- , and π) are all equal. The corresponding Rabi frequencies and the differential two-photon AC Stark shifts are discussed in Appendix C in detail. We initialize the qubit in the $|d_3\rangle$ state, and by applying two 532 nm Raman beams, we drive the populations between all Zeeman $D_{3/2}$ states. The experimental data agrees with the QuTiP evolution simulations within the uncertainty. The QuTiP simulations are

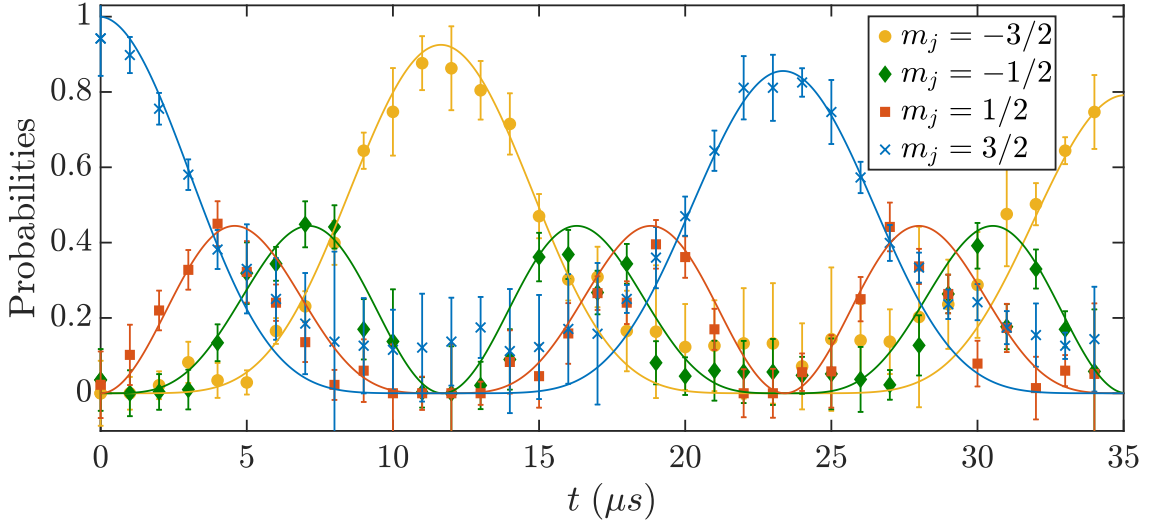


Figure 2.14: State populations during coherent rotations with $\Delta m_j = \pm 1$ in the $D_{3/2}$ manifold. In the presence of the pair of 532 nm Raman beams with all polarizations, all four states are involved in the time evolution. The markers show the experimental data. Yellow circles: $|d_0\rangle$ state ($m_j = -3/2$); green diamonds: $|d_1\rangle$ state ($m_j = -1/2$); red squares: $|d_2\rangle$ state ($m_j = 1/2$); and blue crosses: $|d_3\rangle$ state ($m_j = 3/2$). Solid lines of the corresponding colors show the QuTiP simulations for a four-level system initialized with all the population in the $|d_3\rangle$ state ($m_j = 3/2$) with the effective microwave rotations between the $D_{3/2}$ states. We fit the QuTiP simulations to the experimental data over the Rabi frequency Ω and the decay time τ .

performed for a four-level system with the effective $\Delta m_j = \pm 1$ microwave rotations

that are described by the following interaction Hamiltonian:

$$H_{\Delta m=\pm 1} = \begin{pmatrix} 0 & \sqrt{\frac{3}{18}} \frac{\Omega}{2} & 0 & 0 \\ \sqrt{\frac{3}{18}} \frac{\Omega}{2} & 0 & \sqrt{\frac{4}{18}} \frac{\Omega}{2} & 0 \\ 0 & \sqrt{\frac{4}{18}} \frac{\Omega}{2} & 0 & \sqrt{\frac{3}{18}} \frac{\Omega}{2} \\ 0 & 0 & \sqrt{\frac{3}{18}} \frac{\Omega}{2} & 0 \end{pmatrix}. \quad (2.56)$$

We take into account the Clebsch-Gordan coefficients and all possible pairs of Raman beam polarizations (see Fig. 2.13) when calculating the effective Rabi frequency. In our setup, it takes 12 μs to transfer all the population from one of the edge states, $|d_3\rangle$, to the other one, $|d_0\rangle$, through the middle states.

b. Rotations with $\Delta m = \pm 2$

Next, in Fig. 2.15, we demonstrate $\Delta m_j = \pm 2$ rotations in the $D_{3/2}$ manifold. 532 nm Raman beams with σ^+ and σ^- polarizations are applied. As in the previous case, we initialize the qubit in the $|d_3\rangle$ state. Now, however, we tune the frequency difference between two Raman beams to $\frac{8}{5}\delta_Z B$, and perform rotations only between two states, $|d_3\rangle$ and $|d_1\rangle$, while other two states are unpopulated. We additionally check the rotations between the second pair of states: $|d_0\rangle$ and $|d_2\rangle$. The experimental data agrees with the QuTiP simulations within the uncertainty in this case, as well.

The QuTiP simulations are performed for a four-level system with the effective $\Delta m_j = \pm 2$ microwave rotations that are described by the following interaction

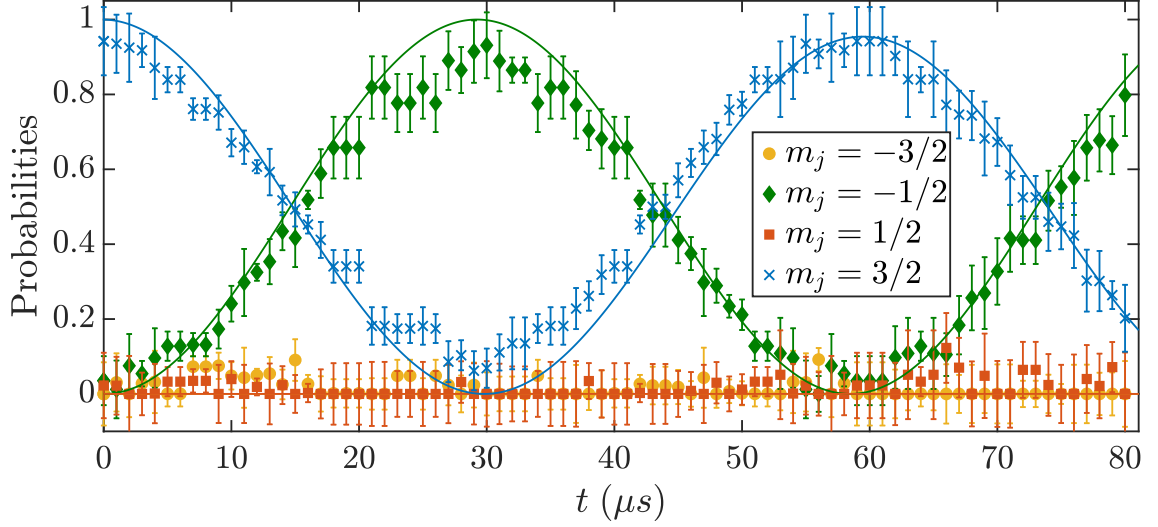


Figure 2.15: State populations during coherent rotations with $\Delta m_j = \pm 2$ in the $D_{3/2}$ manifold. In the presence of a pair of 532 nm Raman beams with σ^+ and σ^- polarizations, only two states are evolving while the other two are unaffected. The markers show the experimental data. Yellow circles: $|d_0\rangle$ state ($m_j = -3/2$); green diamonds: $|d_1\rangle$ state ($m_j = -1/2$); red squares: $|d_2\rangle$ state ($m_j = 1/2$); and blue crosses: $|d_3\rangle$ state ($m_j = 3/2$). Solid lines of the corresponding colors show the QuTiP simulations for a four-level system initialized with all the population in the $|d_3\rangle$ state ($m_j = 3/2$) with the effective microwave rotations between the $D_{3/2}$ states. We fit the QuTiP simulations to the experimental data over the Rabi frequency Ω and the decay time τ .

Hamiltonian:

$$H_{\Delta m=\pm 2} = \begin{pmatrix} 0 & 0 & \frac{\Omega}{2} & 0 \\ 0 & 0 & 0 & \frac{\Omega}{2} \\ \frac{\Omega}{2} & 0 & 0 & 0 \\ 0 & \frac{\Omega}{2} & 0 & 0 \end{pmatrix}. \quad (2.57)$$

The peak amplitude of the oscillations exhibited by the data is lower than that in the simulations due to the background noise and polarization imperfections. This causes state preparation error. As shown in Fig. 2.15, we can perform a $\pi/2$ rotation in $T = 30 \mu\text{s}$, and as a result, end up in the $|d_1\rangle$ state. Therefore, at $t = \frac{2}{3}T = 20 \mu\text{s}$, the electron will be in the state: $\frac{1}{2}|d_3\rangle + e^{i\phi}\frac{\sqrt{3}}{2}|d_1\rangle$, where the phase ϕ is defined by

the phase shift between the two Raman beams. Let $|D_1\rangle$ denote such a state with $\phi = \pi$. Using the same phase shift and the other submanifold of $D_{3/2}$, we create an orthogonal state $|D_2\rangle$, such that:

$$\begin{aligned} |D_1\rangle &= \frac{1}{2}|d_3\rangle - \frac{\sqrt{3}}{2}|d_1\rangle, \\ |D_2\rangle &= \frac{1}{2}|d_0\rangle - \frac{\sqrt{3}}{2}|d_2\rangle. \end{aligned} \tag{2.58}$$

The above description applies to creating $|D_1\rangle$ and $|D_2\rangle$ states using a pair of Raman beams. We also implemented an alternative technique to create those states via a STIRAP procedure. In this case, we initialize the ion in the $|d_3\rangle$ state, and use the resonant 650 nm σ^+ and σ^- beams in the STIRAP configuration to transfer population to $|d_1\rangle$ with the state $|p_1\rangle$ being an excited state with the STIRAP preparation time equal $10\mu\text{s}$.

2.3.2.3 Protected qubit subspace

a. Magnetically insensitive qubit

In contrast to a qubit defined in the $S_{1/2}$ manifold, the qubit consisting of the $|D_1\rangle$ and $|D_2\rangle$ states is insensitive by construction to the magnetic field fluctuations [131, 132]:

$$\langle D_j | J_z | D_i \rangle = 0, \quad \forall i, j \in \{1, 2\}, \tag{2.59}$$

where \mathbf{J} is the angular momentum operator.

To detect the state of the new qubit with $|0\rangle \equiv |D_1\rangle$ and $|1\rangle \equiv |D_2\rangle$, we

perform detection of all four states in the $D_{3/2}$ manifold as discussed in Sec. 2.3.2.1, and then we project them to the $\{|D_1\rangle, |D_2\rangle\}$ subspace.

As discussed in the previous section, when applying a pair of Raman beams to create, for example, $|D_1\rangle$ state, we have a control over the phase shift ϕ . Only when $\phi = \pi$, we can get good coherent rotations between the magnetically insensitive states (discussed below), and that is not the case for any other phase ϕ . When making the $\pi/2$ rotation between two synthetic states, we perform a phase shift scan, and pick the phase that gives us the highest contrast. This was matched first in the QuTiP simulations and then in the experiment.

b. Rotations between the $|D_1\rangle$ and $|D_2\rangle$ states

The coherent $\Delta m_j = \pm 1$ rotations between $|D_1\rangle$ and $|D_2\rangle$ states can be performed by applying microwaves or by sending two off-resonantly coupled Raman beams, as discussed in the beginning of Sec. 2.3.2.2. Fig. 2.16 shows $\Delta m_j = \pm 1$ rotations between $|D_1\rangle$ and $|D_2\rangle$ states. The experimental data agrees with the QuTiP simulations within the uncertainty.

Since the new synthetic qubit is magnetically insensitive, we expect a considerable improvement in the coherence time T_2^* in comparison to a conventional qubit in the $S_{1/2}$ manifold. The major limitation to the coherence time of the $S_{1/2}$ -manifold qubit is magnetic noise, which mainly comes from the lab equipment and the power lines at 60 Hz and higher harmonics. There are several ways to address this issue, such as using μ -metal shielding [129], setting up a feed-forward [139] or feedback

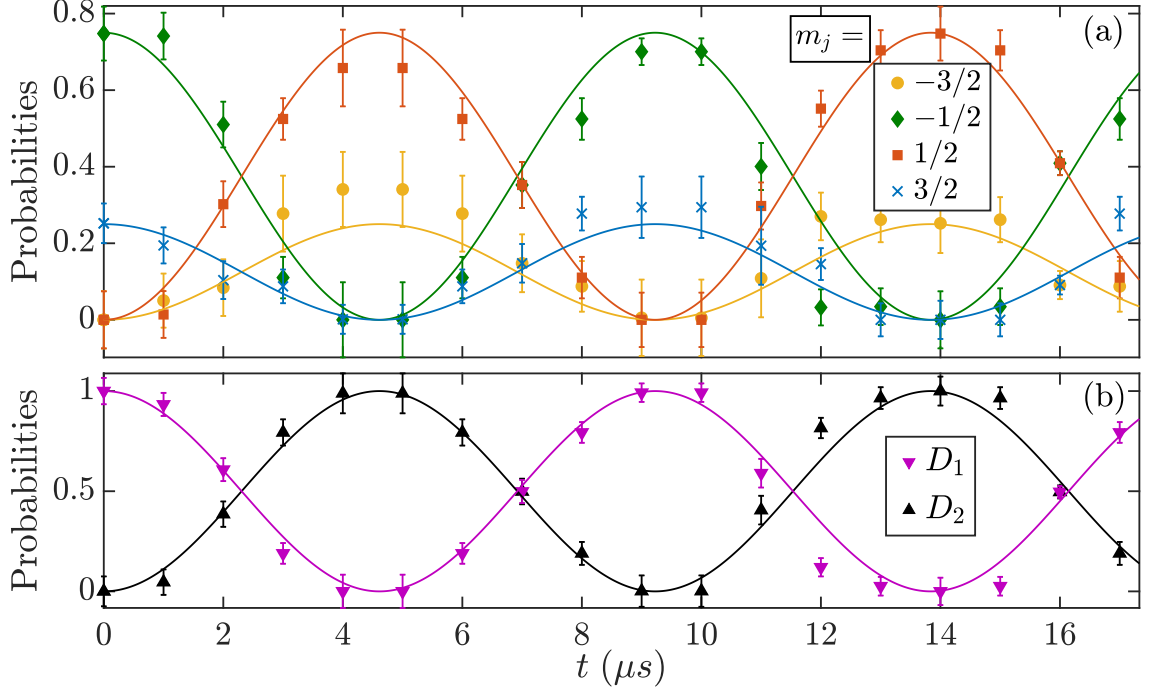


Figure 2.16: Coherent $\Delta m_j = \pm 1$ rotations between the $|D_1\rangle$ and $|D_2\rangle$ states. In the presence of a pair of 532 nm Raman beams, all four $D_{3/2}$ -manifold states are involved in the time evolution. **(a)** The markers show the experimental data. Yellow circles: $|d_0\rangle$ state ($m_j = -3/2$); green diamonds: $|d_1\rangle$ state ($m_j = -1/2$); red squares: $|d_2\rangle$ state ($m_j = 1/2$); and blue crosses: $|d_3\rangle$ state ($m_j = 3/2$). Solid lines of the corresponding colors show the QuTiP simulations for a four-level system starting with the $|D_1\rangle$ state and performing the effective microwave rotations between the $D_{3/2}$ -manifold states. We fit the QuTiP simulations to the experimental data over the Rabi frequency Ω and the decay time τ . **(b)** The synthetic qubit state populations. The markers show the experimental data. Magenta up-pointing triangles: $|D_1\rangle$ state; black down-pointing triangles: $|D_2\rangle$ state. Solid lines of the corresponding colors represent the corresponding QuTiP simulations.

magnetic field stabilization [140], or using an alternative isotope with a magnetically insensitive hyperfine qubit, e.g. $^{133}\text{Ba}^+$ [141]. In our experiment, we do not perform any magnetic field stabilization or shielding. As a first benchmark, we perform a Ramsey experiment on a qubit defined in the $S_{1/2}$ manifold. In this case, $T_2^* = (96 \pm 15)\mu\text{s}$ is obtained, which is a result of high magnetic sensitivity of about 2.8 kHz/mG. As a second benchmark, we perform the same Ramsey experiment for a qubit defined in the $|d_3\rangle$ and $|d_1\rangle$ states from the $D_{3/2}$ manifold (the corresponding

qubit rotations are shown in Fig. 2.15). The magnetic sensitivity for this qubit is about 2.2kHz/mG, which result in a slightly longer $T_2^* = (117 \pm 11)\mu\text{s}$. Next, we perform the Ramsey experiment on the synthetic magnetically insensitive qubit consisting of the $|D_1\rangle$ and $|D_2\rangle$ states. Of the three $^{138}\text{Ba}^+$ qubits we tested, this qubit has the longest coherence time: $T_2^* = (350 \pm 37)\mu\text{s}$, which is about 3 times longer than the coherence time of a magnetically sensitive qubit. The synthetic qubit shows an improvement, but these results are still far from “seconds-long” coherence times observed in hyperfine or optical qubits [25, 26, 27, 33]. However, as a next step, our results can be further improved by introducing a protected qubit subspace [131, 132].

c. Protected qubit subspace

The protected qubit subspace $\{|D_1\rangle, |D_2\rangle\}$ is defined by:

$$\langle D_j | J_z | D_i \rangle = 0, \quad \forall i, j \in \{1, 2\} \quad (2.60)$$

$$H_d | D_i \rangle = 0, \quad \forall i \in \{1, 2\}$$

where H_d is the (continuous) driving Hamiltonian.

$$H_d = \left(\frac{\Omega_1}{2} |p_1\rangle \langle d_1| + \frac{\sqrt{3}\Omega_1}{2} |p_1\rangle \langle d_3| + \frac{\Omega_1}{2} |p_0\rangle \langle d_2| + \frac{\sqrt{3}\Omega_1}{2} |p_0\rangle \langle d_0| \right) + \text{H.c.} \quad (2.61)$$

The Hamiltonian H_d can be decomposed into two uncoupled Λ systems: (i) the $|d_1\rangle$ and $|d_3\rangle$ states simultaneously resonantly coupled to the $|p_1\rangle$ state, resulting in the dark state $|D_1\rangle$, and (ii) the $|d_0\rangle$ and $|d_2\rangle$ states simultaneously resonantly

coupled to the $|p_0\rangle$ state resulting in the dark state $|D_2\rangle$.

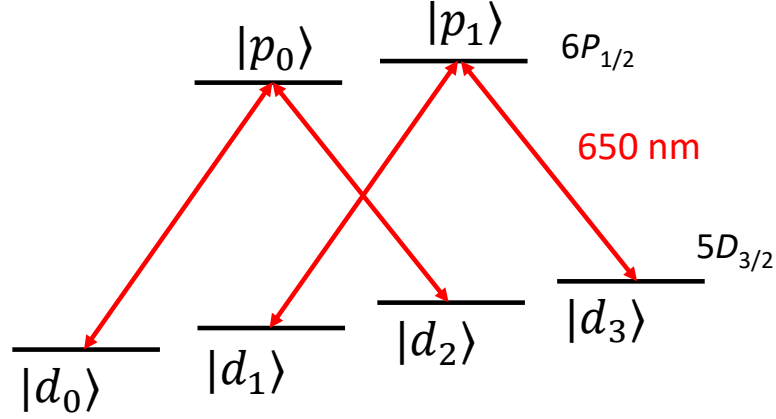


Figure 2.17: Construction of the protected qubit subspace. Two Λ configurations of resonant σ^+ and σ^- 650 nm beams with equal intensities are applied, so that the system is constantly reprojected into the protected subspace \mathcal{H}_D .

In our case, H_d can be implemented by sending resonant σ^+ and σ^- 650 nm beams with equal intensities as shown in Fig. 2.17.

We have already satisfied the first condition in Eq. (2.60) – zero coupling to J_z , which makes the qubit insensitive to magnetic field fluctuations. It ensures that the magnetic noise can cause transitions only between a protected state and a state in the complementary subspace \mathcal{H}_\perp (so that $\mathcal{H} = \mathcal{H}_D \oplus \mathcal{H}_\perp$), for example, the orthogonal bright states $|B_1\rangle$ and $|B_2\rangle$:

$$\begin{aligned} |B_1\rangle &= \frac{1}{2}|d_1\rangle + \frac{\sqrt{3}}{2}|d_3\rangle \\ |B_2\rangle &= \frac{\sqrt{3}}{2}|d_0\rangle + \frac{1}{2}|d_2\rangle. \end{aligned} \tag{2.62}$$

These transitions, however, can reduce the coherence time. By applying the driving Hamiltonian H_d , we would satisfy the second part of Eq. (2.60). This way, the protected subspace becomes the kernel of H_d . Subject to the Hamiltonian H_d , the

system is continuously reprojected into the protected Hilbert subspace \mathcal{H}_D . Therefore, the protected states do not accrue any dynamical phase and are unaffected by the noise related to H_d .

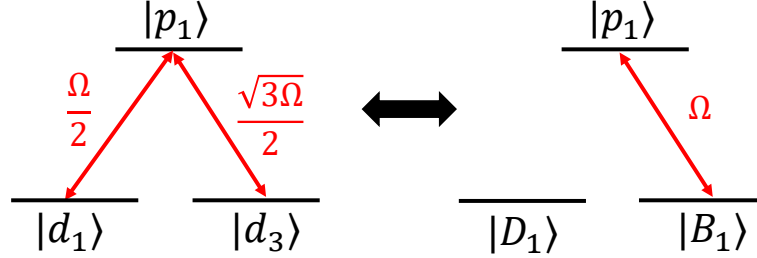


Figure 2.18: Decoupling of a protected qubit state. Effectively, only the state $|B_1\rangle$ is coupled to the excited state $|p_1\rangle$, and the state $|D_1\rangle$ is dark.

The decoupling mechanism is shown in Fig. 2.18, where each one of the Λ systems that comprise H_d is equivalent to a system with only a bright state $|B_i\rangle$ coupled to the excited state $|p_i\rangle$. In other words, in the basis $\{|D_1\rangle, |D_2\rangle, |B_1\rangle, |B_2\rangle, |p_0\rangle, |p_1\rangle\}$, the driving Hamiltonian has the following form:

$$H_d = \Omega (|p_1\rangle\langle B_1| + |p_0\rangle\langle B_2|) + \text{H.c.} \quad (2.63)$$

And now it is obvious that $H_d|D_i\rangle = 0$. The theoretical prediction for the coherence time of the qubit in the protected subspace $\{|D_1\rangle, |D_2\rangle\}$ is $T_2 \sim T_1 \sim 10$ s.

In the experiment, by applying only σ^+ and σ^- 650 nm beams with equal laser intensities, we are able to create the protected subspace and pump the $^{138}\text{Ba}^+$ ion dark. In Fig. 2.19, we show the $^{138}\text{Ba}^+$ ion brightness as a function of the frequency difference δ between σ^+ and σ^- 650 nm beams. When δ matches the frequency difference between the states $|d_1\rangle$ and $|d_3\rangle$ in the $D_{3/2}$ manifold $\left(\delta = \frac{8}{5}\delta_Z B\right)$, the

$^{138}\text{Ba}^+$ ion stops fluorescing and goes completely dark with respect to the driving Hamiltonian H_d .

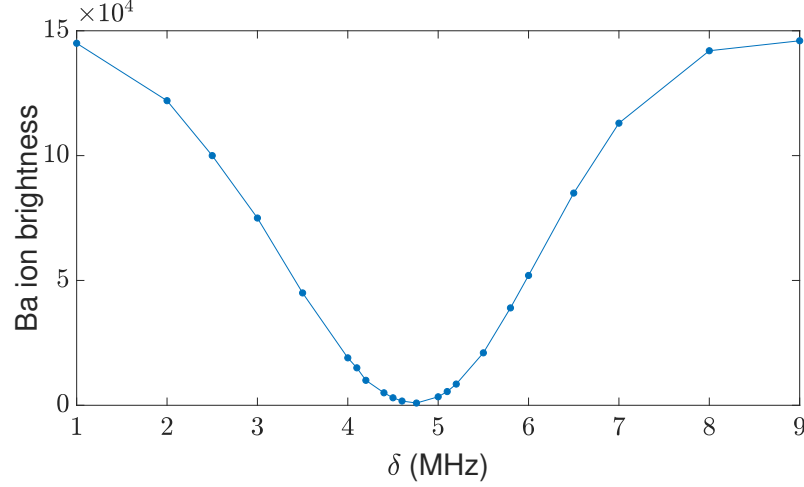


Figure 2.19: Creation of the dark state by applying only σ^+ and σ^- 650 nm beams with the frequency difference δ equal to the frequency difference between the states $|d_1\rangle$ and $|d_3\rangle$ in the $D_{3/2}$ manifold.

Note that this method is very useful when one needs to determine a magnetic field at the ion position without performing qubit state detection and without doing frequency scans of the Raman beams.

d. 532 nm/650 nm phase stability issues

As discussed in the previous section, we attempt to create a protected qubit with long coherence times. For that, we follow the proposal by Aharon, Drewsen, and Retzker [131] and implement the driving Hamiltonian H_d as shown in Fig. 2.20.

In Fig. 2.21, we demonstrate the coherent $\Delta m_j = \pm 1$ rotations between the $|D_1\rangle$ and $|D_2\rangle$ states in the presence of σ^+ and σ^- 650 nm driving laser fields. These results are similar to the ones in Fig. 2.16, where reprojecting fields were not applied. In fact, in the case of the continuous reprojecting into the protected qubit subspace,

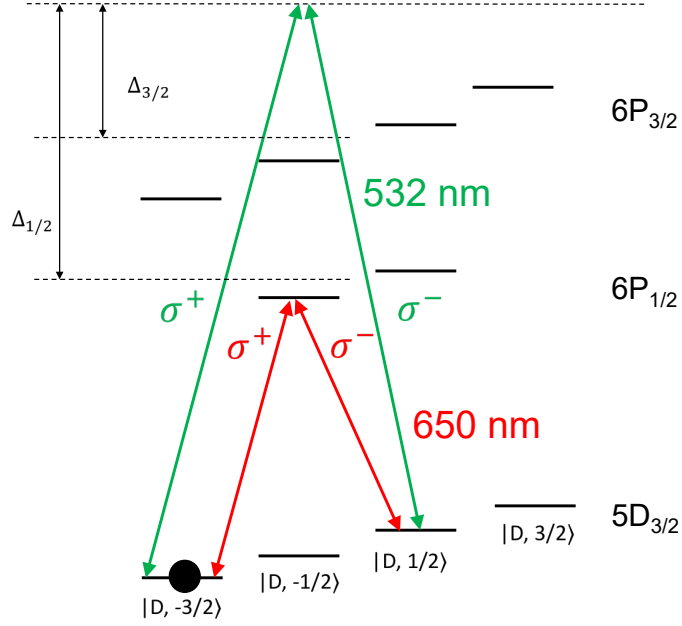


Figure 2.20: System reprojection to the protected qubit subspace by having the driving 650 nm laser fields on during all the Raman operations with 532 nm light.

the coherence time and contrast of the rotations between the $|D_1\rangle$ and $|D_2\rangle$ states appear to be worse. Additionally, the coherence time, obtained in the corresponding Ramsey experiment, $T_2^* = (202 \pm 29)\mu\text{s}$ is lower than $T_2^* = (350 \pm 37)\mu\text{s}$ from the experiment with no reprojecting 650 nm light. And of course, this result is far from being of the order of seconds as was expected. We attribute this problem to the 532 nm/650 nm phase stability issues.

In order to understand the phase stability problem between 650 nm σ^+ and σ^- laser fields and 532 nm Raman beams, we show schematics of RF circuitry in Fig. 2.22. In the experiment, we need to drive three AOMs – 650 nm σ^+ AOM, 650 nm σ^- AOM, and 532 nm Raman AOM with two tones – with different RF fields simultaneously. We had access only to a two-channel AWG². So, we used frequency filtering to send two signals from one AWG channel. In particular, the

²LeCroy ArbStudio 1102

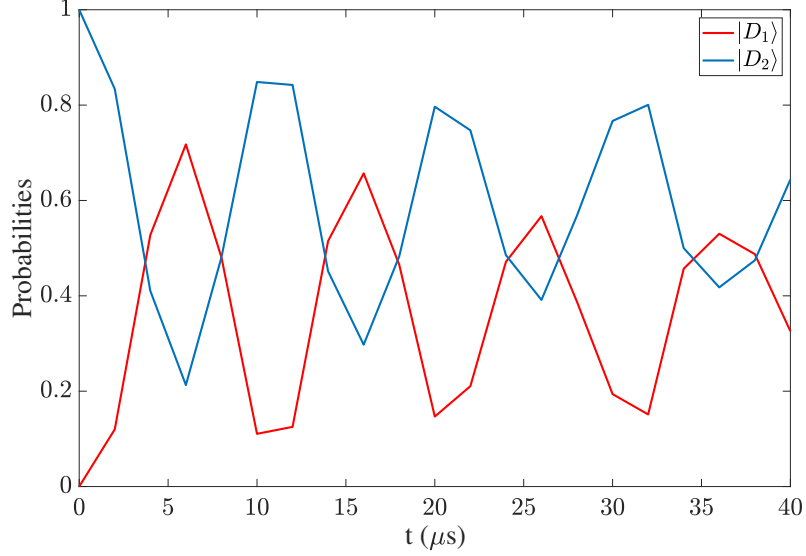


Figure 2.21: Coherent $\Delta m_j = \pm 1$ rotations between the $|D_1\rangle$ and $|D_2\rangle$ states performed by a pair of Raman 532 nm beams in the presence of σ^+ and σ^- 650 nm driving (reprojecting) laser fields.

first channel, AWG₁, sends out two RF signals – for the 532 nm AOM at 110 MHz and for the 650 nm σ^- AOM at 80 MHz. These signals are then frequency filtered to select an appropriate one for each of the branches. The second channel, AWG₂, serves the 650 nm σ^+ AOM at 80 MHz separately. With the current setup, we expect only a fixed offset between the optical phases of 650 nm σ^+ and σ^- beams over the entire duration of the experiment.

Since we noticed rapid decoherence and low contrast during $\Delta m_j = \pm 1$ Rabi flopping as shown in Fig. 2.21, first, we investigated the phase stability between the 650 nm σ^+ and σ^- beams. For that, we looked at the beatnote between two laser beams on the fast photo diode³. Naturally, we “rotate” the polarization of one of the σ beams (so that both beams have the same polarization) to observe this interference. In this case, we can see the interference signal in Fig. 2.23. The

³EOTech ET-2030A

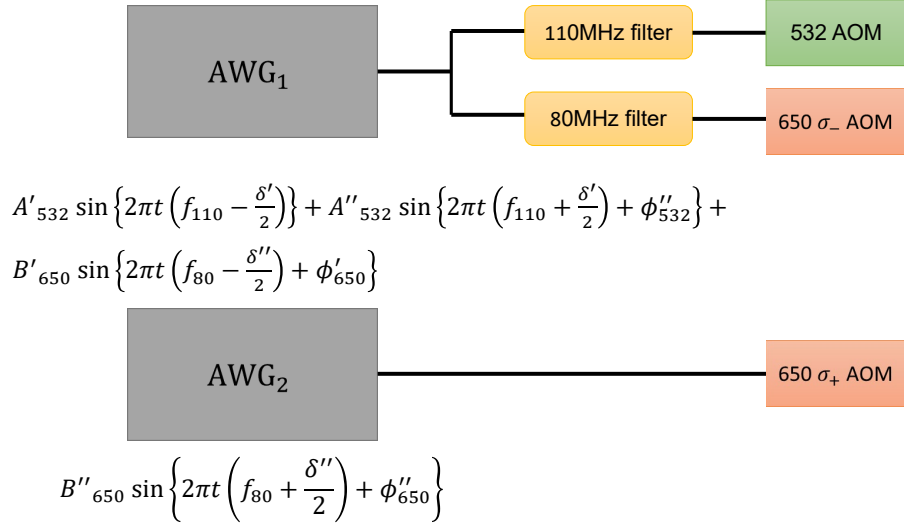


Figure 2.22: Schematic of RF circuitry used for driving coherent operations with 532 nm light in the $D_{3/2}$ manifold and for creating a driving Hamiltonian H_d based on σ^+ and σ^- 650 nm laser fields. Only two AWG channels are used in the experiment to produce three RF signals.

frequency of the oscillations is equal to 5 MHz, which is the frequency difference between the 650 nm σ_+ AOM and 650 nm σ_- AOM. (If polarizations of two 650 nm σ beams are orthogonal, then there are no fringes, but a straight line, just as expected.) When triggered by the experimental repetition rate, the interference signal is not stationary, but is shifting to the left as the time goes. This phase shift happens on the time scales of minutes. That can be explained by the phase instability between two 650 nm σ^+ and σ^- beams due to the phase noise introduced by RF filters and other RF electronics. Additionally, thermal drifts inside AOM crystals might contribute to the phase instability.

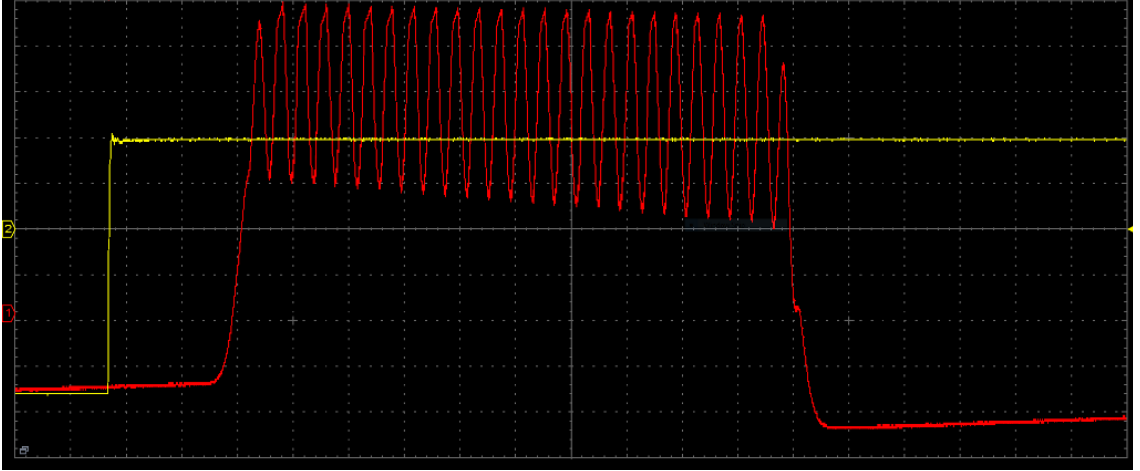


Figure 2.23: Beatnote signal between 650 nm σ^+ and σ^- laser beams on the fast photo diode.

Since the issue of phase stability between two 650 nm σ^+ and σ^- beams originates from RF components of the setup and from the optical pathlength instabilities inside AOMs, we add a phase shifter for an RF signal sent to one of the 650 nm σ AOMs as shown in Fig. 2.24.

By performing a beatnote lock as shown in Fig. 2.24, we are able to improve the phase stability by more than one and a half orders of magnitude. As a metric of phase stability, we use the following experiment. First, we prepare $^{138}\text{Ba}^+$ ion in the state $|D_2\rangle$, and then, while having the driving Hamiltonian H_d turned on, we perform $\pi/2$ rotation to the $|D_1\rangle$ state. We have this experiment in a “step-in-place” mode, where we just repeat it over and over again. If there were no phase stability issues, then in Fig. 2.25 we would expect the system to be in the state $|D_1\rangle$ (red curve) all the time, and the probability to find the system in the state $|D_2\rangle$ (blue curve) would be 0 all the time. We performed the “step-in-place” experiment for 2000 s.

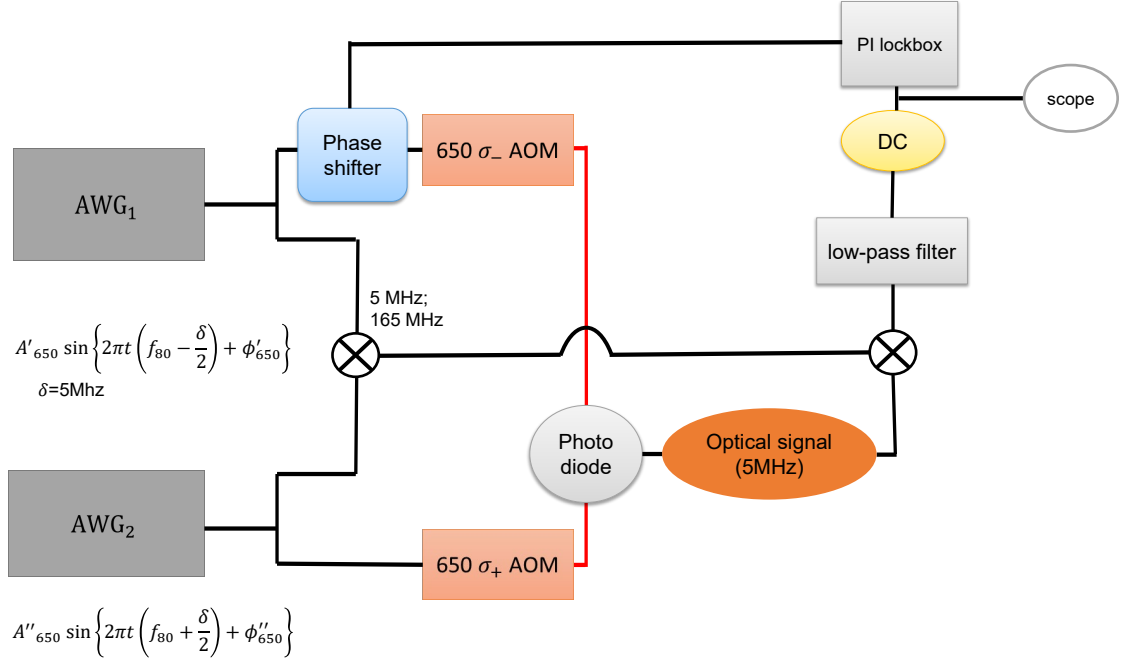


Figure 2.24: Schematic of RF circuitry used for the phase control between σ^+ and σ^- 650 nm laser fields that create a driving Hamiltonian H_d . By implementing beatnote lock, we improve the phase stability. The red line represents the optical 650 nm signal going to the photo diode.

The left panel of Fig. 2.25 shows the “step-in-place” experiment results before the implementation of the phase lock. We see a strong dip in the probability to find our system in the state $|D_1\rangle$ (red curve) at $t = 50$ arb. units that starts around 5 arb. units, which translates to $t = 10$ s. But after the implementation of the phase lock, we are able to push this time to $t = 200$ arb. units or $t = 400$ s, which gives us the improvement by a factor of 40. With this technique, we achieve the coherence time, obtained in the corresponding Ramsey experiment, $T_2^* = (202 \pm 29) \mu\text{s}$. In comparison, the non-phase-stabilized coherence time was $T_2^* = (86 \pm 11) \mu\text{s}$.

There are still some phase-related issues left that we could not address and resolve with the current experimental setup. We believe that all the additional RF components, such as mixers and filters, that we use introduce the phase stability

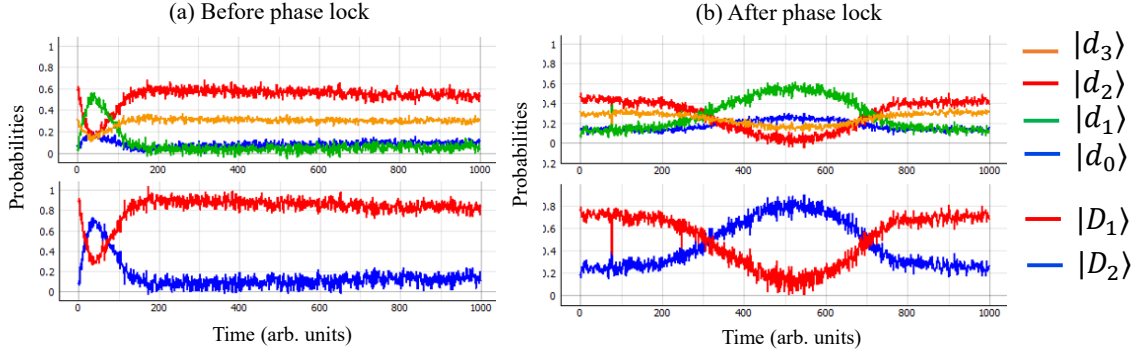


Figure 2.25: Improvement of the phase stability. In the “step-in-place” experiment where the rotation to $|D_1\rangle$ is performed with the driving H_d turned on, (a) before the implementation of the phase lock, the state flip starts around $t = 5$ arb. units and completes at $t = 50$ arb. units; (b) after the implementation of the phase lock, the state flip does not start until $t = 200$ arb. units and only completes at $t = 500$ arb. units.

issues. And a three-channel AWG might give us good enough RF signals that would help us achieve much longer coherence times for the protected qubit $\{|D_1\rangle, |D_2\rangle\}$.

Chapter 3: Mixed-Species Gates

Trapped-ion-based quantum computers are among the best to date, with characteristic long coherence times and high gate fidelities [98, 99, 100, 101]. One of the most promising directions in scaling up such systems is a modular architecture consisting of separate traps with memory/processing qubits and communication qubits that provide photonic links between the traps for remote entanglement [51, 102]. To eliminate cross-talk between photonic-link qubits and memory qubits, one of the solutions is to co-trap different atomic species. Once the remote entanglement between the communication ions is established via the photonic links, the information is swapped between a communication ion and one of the memory ions within the same module. The same procedure is performed in the other module, which results in entanglement between two memory qubits in separate modules. The entanglement swapping scheme can utilize a direct Cirac-Zoller mapping – also known as Quantum Logic Spectroscopy [10, 97] – or two Mølmer-Sørensen gates [142, 143, 144] with appropriate relative phase control of the two gates [82]. A high-fidelity mixed-species entangling gate is an essential ingredient for future quantum networks. Entangling quantum gates have been performed in various mixed-species ion systems, including ${}^9\text{Be}^+{}^{-25}\text{Mg}^+$ [128], ${}^9\text{Be}^+{}^{-40}\text{Ca}^+$ [145], ${}^{40}\text{Ca}^+{}^{-88}\text{Sr}^+$ [146], ${}^{171}\text{Yb}^+{}^{-138}\text{Ba}^+$ [123], and

$^{40}\text{Ca}^+ - ^{43}\text{Ca}^+$ [147].

Quantum entangling gates are mediated by Coulomb collective phonon modes of motion via qubit-state-dependent forces. In order to decouple the internal qubit states from the motional states at the end of a gate, it is necessary to know the frequencies and normal modes of motion, and satisfy all the spin-motion decoupling conditions discussed below [after Eq. (3.40)]. For that, the suitable amplitude [148, 149, 150, 151, 152], frequency [153, 154, 155], or phase [156, 157, 158] modulation of the driving laser fields, as well as multitone gates [159, 160, 161] have been proposed and implemented in long single-species ion chains.

In addition to network interconnections, a multi-species setup has another advantage – the communication ions can also serve for sympathetic cooling of the processing qubits in the long ion chains [88, 89, 90, 91, 92]. Usually, ions experience heating caused by fluctuations in the electric potential at the ion positions [93, 94], or the shuttling, separation, and recombination of ion strings [95, 96]. The ability to cool the memory qubits efficiently allows for longer computational times and for operations with higher fidelity, leading to a wider range of applications for quantum information processing.

Since in our experiments, $^{171}\text{Yb}^+$ ions are used for quantum memory, while $^{138}\text{Ba}^+$ ions are used as communication qubits, all the calculations and experiments are performed for this pair of species.

3.1 Two-Species Entangling Gates

3.1.1 Normal mode participation

We start with motional normal modes in mixed-species ion chains and their role in mixed-species entangling gates. Consider a chain of N ions with charge e and different masses m_j , $j = 1, \dots, N$, in a linear Paul trap [89, 162, 163]. Then the dynamics of the system are described by the Lagrangian

$$\mathcal{L} = \sum_{j=1}^N \frac{m_j \dot{\mathbf{r}}_j^2}{2} - U, \quad (3.1)$$

where U is the potential energy:

$$U = \sum_{j=1}^N \Phi(\mathbf{r}_j, m_j) + \frac{1}{2} \sum_{\substack{i,j=1 \\ i \neq j}}^N \frac{e^2}{4\pi\epsilon_0 |\mathbf{r}_i - \mathbf{r}_j|}. \quad (3.2)$$

Here $\Phi(\mathbf{r}_j, m_j)$ is the potential energy of an ion j with the mass m_j at a position \mathbf{r}_j in the harmonic potential of the trap electrodes.

The equilibrium position of an ion j along the trap axis, $z_j^{(0)}$, is determined by $\partial U / \partial z_j = 0$. By symmetry, $x_j^{(0)} = 0$ and $y_j^{(0)} = 0$. The standard Taylor expansion of the Lagrangian around the equilibrium positions yields:

$$\mathcal{L} \approx \frac{1}{2} \left(\sum_{j=1}^N m_j \dot{q}_j^2 - \sum_{i,j=1}^N V_{ij} q_i q_j \right), \quad (3.3)$$

$$V_{ij} = \left. \frac{\partial^2 U}{\partial q_i \partial q_j} \right|_0,$$

where in the axial case: $q_i = z_i - z_i^{(0)}$, and in the radial case: $q_i = x_i$ or y_i . The Lagrange equations for the normal modes of motion are then given by:

$$\sum_{j=1}^N V_{ij} b_j^k = \lambda_k m_i b_i^k, \quad (3.4)$$

where $\lambda_k = \omega_k^2$ is an eigenvalue and ω_k is a frequency of the normal mode b_j^k . Each normal mode represents an individual harmonic oscillator that can be quantized. We introduce the creation and annihilation operators, \hat{a}_k^\dagger and \hat{a}_k , for the mode k , and the original set of coordinates assumes the following standard quantized form:

$$\hat{x}_j = \sum_{k=1}^N b_j^k \sqrt{\frac{\hbar}{2m_j\omega_k}} (\hat{a}_k + \hat{a}_k^\dagger). \quad (3.5)$$

3.1.2 Mølmer-Sørensen interaction

In Eq. (3.4), we found the normal motional modes, and in the case of two ions, there are two normal modes in each dimension. The unperturbed Hamiltonian for the collective system of electronic and vibrational states of both ions is:

$$\hat{H}_0 = \sum_{i=1,2} \frac{\hbar\omega_i^{(0)}}{2} \sigma_i^z + \sum_{k=1,2} \hbar\omega_k a_k^\dagger a_k. \quad (3.6)$$

The interaction Hamiltonian is constructed using stimulated Raman transitions:

$$\begin{aligned} \hat{H}_1 = & \frac{\hbar\Omega_1}{2} [\sigma_1^+ \exp i(\mathbf{k}_1 \cdot \mathbf{r}_1 - \mu_1 t + \phi_1) + \text{H.c.}] \\ & + \frac{\hbar\Omega_2}{2} [\sigma_2^+ \exp i(\mathbf{k}_2 \cdot \mathbf{r}_2 - \mu_2 t + \phi_2) + \text{H.c.}], \end{aligned} \quad (3.7)$$

where Ω_i is a Rabi frequency, and σ_i^+ and σ_i^- are the spin raising and lowering operators. We use two pairs of laser beams with wave-vector difference k_i , frequency difference μ_i , and phase difference ϕ_i . We introduce the standard Lamb-Dicke parameters η_j^k :

$$\eta_j^k = |k_j| b_j^k \sqrt{\frac{\hbar}{2m_j\omega_k}}. \quad (3.8)$$

In the interaction picture, the interaction Hamiltonian is given by:

$$\hat{H}_I = \exp\left(\frac{i\hat{H}_0 t}{\hbar}\right) \hat{H}_1 \exp\left(-\frac{i\hat{H}_0 t}{\hbar}\right). \quad (3.9)$$

To simplify the interaction Hamiltonian in the interaction picture, we use the following identities obtained using the Baker-Campbell-Hausdorff (BCH) formula:

$$\exp\left(\frac{i\omega^{(0)}t}{2}\sigma^z\right)\sigma^+\exp\left(\frac{-i\omega^{(0)}t}{2}\sigma^z\right) = \exp(i\omega^{(0)}t)\sigma^+; \quad (3.10)$$

$$\exp\left(\frac{i\omega^{(0)}t}{2}\sigma^z\right)\sigma^-\exp\left(\frac{-i\omega^{(0)}t}{2}\sigma^z\right) = \exp(-i\omega^{(0)}t)\sigma^-; \quad (3.11)$$

$$\begin{aligned} & e^{(i\omega_1 t a_1^\dagger a_1)} \exp[i\eta_1 A (\hat{a}_1 + \hat{a}_1^\dagger)] e^{(-i\omega_1 t a_1^\dagger a_1)} \\ &= \exp[i\eta_1 A (\hat{a}_1 e^{-i\omega_1 t} + \hat{a}_1^\dagger e^{i\omega_1 t})]; \end{aligned} \quad (3.12)$$

$$\begin{aligned} & e^{(i\omega_2 t a_2^\dagger a_2)} \exp[i\eta_2 A (\hat{a}_2 + \hat{a}_2^\dagger)] e^{(-i\omega_2 t a_2^\dagger a_2)} \\ &= \exp[i\eta_2 A (\hat{a}_2 e^{-i\omega_2 t} + \hat{a}_2^\dagger e^{i\omega_2 t})]. \end{aligned} \quad (3.13)$$

From Eqs. (3.10) – (3.13), we get:

$$\hat{H}_I = \sum_i \Omega_i \exp \left[i \sum_k \eta_k^i (\hat{a}_k e^{-i\omega_k t} + \hat{a}_k^\dagger e^{i\omega_k t}) \right] \sigma_i^+ e^{-i(\delta_i t + \phi_i)} + \text{H.c.}, \quad (3.14)$$

where $\delta_i = \mu_i - \omega_i^{(0)}$ are the laser detunings.

Since we operate in the Lamb-Dicke regime, where the Lamb-Dicke parameters are small, we can use the Taylor expansion up to the first order to obtain:

$$\begin{aligned} \hat{H}_I &= \sum_k \eta_k^1 \Omega_1 (\hat{a}_k e^{-i\omega_k t} + \hat{a}_k^\dagger e^{i\omega_k t}) \sigma_1^+ e^{-i(\delta_1 t + \phi_1)} \\ &+ \sum_k \eta_k^2 \Omega_2 (\hat{a}_k e^{-i\omega_k t} + \hat{a}_k^\dagger e^{i\omega_k t}) \sigma_2^+ e^{-i(\delta_2 t + \phi_2)} + \text{H.c.}, \end{aligned} \quad (3.15)$$

The Mølmer-Sørensen Hamiltonian can be expressed in the form of the sum of a Jaynes-Cumming Hamiltonian (produced by the red sideband) and an “anti-Jaynes-Cumming Hamiltonian” (produced by the blue sideband):

$$\begin{aligned} \hat{H}_I &= \sum_k \left[\frac{\eta_k^1 \Omega_1}{2} \sigma_1^+ \hat{a}_k e^{-i(\delta_r^{(1)} t - \phi_r^{(1)})} + \frac{\eta_k^1 \Omega_1}{2} \sigma_1^+ \hat{a}_k^\dagger e^{-i(\delta_b^{(1)} t - \phi_b^{(1)})} \right. \\ &\left. + \frac{\eta_k^2 \Omega_2}{2} \sigma_2^+ \hat{a}_k e^{-i(\delta_r^{(2)} t - \phi_r^{(2)})} + \frac{\eta_k^2 \Omega_2}{2} \sigma_2^+ \hat{a}_k^\dagger e^{-i(\delta_b^{(2)} t - \phi_b^{(2)})} \right] + \text{H.c.} \end{aligned} \quad (3.16)$$

By choosing symmetric detunings: $\delta_r^{(i)} = -\delta_b^{(i)} = \delta^{(i)}$, we can express this interaction Hamiltonian in the following form:

$$\begin{aligned} \hat{H}_I &= \sum_k \left[\frac{\eta_k^1 \Omega_1}{2} \left(\hat{a}_k e^{-i(\delta^{(1)} t - \phi_m^{(1)})} + \hat{a}_k^\dagger e^{i(\delta^{(1)} t - \phi_m^{(1)})} \right) \cdot \hat{\sigma}_{\phi_{S_1}} + \right. \\ &\left. \frac{\eta_k^2 \Omega_2}{2} \left(\hat{a}_k e^{-i(\delta^{(2)} t - \phi_m^{(2)})} + \hat{a}_k^\dagger e^{i(\delta^{(2)} t - \phi_m^{(2)})} \right) \cdot \hat{\sigma}_{\phi_{S_2}} \right], \end{aligned} \quad (3.17)$$

where

$$\hat{\sigma}_{\phi_{S_1}} = \sigma_1^+ e^{i\phi_s^{(1)}} - \sigma_1^- e^{-i\phi_s^{(1)}}, \quad (3.18)$$

$$\hat{\sigma}_{\phi_{S_2}} = \sigma_2^+ e^{i\phi_s^{(2)}} - \sigma_2^- e^{-i\phi_s^{(2)}},$$

$$\phi_s^{(i)} = \frac{\phi_r^{(i)} + \phi_b^{(i)}}{2}, \quad \text{and} \quad \phi_m^{(i)} = \frac{\phi_r^{(i)} - \phi_b^{(i)}}{2}. \quad (3.19)$$

We decide to implement the MS gate based only on one of the normal modes, say \hat{a}_2 and \hat{a}_2^\dagger , and in this case, the electronic states do not couple to the other mode. In particular, the axial out-of-phase mode is used in the experiment due to its lower heating rate and a higher mode frequency compared to the in-phase mode.

We can set $\delta^{(1)} = \delta^{(2)} = \delta$, in which case the Hamiltonian reduces to:

$$\hat{H}_I = \mathcal{F}^* e^{i\delta t} \hat{a}_2^\dagger + \mathcal{F} e^{-i\delta t} \hat{a}_2, \quad (3.20)$$

where

$$\mathcal{F} = F_1 \hat{\sigma}_{\phi_{S_1}} + F_2 \hat{\sigma}_{\phi_{S_2}}, \quad \text{and} \quad F_i = \frac{\eta_2^i \Omega_i}{2} e^{i\phi_m^{(i)}}. \quad (3.21)$$

Following Refs. [164, 165], we interpret Eq. (3.20) as a Hamiltonian of a forced harmonic oscillator and use our knowledge of its time evolution. In one period of

evolution under this force, the acquired phase is:

$$\begin{aligned}\Phi_0 &= \frac{\pi}{2(\hbar\delta)^2} |F_1 \hat{\sigma}_{\phi_{S_1}} + F_2 \hat{\sigma}_{\phi_{S_2}}|^2 \\ &= \frac{\pi}{2(\hbar\delta)^2} \left[|F_1|^2 \hat{\sigma}_{\phi_{S_1}}^2 + |F_2|^2 \hat{\sigma}_{\phi_{S_2}}^2 + \hat{\sigma}_{\phi_{S_1}} \hat{\sigma}_{\phi_{S_2}} (F_1 F_2^* + F_2 F_1^*) \right].\end{aligned}\quad (3.22)$$

The operator $\hat{\sigma}_{\phi_{S_i}}$ has eigenstates:

$$\begin{aligned}|\uparrow_\phi\rangle_i &= \frac{1}{\sqrt{2}} \left(|\uparrow\rangle_i + e^{i\phi_s^{(i)}} |\downarrow\rangle_i \right) \quad \text{with eigenvalue } \epsilon_i = 1, \\ |\downarrow_\phi\rangle_i &= \frac{1}{\sqrt{2}} \left(|\downarrow\rangle_i - e^{-i\phi_s^{(i)}} |\uparrow\rangle_i \right) \quad \text{with eigenvalue } \epsilon_i = -1.\end{aligned}\quad (3.23)$$

The eigenstates of $\hat{\sigma}_z$ can be expressed via these states as:

$$\begin{aligned}|\uparrow\rangle_i &= \frac{1}{\sqrt{2}} \left(|\uparrow_\phi\rangle_i - e^{i\phi_s^{(i)}} |\downarrow_\phi\rangle_i \right), \\ |\downarrow\rangle_i &= \frac{1}{\sqrt{2}} \left(|\downarrow_\phi\rangle_i + e^{-i\phi_s^{(i)}} |\uparrow_\phi\rangle_i \right).\end{aligned}\quad (3.24)$$

It is easy to show that $\hat{\sigma}_{\phi_{S_i}}^2 |\uparrow\rangle_i = |\uparrow\rangle_i$, and $\hat{\sigma}_{\phi_{S_i}}^2 |\downarrow\rangle_i = |\downarrow\rangle_i$, or in other words, $\hat{\sigma}_{\phi_{S_i}}^2 = \mathbb{1}$.

We can set the phases of the forces acting on the two ions to be opposite $F_1 = -F_2$, then the phase Φ_0 is given by:

$$\Phi_0 = \frac{\pi}{2(\hbar\delta)^2} |F|^2 (2 - \hat{\sigma}_{\phi_{S_1}} \hat{\sigma}_{\phi_{S_2}}). \quad (3.25)$$

Therefore,

$$e^{i\Phi_0} = \exp \left\{ \frac{i\pi}{(\hbar\delta)^2} |F|^2 \right\} \exp \left\{ -\frac{i\pi|F|^2}{2(\hbar\delta)^2} \hat{\sigma}_{\phi_{S_1}} \hat{\sigma}_{\phi_{S_2}} \right\}. \quad (3.26)$$

Let us consider $\exp(-i\xi \hat{\sigma}_{\phi_{S_1}} \hat{\sigma}_{\phi_{S_2}})$, where $\xi = \frac{\pi|F|^2}{2(\hbar\delta)^2}$. Starting with the initial state $|\uparrow\uparrow\rangle = |\uparrow\rangle_1 |\uparrow\rangle_2$, we obtain the following evolution:

$$\begin{aligned} e^{-i\xi \hat{\sigma}_{\phi_{S_1}} \hat{\sigma}_{\phi_{S_2}}} |\uparrow\uparrow\rangle &= e^{-i\xi \hat{\sigma}_{\phi_{S_1}} \hat{\sigma}_{\phi_{S_2}}} \frac{1}{2} \left(|\uparrow_\phi\rangle_1 - e^{i\phi_s^{(1)}} |\downarrow_\phi\rangle_1 \right) \left(|\uparrow_\phi\rangle_2 - e^{i\phi_s^{(2)}} |\downarrow_\phi\rangle_2 \right) \\ &= \frac{1}{2} \left(e^{-i\xi} |\uparrow_\phi\rangle_1 |\uparrow_\phi\rangle_2 + e^{-i\xi} e^{i(\phi_s^{(1)} + \phi_s^{(2)})} |\downarrow_\phi\rangle_1 |\downarrow_\phi\rangle_2 \right. \\ &\quad \left. - e^{i\xi} e^{i\phi_s^{(1)}} |\downarrow_\phi\rangle_1 |\uparrow_\phi\rangle_2 - e^{i\xi} e^{i\phi_s^{(2)}} |\uparrow_\phi\rangle_1 |\downarrow_\phi\rangle_2 \right) \\ &= \frac{1}{2} \left[(e^{i\xi} + e^{-i\xi}) |\uparrow\uparrow\rangle + e^{i(\phi_s^{(1)} + \phi_s^{(2)})} (-e^{i\xi} + e^{-i\xi}) |\downarrow\downarrow\rangle \right] \\ &= \cos \xi |\uparrow\uparrow\rangle - i e^{i(\phi_s^{(1)} + \phi_s^{(2)})} \sin \xi |\downarrow\downarrow\rangle. \end{aligned} \quad (3.27)$$

When $\xi = \frac{\pi|F|^2}{2(\hbar\delta)^2} = \frac{\pi}{4}$, we get the desired entangled state:

$$|\uparrow\uparrow\rangle \rightarrow \frac{1}{\sqrt{2}} \left[|\uparrow\uparrow\rangle - i e^{i(\phi_s^{(1)} + \phi_s^{(2)})} |\downarrow\downarrow\rangle \right]. \quad (3.28)$$

Starting with the initial state $|\uparrow\downarrow\rangle = |\uparrow\rangle_1 |\downarrow\rangle_2$, we obtain the following evolution:

$$\begin{aligned}
e^{-i\xi\hat{\sigma}_{\phi_{S_1}}\hat{\sigma}_{\phi_{S_2}}} |\uparrow\downarrow\rangle &= e^{-i\xi\hat{\sigma}_{\phi_{S_1}}\hat{\sigma}_{\phi_{S_2}}} \frac{1}{2} \left(|\uparrow\phi\rangle_1 - e^{i\phi_s^{(1)}} |\downarrow\phi\rangle_1 \right) \left(|\downarrow\phi\rangle_2 + e^{-i\phi_s^{(2)}} |\uparrow\phi\rangle_2 \right) \\
&= \frac{1}{2} \left(e^{i\xi} |\uparrow\phi\rangle_1 |\downarrow\phi\rangle_2 + e^{-i\xi} e^{-i\phi_s^{(2)}} |\uparrow\phi\rangle_1 |\uparrow\phi\rangle_2 \right. \\
&\quad \left. - e^{-i\xi} e^{i\phi_s^{(1)}} |\downarrow\phi\rangle_1 |\downarrow\phi\rangle_2 - e^{i\xi} e^{i(\phi_s^{(1)} - \phi_s^{(2)})} |\downarrow\phi\rangle_1 |\uparrow\phi\rangle_2 \right) \\
&= \frac{1}{2} \left[e^{i\xi} \left(|\uparrow\rangle_1 + e^{i\phi_s^{(1)}} |\downarrow\rangle_1 \right) \left(|\downarrow\rangle_2 - e^{-i\phi_s^{(2)}} |\uparrow\rangle_2 \right) \right. \\
&\quad + e^{-i\xi} e^{-i\phi_s^{(2)}} \left(|\uparrow\rangle_1 + e^{i\phi_s^{(1)}} |\downarrow\rangle_1 \right) \left(|\uparrow\rangle_2 + e^{i\phi_s^{(2)}} |\downarrow\rangle_2 \right) \\
&\quad - e^{-i\xi} e^{i\phi_s^{(1)}} \left(|\downarrow\rangle_1 - e^{-i\phi_s^{(1)}} |\uparrow\rangle_1 \right) \left(|\downarrow\rangle_2 - e^{-i\phi_s^{(2)}} |\uparrow\rangle_2 \right) \\
&\quad \left. - e^{i\xi} e^{i(\phi_s^{(1)} - \phi_s^{(2)})} \left(|\downarrow\rangle_1 - e^{-i\phi_s^{(1)}} |\uparrow\rangle_1 \right) \left(|\uparrow\rangle_2 + e^{i\phi_s^{(2)}} |\downarrow\rangle_2 \right) \right] \\
&= \frac{1}{2} \left[(e^{i\xi} + e^{-i\xi}) |\uparrow\downarrow\rangle + e^{i(\phi_s^{(1)} - \phi_s^{(2)})} (-e^{i\xi} + e^{-i\xi}) |\downarrow\uparrow\rangle \right] \\
&= \cos \xi |\uparrow\downarrow\rangle - ie^{i(\phi_s^{(1)} - \phi_s^{(2)})} \sin \xi |\downarrow\uparrow\rangle.
\end{aligned} \tag{3.29}$$

And when $\xi = \frac{\pi|F|^2}{2(\hbar\delta)^2} = \frac{\pi}{4}$, we get the desired entangled state:

$$|\uparrow\downarrow\rangle \rightarrow \frac{1}{\sqrt{2}} \left[|\uparrow\downarrow\rangle - ie^{-i(\phi_s^{(2)} - \phi_s^{(1)})} |\downarrow\uparrow\rangle \right]. \tag{3.30}$$

Following the same derivations as those in Eqs. (3.27) and (3.29) for the two remaining states – $|\downarrow\downarrow\rangle$ and $|\downarrow\uparrow\rangle$, – we arrive to the complete truth table for MS

gate:

$$\begin{aligned}
|\downarrow\downarrow\rangle &\rightarrow \frac{1}{\sqrt{2}} \left[|\downarrow\downarrow\rangle - ie^{-i(\phi_s^{(1)} + \phi_s^{(2)})} |\uparrow\uparrow\rangle \right]; \\
|\downarrow\uparrow\rangle &\rightarrow \frac{1}{\sqrt{2}} \left[|\downarrow\uparrow\rangle - ie^{i(\phi_s^{(2)} - \phi_s^{(1)})} |\uparrow\downarrow\rangle \right]; \\
|\uparrow\downarrow\rangle &\rightarrow \frac{1}{\sqrt{2}} \left[|\uparrow\downarrow\rangle - ie^{-i(\phi_s^{(2)} - \phi_s^{(1)})} |\downarrow\uparrow\rangle \right]; \\
|\uparrow\uparrow\rangle &\rightarrow \frac{1}{\sqrt{2}} \left[|\uparrow\uparrow\rangle - ie^{i(\phi_s^{(1)} + \phi_s^{(2)})} |\downarrow\downarrow\rangle \right].
\end{aligned} \tag{3.31}$$

3.1.3 Experimental demonstration of entangling gates

In this section, we discuss our experimental realization of two alternative approaches to reach entanglement in such a way: (i) a direct Cirac-Zoller (CZ) mapping process by resonantly coupling to the collective motion of trapped ions [10, 97] and (ii) a dispersive Mølmer-Sørensen (MS) quantum gate [142, 143, 144] between the qubits.

3.1.3.1 Cirac-Zoller SWAP operations

First, we demonstrate a Cirac-Zoller SWAP operation [10] in which phonons are used as a bus to transfer information between communication (Ba^+) and memory (Yb^+) qubits. We initialize the system in the following state:

$$|\Psi_0\rangle = |\downarrow\rangle_{\text{Ba}^+} |\downarrow\rangle_{\text{Yb}^+} |0\rangle_n, \tag{3.32}$$

where $^{138}\text{Ba}^+$ and $^{171}\text{Yb}^+$ qubits are in the $|\downarrow\rangle$ state, and the ions are in the collective motional ground state, $|0\rangle_n$, i.e. there are no phonons. We follow the experimental procedure described in Ref. [97] where the quantum logic spectroscopy was performed between $^9\text{Be}^+$ and $^{27}\text{Al}^+$. Since we want to show the mapping of an arbitrary state from a $^{138}\text{Ba}^+$ ion to a nearby $^{171}\text{Yb}^+$ ion, we perform a variable rotation on the $^{138}\text{Ba}^+$ qubit:

$$|\Psi_1\rangle = (\alpha |\downarrow\rangle + \beta |\uparrow\rangle)_{\text{Ba}^+} |\downarrow\rangle_{\text{Yb}^+} |0\rangle_n, \quad (3.33)$$

that is transferred afterwards to the $^{171}\text{Yb}^+$ qubit as shown in Fig. 3.1(a). Then, we apply a red sideband (RSB) π rotation to the $^{138}\text{Ba}^+$ ion using 532 nm Raman beams. Since only the $|\uparrow\rangle_{\text{Ba}^+} |0\rangle_n \rightarrow |\downarrow\rangle_{\text{Ba}^+} |1\rangle_n$ transition can be driven by the RSB light, we obtain the joint state:

$$|\Psi_2\rangle = |\downarrow\rangle_{\text{Ba}^+} |\downarrow\rangle_{\text{Yb}^+} (\alpha |0\rangle_n + \beta |1\rangle_n). \quad (3.34)$$

Now the quantum information is stored in the motional degree of freedom, and to transfer it to the $^{171}\text{Yb}^+$ qubit, we we apply a red sideband (RSB) π rotation to the $^{171}\text{Yb}^+$ ion using 355 nm Raman beams. Similarly, we can drive only the $|\downarrow\rangle_{\text{Yb}^+} |1\rangle_n \rightarrow |\uparrow\rangle_{\text{Yb}^+} |0\rangle_n$ transition, which leads us to:

$$|\Psi_3\rangle = |\downarrow\rangle_{\text{Ba}^+} (\alpha |\downarrow\rangle + \beta |\uparrow\rangle)_{\text{Yb}^+} |0\rangle_n. \quad (3.35)$$

We see that the state of the $^{138}\text{Ba}^+$ ion from Eq. (3.33) can be perfectly mapped to the state of the $^{171}\text{Yb}^+$ ion in Eq. (3.35) only under one condition – we must start in the motional ground state, $|0\rangle_n$. This can be achieved by implementing sub-Doppler cooling procedures, such as Electromagnetically Induced Transparency (EIT) cooling [166, 167, 168], or Raman sideband cooling [169].

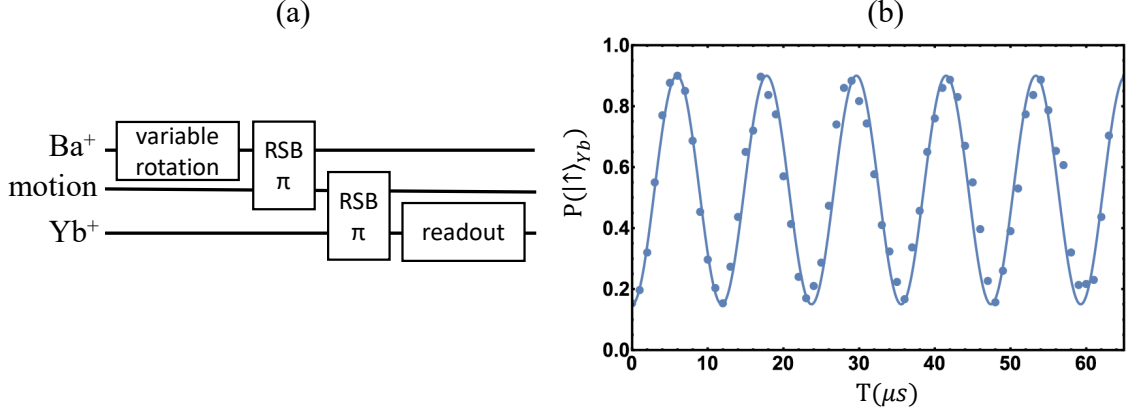


Figure 3.1: (a) Experimental sequence of Cirac-Zoller (CZ) entangling gate. (b) Rabi flopping performed on the $^{138}\text{Ba}^+$ ion and then read from the $^{171}\text{Yb}^+$ ion after the state mapping. The low mapping efficiency of 0.75 is due to imperfect cooling with the average number of quanta equal $\bar{n} \approx 0.1$.

In Fig. 3.1(b), we demonstrate the experimental results of the successful $^{138}\text{Ba}^+$ qubit state mapping to the $^{171}\text{Yb}^+$ ion. We achieve the mapping efficiency of 0.75. The limitation on this number is coming from the imperfect cooling – the average number of quanta is $\bar{n} \approx 0.1$. The requirement of the cooling to the motional ground state is a disadvantage since it is hard to achieve in the experiment and it requires the additional sub-Doppler cooling time that will eventually lead to extremely low remote entanglement generation rate in the future quantum network experiments. Therefore, the Mølmer-Sørensen (MS) interaction provides a better alternative to CZ SWAP operations between communication and memory qubits.

3.1.3.2 Mølmer-Sørensen gates

In the case of Mølmer-Sørensen entangling gate, we do not require cooling down to the ground state [143]. This makes MS a preferred quantum-state mapping operation. The MS interaction [142, 143, 144] is induced by simultaneous excitation of the off-resonant red and blue sideband transitions as shown in Fig. 3.2. The detailed explanation and derivation of the MS gate was given in Section 3.1.2.

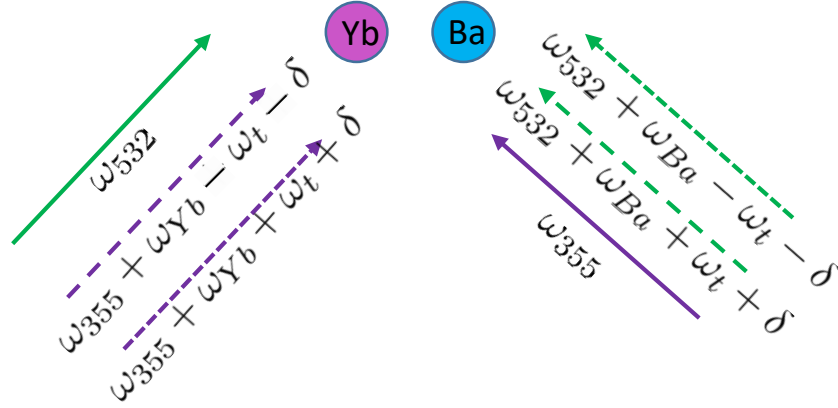


Figure 3.2: The Raman beam configuration for MS interaction between $^{171}\text{Yb}^+$ and $^{138}\text{Ba}^+$ ions. MS interaction is induced by simultaneous excitation of the off-resonant red and blue sideband transitions. The resulting $\Delta\mathbf{k}$ is along the trap axis, so that we address axial modes of motion.

As we discussed in Section 2.3.1.2, we use 355 nm light and 532 nm light to perform quantum operations on $^{171}\text{Yb}^+$ and $^{138}\text{Ba}^+$ ions, respectively. Conveniently, both colors come from the same laser, the Spectra Physics Vanguard pulsed laser. 355 nm is the third harmonic of the 1064 nm Nd:YVO4 source, while the second harmonic is at 532 nm. Note that 355 nm and 532 nm laser pulses do not follow the same path, and this leads to a shift in time when the spin dependent forces are applied to $^{171}\text{Yb}^+$ and $^{138}\text{Ba}^+$ ions. This time shift can be of the order of

$\frac{1}{\nu_r}$, where $\nu_r \approx 80$ MHz is the repetition rate of the pulsed laser. We can zero this time shift by delaying one beam with respect to the other, but it would be translated to the pathlength difference of the order of 1 m introducing additional pathlength fluctuations. According to our calculations presented in Appendix B, this shift in time does not affect the MS gate significantly, but only introduces an additional phase, $\phi_s^{(2)} \rightarrow \phi_s^{(2)} + \xi$, which leads to the following modified truth table [as compared to Eq. (3.31)]:

$$\begin{aligned}
|\uparrow\uparrow\rangle &\rightarrow |\uparrow\uparrow\rangle - ie^{i(\phi_s^{(1)} + \phi_s^{(2)} + \xi)} |\downarrow\downarrow\rangle, \\
|\uparrow\downarrow\rangle &\rightarrow |\uparrow\downarrow\rangle - ie^{-i(\phi_s^{(2)} - \phi_s^{(1)} + \xi)} |\downarrow\uparrow\rangle, \\
|\downarrow\uparrow\rangle &\rightarrow |\downarrow\uparrow\rangle - ie^{i(\phi_s^{(2)} - \phi_s^{(1)} + \xi)} |\uparrow\downarrow\rangle. \\
|\downarrow\downarrow\rangle &\rightarrow |\downarrow\downarrow\rangle - ie^{-i(\phi_s^{(1)} + \phi_s^{(2)} + \xi)} |\uparrow\uparrow\rangle.
\end{aligned} \tag{3.36}$$

The additional phase ξ can be compensated by adjusting the other phases. And after this phase tuning, the proper Mølmer-Sørensen gate is restored independently of the time shift between the optical-frequency combs acting on different ions.

We perform MS entangling operation based on the out-of-phase axial motional mode [123]. We choose the axial modes, because the radial modes are plagued by a strong mismatch between the amplitudes of motion of different species (see the detailed discussion of this point in Section 3.2). More experimental details can be found in Ref. [83].

In Fig. 3.3, we demonstrate the experimental results for MS entangling gate

between $^{171}\text{Yb}^+$ and $^{138}\text{Ba}^+$ ions. We show correlations between $^{171}\text{Yb}^+$ and $^{138}\text{Ba}^+$ spin states measured in the z -basis and in the x -basis. We measured the MS fidelity of $\mathcal{F} = 0.6$, and its low value is related to an excessive heating rate of the axial out-of-phase mode: $\dot{n} \approx 5 \text{ ms}^{-1}$, .

Unfortunately, the fidelity of MS gate is too low to perform a SWAP operation which includes two Mølmer-Sørensen gates with an appropriate relative phase control of the two gates [82].

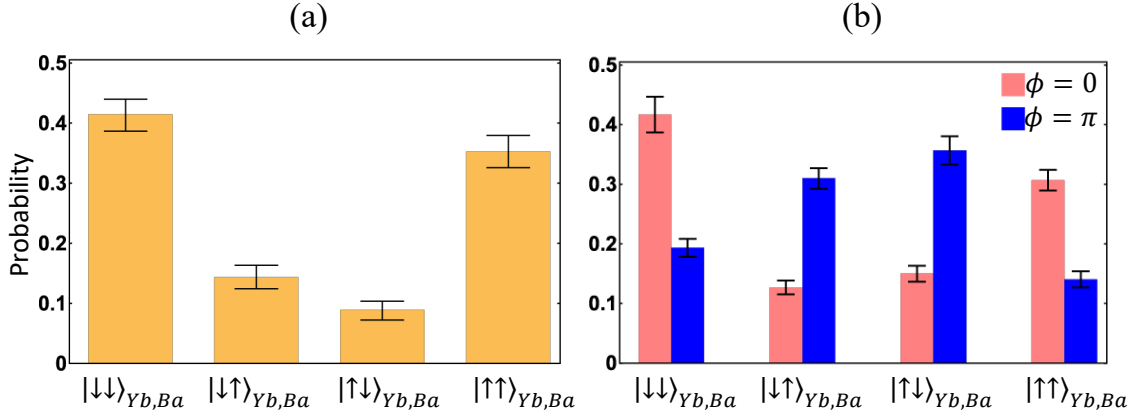


Figure 3.3: The experimental data for the MS entangling gate between $^{171}\text{Yb}^+$ and $^{138}\text{Ba}^+$ ions. (a) The correlations between $^{171}\text{Yb}^+$ and $^{138}\text{Ba}^+$ spin states measured in the z -basis. (b) The correlations between $^{171}\text{Yb}^+$ and $^{138}\text{Ba}^+$ spin states measured in the x -basis. After the MS interaction, we apply $\frac{\pi}{2}$ pulses on both qubits. $^{171}\text{Yb}^+$ $\frac{\pi}{2}$ rotation phase is scanned to achieve maximum contrast points, while $^{138}\text{Ba}^+$ $\frac{\pi}{2}$ rotation phase is fixed.

3.2 Long ion chains

In this section, we discuss long mixed-species ion chains, and investigate the role of axial and radial normal modes in entangling gates and in sympathetic cooling of the mixed-species ion chains. First, we perform calculations on the amplitude modulation (AM) and frequency modulation (FM) of the driving laser fields. With

these techniques, we optimize laser amplitude and frequency profiles, respectively, to achieve high fidelity of Mølmer-Sørensen entangling gates between different species within a long mixed-species ion chain. We compare the suitability of axial and radial modes for AM and FM pulse-shaping schemes. In the case of radial modes, the amount of laser power required to satisfy all the spin-motion decoupling conditions is very difficult to achieve in a real experiment, because there is a strong radial mode mismatch between different species. The required laser power in the case of axial modes is at least one order of magnitude lower and is routinely available in experiments. So, the axial modes are preferential for mixed-species gates. The calculations presented in this paper are performed for $^{171}\text{Yb}^+ - ^{138}\text{Ba}^+$ five-ion chains. However, the results of our calculations apply to both shorter and longer mixed-species ion chains with ions of masses that differ by over 10% [128, 145, 146].

Next, we study sympathetic cooling in the mixed-species chains and how this cooling process depends on normal modes. With the high mass ratio between the species, radial modes are much harder to cool than axial modes regardless of the configuration of the ions. It is crucial, however, to be able to cool the modes which are used for entangling gates in a given quantum computing procedure. We find that in the case of $^{171}\text{Yb}^+ - ^{138}\text{Ba}^+$ chains, the mass ratio is significant, and it makes the sympathetic cooling of the radial modes inefficient. For the processing $^{171}\text{Yb}^+$ qubits, $^{172}\text{Yb}^+$ or $^{174}\text{Yb}^+$ ions would instead be preferred for sympathetic cooling. Note, however, that this choice is not suitable for quantum-network communication due to crosstalk and fast attenuation of UV light in fibers.

3.2.1 Role of normal modes in MS gates

In Section 3.1.1, we discussed the construction and the solution of the problem of finding normal motional modes for long mixed-species ion chains. We start our discussion of multi-ion entangling quantum gates by introducing a generic laser-ion interaction Hamiltonian:

$$H_I = \sum_j \left(\Omega_j e^{i\mu t} e^{i(\Delta k x_j + \Delta \phi_j)} \hat{\sigma}_j^+ + \text{H.c.} \right), \quad (3.37)$$

where Ω_j is a Rabi frequency. We use two laser beams with wave-vector difference Δk , frequency difference μ , and phase difference $\Delta \phi_j$. After substituting Eq. (3.5) into Eq. (3.37), one can separate out the standard Lamb-Dicke parameters η_j^k in the exponents:

$$\eta_j^k = |\Delta k| b_j^k \sqrt{\frac{\hbar}{2m_j \omega_k}}. \quad (3.38)$$

We create the Mølmer-Sørensen interaction [142, 143, 144] by simultaneously driving off-resonant red and blue sideband transitions on each of the qubits. Similarly to the derivation from Section 3.1.1, we get the corresponding evolution operator in the following form [170]:

$$U(\tau) = \exp \left[\sum_{i,k} \left(\alpha_{ik}(\tau) \hat{a}_k^\dagger - \alpha_{ik}^*(\tau) \hat{a}_k \right) \hat{\sigma}_i^x + i \sum_{i,j} \chi_{ij} \hat{\sigma}_i^x \hat{\sigma}_j^x \right], \quad (3.39)$$

where

$$\begin{aligned}
\alpha_{ik}(\tau) &= - \int_0^\tau \eta_i^k \Omega_i(t) \exp(i\omega_k t) dt, \\
\chi_{ij}(\tau) &= \frac{1}{\hbar^2} \sum_k \eta_i^k \eta_j^k \int_0^\tau dt_1 \int_0^{t_1} dt_2 \sin[\omega_k(t_1 - t_2)] \\
&\quad \times [\Omega_i(t_1)\Omega_j(t_2) + \Omega_j(t_1)\Omega_i(t_2)].
\end{aligned} \tag{3.40}$$

To be able to drive the entangling gate between ions i and j in time τ , we require $\chi_{ij}(\tau) = \pi/4$. In order to decouple the motional and the spin degrees of freedom by the end of the gate evolution, we also require $\alpha_{ik}(\tau) = 0$. So, there are $2N + 1$ conditions in total that need to be satisfied: one $\pi/4$ phase condition and $2N$ spin-motion decoupling conditions (counting independently the real and imaginary components that correspond to coordinates and momenta, respectively). In this case, the evolution operator $U(\tau)$ reduces to $U_{ij} = \exp(i\pi\hat{\sigma}_i^x\hat{\sigma}_j^x/4)$. A number of methods have been introduced to fulfill these requirements. Among them are the pulse-shaping techniques – using amplitude [148, 149, 150, 151, 152], frequency [153, 154, 155], or phase [156, 157, 158] modulation of the driving laser fields, – as well as multitone gates [159, 160, 161].

The normal modes following from Eq. (3.4) enter both $\alpha_{ik}(\tau)$ and $\chi_{ij}(\tau)$ expressions. In the present work, we consider multi-species ion chains with 5 and 13 ions for visualization clarity, but we tested all our findings and conclusions in longer ion chains of up to 50 ions.

In Fig. 3.4, we show the frequencies and the normal modes for a five-ion chain with four $^{171}\text{Yb}^+$ ions and one $^{138}\text{Ba}^+$ ion located at the edge of the chain. We find

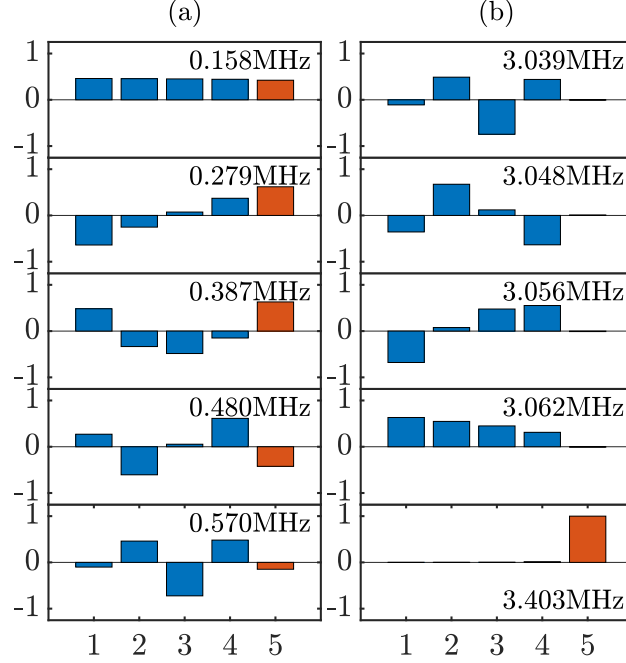


Figure 3.4: (a) Axial normal modes and their frequencies for a five-ion chain – four $^{171}\text{Yb}^+$ ions (blue) and one $^{138}\text{Ba}^+$ ion (red) located at the edge of the ion chain. (b) The same for the radial normal modes.

this configuration the most experimentally convenient for individual addressing and re-ordering purposes. Moreover, we have to avoid configurations with $^{138}\text{Ba}^+$ ion in the center of the chain, since due to the associated reflection symmetry, there are modes in which $^{138}\text{Ba}^+$ ion does not move at all. The trapping parameters used in the calculations are the radial trapping frequency $\omega_x = 3.06$ MHz and the axial trapping frequency $\omega_z = 0.16$ MHz. The axial frequency is chosen to be relatively low in order to keep long ion chains (up to 50 ions) linear.

The axial normal modes and frequencies for a chain of four $^{171}\text{Yb}^+$ ions and one $^{138}\text{Ba}^+$ ion [see Fig. 3.4(a)] do not differ much from those in a pure five $^{171}\text{Yb}^+$ chain. This indicates that entangling gates will work as efficiently as in a chain of five $^{171}\text{Yb}^+$ ions. On the other hand, the radial normal modes and frequencies differ significantly from those in the pure 5 $^{171}\text{Yb}^+$ chain. The drastic mismatch

can be seen, e.g., in the center-of-mass (CM) mode – the mode with the highest frequency in the bottom panel in Fig. 3.4(b). Given a moderate mass difference, we expect the amplitudes of motion for all ions in the CM mode to be close to each other, as in the axial case. For the radial modes, however, the $^{138}\text{Ba}^+$ ion motion decouples from that of the $^{171}\text{Yb}^+$ ions. Furthermore, the greater the ion mass difference is, the larger the mismatch we expect. The difference between the ways in which the axial and radial modes are affected by the ion mass difference can be explained as follows. The effective radial potential is primarily determined by the mass-dependent pseudopotential, while the effective axial potential is dominated by static terms. Also in the case of radial normal modes, note that the highest frequency is distant and isolated from the rest of the frequencies with a gap of 340 kHz, while the average frequency difference is about 8 kHz. This fact is relevant for the discussion of sympathetic cooling below.

The radial modes present difficulties associated with the mode mismatch. However, they are preferable for quantum entangling gate operations because they allow to maximize the value of Δk in Eq. (3.37) leading to faster gates – by setting it to $\Delta k = 2k$ in the counter-propagating beam geometry – and simultaneously support individual addressing [171]. So, in the current work, we focus on various techniques that might allow us to perform fast radial entangling mixed-species gates.

3.2.2 AM gates

First, we consider amplitude modulation (AM) of the driving field [148, 149, 150, 151, 152] to satisfy the $2N + 1$ conditions discussed in Sec. 3.2.1. In particular, the Rabi frequency $\Omega(t)$ is modulated in time as a piecewise-constant segmented pulse defined as:

$$\Omega(t) = \begin{cases} \Omega_1, & 0 \leq t \leq \tau/P \\ \Omega_2, & \tau/P \leq t \leq 2\tau/P \\ \vdots & \\ \Omega_P, & (P-1)\tau/P \leq t \leq \tau \end{cases}, \quad (3.41)$$

where τ is the gate time.

Using Eq. (3.41), we can rewrite Eq. (3.40) in the following form [172, 173]:

$$\begin{aligned} \alpha_{ik}(\tau) &= \sum_{p=1}^P \Omega_p A_i^k(p), \\ \chi_{ij}(\tau) &= \sum_{p=1}^P \sum_{p'=1}^P \Omega_p \Omega_{p'} \gamma'_{pq}, \end{aligned} \quad (3.42)$$

where

$$\begin{aligned} A_i^k(p) &= -\eta_i^k \int_{(p-1)\tau/P}^{p\tau/P} \sin(\mu t) e^{i\omega_k t} dt, \\ \gamma'_{pq} &= \sum_{k=1}^N \int_{(p-1)\tau/P}^{p\tau/P} dt_2 \int_{(q-1)\tau/P}^{q\tau/P} dt_1 \eta_i^k \eta_j^k \sin \omega_k(t_2 - t_1) \sin \mu t_2 \sin \mu t_1. \end{aligned} \quad (3.43)$$

Therefore, in the matrix form, the gate criteria can be written as:

$$\mathbf{A}\mathbf{\Omega} = 0, \quad \mathbf{\Omega}^T \gamma' \mathbf{\Omega} = \frac{\pi}{4}. \quad (3.44)$$

As a quality metric for the MS gate, we use the fidelity \mathcal{F} of the MS operation represented by a density matrix ρ_f :

$$\mathcal{F} = \langle \Psi_{\text{ideal}} | \rho_f | \Psi_{\text{ideal}} \rangle, \quad (3.45)$$

where the ideal final state $|\Psi_{\text{ideal}}\rangle$ is defined as a right-hand side of Eq. (3.31) corresponding to the respective initial state. Note that ρ_f is a reduced density matrix, in which the motional states are traced over. We assume that the initial motional state is thermal with a distribution given by:

$$\rho_k = \sum_{n=0}^{\infty} \left(\frac{n_k}{1 - \bar{n}_k} \right)^{n_k} e^{-n_k \hbar \omega_k / k_B T} |n_k\rangle \langle n_k|, \quad (3.46)$$

where mode k has the average energy of $k_B T = \bar{n}_k \hbar \omega_k$.

Following Refs. [172, 173], we simplify the fidelity expression to:

$$\begin{aligned} \mathcal{F} &\approx 1 - \frac{4}{5} \sum_k (|\alpha_{ik}|^2 + |\alpha_{jk}|^2) \cosh \frac{\hbar \omega_k}{2k_B T} \\ &= 1 - \frac{4}{5} \mathbf{\Omega}^T \left[\sum_k \left(A_i^{k\dagger} A_i^k + A_j^{k\dagger} A_j^k \right) \cosh \frac{\hbar \omega_k}{2k_B T} \right] \mathbf{\Omega} \\ &\equiv 1 - \mathbf{\Omega}^T \mathbf{M} \mathbf{\Omega}. \end{aligned} \quad (3.47)$$

During the optimization, we need to minimize the infidelity of the MS gate, $1 - \mathcal{F}$, subject to a constraint that $\mathbf{\Omega}^T \gamma' \mathbf{\Omega} = \frac{\pi}{4}$. For this purpose, we use the method of Lagrange multipliers and consider the minimization problem for $\Lambda(\mathbf{\Omega}, \lambda)$:

$$\Lambda(\mathbf{\Omega}, \lambda) = \mathbf{\Omega}^T \mathbf{M} \mathbf{\Omega} - \lambda \left(\mathbf{\Omega}^T \gamma' \mathbf{\Omega} - \frac{\pi}{4} \right). \quad (3.48)$$

Then we obtain the following set of Euler-Lagrange equations:

$$\begin{aligned} \frac{\partial \Lambda}{\partial \mathbf{\Omega}} &= (\mathbf{M} + \mathbf{M}^T) \mathbf{\Omega} - \lambda (\gamma' + \gamma'^T) \mathbf{\Omega} = 0, \\ \frac{\partial \Lambda}{\partial \lambda} &= \mathbf{\Omega}^T \gamma' \mathbf{\Omega} - \frac{\pi}{4} = 0. \end{aligned} \quad (3.49)$$

By solving Eq. (3.49), we find the optimal expression for the Rabi frequency $\mathbf{\Omega}$ with the vector components representing the pulse segments.

If $\Omega(t)$ has $2N + 1$ segments, the existence of the solution for $2N + 1$ constraints is guaranteed, and the problem is reduced to a system of linear equations. However, for long single-species chains, one can use less than N segments to achieve high fidelities of entangling gates, since most of the motional modes have relatively low populations [155]. As we discussed in Sec. 3.1.1, the axial normal modes in the $4 \text{ }^{171}\text{Yb}^+ - ^{138}\text{Ba}^+$ chain are similar to those in the pure $5 \text{ }^{171}\text{Yb}^+$ chain, and all the findings and techniques used in single-species chains apply.

In Table 3.1, we show the results of our calculations for a five-segment AM pulse applied to a five-ion ($4 \text{ }^{171}\text{Yb}^+ - ^{138}\text{Ba}^+$) chain with a pulse duration $\tau = 200 \mu\text{s}$. The $^{138}\text{Ba}^+$ ion is located at the edge of the chain – see Fig. 3.4. As shown in the

Ion pair	Axial gates		Radial gates	
	Ω_{peak} , kHz	F , %	Ω_{peak} , kHz	F , %
(1 – 5)	11	99.86	400	81.03
(2 – 5)	11	99.86	310	85.86
(3 – 5)	12	99.82	175	95.65
(4 – 5)	9	99.81	70	99.22

Table 3.1: Peak Rabi frequencies Ω_{peak} and average fidelities F of five-segment AM entangling gates between different $^{171}\text{Yb}^+ - ^{138}\text{Ba}^+$ pairs in a five-ion chain based on axial and radial modes. The $^{138}\text{Ba}^+$ ion is located at the position 5.

table, for axial gates, we need low Rabi frequencies – of the order of 10 kHz – to achieve high-fidelity entangling gates between any pair of qubits. On the contrary, for radial gates, the required Rabi frequencies are much higher, while the fidelities are way lower. This drastic difference comes from the large mismatch between $^{138}\text{Ba}^+$ and $^{171}\text{Yb}^+$ radial modes, as shown in Fig. 3.4. The ion pair (1 – 5) has the worst amplitude mismatch, which leads to the highest Ω_{peak} and the lowest fidelity F , as shown in Table 3.1 and Fig. 3.5(a). Obviously, five segments of the AM pulse are not enough to perform a high-fidelity radial gate in the pair (1 – 5). By increasing the segment number to $2N = 10$, we obtain an average gate fidelity $F = 99.996\%$. However, in this case, an even higher Rabi frequency is required [see Fig. 3.5(b)], which is definitely a disadvantage. To be able to perform high-fidelity entangling radial gates between $^{171}\text{Yb}^+$ and $^{138}\text{Ba}^+$, we require a Rabi frequency about 80 times higher than for axial gates between the same pair of ions, and the corresponding intensities are not feasible in real experiments. From now on, we will focus on the most difficult case – on the entangling gates in the ion pair (1 – 5) due to the largest radial mode mismatch.

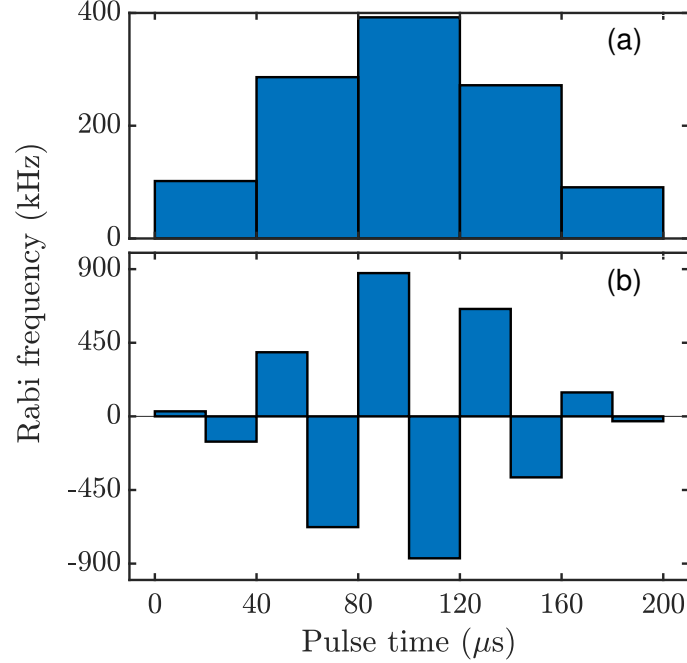


Figure 3.5: Amplitude-modulated pulses of the driving field for a radial AM entangling gate between $^{171}\text{Yb}^+$ and $^{138}\text{Ba}^+$ ions in a five-ion chain for the ion pair (1 – 5). (a) Five-segment pulse with the peak Rabi frequency $\Omega_{\text{peak}} = 400$ kHz; (b) ten-segment pulse with the peak Rabi frequency $\Omega_{\text{peak}} = 900$ kHz. In both cases, the pulse duration $\tau = 200$ μs .

Previously, we assumed equal intensities for each driving field, and arrived at extremely high laser intensities required to drive the entangling radial gates between $^{171}\text{Yb}^+$ and $^{138}\text{Ba}^+$ ions. However, we can instead apply 355 nm and 532 nm beams with different powers on $^{171}\text{Yb}^+$ and $^{138}\text{Ba}^+$ ions, respectively, and thereby generalize the conventional AM pulse-shaping technique. We will refer to this approach as dual AM pulse shaping. Now, in Eq. (3.41), we allow different values Ω_j^{355} and Ω_j^{532} , $j = 1, \dots, P$ and perform optimization of these $2P$ independent parameters to find $\Omega_{355}(t)$ and $\Omega_{532}(t)$.

In this case, we construct the Lagrangian similarly to the way we obtained

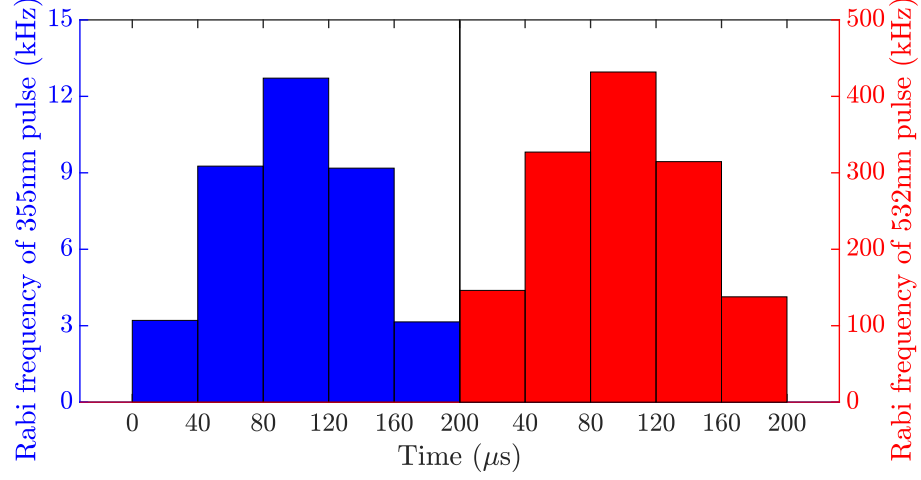


Figure 3.6: Dual five-segment amplitude modulation of the driving fields for an entangling radial gate between $^{171}\text{Yb}^+$ and $^{138}\text{Ba}^+$ ions in a five-ion chain, ion pair (1 – 5). 355 nm AM pulse shape and the corresponding vertical axis on the left side are shown in blue; 532 nm pulse and the corresponding vertical axis on the right side are in red. The pulse duration $\tau = 200 \mu\text{s}$.

Eq. (3.48) using the method of Lagrange multipliers:

$$\Lambda(\Omega_{355}, \Omega_{532}, \lambda) = \Omega_{355}^T \mathbf{M}_{355} \Omega_{355} + \Omega_{532}^T \mathbf{M}_{532} \Omega_{532} - \lambda \left(\Omega_{355}^T \gamma' \Omega_{532} - \frac{\pi}{4} \right), \quad (3.50)$$

and the corresponding equations have the following form similar to those in Eq. (3.49):

$$\begin{aligned} \frac{\partial \Lambda}{\partial \Omega_{355}} &= (\mathbf{M}_{355} + \mathbf{M}_{355}^T) \Omega_{355} - \lambda \gamma' \Omega_{532} = 0, \\ \frac{\partial \Lambda}{\partial \Omega_{532}} &= (\mathbf{M}_{532} + \mathbf{M}_{532}^T) \Omega_{532} - \lambda \gamma'^T \Omega_{355} = 0, \\ \frac{\partial \Lambda}{\partial \lambda} &= \Omega_{355}^T \gamma' \Omega_{532} - \frac{\pi}{4} = 0. \end{aligned} \quad (3.51)$$

Then, we can present this optimization problem for $\tilde{\Omega} = \begin{pmatrix} \Omega_{355} \\ \Omega_{532} \end{pmatrix}$ in the matrix

form:

$$\begin{aligned}\mathbf{M}\check{\Omega} &= \lambda\Gamma\check{\Omega}, \\ \check{\Omega}^T\Gamma\check{\Omega} &= \frac{\pi}{4},\end{aligned}\tag{3.52}$$

where

$$\mathbf{M} = \begin{pmatrix} \mathbf{M}_{355} + \mathbf{M}_{355}^T & 0 \\ 0 & \mathbf{M}_{532} + \mathbf{M}_{532}^T \end{pmatrix}, \quad \Gamma = \begin{pmatrix} 0 & \gamma \\ \gamma^T & 0 \end{pmatrix}.\tag{3.53}$$

This way, we generalized the conventional AM pulse-shaping technique to the dual AM pulse shaping, in which the Rabi frequencies of the two beams are optimised independently.

We simulate the five-segment entangling radial gate between $^{171}\text{Yb}^+$ and $^{138}\text{Ba}^+$ ions in the five-ion chain, but due to independent intensities, still have $2N$ parameters to vary. The optimization results are presented in Fig. 3.6. In the case of independent Rabi frequencies, since we have twice as many degrees of freedom, the fidelity of the quantum operation $F = 95.22\%$ is significantly higher than in the conventional five-segment AM pulse-shaping technique (81.03%, see Table 3.1). The optimization procedure finds the gate frequency $\mu \approx \omega_4 + 8$ kHz, which is close to the lower four frequencies and distant from the highest, isolated one [see the frequencies in Fig. 3.4(b)]. Also, since the radial modes have a strong amplitude mismatch for the pair (1–5) that we focus on in the calculations, the Rabi frequencies of the 355 nm and the 532 nm pulses differ by a factor of ~ 32 : $\Omega_{\text{peak}}^{355} = 13$ kHz

and $\Omega_{\text{peak}}^{532} = 420$ kHz. The latter one would be hard to achieve in the experiment due to the laser power limitations. Currently available laser power would make the MS gates forbiddingly long. For comparison, we also performed calculations for the seven-segment dual AM pulse. We improved the gate fidelity to $F = 99.53\%$ with similar Rabi frequencies, $\Omega_{\text{peak}}^{355} = 20$ kHz and $\Omega_{\text{peak}}^{532} = 440$ kHz, while the conventional seven-segment AM model gives us $F = 96.5\%$ with $\Omega_{\text{peak}} = 540$ kHz.

3.2.3 AM-FM gates

As we discussed in Sec. 3.2.2, the AM radial gates require high Rabi frequencies of the driving fields. In this section, we first consider a different way of satisfying the $2N + 1$ conditions ($\pi/4$ phase condition and conditions on decoupling motion from spin) – frequency modulation (FM) of the driving fields [153, 154, 155]. In this case, we allow the frequency of the driving field to vary in time, but the Rabi frequencies Ω stay constant in time. With that, $\alpha_{ik}(\tau)$ and $\chi_{ij}(\tau)$ acquire the following form [153]:

$$\begin{aligned}\alpha_{ik}(\tau) &= -\eta_i^k \Omega \int_0^\tau e^{i\theta_k(t)} dt, \\ \chi_{ij}(\tau) &= \frac{\Omega^2}{\hbar^2} \sum_{k=1}^N \eta_i^k \eta_j^k \int_0^\tau dt_1 \int_0^{t_1} dt_2 \sin[\theta_k(t_1) - \theta_k(t_2)], \\ \theta_k(t) &= \int_0^t \delta_k(t') dt',\end{aligned}\tag{3.54}$$

where $\delta_k(t)$ is the detuning of the driving field relative to the mode k . Here, we assume equal Rabi frequencies for 355 nm and 532 nm light. First, we try to satisfy

$2N$ conditions $\alpha_{ik}(\tau) = 0$ by performing the optimization of the cost function [153]. Once the frequency profile is found, we choose the Rabi frequency Ω_{peak} to satisfy the remaining entanglement condition for a given pair of qubits (the $\pi/4$ phase condition).

Following Ref. [154], we choose FM pulse shape to be symmetric in time and combine this frequency modulation optimization with a fixed amplitude modulation $\Omega(t)$ of the shape presented in Fig. 3.7(a) (three plateaus connected by smooth cosine ramps). The resulting scheme is referred to as the AM-FM gate.

Not surprisingly, similarly to the case in Sec. 3.2.2, high-fidelity axial gates between any pair of ions in the mixed-species chain require low Rabi frequencies of the order of 10 kHz. The radial entangling gates, however, still require much higher Rabi frequencies of the driving fields due to the strong amplitude mismatch between $^{171}\text{Yb}^+$ and $^{138}\text{Ba}^+$ ions, despite the more sophisticated driving.

In Fig. 3.7, we show the frequency and amplitude modulation of the driving laser fields for the AM-FM entangling operation between $^{171}\text{Yb}^+$ and $^{138}\text{Ba}^+$ ions for the ion pair (1 – 5). As shown in panel (b), we first try a pulse with four distinct turning points in the frequency domain [the intensity-domain shape is fixed to that shown in panel (a)]. For this example, as an initial guess, we choose the reference frequency $\mu = \omega_4 + 2.5$ kHz that represents the 0 level in panel (b). The fidelity of this entangling gate $F = 99.76\%$, and the peak Rabi frequency $\Omega_{\text{peak}} = 125$ kHz [see Fig. 3.7(a)]. By increasing the number of the turning points in the frequency domain, we achieved a much higher gate fidelity, but it did not allow us to lower the required Rabi frequencies. Although the required Rabi frequency in the AM-FM

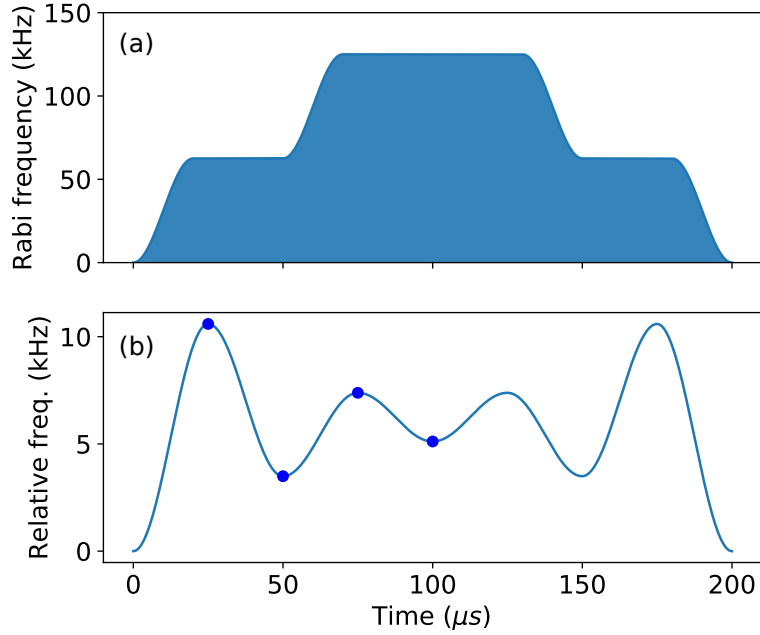


Figure 3.7: Amplitude and frequency modulation of the driving fields for an AM-FM entangling gate between $^{171}\text{Yb}^+$ and $^{138}\text{Ba}^+$ ions in a five-ion chain – ion pair (1 – 5). (a) Fixed amplitude modulation consists of three plateaus connected with cosine ramps. (b) Optimized frequency modulation has a set of turning points (blue dots) connected via cosine curves. Note that the pulse is set to be symmetric in time. The gate duration $\tau = 200 \mu\text{s}$.

gate is much lower than that for the AM gate, it is still over one order of magnitude higher than the Rabi frequency necessary for the axial entangling gates. However, while it remains difficult to achieve the required powers in experiment, this approach to radial gates is much more promising than pure AM or FM techniques.

The calculations presented in this thesis are performed for $^{171}\text{Yb}^+ - ^{138}\text{Ba}^+$ five-ion chains. However, our findings are readily generalized to shorter and longer mixed-species ion chains (we checked the lengths between 2 and 50 ions) with relatively high mass ratio. This includes $^9\text{Be}^+ - ^{25}\text{Mg}^+$ [128], $^9\text{Be}^+ - ^{40}\text{Ca}^+$ [145], and $^{40}\text{Ca}^+ - ^{88}\text{Sr}^+$ [146]. In fact, in Refs. [123, 128, 145, 146], only axial entangling gates

were performed between mixed species in a two-ion crystals due to the strong radial mode mismatch. Even in the case of $^{40}\text{Ca}^+ - ^{43}\text{Ca}^+$ chain [147], where the masses did not differ much, the axial gates were chosen.

3.2.4 Sympathetic cooling

In Secs. 3.2.2–3.2.3, we discussed the role of the normal modes in the mixed-species entangling operations in long ion chains. These operations are a necessary element of modular quantum networks. Another important application of the mixed-species ion chains is sympathetic cooling [88, 89, 90, 91, 92]. The idea is that we can constantly cool certain ions in the chain (“coolant” ions) – $^{138}\text{Ba}^+$ in our case – while continuously doing quantum computations with the processing ions – $^{171}\text{Yb}^+$ in our case – with no disruptions [27].

3.2.4.1 Cooling rate calculations

Following Ref. [89], we define the cooling rate W_k as:

$$W_k = \sum_{\{j\}} |\eta_j^k|^2, \quad (3.55)$$

where the cooling ions are represented by $\{j\}$, and η_j^k is the Lamb-Dicke parameter for the mode k and ion j from Eq. (3.38). Naturally, we can achieve the largest cooling rate when all the ions are subject to the cooling laser. Since the Lamb-Dicke parameters enter Eq. (3.55) directly, we expect the cooling rates for the radial and axial mixed-species modes to differ dramatically from each other.

An alternative way to characterize cooling is to look at the average position fluctuation $\delta q_i = \sqrt{\langle q_i^2 \rangle}$ of the ions [174] with $q_i = x_i$ for the radial modes and $q_i = z_i - z_i^{(0)}$ for the axial modes. Then from Eq. (3.5), we obtain:

$$\langle q_i^2 \rangle = \sum_k \frac{\hbar}{2m_i\omega_k} [b_i^k]^2 \left[n_k^B(T) + \frac{1}{2} \right], \quad (3.56)$$

where b_i^k is the normal mode, and $n_k^B(T)$ is the phonon number in the k mode at temperature T .

A few “coolant-ion” configurations were proposed for long ion chains [174], including edge cooling (the “coolant” ions are located at the edges of the chain), and periodic-node cooling (the “coolant” ions are positioned periodically in the chain). We explored these approaches via the metrics in Eqs. (3.55) and (3.56) and, as expected, found that the axial modes are easy to cool even with a small number of the “coolant” ions, while it is hard to cool the radial modes, especially the higher-frequency ones, due to the strong amplitude mismatch between different species.

To get an intuitive understanding of the difficulties in cooling the radial modes, we show all the radial modes for a 13-ion chain in Fig. 3.8. In this example, we follow Ref. [174], and place four “coolant” $^{138}\text{Ba}^+$ ions periodically in the chain (see Fig. 3.8, top-left panel). The mode with the highest frequency (bottom-right panel) is the CM mode. Only two edge $^{138}\text{Ba}^+$ ions are moving in this case, while the motion of all $^{171}\text{Yb}^+$ ions is virtually absent and is thus completely decoupled from the motion of the $^{138}\text{Ba}^+$ ions. The next three modes have similar character. At the same time,

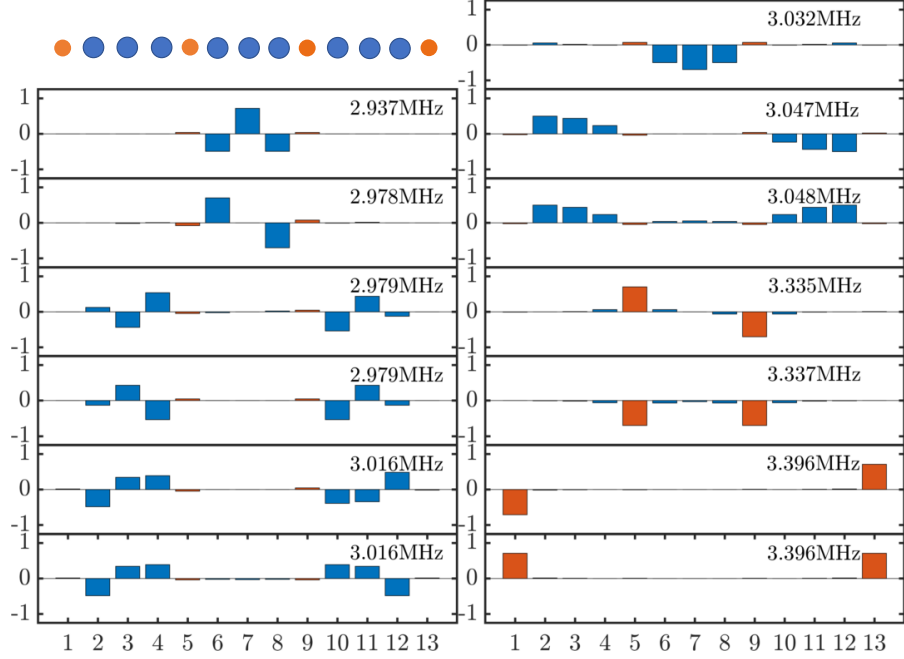


Figure 3.8: Frequencies and radial normal modes for a 13-ion-long chain - nine $^{171}\text{Yb}^+$ ions (blue) and four $^{138}\text{Ba}^+$ ion (red) placed periodically in the ion chain. The mode with the highest frequency is the center-of-mass (CM) mode.

the rest of the modes have virtually no $^{138}\text{Ba}^+$ motion. Note that there are four higher frequencies distant from the other nine frequencies with the gap of 350 kHz, while the average frequency difference is about 15 kHz. We have already discussed a similar feature in Sec. 3.1.1, where in the ion chain there was only one $^{138}\text{Ba}^+$ ion, and the highest frequency was isolated from the rest of the spectrum. The number of the isolated spectral lines here is equal to number of the $^{138}\text{Ba}^+$ ions in the chain as well, and these frequencies correspond to the modes with the most pronounced $^{138}\text{Ba}^+$ motion.

In Fig. 3.9, we show the cooling rate of the axial modes as a function of the total number of ions in the ion chain, while the number of the “coolant” $^{138}\text{Ba}^+$ ions is fixed to four, and they are always positioned periodically in the chain. We

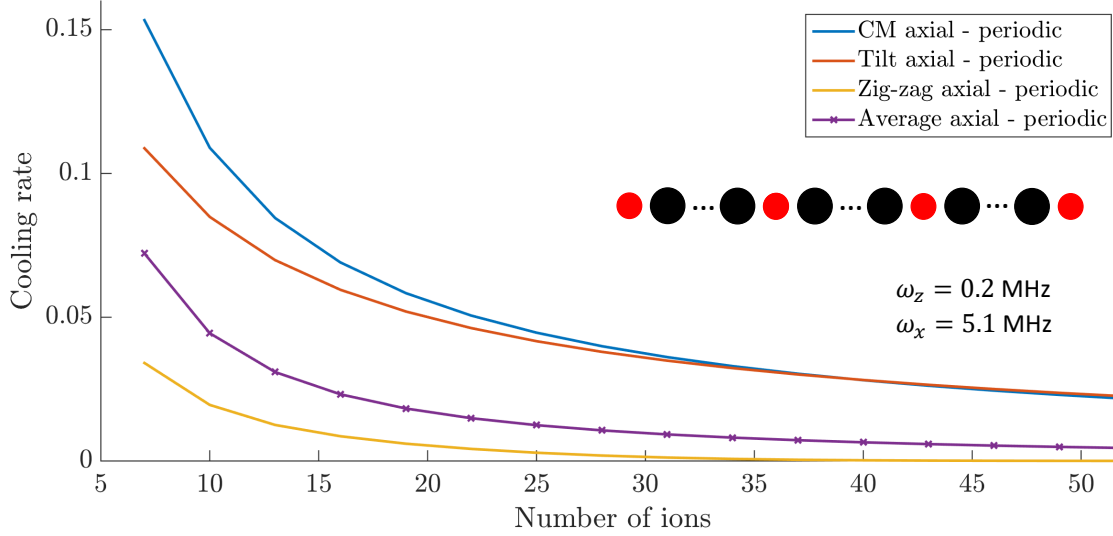


Figure 3.9: Cooling rates for the axial modes in a mixed-species chain with four periodically set “coolant” $^{138}\text{Ba}^+$ ions. The cooling rates are plotted as functions of the total number of ions in the chain. $^{138}\text{Ba}^+$ ions are represented as red circles, the rest of the ions – black circles – are $^{171}\text{Yb}^+$.

present the calculated cooling rate for the CM, tilt, and zig-zag axial modes, as well as the cooling rate averaged over all axial modes (there are as many of them as there are ions in the chain). In agreement with intuition, the longer the ion chain is, the lower the cooling rate becomes. We also verify that the respective cooling rates are at least on par or better than the cooling rates obtained in a pure $^{171}\text{Yb}^+$ ion chain, in which we also only cool four periodically-positioned $^{171}\text{Yb}^+$ ions as shown in Fig. 3.10. This is related to two factors. First, the structure of the axial normal modes in this mixed-species chain is close to that in the pure one. Second, the $^{138}\text{Ba}^+$ ions are lighter, and the cooling rate scales as $1/m$ – see Eqs. (3.38) and (3.55).

In Fig. 3.11, we show the cooling rate of the radial modes as a function of the total number of ions in the ion chain, while the number of the “coolant” $^{138}\text{Ba}^+$ ions is fixed to four, and they are always positioned periodically in the chain. Similarly

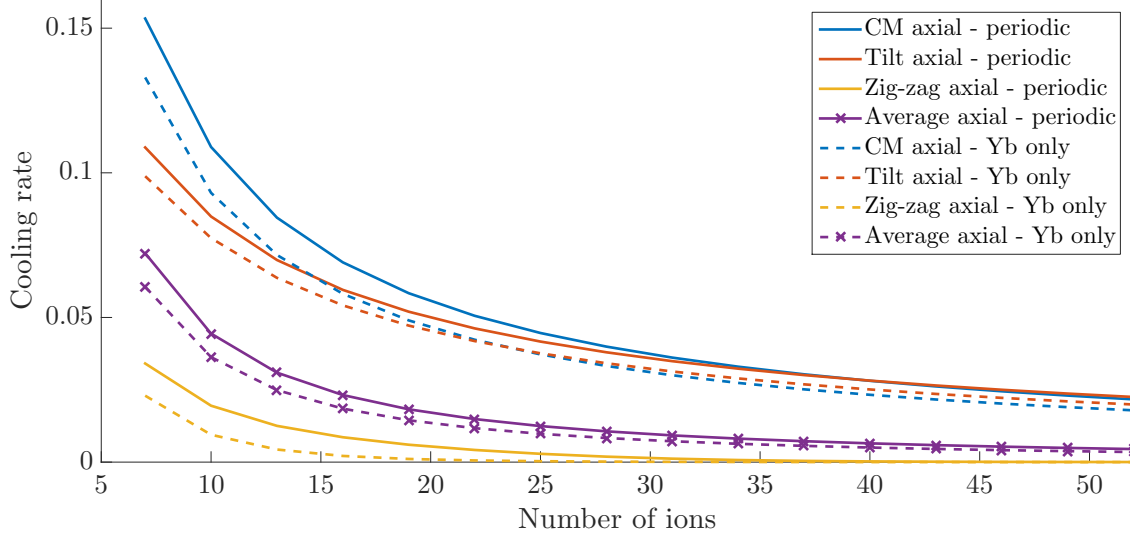


Figure 3.10: Cooling rates for the axial modes. Solid lines represent cooling rates in a mixed-species chain with four periodically set “coolant” $^{138}\text{Ba}^+$ ions (as in Fig. 3.9); dashed lines represent cooling rates in a pure $^{171}\text{Yb}^+$ ion chain with four of the $^{171}\text{Yb}^+$ ions in the respective positions used as “coolant” ions. The cooling rates are plotted as functions of the total number of ions in the chain.

to Fig. 3.9, we present the calculations for the CM, tilt, and zig-zag modes, as well as the cooling rate averaged over all radial modes.

The biggest difference between these two cases is that the cooling rates for the radial modes in mixed-species chains are about one order of magnitude lower than the cooling rates for the axial modes. Consequently, sympathetic cooling of the radial modes in these chains is inefficient. Also, the average radial-mode cooling rate dependence on the number of ions has a shape similar to the one for the axial modes, but some radial modes (e.g. the CM or zig-zag ones) are virtually not susceptible to cooling at all. From Figs. 3.9 and 3.11, we can see that the cooling rates of the radial modes are one order of magnitude lower than the cooling rates of the axial modes.

Due to the high mass ratio between $^{171}\text{Yb}^+$ and $^{138}\text{Ba}^+$, we observe a strong

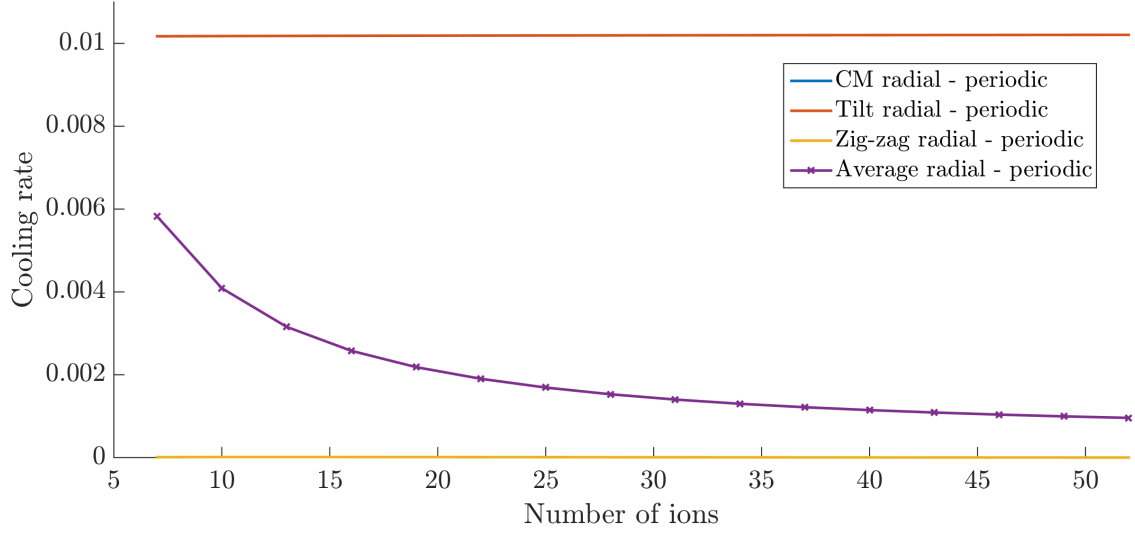


Figure 3.11: Cooling rates for the radial modes in a mixed-species chain with four periodically set “coolant” $^{138}\text{Ba}^+$ ions. The cooling rates are plotted as functions of the total number of ions in the chain.

amplitude mismatch in the radial modes, leading to inefficient sympathetic cooling of the radial modes. These results can be easily generalized to any long ion chain with mixed species. In our case, for the memory $^{171}\text{Yb}^+$ qubits, the suitable cooling ions would be $^{172}\text{Yb}^+$ or $^{174}\text{Yb}^+$. In this scenario, however, we will face an addressability problem, since $^{172}\text{Yb}^+$ or $^{174}\text{Yb}^+$ cooling light can affect the memory $^{171}\text{Yb}^+$ qubits, because this light’s frequency is only a few GHz away from the $^{171}\text{Yb}^+$ resonant $S_{1/2} \leftrightarrow P_{1/2}$ transition. In Section 5.2.2, we discuss crosstalk probability between different isotopes of Ba. We find that the beams have to be focused tightly to achieve low crosstalk probabilities, and this can be applied to Yb case, as well. Moreover, we believe that the crosstalk will be completely dominated by the non-Gaussian part of the beam leading to much higher intensities on neighboring ions than those expected for the Gaussian profile (this issue only worsens with tighter focusing). One of the promising solutions is to implement integrated photonics for light delivery [175], for

example, based on an optical waveguide [176, 177], which is essentially an optical fiber fabricated into the chip substrate.

3.2.4.2 Re-ordering ions of different masses

As we discussed in Section 3.2.1, the frequencies and amplitudes of the normal modes of the mixed-species ion chains strongly depend on the ion masses, and also on the ion order in the chain. Therefore, the implementation of the entangling gates, for example MS gate, relies on the ion chain configuration, and it is desirable to keep it stable. Due to collisions with high-energy background gas particles, ion chain can get decrystallized, and when cooled again, ions are rearranged randomly. Usually, background collisions happen once every few minutes in a room-temperature ultra-high-vacuum (UHV) setup. This can definitely be improved by introducing a cryogenic setup. To check the correctness of the ion configuration, one can perform a fluorescence detection of the ion positions on camera or measure the sideband spectrum of the ion chain.

Ion re-ordering techniques based on the mass dependence of the potential are widely used in experiments with mixed-species ions [92, 145, 178]. These techniques have probabilistic nature. Other techniques, which are based on the control of the trapping potentials, are deterministic and have been used in experiments to re-order ions of the same species [47, 95, 179].

We developed a new re-ordering method for long symmetric mixed-species ion chains based on the technique described in Ref. [163]. In Fig. 3.12, we show the

following step-by-step sequence for this novel procedure.

- (a) First, we perform symmetric re-ordering of the ions [92, 163]. We start this step by increasing the axial potential, and since the heavier ions are less strongly confined by the pseudopotential, they are the first to move off-axis. Then, we decrease the axial potential and bring the trap voltages back, so that the ions relax back to a configuration with heavier ions in the center, as shown in Fig. 3.12(a).
- (b) Second, we split the ion chain in half, as shown in Fig. 3.12(b), which can be done by varying the potentials on the trapping electrodes.
- (c) Then, we perform symmetric re-ordering on each half of the ion chain as discussed in the first step. The resulting ion configuration is presented in Fig. 3.12(c).
- (d) In the final step, we recombine two separate ion chains into one, as shown in Fig. 3.12(d). As a result, we end up with two lighter ions next to each other in the middle of the chain.

The steps (a)-(c) can be repeated many times to obtain finer positioning of the lighter ions throughout the chain. Note that the lighter ions will always come in pairs (except those at the very edges of the total chain). The final configuration is close to the one with the “coolant” ions placed periodically in the ion chain [174], however we have to “pair” the “coolant” ions for efficient re-ordering. We performed calculations similar to the ones described in Section 3.2.4.1 with $^{171}\text{Yb}^+$ and $^{138}\text{Ba}^+$

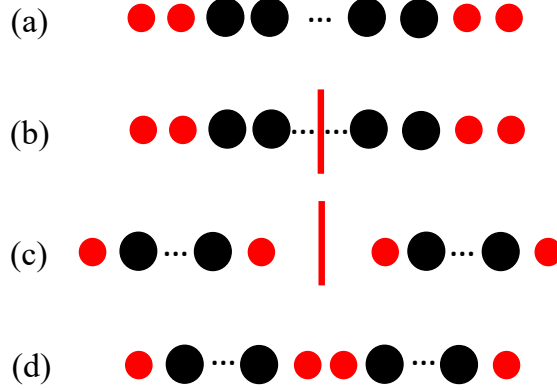


Figure 3.12: (a)-(d) Successive stages of re-ordering within the novel technique discussed in the text. Black circles represent heavier ions, and red circles represent lighter ions.

ions, and found that our proposed configuration with paired “coolant” ions shows the results that are on par with those obtained in the periodic configuration. We still observe a strong amplitude mismatch in the radial modes due to the high mass ratio between $^{171}\text{Yb}^+$ and $^{138}\text{Ba}^+$ ions leading to inefficiency of sympathetic cooling on radial modes.

3.2.5 Summary

In conclusion, we investigated the role of normal modes in entangling operations and sympathetic cooling in mixed-species ion chains. First, we performed calculations on AM pulse shaping to create Mølmer-Sørensen entangling gates between different species based on both axial and radial modes. Due to the strong mismatch in radial modes between the amplitudes of motion of different species, the amount of laser power required to satisfy all the spin-motion decoupling conditions is difficult to achieve in a real experiment. Then we performed calculations for a more advanced, combined AM-FM pulse shaping approach that allowed a considerable

Rabi frequency improvement towards potentially achievable levels in experiments. However, the laser power required for high-fidelity radial entangling gates is still at least one order of magnitude higher than that for the axial gates.

High-fidelity entangling gates between different species – the communication and processing qubits – in mixed-species ion chains are essential ingredients in the future quantum networks. The communication qubits will then be efficiently entangled with the corresponding photonic states and can thus become the foundation for a large-scale distributed quantum-computing network [51], in which multiple nodes will be connected by photonic Bell-state analyzers [80, 180].

Moreover, the ability to cool ions down near the motional ground state while preserving the stored quantum information in the processing qubits is crucial for quantum computing. The communication ions can be used for sympathetic cooling of the quantum memory qubits in order to facilitate longer computations. We discussed the sympathetic cooling in the mixed-species chains and how this process depends on normal modes. With the high mass ratio between the species, radial modes are much harder to cool than axial ones regardless of the configuration of the ions.

Chapter 4: Barium ions as communication qubits

4.1 Pure single photon generation

Trapped atomic ions are a promising platform for quantum information networks, with long-lived identical qubit memories that interact locally via phonons within ion-trap modules, and the ability to connect separate modules via photonic buses [51]. The single-photon purity is of crucial importance for such quantum information networks [53, 54, 55], as well as for quantum repeaters [56, 57, 58, 59], secure quantum key distribution [60, 61, 62], quantum random number generation [63, 64, 65], cluster state computation [66, 67], and other applications of quantum information processing and communication. Single atoms are natural candidates for pure single photon sources, since they are incapable of multi-photon emission in a spontaneous decay event, and thus generate perfect single photons. Apart from that, identical atomic qubits guarantee indistinguishability of emitted photons – a critical requirement for quantum network applications. By contrast, other candidates, such as NV centers and semiconductor quantum dots, are not perfectly identical due to their presence in a solid state medium [21, 22].

4.1.1 Autocorrelation function $g^{(2)}$

We implement a single-photon source based on $^{138}\text{Ba}^+$ ions. To investigate the purity of single photons emitted by our source, we build the Hanbury Brown – Twiss setup [181] shown in Fig. 4.1. The 493 nm photons coming from the $^{138}\text{Ba}^+$ ion are collected by the objective with NA 0.6, and then sent into the beamsplitter. We have detectors on each side of the beamsplitter: a trigger detector and a signal one, and we look at the correlations in photon arrival time.

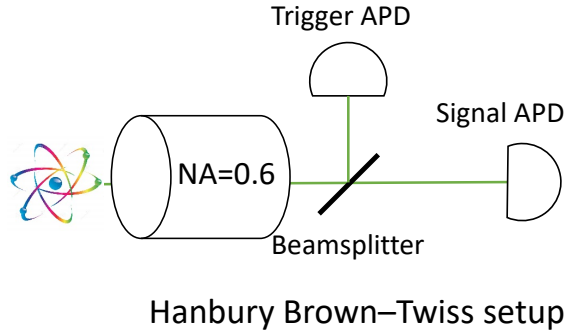


Figure 4.1: Experimental Hanbury Brown – Twiss setup to investigate the purity of single 493 nm photons emitted by $^{138}\text{Ba}^+$ ion.

The appropriate measure to characterize the purity of single photons is the second-order correlation function $g^{(2)}(\tau)$:

$$g^{(2)}(\tau) = \frac{\langle E^*(t)E^*(t+\tau)E(t)E(t+\tau) \rangle}{\langle |E(t)|^2 \rangle \langle |E(t+\tau)|^2 \rangle}, \quad (4.1)$$

where $E(t)$ is an electric field operator, and $\langle \dots \rangle$ represents the ensemble (statistical) average. $g^{(2)}(\tau)$ is proportional to the probability of detecting a photon at time $t+\tau$ given that a photon was detected at time t . In the experiment (see Fig. 4.1), the trigger detector fires at time t , and the signal detector records a click at some time

$t + \tau$.

We can express $g^{(2)}(\tau)$ in terms of intensities:

$$g^{(2)}(\tau) = \frac{\langle I(t)I(t+\tau) \rangle}{\langle I(t) \rangle^2}, \quad (4.2)$$

where $I(t)$ is the intensity of the electric field. The expression remains the same if $I(t)$ is replaced with the number of photons collected $\langle n(t) \rangle$. Note that this expression is even: $g^{(2)}(-\tau) = g^{(2)}(\tau)$.

It can be shown [182] that the photon counting rate $\frac{\langle n \rangle}{T}$ in the steady state regime is proportional to the probability of finding the ion in its excited states $|3\rangle$ and $|4\rangle$ defined in Section 2.1.3 (where $^{138}\text{Ba}^+$ ion is modeled as an 8-level system):

$$\frac{\langle n \rangle}{T} \propto \rho_{33}(\infty) + \rho_{44}(\infty). \quad (4.3)$$

Therefore, for $g^{(2)}(\tau)$ we obtain:

$$g^{(2)}(\tau) = \frac{\rho_{33}(\tau) + \rho_{44}(\tau)}{\rho_{33}(\infty) + \rho_{44}(\infty)}. \quad (4.4)$$

Before we turn to the discussion of the experimental results of the second-order correlation function, let us consider various examples of the light sources to understand what $g^{(2)}(\tau)$ represents. For instance, classical light sources always satisfy $g^{(2)}(0) \geq 1$. Other important examples are the following:

- bunched light: $g^{(2)}(0) > 1$;

- coherent light: $g^{(2)}(0) = 1$;
- antibunched light: $g^{(2)}(0) < 1$;
- pure single photons: $g^{(2)}(0) = 0$.

We will focus on the last case – pure single photons with $g^{(2)}(0) = 0$ – since single atoms are natural emitters of pure single photons.

Using the Hanbury Brown – Twiss setup (see Fig. 4.1), we performed measurements of the second-order correlation function $g^{(2)}(\tau)$ with various powers of the 493 nm laser light, while 650 nm laser power, the magnetic field B , and the detunings Δ_g and Δ_r of 493 nm and 650 nm beams, respectively, were fixed.

In Fig. 4.2, we present the measurement of the second-order correlation function $g^{(2)}(\tau)$ with a 493 nm laser power of 32 μW . The experimental data is shown in blue, while the result of plugging the theoretical solutions of the optical Bloch equations (for an 8-level model of $^{138}\text{Ba}^+$) into Eq. (4.4) is shown in red. We can see a strong dip at $\tau = 0$ (5 ns delay is present because of the difference in optical path lengths and in the cable lengths). This demonstrates photon antibunching. Background noise and dark counts prevent the dip from reaching zero. According to our simulations, the 493 nm laser intensity in our experiment was much higher than the saturation intensity for the $S_{1/2} \leftrightarrow P_{1/2}$ transition, and the saturation parameter was $S_g \sim 4$. The peaks at $\tau = \pm 6$ ns are due to Rabi flopping between the $S_{1/2}$ and $P_{1/2}$ levels after the single-photon detection. At longer times, $g^{(2)}(\tau)$ reaches saturation: $g^{(2)}(\tau \rightarrow \infty) \rightarrow 1$, as we expect.

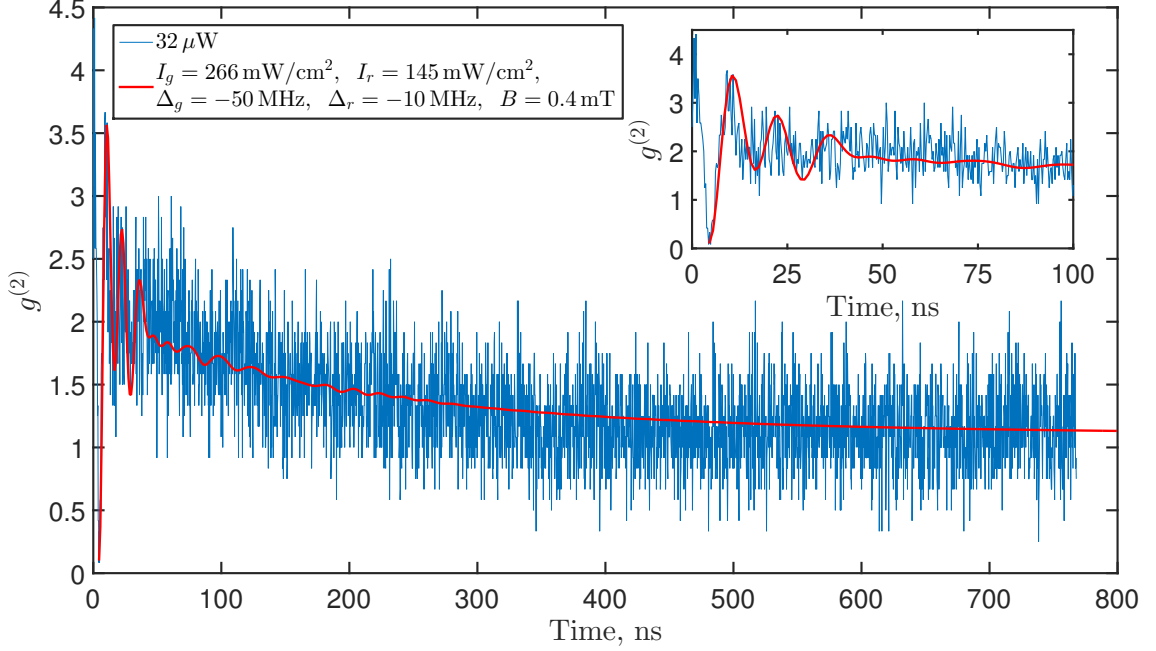


Figure 4.2: The second-order correlation function $g^{(2)}(\tau)$ that demonstrates photon antibunching at $\tau = 0$. Photons are generated with 493 nm excitation line shown in Fig. 4.4(a). Experimental data is shown in blue with 493 nm laser power of $32 \mu\text{W}$. Theoretical calculations based on the solutions of the optical Bloch equations for an 8-level model of $^{138}\text{Ba}^+$ are shown in red. The inset shows the same data as the main plot, but zoomed in at short times. A 5 ns delay is present due to the difference in optical path lengths and in the cable lengths, so the horizontal axes show $\tau + 5$ ns. Fitting parameters are: intensities of 493 nm and 650 nm laser beams, I_g and I_r ; detunings Δ_g and Δ_r ; and magnetic field B .

Next, in Fig. 4.3, we present the measurement of the second-order correlation function $g^{(2)}(\tau)$ with the 493 nm laser power of $85 \mu\text{W}$, while the rest of the parameters – 650 nm laser power, the magnetic field B , and the detunings Δ_g and Δ_r of 493 nm and 650 nm beams, respectively – are the same as in Fig. 4.2. Similarly, the experimental data is shown in blue, while the theoretical calculations are shown in red. We can see a strong dip at $\tau = 0$ (taking into account the 5 ns delay). Since the 493 nm laser power is higher this time, we can see the Rabi flops with higher amplitude. Again, at longer times, $g^{(2)}(\tau)$ reaches saturation.

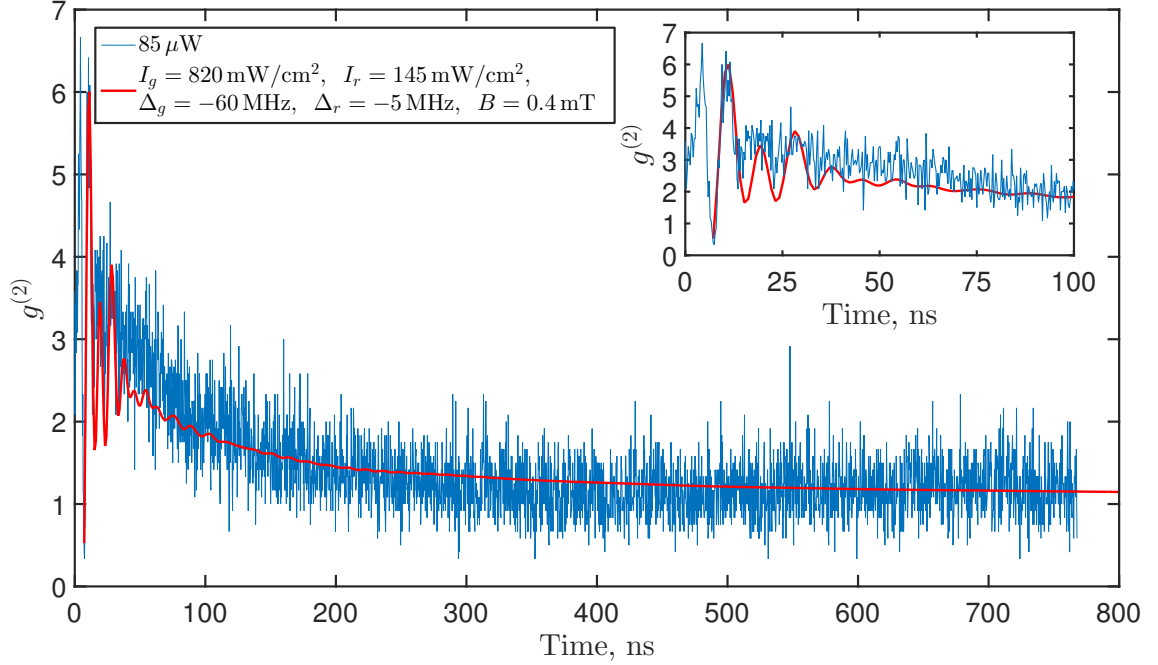


Figure 4.3: The second-order correlation function $g^{(2)}(\tau)$ that demonstrates photon antibunching at $\tau = 0$. Photons are generated with 493 nm excitation line shown in Fig. 4.4(a). Experimental data is shown in blue with 493 nm laser power of $85 \mu\text{W}$. Theoretical calculations based on the solutions of the optical Bloch equations for an 8-level model of $^{138}\text{Ba}^+$ are shown in red. The inset shows the same data as the main plot, but zoomed in at short times. A 5 ns delay is present due to the difference in optical path lengths and in the cable lengths, so the horizontal axes show $\tau + 5$ ns. Fitting parameters are: intensities of 493 nm and 650 nm laser beams, I_g and I_r ; detunings Δ_g and Δ_r ; and magnetic field B .

In Fig. 4.2, one can notice a weak modulation with a period of about 50 ns, which corresponds to a frequency of 18 MHz which is the trap RF frequency. This modulation is almost undetectable in Fig. 4.3, because the micromotion had been compensated following the procedure in Ref. [183]. When the micromotion is not compensated, the details of the internal atomic dynamics are usually hidden by this micromotion modulation.

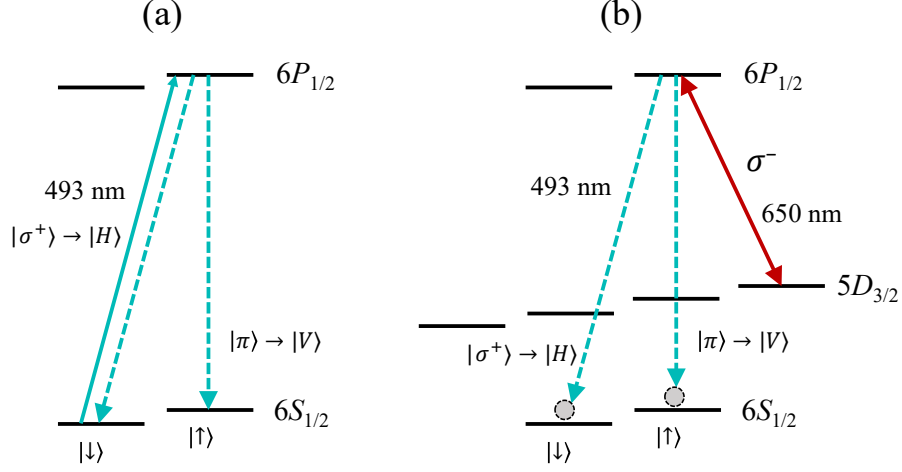


Figure 4.4: Excitation schemes for a $^{138}\text{Ba}^+$ ion. (a) Fast excitation using 493 nm line with σ^+ polarization. (b) Fast excitation using 650 nm line with σ^- polarization. As a result of each of these schemes, all the population is transferred to the excited state $6P_{1/2} |m_J = +1/2\rangle$, from where it spontaneously decays, and 493 nm photons are collected.

4.1.2 650 nm excitation

In order to obtain dramatically lower $g^{(2)}(0)$ results, we introduce a new excitation technique shown in Fig. 4.4(b) and based on the $^{138}\text{Ba}^+$ ion preparation in a low-lying $5D_{3/2}$ manifold [87, 184, 185]. There are several advantages of using $^{138}\text{Ba}^+$ $5D_{3/2}$ state as a “ground” state. The lifetime of the $5D_{3/2}$ state is about 80 s [130], which is much longer than the time required for any experimental operation. Additionally, the fairly low branching ratio from the $6P_{1/2}$ state to the $6S_{1/2}$ and $5D_{3/2}$ states of 3 : 1 allows for short pumping times, and therefore high experimental repetition rates. Thus, any disadvantages of operating based out of the $5D_{3/2}$ manifold are minimal, and there are several advantages to doing so. Moreover, the 650 nm $P_{1/2} \leftrightarrow D_{3/2}$ transition is spectrally distant from the 493 nm $S_{1/2} \leftrightarrow P_{1/2}$ transition [see Fig. 4.4(b)], which allows simple filtering of the desired 493 nm photons emitted

from the ion from any 650 nm excitation laser light scattered from the trap into the imaging system. Additionally, 650 nm light is compatible with highly efficient fiber technologies, such as in-fiber fast AOMs and EOMs, in-fiber switches. With the help of the 650 nm excitation method demonstrated in Fig. 4.4(b), we also obtain extremely low double excitation errors (less than 0.4% with 10 ns 650 nm excitation pulse). It is discussed in detail in Section 4.1.4.

Let us now describe the 650 nm excitation scheme shown in Fig. 4.4(b). First, we pump a $^{138}\text{Ba}^+$ ion into the edge state $5^2D_{3/2}|m_J = +3/2\rangle$ by applying an unpolarized cooling 493 nm beam, and only π and σ_+ polarizations of a repump beam at 650 nm. After that, we apply a 10 ns 650 nm pulse with σ_- polarization to excite all the population to the $6^2P_{1/2}$ manifold. The emitted 493 nm photons are collected with a high-numerical-aperture lens ($\text{NA} = 0.6$) in the direction perpendicular to the quantization axis.

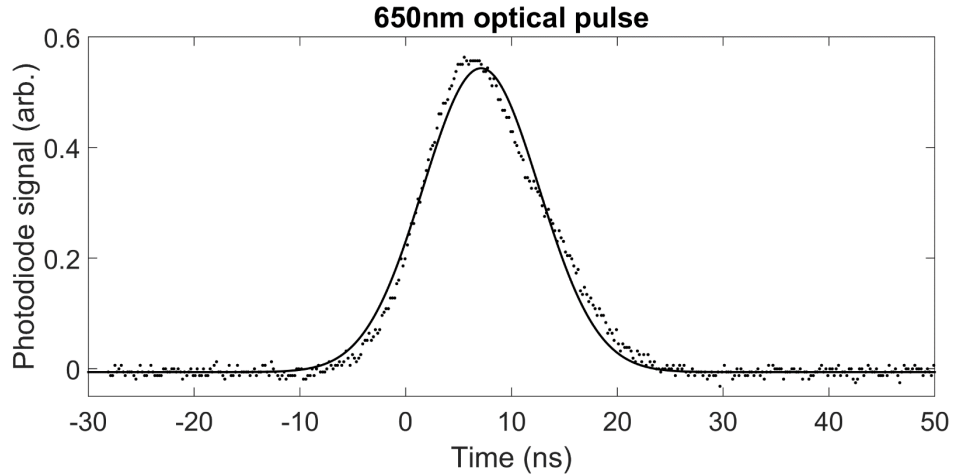


Figure 4.5: 650 nm optical pulse with pulse time of 10 ns. The optical 650 nm pulse is created by a fast AOM and measured on a fast photodiode. The experimental data is fitted to a Gaussian.

The fast 650 nm pulse is created by a free-space AOM¹ with a 5.1 ns rise time. In Fig. 4.5, we demonstrate a fast 650 nm optical pulse that is fitted to a Gaussian with FWHM of 10 ns. Then we apply the excitation pulse to the ion and adjust the intensity of the 650 nm laser pulse in order to drive a π rotation such that all the population is excited into the $6^2P_{1/2}$ manifold.

In Figs. 4.6 and 4.7, we demonstrate temporal profiles of single 493 nm photons emitted by a $^{138}\text{Ba}^+$ ion subject to short 650 nm pulses. The profile shapes are defined by the convolution of the Gaussian shapes of the excitation pulses and an exponential decay due to spontaneous emission.

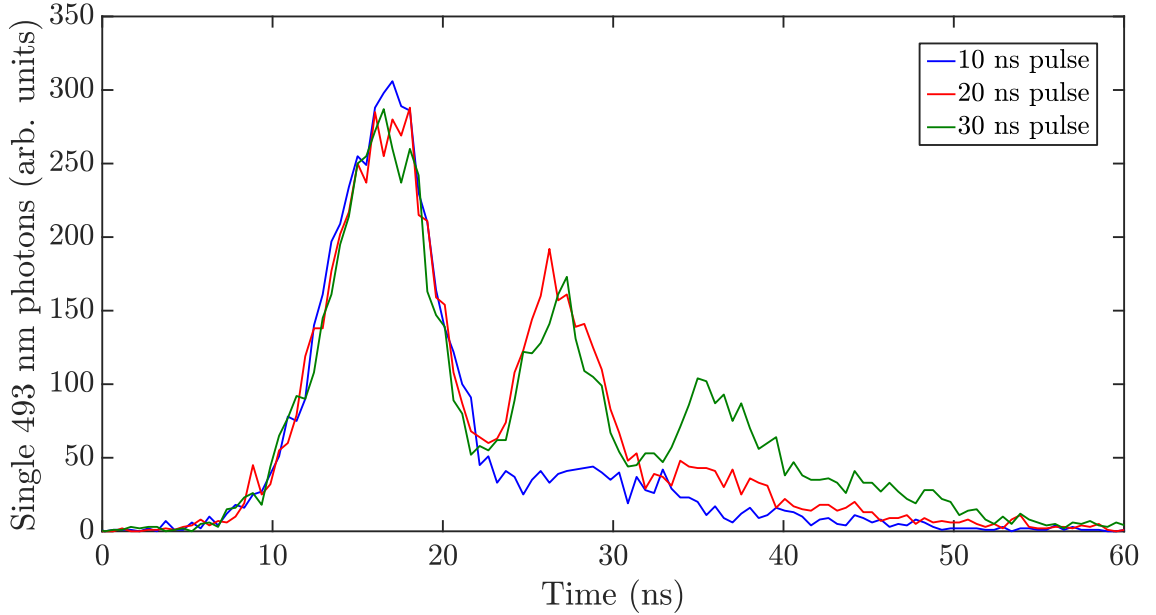


Figure 4.6: Single 493 nm photon temporal profiles. First, we drive the π rotation with a 10 ns 650 nm pulse, so that all the population is excited to the $6^2P_{1/2}$ manifold. The resulting single-photon temporal profile is shown by the blue curve. Next, we apply longer 650 nm pulses with 20 ns and 30 ns lengths, and the resulting temporal profiles are shown by the red and green curves, respectively.

In Fig. 4.6, we show the temporal profile of single 493 nm photons obtained

¹Brimrose GPM-400-100

via a π pulse of 650 nm light with the length of 10 ns (blue curve). In this case, FWHM of the profile is about 10 ns. When the pulse time is increased to 20 ns (red curve), we obtain the second peak in the photon temporal profile. In this case, we overdrive the rotation from the $D_{3/2}$ to the $P_{1/2}$ state, which results in Rabi flopping between these states. Similarly, when the 650 nm pulse duration is 30 ns (green curve), three pronounced peaks can be distinguished.

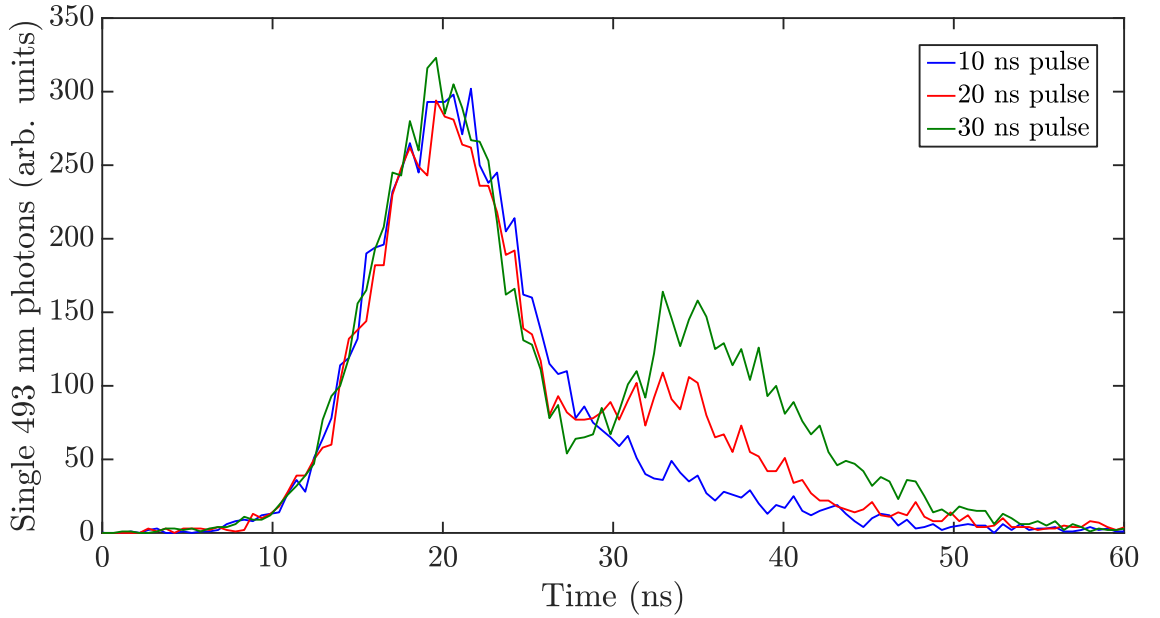


Figure 4.7: Single 493 nm photon temporal profiles. The intensity of 650 nm pulse is reduced by half in comparison to Fig. 4.6. In this case, the π rotation corresponds to a 15 ns 650 nm pulse. We show single-photon temporal profiles at the same pulse lengths as in Fig. 4.6.

In Fig. 4.7, single 493 nm photon temporal profiles are shown at half the intensity of the 650 nm pulse as compared to the previous case. When the 650 nm pulse time is 30 ns, we see two tall peaks. We can infer from it that the π time in this case is ~ 15 ns, as we expect. Indeed, since the Rabi frequency g relates to the

intensity of the laser field I as:

$$g = C\gamma\sqrt{\frac{I}{2I_{sat}}}, \quad (4.5)$$

the intensity of the 650 nm pulse reduced by half leads to the increase of the π time by factor of $\sqrt{2}$.

4.1.3 Pure single photons

In our work [87, 186], in order to investigate the single-photon purity, we perform the same $g^{(2)}$ measurement using the setup displayed in Fig. 4.1. Fig. 4.8(a) shows the histogram of the normalized second-order autocorrelation function after integrating for 18 hours with a detection window of 200 ns in hardware to filter out 493 nm photons coming from the cooling and pumping parts of the experiment. Note that 200 ns detection window is excessively large since the atomic decay time is only about 10 ns. We do not perform any background subtraction. Note that the data is presented on a logarithmic scale. The peak at $\tau = 0$ is strongly suppressed, which indicates the purity of the single-photon source. The other (“side”) peaks are 26.8 μs apart, which corresponds to the repetition rate of the experiment.

In Fig. 4.8(b), we present the second-order coherence of $g^{(2)}(0)$ as a function of the fraction of light collected if we consider shorter times for integration around the center of the peak. We choose a 30 ns integration window that contains only 12 ± 3 coincidence events around $\tau = 0$, while there are 149145 ± 386 coincidence events in a side peak within 30 ns of the peak center. With this 30 ns window,

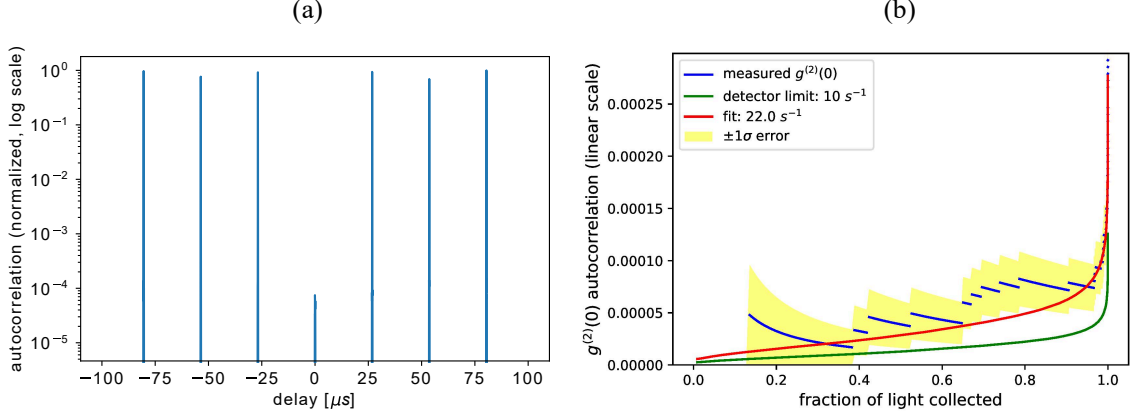


Figure 4.8: (a) Normalized second-order autocorrelation function in a semi-log scale. Side peaks are located 26.8μ s apart, which corresponds to the repetition rate of the experiment. The strong dip at $\tau = 0$ demonstrates the high purity of single photon source. (b) Autocorrelation $g^{(2)}(0)$ as a function of the fraction of light collected if we consider shorter times for integration around the center of the peak. The experimental data is shown in blue; 1σ error bars for this data are shown in yellow. The detector dark-count limited $g^{(2)}(0)$ is shown in green; the fitted effective dark-count limited $g^{(2)}(0)$ is shown in red.

we ensure that we collect more than 97% of the generated photons, while keeping excessive dark counts from contaminating the signal. As a result, we arrive at $g^{(2)}(0) = (8.1 \pm 2.3) \times 10^{-5}$ – more than an order of magnitude improvement over the previous best single-photon measurement for an atomic source [185], and consistent with the overall best single-photon measurement obtained in quantum dots [187]. Our choice of the detection window represents an favorable trade-off between light collection and the photon purity. The discontinuous jumps in the blue data plot correspond to coincidence detection events. A detector dark-count limited measurement in our experiment would yield $g^{(2)}(0) = 3.0 \times 10^{-5}$, as shown by the green curve in Fig. 4.8(b). The fitted effective dark-count limited $g^{(2)}(0)$ is shown by the red curve, with the constant background count rate of 22 s^{-1} . This remaining inconsistency between our measurement and the background-free measurement is

due to the observed transient AOM light leakage. We tried to address this issue by adding a delay after the initialization step, decreasing the overall repetition rate of the experiment. We verified experimentally that it takes more than 1 ms delay time to eliminate that transient AOM light leakage completely, and that would make the experiment too slow.

4.1.4 Double excitations

In our previous work [123], we performed fast excitation using 493 nm light with σ^+ polarization. To reduce the frequency of double scattering events, the weak CW excitation was implemented with only 10% excitation probability. As we mentioned in Section 4.1.2, the 650 nm excitation method delivers very low double excitation errors. Indeed, we calculate them and find that they are below 0.4% when a 10 ns 650 nm excitation pulse is applied. In this section, we give a detailed description of how these calculations are performed and investigate how the parameters of the fast 650 nm pulses affect these errors.

As shown in Fig. 4.4(b), we send a 650 nm excitation pulse, so that all the population is transferred to the $P_{1/2} |m_J = +1/2\rangle$ state. However, the second excitation can happen if the ion decays back to the $D_{3/2}$ manifold. If after the second excitation, the ion ends up in the $P_{1/2} |m_J = -1/2\rangle$ state, such a process will introduce an infidelity of the ion-photon entanglement.

To track down such a “bad” double decay, we solve the optical Bloch equations (as in Section 2.1.3) and investigate the time evolution of all the $^{138}\text{Ba}^+$ states. We

introduce two auxiliary levels into the $S_{1/2}$ manifold where the $P_{1/2} |m_J = -1/2\rangle$ state can decay only when emitting 493 nm photons with σ and π polarization, respectively. We solve the equations for the time evolution of the resulting 10-level system. The sum of the populations of these two auxiliary states normalized by the total $S_{1/2}$ state population represents the ion-photon entanglement infidelity.

We begin investigating the fidelity loss in the case when the 650 nm excitation pulse is square-shaped. Since we want to achieve the transfer of all the populations to the $P_{1/2}$ manifold, the Rabi frequency Ω has to satisfy the following condition:

$$\Omega T_p = \pi, \quad (4.6)$$

where T_p is the 650 nm pulse duration. Eq. (4.6) is valid only for short pulses – below or about the lifetime of the $P_{1/2}$ manifold. In Fig. 4.9, we plot the fidelity

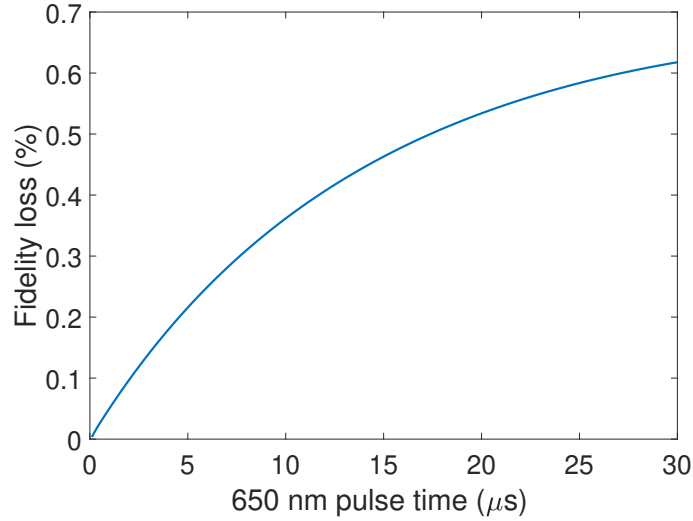


Figure 4.9: $^{138}\text{Ba}^+$ subject to square-shaped 650nm excitation pulse. Fidelity loss as a function of pulse time.

loss as a function of the pulse duration. In our experiments, we implement 10 ns

650 nm pulses, so the double excitation error that we expect in this case is less than 0.4%. Currently, there is no significant advantage in making the 650 nm pulses shorter, since this fidelity loss is not the bottleneck, and other sources of errors – the detection and initialization fidelity, polarization mixing, etc. – dominate in the ion-photon entanglement experiment. If, however, in the future, we need a shorter pulse, we can achieve this by adding an in-fiber EOM switch², which can create 1 ns pulses.

Next, we proceed to consider the fidelity loss with different – not square, but more physically inspired – 650 nm pulse shapes. We perform all the same calculations for two physical 650 nm pulse shapes:

1) a Gaussian shape:

$$\Omega(t) = \Omega_0 \exp\left(-\frac{t^2}{w^2}\right) \quad (4.7)$$

with the peak intensity Ω_0 and the width w ; the corresponding phase θ is

$$\theta = \int_{-\infty}^{\infty} \Omega(t) dt = \frac{\Omega_0 w}{\sqrt{\pi}} \quad (4.8)$$

(naturally for a π rotation, we need $\theta = \pi$) and

2) a sech-shape pulse [188]:

$$\Omega(t) = \Omega_0 \operatorname{sech}\left(\frac{1.76 t}{\tau_{\text{FWHM}}}\right) \quad (4.9)$$

with the peak intensity Ω_0 and the full width half max (FWHM) τ_{FWHM} .

²Jenoptik, amplitude modulator LiNbO₃ AM660b

Similarly, we write the phase θ as:

$$\theta = \int_{-\infty}^{\infty} \Omega(t) dt = \frac{\pi \Omega_0 \tau_{\text{FWHM}}}{1.76} \quad (4.10)$$

All the considered pulse shapes yield very similar results shown in Table 4.1, so that we get a fidelity loss $< 0.4\%$ for all 10 ns pulses, and the difference between them is negligible.

Pulse shape	$T_p = 1$ ns, %	$T_p = 5$ ns, %	$T_p = 10$ ns, %	$T_p = \infty$, %
square	0.0505	0.220	0.360	8.040
sech	0.0494	0.212	0.355	8.038
gaussian	0.0494	0.211	0.355	8.038

Table 4.1: Fidelity loss in % calculated for various pulse shapes with different pulse durations ranging between 1 ns and ∞ .

Note that, as shown in Table 4.1, in the limit of $T_p \gg \tau_e$, when the decay time $\tau_e \simeq 10$ ns, the double excitations only introduce an error of 8%, not 11% as estimated in Ref. [184].

As discussed above, Eq. (4.6) is not valid if the pulse duration is much longer than the 10 ns decay time from the $P_{1/2}$ state to the $D_{3/2}$ state. In order to perform a π rotation with a pulse that is much longer than the decay time, we have to use a large Rabi frequency Ω and solve the optical Bloch equations to find the appropriate Rabi frequencies. In Figs. 4.10 – 4.13, we show the results of the analysis of the $S_{1/2}$ manifold populations and the fidelity loss as a function of Rabi frequency at four fixed values of the pulse duration.

For short 650 nm pulses (1 ns – 10 ns), we are able to perform π rotations so

that all the population is transferred to the $P_{1/2}$ manifold with $\Omega = \Omega_0$, where Ω_0 is defined in Eq. (4.6). This conclusion is obtained from the $S_{1/2}$ state population behaviour shown in Figs. 4.10 – 4.12. With higher Rabi frequencies, $\Omega > \Omega_0$, we overdrive the rotations, as can be seen from the subsequent oscillations. On the other hand, in the case of the 50 ns 650 nm excitation pulse, we need $\Omega \approx 3\Omega_0$ to reach the maximum of the $S_{1/2}$ manifold population – see Fig. 4.13. However, for such a long pulse, the fidelity loss is about 7%, which is very close to the maximum possible loss of 8%.

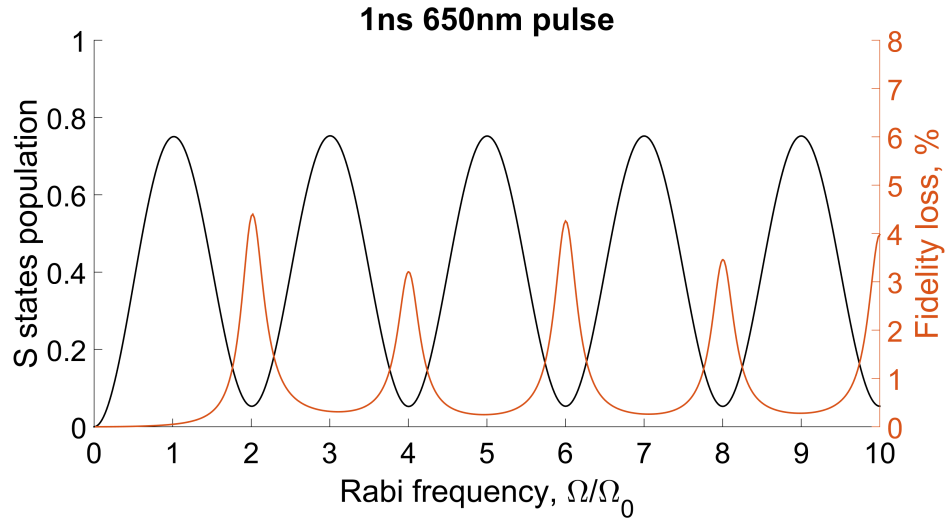


Figure 4.10: Population transfer in $^{138}\text{Ba}^+$ subject to a 1 ns-long 650 nm excitation pulse. Black curve and left vertical axis: $S_{1/2}$ manifold population. Red curve and right vertical axis: fidelity loss. Both are plotted as functions of the normalized Rabi frequency Ω/Ω_0 .

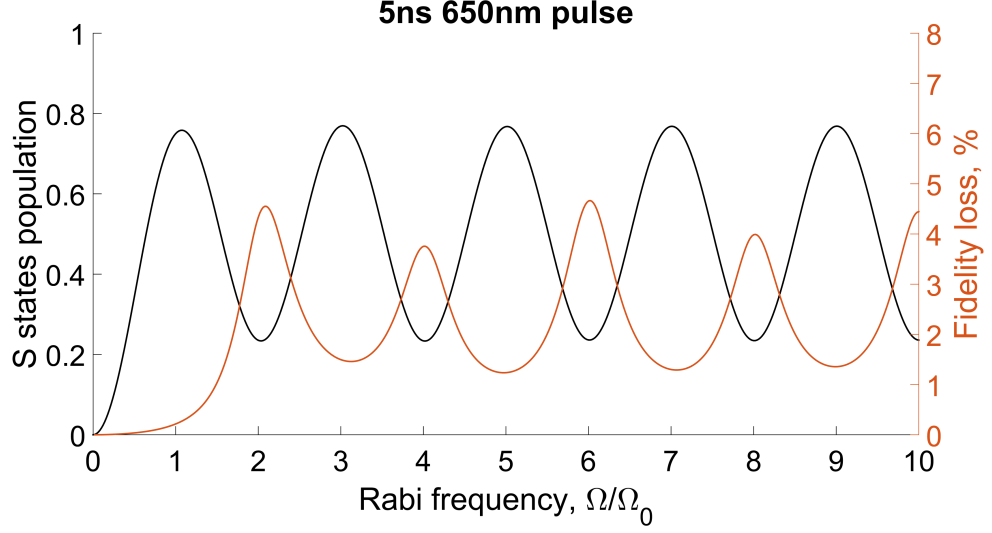


Figure 4.11: Population transfer in $^{138}\text{Ba}^+$ subject to a 5 ns-long 650 nm excitation pulse. Black curve and left vertical axis: $S_{1/2}$ manifold population. Red curve and right vertical axis: fidelity loss. Both are plotted as functions of the normalized Rabi frequency Ω/Ω_0 .

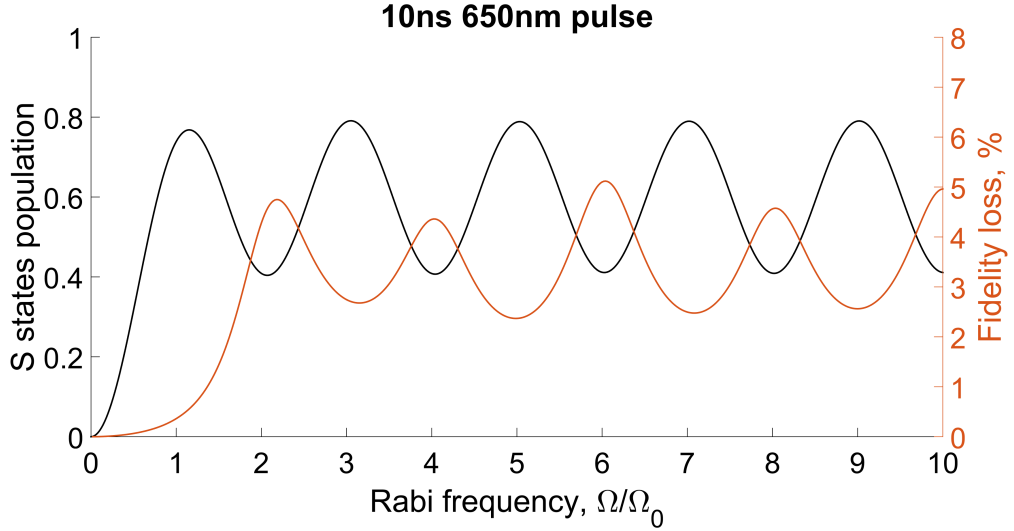


Figure 4.12: Population transfer in $^{138}\text{Ba}^+$ subject to a 10 ns-long 650 nm excitation pulse. Black curve and left vertical axis: $S_{1/2}$ manifold population. Red curve and right vertical axis: fidelity loss. Both are plotted as functions of the normalized Rabi frequency Ω/Ω_0 .

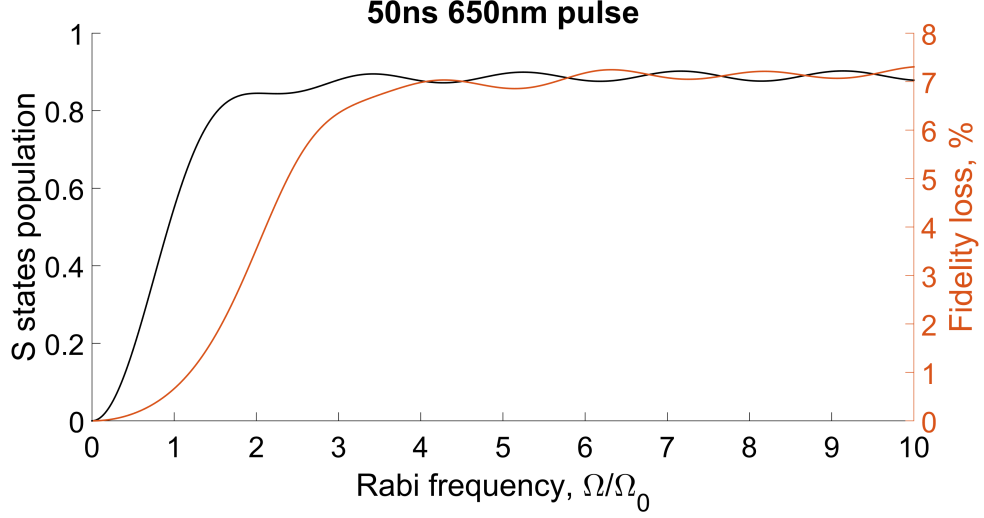


Figure 4.13: Population transfer in $^{138}\text{Ba}^+$ subject to a 50 ns-long 650 nm excitation pulse. Black curve and left vertical axis: $S_{1/2}$ manifold population. Red curve and right vertical axis: fidelity loss. Both are plotted as functions of the normalized Rabi frequency Ω/Ω_0 .

4.2 Ion-photon entanglement

In Section 4.1, we discussed generation of pure single photons. There is another key element necessary for these applications – entanglement between atoms and emitted photons. We proceed now to discuss this matter and demonstrate experimental results for ion-photon entanglement. Our ion-photon entanglement verification procedure [87] is similar to that in Refs. [75, 84].

4.2.1 Experimental demonstration of ion-photon entanglement

We excite $^{138}\text{Ba}^+$ ion with a fast 650 nm pulse as shown in Fig. 4.4(b) to the excited state $P_{1/2}|m_J = +1/2\rangle$ and let it decay. σ^+ photons are emitted when the ion decays back to the $|\downarrow\rangle$ state, and π photons – when the ion decays to the $|\uparrow\rangle$

state. As a result, we obtain the following entangled state:

$$|\Psi\rangle = \sqrt{\frac{2}{3}} |\downarrow\rangle |\sigma^+\rangle + \sqrt{\frac{1}{3}} |\uparrow\rangle |\pi\rangle. \quad (4.11)$$

As demonstrated in Fig. 4.14, we collect the photons with a high-NA objective installed perpendicular to the quantization axis which is defined by the direction of the magnetic field. Then we project σ^+ and π polarizations onto the horizontal (H) and vertical (V) axes, respectively, and taking into account the spatial emission patterns of each polarization given in Eqs. (4.14) - (4.15), we arrive to the final entangled state:

$$|\Psi\rangle = \frac{1}{\sqrt{2}} (|\downarrow\rangle |H\rangle + |\uparrow\rangle |V\rangle). \quad (4.12)$$

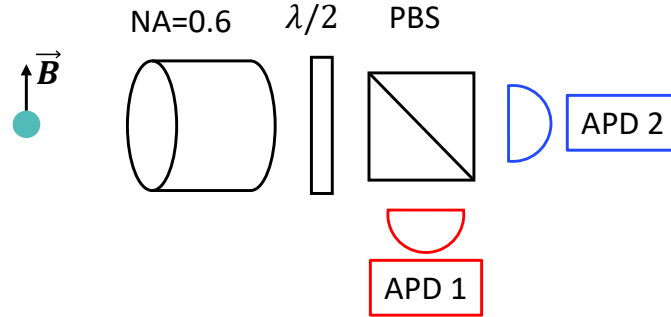


Figure 4.14: Experimental setup for showing entanglement between the state of a $^{138}\text{Ba}^+$ ion and the polarization of the emitted 493 nm photon.

First, we show the correlations between the state of the ion and polarization of the photon in the z -basis. After a photon detection event on APD_1 or APD_2 , which are located at both output ports of a polarizing beamsplitter (PBS), the qubit state is measured. In Fig. 4.15(a), we demonstrate the ion-photon correlation as a function of the half-wave plate (HWP) rotation angle that is responsible for the

photon polarization rotation.

It is important to show ion-photon correlation in a rotated basis, because this way we can verify that after a spontaneous photon emission, the atom still preserves phase coherence of the resulting qubit state. We show the ion-photon correlation in the x -basis. For that, first, we rotate the photon polarization by $\frac{\pi}{2}$:

$$\begin{aligned} R_p\left(\frac{\pi}{2}\right)|\Psi\rangle &= \frac{1}{2} [|\downarrow\rangle(|V\rangle + |H\rangle) + |\uparrow\rangle(|V\rangle - |H\rangle)] \\ &= \frac{1}{2} [(|\uparrow\rangle + |\downarrow\rangle)|V\rangle + (|\downarrow\rangle - |\uparrow\rangle)|H\rangle]. \end{aligned} \quad (4.13)$$

Then, following a photon detection event, the atomic qubit is rotated by $\frac{\pi}{2}$ with a variable phase.

In Fig. 4.15(b), we plot the corresponding coherences (correlations measured in the x -basis). The experimental data in both figures is fitted to a sine function, and its amplitude represents the corresponding fidelity. The final entanglement fidelity, $F = 0.884(4)$, is calculated as an average fidelity from both measurements. As we discussed in Section 4.1.4, the double-excitation errors are below 0.4% for 10 ns-long 650 nm pulses, meaning that we have to investigate other sources of errors. As a result of the corresponding analysis, we attribute the remaining errors to imperfect state initialization/detection (1.5%), polarization mixing due to the large solid angle (5% for the 0.6-NA objective), and polarization mixing in the collection optics (5%) [79].

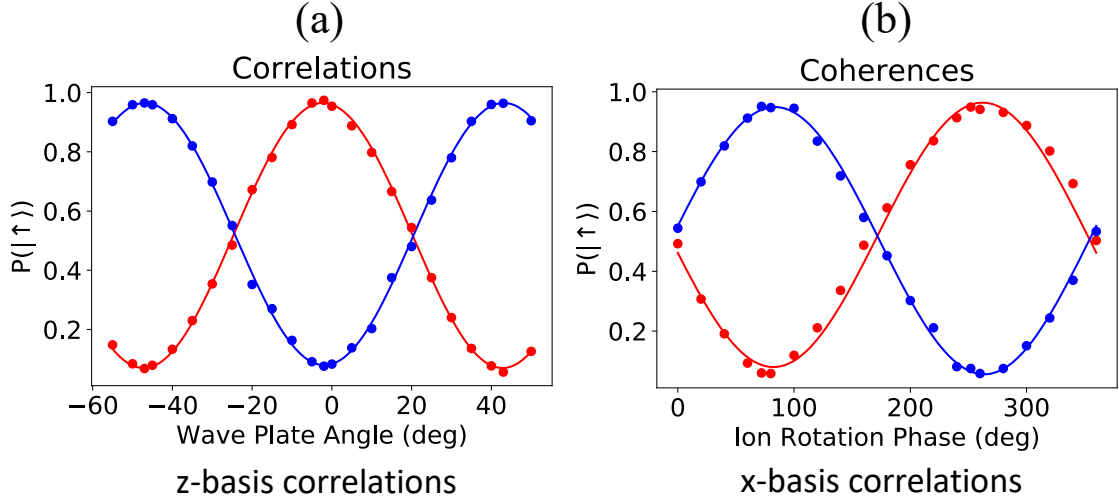


Figure 4.15: (a) Ion-photon correlations as a function of the wave-plate rotation angle. The red (blue) curve shows the probability of finding the ion in the $|\uparrow\rangle$ state when the photon is detected on APD₁ (APD₂). No stops are implemented for this experiment (see Section 4.2.2). (b) Ion-photon coherences (correlations measured in the x -basis) as a function of the phase of the $\pi/2$ rotation performed on the ion qubit. No stops are implemented for this experiment, as well. Amplitudes represent the corresponding entanglement fidelity $F = 0.884(4)$.

4.2.2 Polarization mixing

In this section, we investigate polarization mixing errors due to the large solid angle and we try to find the ways to reduce these errors. For this purpose, let us look at the radiation patterns of σ^+ and π photons that $^{138}\text{Ba}^+$ ion emits. The magnetic field direction (the quantization axis) is along the z -direction. After taking into account the Clebsch-Gordan coefficients and our excitation scheme that does not allow for σ^- -photon emission, we obtain 493 nm emission patterns plotted in

Fig. 4.16 and written down in the following form [73, 118]:

$$\pi = i\sqrt{\frac{3}{16}}\sin\theta \hat{\theta}, \quad (4.14)$$

$$\sigma^+ = ie^{i\phi}\sqrt{\frac{3}{16}}(\cos\theta \hat{\theta} + i\hat{\phi}), \quad (4.15)$$

$$\sigma^- = 0, \quad (4.16)$$

where θ and ϕ are the spherical coordinates.

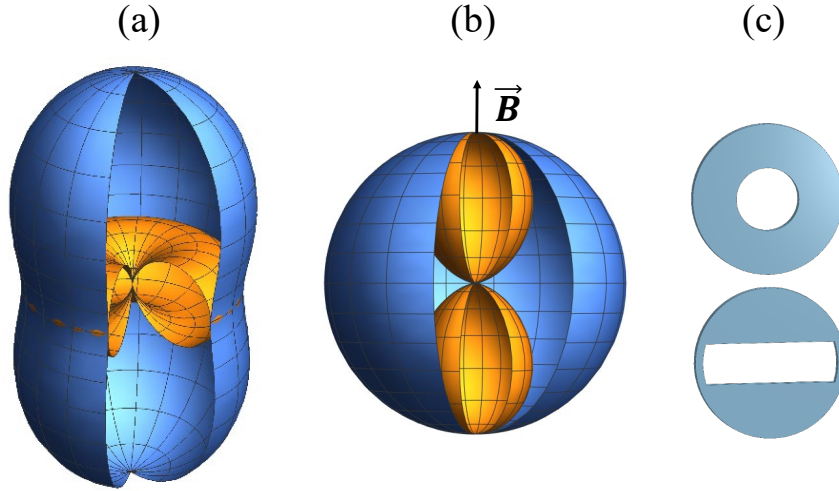


Figure 4.16: (a) Radiation pattern of a σ -polarized (blue surface) and π -polarized (yellow surface) light emitted along the z quantization axis; (b) Radiation patterns for the decomposition of the σ -polarized light [the blue surface in the panel (a)] into the H (blue surface) and V (yellow surface) linear polarization components; (c) Two types of apertures used in the experiment to reduce the V-polarized light collection angle thereby improving the ion-photon entanglement fidelity.

In Fig. 4.16(a), we plot the radiation patterns of both σ^+ and π photons. The π -polarized photons are shown in yellow, and in the V-H basis, they only have a V component, i.e. the π polarization coincides with the V polarization. On the other hand, the σ -polarized photons [shown in blue in Fig 4.16(a)] have to be decomposed into the H and V polarization components, as demonstrated in

Fig. 4.16(b). Note that at $\theta = \frac{\pi}{2}$, there is no V component in the σ^+ light, and hence there is no polarization mixing. However, as the angle changes from $\theta = \frac{\pi}{2}$, there is an increasingly large V component. After projecting the σ^+ and π polarizations onto the horizontal (H) and vertical (V) axes, we obtain the resulting ion-photon entangled state:

$$|\Psi_r\rangle = \frac{1}{\sqrt{2}} \left(-e^{i\phi} |\downarrow\rangle |H\rangle + ie^{i\phi} \cos\theta |\downarrow\rangle |V\rangle + 0 \cdot |\uparrow\rangle |H\rangle + i\sin\theta |\uparrow\rangle |V\rangle \right). \quad (4.17)$$

The desired final entangled state is $|\Psi_d\rangle$ defined in Eq. (4.12). Therefore, the ion-photon entanglement fidelity is given by $F = |\langle\Psi_d|\Psi_r\rangle|^2 = \frac{1}{4}(1 + \sin\theta)^2$. In order to reduce the vertical light collection angle, we manufactured two types of apertures (stops) using 3D printers. They allow us to improve the ion-photon entanglement fidelity, but they also reduce the photon collection rate, leading to a trade-off between the photonic generation rate and the ion-photon entanglement fidelity. These stops shown in Fig. 4.16(c) are inserted immediately after the last lens of the microscope objective. We repeat the ion-photon correlation experiment with these apertures installed. The circular and rectangular apertures are both designed to block half of the light. The corresponding improvements to the fidelities are presented in Table 4.2.

Aperture type	Solid angle/ 4π	Calculated F	Measured F
None	0.10	0.887	0.884(4)
Circular	0.05	0.912	0.912(5)
Rectangular	0.05	0.927	0.930(3)

Table 4.2: Ion-photon entanglement fidelities obtained by spatial filtering of ion light: simulation and experimental results for various apertures.

Since the rectangular aperture blocks the ion light only in the V direction and preserves the entire H component, it results in higher ion-photon entanglement fidelity than the symmetrical circular stop does. If the ion light is collected in free space, then there is a trade-off between the collection rate and the ion-photon entanglement fidelity, and the width of the aperture has to be optimized with respect to these two factors.

4.2.3 Photon collection into a single-mode fiber

As we discussed in Sections 4.1.3 and 4.2.1, trapped atomic ions are ideal single photon emitters with long-lived internal states which can be efficiently entangled with emitted photons. However, transmitting these photons over long distances in a large-scale distributed quantum network [189] is still a challenge. Several experiments have demonstrated long-distance (> 10 km) photon transmission in single-mode fibers [69, 70] via frequency conversion [190, 191]. We stress that apart from the very important role that single-mode fibers play in such long-distance photon transmission, the key advantages of these fibers are that they allow perfect matching of spatial modes and filtering out photons with unwanted polarizations [73, 192].

As is commonly known, when photons are collected along the quantization

axis (defined by the direction of the magnetic field), π -polarized photons cannot be coupled into a single-mode fiber due to the cylindrical symmetry [73, 192]. It turns out that when photons are collected in the direction perpendicular to the quantization axis, and the light is being coupled into a single-mode fiber, there is no polarization mixing, or in other words, the polarizations are orthogonal [193].

The amount of light from the mode \vec{E}_ϵ that will couple into a single-mode fiber is given by the mode overlap:

$$\begin{aligned} T_\epsilon &\propto \left| \int_0^{2\pi} d\phi \int_0^\pi d\theta \sin\theta \vec{E}_\epsilon \cdot \vec{G} \right|^2, \\ \vec{G} &= \exp\left(-\frac{r^2}{w^2}\right) [\alpha \hat{x} + \beta \hat{z}], \end{aligned} \quad (4.18)$$

where \vec{G} is the Gaussian mode of a single-mode fiber oriented along the y -axis with $|\alpha|^2 + |\beta|^2 = 1$. As we discussed, π -polarized photons described in Eq. (4.14) have projection only on the V polarization – along the z -axis, but not on the H polarization, which is along the x -axis. Once the vector $\hat{\theta}$ is expressed in the Cartesian coordinates,

$$\hat{\theta} = \cos\theta(\cos\phi \hat{x} + \sin\phi \hat{y}) - \sin\theta \hat{z}, \quad (4.19)$$

we can determine whether the mode \vec{E}_π can be coupled into a single-mode fiber along the x -axis or along the z -axis:

- along the x -axis (H polarization):

$$T_\pi^H \propto \int_0^\pi d\theta \sin^2\theta (\hat{\theta} \cdot \hat{x}) \propto \int_0^\pi d\theta \sin^2\theta \cos\theta = 0;$$

- along the z -axis (V polarization):

$$T_{\pi}^V \propto \int_0^{\pi} d\theta \sin^2\theta (\hat{\theta} \cdot \hat{z}) \propto \int_0^{\pi} d\theta \sin^3\theta \neq 0.$$

Similarly, we can analyse σ^+ -polarized photons described in Eq. (4.15) and investigate whether the mode \vec{E}_{σ} can be coupled into a single-mode fiber along the x -axis or along the z -axis. \vec{E}_{σ} consists of two terms, and only the first one, $\propto \cos\theta \hat{\theta}$, is relevant for this discussion:

- along the x -axis (H polarization):

$$T_{\sigma}^H \propto \int_0^{\pi} d\theta \sin\theta \cos\theta (\hat{\theta} \cdot \hat{x}) \propto \int_0^{\pi} d\theta \sin\theta \cos^2\theta \neq 0$$

- along the z -axis (V polarization):

$$T_{\sigma}^V \propto \int_0^{\pi} d\theta \sin\theta \cos\theta (\hat{\theta} \cdot \hat{z}) \propto \int_0^{\pi} d\theta \sin^2\cos\theta = 0.$$

Thus, once the σ -polarized photons are coupled into a single-mode fiber, the polarizations are orthogonal, and there is none of the polarization mixing that we discussed in Section 4.2.2.

Chapter 5: Outlook

In this thesis, we have demonstrated the key elements of the quantum network (based on the memory $^{171}\text{Yb}^+$ qubits and communication $^{138}\text{Ba}^+$ qubits) such as ion-photon entanglement, generation of pure single photons, and entangling gates between $^{171}\text{Yb}^+$ and $^{138}\text{Ba}^+$ ions together with the theoretical analysis of entangling gates for long mixed-species ion chains.

5.1 Quantum network with several nodes

Since we have two fully operational ion traps on the optical table, the next step of our experiment is to show 2×2 quantum network based on two nodes with one $^{171}\text{Yb}^+$ ion and one $^{138}\text{Ba}^+$ ion in each trap.

Following the quantum network protocol, first, we create remote entanglement between $^{138}\text{Ba}^+$ ions in different traps. With the achieved fiber coupling efficiency of 30% ¹ for 0.6 NA objectives, we expect to get the remote entanglement rate of 80-100 s^{-1} . The best result to date that has recently been reported by the Oxford ion trap group is 182 s^{-1} [193].

¹We achieved coupling of a $^{138}\text{Ba}^+$ ion light into a single-mode (SM) fiber with the coupling efficiency of 30%. We take into account the fact that 80% of the light emitted to 0.6 NA has non-zero overlap with the Gaussian mode of the SM fiber. If we ignore this fact then the observed fiber coupling efficiency would be about 25% with respect to the free-space light collection.

Next, after performing two MS gates between $^{171}\text{Yb}^+$ and $^{138}\text{Ba}^+$ ions in each trap, we end up with two entangled $^{171}\text{Yb}^+$ ions.

Following the modular approach, a natural next step for our experiment is to expand the network to three nodes [194, 195] and then further to the larger number of ion-trap nodes. In this outlook, we discuss these network protocols and our experimental attempts in this direction.

5.1.1 Three-node network

In this section, we present a protocol for a three-node network with one memory $^{171}\text{Yb}^+$ ion and one communication $^{138}\text{Ba}^+$ ion in each ion trap. The goal is to construct an entangled state of three Yb qubits with Ba ions being disentangled from the system of interest. In addition, we have requirements of minimizing the number of the MS gates (since the MS gate fidelity is not high) and minimizing the number of the $^{138}\text{Ba}^+$ qubit state detection operations (since the $^{138}\text{Ba}^+$ qubit state detection is probabilistic, as discussed in Section 2.3.1.1; this limitation can be lifted once the $^{138}\text{Ba}^+$ detection scheme is replaced with a deterministic one).

In Fig. 5.1, we show a schematics for a three-node network. For this network, we provide the following protocol:

1. $\text{Ba}_1\text{-Ba}_2$ remote entanglement.

Note that we can do either $\text{Ba}_1\text{-Ba}_2$ or $\text{Ba}_2\text{-Ba}_3$ entanglement first so we try to generate entanglement with either pair and whichever succeeds is the one we treat as $\text{Ba}_1\text{-Ba}_2$ in the following protocol.

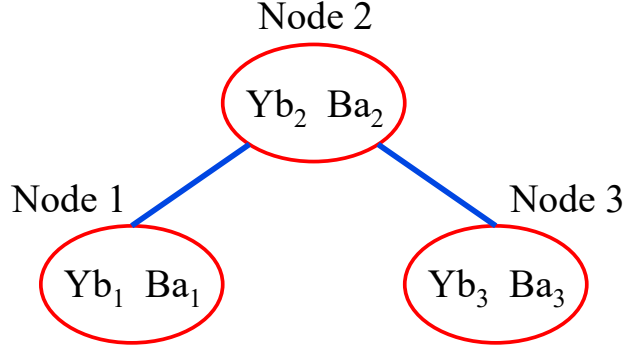


Figure 5.1: Three-node network. Red circles represent separate ion traps with one $^{171}\text{Yb}^+$ ion and one $^{138}\text{Ba}^+$ ion; blue lines represent photonic interconnections between ion traps.

As a result, the joint state is $|\text{Ba}_1\rangle |\text{Ba}_2\rangle = |00\rangle + |11\rangle$.

2. Initialization of $|\text{Yb}_1\rangle = |0\rangle$, and then $\text{Ba}_1\text{-Yb}_1$ SWAP operation.
3. Initialization of $|\text{Yb}_2\rangle = |0\rangle$, and then $\text{Ba}_2\text{-Yb}_2$ SWAP operation.

As a result, the joint state is $|\text{Yb}_1\rangle |\text{Yb}_2\rangle = |00\rangle + |11\rangle$.

4. $\text{Ba}_2\text{-Ba}_3$ remote entanglement.

As a result, the joint state is $|\text{Ba}_2\rangle |\text{Ba}_3\rangle = |00\rangle + |11\rangle$.

5. Initialization of $|\text{Yb}_3\rangle = |0\rangle$, and then $\text{Ba}_3\text{-Yb}_3$ SWAP operation.

As a result, the the joint state of Yb_1 , Yb_2 , Ba_2 , and Yb_3 is given by

$$|\text{Yb}_1\rangle |\text{Yb}_2\rangle |\text{Ba}_2\rangle |\text{Yb}_3\rangle = (|00\rangle + |11\rangle)(|00\rangle + |11\rangle) = |0000\rangle + |1100\rangle + |0011\rangle + |1111\rangle.$$

6. CNOT $\text{Yb}_2\text{-Ba}_2$, where $|\text{Yb}_2\rangle$ is a control qubit.

$$\text{Then, } |\text{Yb}_1\rangle |\text{Yb}_2\rangle |\text{Ba}_2\rangle |\text{Yb}_3\rangle = |0000\rangle + |1110\rangle + |0011\rangle + |1101\rangle$$

7. Measurement of $|\text{Ba}_2\rangle$ and a conditional rotation on $|\text{Yb}_3\rangle$.

$$\text{If } |\text{Ba}_2\rangle = |0\rangle, \text{ then } |\text{Yb}_1\rangle |\text{Yb}_2\rangle |\text{Yb}_3\rangle = |000\rangle + |111\rangle.$$

If $|\text{Ba}_2\rangle = |1\rangle$, then $|\text{Yb}_1\rangle |\text{Yb}_2\rangle |\text{Yb}_3\rangle = |110\rangle + |001\rangle$. After the π rotation on $|\text{Yb}_3\rangle$, we get the final GHZ state: $|\text{Yb}_1\rangle |\text{Yb}_2\rangle |\text{Yb}_3\rangle = |000\rangle + |111\rangle$.

8. Measurement of $|\text{Yb}_1\rangle$, $|\text{Yb}_2\rangle$, and $|\text{Yb}_3\rangle$ states.

Note that each SWAP operation requires two MS gates, and each CNOT requires only one MS gate. As a result, we have to perform seven MS gates and one detection of a Ba qubit. Since two photons are required to establish remote entanglement between two Ba ions, the success probability of this operation scales as p^2 . Since currently the Ba state detection is probabilistic, it adds a power of p leading to the total success probability of p^3 . This results in a much lower fraction of experimental trials that produce a desired entangled state in comparison with p^2 protocols achievable when deterministic detection is utilized. Also, if we want to achieve 70% of the final fidelity of this protocol, the MS gate fidelity has to be 95% or higher.

We can modify this protocol to avoid measuring the state of the Ba ion, and keep the success probability of the order of p^2 . For that, we change all the protocol steps starting with step 6:

6. CNOT Yb_2 - Ba_2 , where $|\text{Ba}_2\rangle$ is a control qubit.

Then, $|\text{Yb}_1\rangle |\text{Yb}_2\rangle |\text{Ba}_2\rangle |\text{Yb}_3\rangle = |0000\rangle + |1100\rangle + |0111\rangle + |1011\rangle$

7. Measurement of $|\text{Yb}_2\rangle$ and a conditional rotation on $|\text{Yb}_1\rangle$.

If $|\text{Yb}_2\rangle = |0\rangle$, then $|\text{Yb}_1\rangle |\text{Ba}_2\rangle |\text{Yb}_3\rangle = |000\rangle + |111\rangle$.

If $|\text{Yb}_2\rangle = |1\rangle$, then $|\text{Yb}_1\rangle |\text{Ba}_2\rangle |\text{Yb}_3\rangle = |100\rangle + |011\rangle$. After the π rotation on $|\text{Yb}_1\rangle$, we get the GHZ state: $|\text{Yb}_1\rangle |\text{Ba}_2\rangle |\text{Yb}_3\rangle = |000\rangle + |111\rangle$.

8. Initialization of $|\text{Yb}_2\rangle = |0\rangle$, and then Ba_2 - Yb_2 SWAP operation.

Then, we get the final GHZ state: $|\text{Yb}_1\rangle |\text{Yb}_2\rangle |\text{Yb}_3\rangle = |000\rangle + |111\rangle$.

In this case, we perform a total of nine MS gates and no Ba state detection. As a result, if we want to achieve 70% total fidelity of this protocol, the MS gate fidelity has to be 96% or higher.

5.1.2 Four-node network

In this section, we present a protocol for a four-node network with one memory $^{171}\text{Yb}^+$ ion and one communication $^{138}\text{Ba}^+$ ion in each ion trap. The goal is to construct a distributed entanglement between four traps. Similarly to the previous Section 5.1.1, we have requirements of minimizing the number of the MS gates and the number of the Ba qubit state detection operations.

In Fig. 5.2, we show a schematics of a four-node network. For this network, we provide the following protocol:

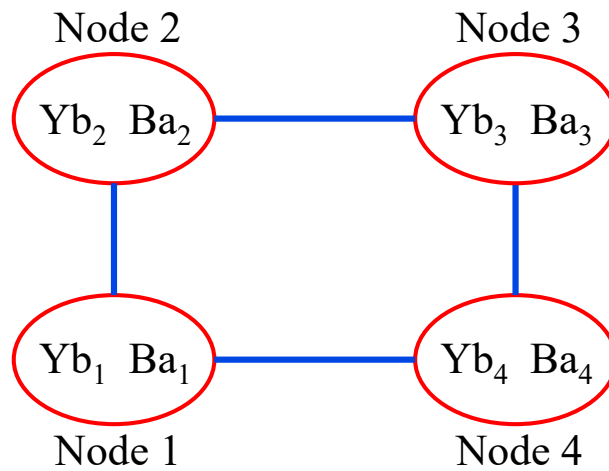


Figure 5.2: Four-node network. Red circles represent separate ion traps with one $^{171}\text{Yb}^+$ ion and one $^{138}\text{Ba}^+$ ion; blue lines represent photonic interconnections between the ion traps.

1. Ba₁-Ba₂ remote entanglement.

As a result, the joint state is $|Ba_1\rangle |Ba_2\rangle = |00\rangle + |11\rangle$.

2. Initialization of $|Yb_1\rangle = |0\rangle$, and then Ba₁-Yb₁ SWAP operation.

3. Initialization of $|Yb_2\rangle = |0\rangle$, and then Ba₂-Yb₂ SWAP operation.

As a result, the joint state is $|Yb_1\rangle |Yb_2\rangle = |00\rangle + |11\rangle$.

4. Ba₃-Ba₄ remote entanglement.

As a result, the joint state is $|Ba_3\rangle |Ba_4\rangle = |00\rangle + |11\rangle$.

5. Initialization of $|Yb_3\rangle = |0\rangle$, and then Ba₃-Yb₃ SWAP operation.

6. Initialization of $|Yb_4\rangle = |0\rangle$, and then Ba₄-Yb₄ SWAP operation.

As a result, the joint state is $|Yb_3\rangle |Yb_4\rangle = |00\rangle + |11\rangle$.

7. Ba₂-Ba₃ remote entanglement.

As a result, the joint state is $|Ba_2\rangle |Ba_3\rangle = |00\rangle + |11\rangle$.

8. Ba₄-Ba₁ remote entanglement.

As a result, the joint state is $|Ba_4\rangle |Ba_1\rangle = |00\rangle + |11\rangle$.

9. CNOT Yb₂-Ba₂, where $|Yb_2\rangle$ is a control qubit.

Then, $|Yb_1\rangle |Yb_2\rangle |Ba_2\rangle |Ba_3\rangle = |0000\rangle + |1110\rangle + |0011\rangle + |1101\rangle$, where the order of the qubits has to be preserved.

10. Then we add $|Yb_3\rangle |Yb_4\rangle = |00\rangle + |11\rangle$ to the right side, and at this point we

are working with six qubits: $|Yb_1\rangle |Yb_2\rangle |Ba_2\rangle |Ba_3\rangle |Yb_3\rangle |Yb_4\rangle$.

CNOT Ba₃-Yb₃, where $|Ba_3\rangle$ is a control qubit.

Then, $|Yb_1\rangle |Yb_2\rangle |Ba_2\rangle |Ba_3\rangle |Yb_3\rangle |Yb_4\rangle = |000000\rangle + |000011\rangle + |111000\rangle + |111011\rangle + |001110\rangle + |001101\rangle + |110110\rangle + |110101\rangle$.

11. Then we add $|Ba_4\rangle |Ba_1\rangle = |00\rangle + |11\rangle$ to the right side, and at this point we are working with all the eight qubits: $|Yb_1\rangle |Yb_2\rangle |Ba_2\rangle |Ba_3\rangle |Yb_3\rangle |Yb_4\rangle |Ba_4\rangle |Ba_1\rangle$. CNOT Yb_4 - Ba_4 , where $|Yb_4\rangle$ is a control qubit.

Then, $|Yb_1\rangle |Yb_2\rangle |Ba_2\rangle |Ba_3\rangle |Yb_3\rangle |Yb_4\rangle |Ba_4\rangle |Ba_1\rangle = |00000000\rangle + |00000011\rangle + |00001110\rangle + |00001101\rangle + |11100000\rangle + |11100011\rangle + |11101110\rangle + |11101101\rangle + |00111000\rangle + |00111011\rangle + |00110110\rangle + |00110101\rangle + |11011000\rangle + |11011011\rangle + |11010110\rangle + |11010101\rangle$.

12. CNOT Ba_1 - Yb_1 , where $|Ba_1\rangle$ is a control qubit.

Then, $|Yb_1\rangle |Yb_2\rangle |Ba_2\rangle |Ba_3\rangle |Yb_3\rangle |Yb_4\rangle |Ba_4\rangle |Ba_1\rangle = |00000000\rangle + |10000011\rangle + |00001110\rangle + |10001101\rangle + |11100000\rangle + |01100011\rangle + |11101110\rangle + |01101101\rangle + |00111000\rangle + |10111011\rangle + |00110110\rangle + |10110101\rangle + |11011000\rangle + |01011011\rangle + |11010110\rangle + |01010101\rangle$.

13. Measurement of $|Yb_1\rangle |Ba_2\rangle |Yb_3\rangle |Ba_4\rangle$ and conditional rotations.

For simplicity, we discuss only some of the measurement results.

If $|Yb_1\rangle |Ba_2\rangle |Yb_3\rangle |Ba_4\rangle = |0000\rangle$, then only the states highlighted in red remain in the superposition, and $|Yb_2\rangle |Ba_3\rangle |Yb_4\rangle |Ba_1\rangle = |0000\rangle + |1111\rangle$.

If $|Yb_1\rangle |Ba_2\rangle |Yb_3\rangle |Ba_4\rangle = |0110\rangle$, then only the states highlighted in green remain in the superposition, and $|Yb_2\rangle |Ba_3\rangle |Yb_4\rangle |Ba_1\rangle = |0100\rangle + |1011\rangle$.

Next, we perform a π rotation on $|Ba_3\rangle$ and obtain the final GHZ state:

$|Yb_2\rangle |Ba_3\rangle |Yb_4\rangle |Ba_1\rangle = |0000\rangle + |1111\rangle$.

If $|Yb_1\rangle|Ba_2\rangle|Yb_3\rangle|Ba_4\rangle = |1111\rangle$, then only the states highlighted in blue remain in the superposition, and $|Yb_2\rangle|Ba_3\rangle|Yb_4\rangle|Ba_1\rangle = |1010\rangle + |0101\rangle$. Next, we perform π rotations on $|Yb_2\rangle$ and $|Yb_4\rangle$ and obtain the final GHZ state: $|Yb_2\rangle|Ba_3\rangle|Yb_4\rangle|Ba_1\rangle = |0000\rangle + |1111\rangle$.

As a result, for this protocol, we have to perform twelve MS gates and four detections of Ba ions. Since currently the Ba state detection is probabilistic, it leads to the final success probability of p^6 , which is not acceptable. However, if the conventional deterministic Ba state detection scheme is used instead, then the total success probability becomes p^2 [124, 125], and this issue is resolved. Also, some of the steps of this protocol can be done in parallel – for example SWAP or CNOT operations in different traps. We estimate the total time required for the execution of this protocol to be around $500\ \mu\text{s}$ - $1\ \text{ms}$, leading to the necessity to stabilize the magnetic field to improve the Ba coherence time.

Similarly to the three-trap case, we can modify this protocol to avoid measuring the state of the Ba ion, and keep the success probability of the order of p^2 . After the step 7, we perform CNOT gates for the pairs Yb_2 - Ba_2 and Yb_3 - Ba_3 , and after measuring the states of Yb_2 and Yb_3 , we swap the information stored in Ba_2 and Ba_3 to Yb_2 and Yb_3 , respectively. As a result, this protocol requires 14 MS gates and no Ba detection. If we want to achieve 70% total fidelity for this protocol, the MS gate fidelity has to be 97.5% or higher.

We can generalize these protocols to a larger number of quantum nodes, and

the number of entangling operations required scales linearly with the number of nodes. However, since some operations in different nodes can be performed at the same time, we expect to get sublinear dependence on time.

5.1.3 New trap design

As we discussed in Section 5.1.1 and in the corresponding network protocol, we want to have a middle node # 2 connected to two other nodes – # 1 and # 3 – via a photonic link. A fiber switch can be implemented in order to create the photonic connections with nodes # 1 and # 3. Unfortunately, attenuation of a fiber switch at 493 nm wavelength is relatively high, and it would result in a significant light loss. Moreover, fiber switches are quite slow for our remote entanglement experiments resulting in a low experimental rate (the switching speed is of the order of 1 ms).

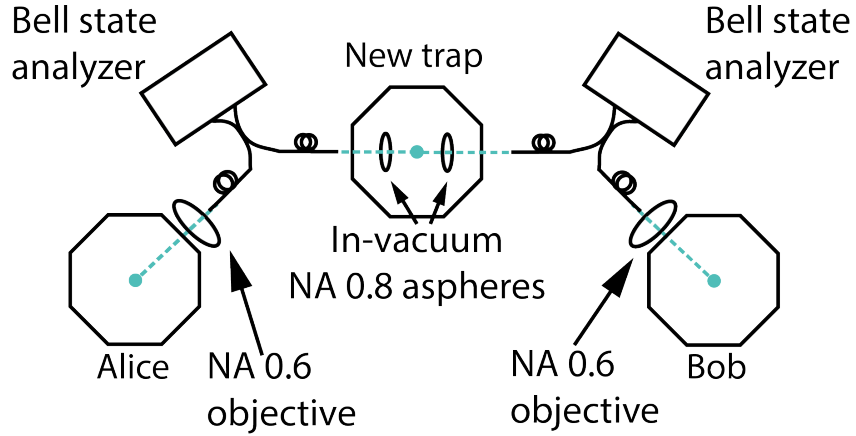


Figure 5.3: Three-trap network. Alice and Bob are currently on the optical table, and have free-space 0.6 NA objectives for 493 nm light collection and its coupling into an SM fiber. A new node will support 493 nm light collection from both sides with the help of 0.8 NA in-vacuum optics.

Therefore, to connect both nodes # 1 and # 3 with the node # 2, we design a new vacuum chamber with 493 nm light collection from two sides as shown in

Fig. 5.3. To increase the amount of the 493 nm light that we collect, we are planning to utilize two 0.8 NA objectives. These lenses are placed inside the vacuum chamber to achieve this high NA. The two working systems that we have on the optical table now will correspond to Alice and Bob in Fig. 5.3. Free-space 0.6 NA objectives ² for 493 nm light collection are used in the Alice and Bob setups.

In Fig. 5.4, we demonstrate a design of a new vacuum chamber. $^{171}\text{Yb}^+$ and $^{138}\text{Ba}^+$ ions are trapped in a four-rod trap. To achieve 0.8 NA 493 nm light collection, collection optics is placed inside the vacuum chamber, 6 mm away from the ion position. Two custom single-element aspheres ³ collimate 493 nm light and can be linearly adjusted by two three-axis piezo stages ⁴. Since the 493 nm light is collimated, any tip or tilt of the in-vacuum asphere results in a displacement of the beam that can be addressed by the second pair of custom 0.1 NA aspheres which are located outside of the vacuum chamber. Since the in-vacuum aspheres are made from a dielectric material and are located very close to the ions, we are planning to coat these lenses with Indium Tin Oxide (ITO) coating which is a transparent conductor and would be grounded to the vacuum chamber.

In Alice and Bob, we collect 493 nm light with 0.6 NA objectives, and we noticed that the rods of the four-rod trap, used in the experiments and shown in Fig. 5.5(a), block about 20% of the light. In the new trap, we solve this light-clipping problem by introducing a high optical access trap design which is demonstrated in Fig. 5.5(b). The square aspect ratio trap design used in Alice and Bob is modified

²Photon Gear Inc.

³Asphericon

⁴SmarAct, UHV compatible

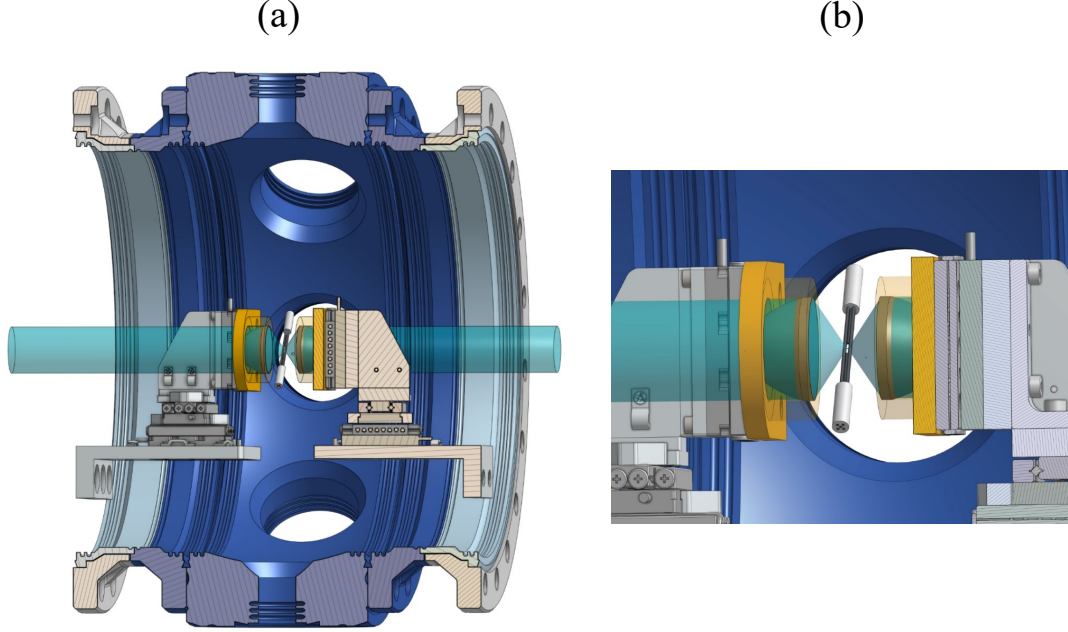


Figure 5.4: Design of a new vacuum chamber. (a) $^{171}\text{Yb}^+$ and $^{138}\text{Ba}^+$ ions are trapped in a four-rod trap with an enhanced 493 nm light collection with the help of two 0.8 NA in-vacuum custom aspheres that collimate $^{138}\text{Ba}^+$ light. Two three-axis piezo stages are used for fine linear adjustment of the in-vacuum aspheres. Outside of the vacuum chamber, two 0.1 NA custom aspheres are utilized for the fiber coupling. (b) The four-rod trap and in-vacuum aspheres are shown in a zoomed-in view.

by stretching it in one direction and squeezing it in the other one. We verify that the trap frequencies – both axial and radial – do not change dramatically with this trap modification. Namely, Alice (the old four-rod trap) has the radial frequencies $\omega_x = 2.44$ MHz and $\omega_y = 2.38$ MHz and the axial frequency $\omega_z = 0.29$ MHz. The new high optical access four-rod trap has lower radial frequencies – $\omega_x = 1.6$ MHz and $\omega_y = 1.4$ MHz – and a higher axial frequency, $\omega_z = 0.4$ MHz, assuming a 1000 V RF signal is applied to the trap electrodes, and 200 V are applied to the needles.

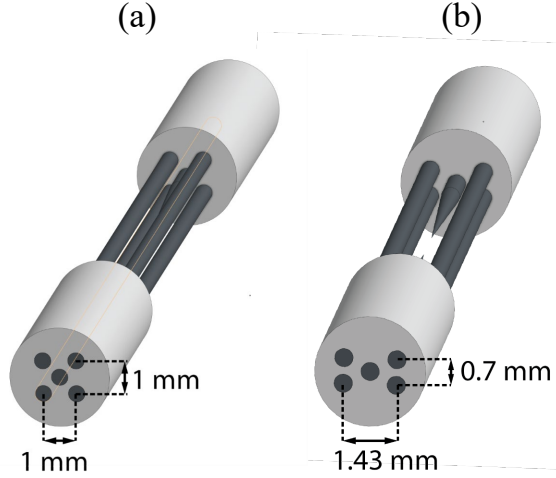


Figure 5.5: Designs of a four-rod trap. (a) Square aspect-ratio trap design used in Alice and Bob. When collecting 493 nm light with free-space 0.6 NA objective, rods are clipping about 20% of the light. (b) High optical access trap design intended to collect 493 nm light with 0.8 NA in-vacuum aspheres on two sides.

5.2 $^{133}\text{Ba}^+$ as a memory qubit

We use $^{171}\text{Yb}^+$ ions as memory qubits since they are insensitive to magnetic field and have long coherence times [26, 27]. But the major drawback associated with the use of $^{171}\text{Yb}^+$ ions is that the main cooling transition at 369 nm is in the UV range, and currently, the development of the corresponding photonics infrastructure is limited. As a solution to this problem, a synthetic $A = 133$ isotope of barium is under development for quantum information applications [34, 141]. $^{133}\text{Ba}^+$ has a non-zero nuclear spin $I = 1/2$ which means it has an atomic level structure similar to $^{171}\text{Yb}^+$. This guarantees robust state preparation and readout of the hyperfine qubit, magnetic field insensitivity, and long coherence times. In addition, its metastable $D_{3/2}$ state ($\tau \approx 80$ s) allows high-fidelity readout [34], and long-wavelength transitions facilitate the use of photonic technologies developed for the

visible and near-infrared spectrum.

$^{133}\text{Ba}^+$ isotope is radioactive with a halflife of 10.5 years and an average emitted gamma energy of 0.266 MeV. Hence, additional safety procedures are required during oven loading and trapping (such as a few-cm-thick lead screen to provide adequate radiation shielding).

At the current stage of our experiment, we use different species for memory qubits and communication qubits to eliminate crosstalk between them and preserve the information stored in the memory qubit during single photon generation and optical pumping steps. Now, we consider a possibility of switching to still a mixed-species, but an all-Barium network with $^{133}\text{Ba}^+$ as a memory qubit and $^{138}\text{Ba}^+$ as a communication qubit. For this purpose, we need to investigate crosstalk probabilities. Crosstalk can occur if $^{133}\text{Ba}^+$ (which is storing information in the hyperfine states in the $S_{1/2}$ manifold) absorbs a 493 nm photon emitted from $^{138}\text{Ba}^+$ during remote entanglement generation or from a 493 nm laser beam that performs optical pumping of $^{138}\text{Ba}^+$.

5.2.1 Crosstalk during single photon generation

First, we investigate the crosstalk between $^{133}\text{Ba}^+$ and $^{138}\text{Ba}^+$ qubits during single photon generation process [196]. To create remote entanglement between separate quantum nodes, we excite $^{138}\text{Ba}^+$ ions in both traps simultaneously and collect the emitted 493 nm photons into single-mode fibers. Since the success rate of this whole procedure is low, we initiate 10^5 excitation events per second, and many

493 nm photons are emitted in all directions (4π solid angle). Since we perform excitation with 650 nm pulses, 493 nm laser light is off and does not cause any additional crosstalk.

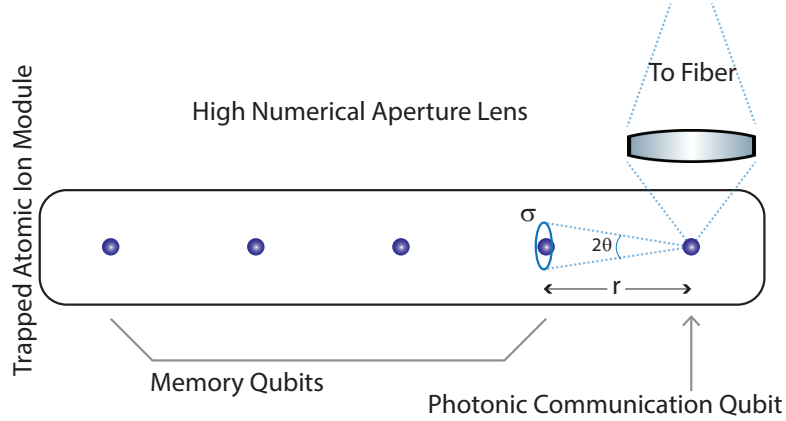


Figure 5.6: Representation of crosstalk between a memory qubit and a photonic communication qubit located a distance r away from its neighbor in an ion-trap node. The resonant absorption cross section σ is described by the angle $2\theta(r)$.

We assume the ions are equally spaced, as shown in Fig. 5.6, with the inter-ionic distance of $r = 5 \mu\text{m}$, and the resonant absorption cross section σ is described by the angle $2\theta(r)$. The ratio of the solid angle in which scattered photons can be absorbed by the memory ion to the total solid angle of 4π is given as:

$$\frac{\Omega}{4\pi} = \frac{2\pi \int_0^\theta \sin \theta' d\theta'}{4\pi} = \frac{1 - \cos \theta(r)}{2}, \quad (5.1)$$

where

$$2\theta(r) = 2 \arctan \left(\frac{\sqrt{3\lambda^2/2\pi^2}}{r} \right). \quad (5.2)$$

The crosstalk probability is determined by a few factors. One of them, the solid angle factor [Eq. (5.1)], is about 10^{-3} in our case. Another factor that contributes to the

crosstalk probability is given by $\left(\frac{\gamma/2\pi}{\Delta}\right)^2$, where $\gamma/2\pi = 15.2$ MHz is the natural linewidth of the $P_{1/2}$ level and Δ is the detuning between the relevant transitions in $^{133}\text{Ba}^+$ and $^{138}\text{Ba}^+$ ions.

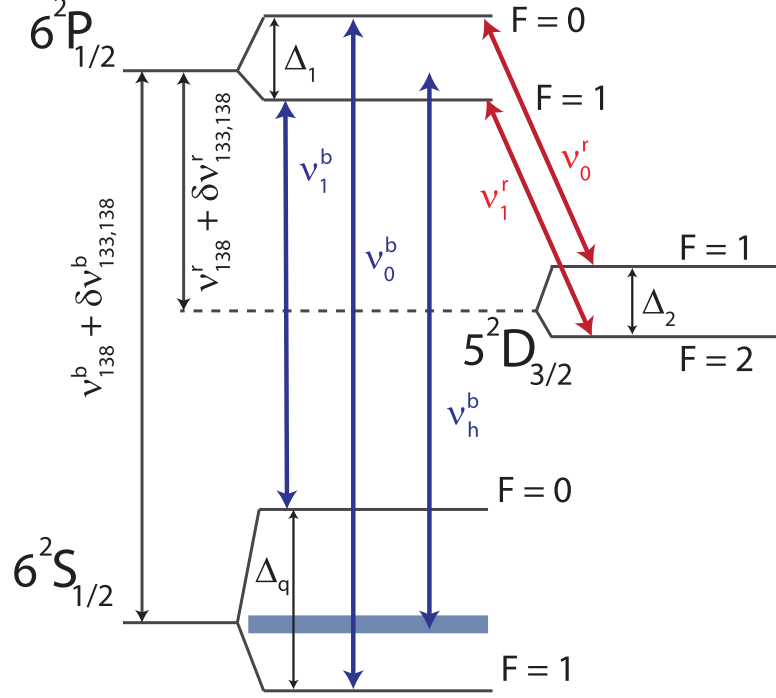


Figure 5.7: Energy level diagram for $^{133}\text{Ba}^+$. The qubit is defined within the hyperfine sublevels of the $S_{1/2}$ manifold, with the qubit splitting $\Delta_q = 9.93$ GHz. The hyperfine splittings in the $P_{1/2}$ and $D_{3/2}$ manifolds are $\Delta_1 = 1.84$ GHz and $\Delta_2 = 0.94$ GHz, respectively. The other relevant frequencies are $\nu_0^b = \nu_{138}^b + 4.22$ GHz, and $\nu_1^b = \nu_{138}^b - 7.53$ GHz, where $\nu_{138}^b = 607.4263$ THz is the resonant frequency of the $S_{1/2} \leftrightarrow P_{1/2}$ transition in $^{138}\text{Ba}^+$.

In Fig. 5.7, which is based on Ref. [141], we demonstrate a diagram of the relevant energy levels in $^{133}\text{Ba}^+$ for our crosstalk calculations. We find several crosstalk channels:

- If the $^{133}\text{Ba}^+$ qubit has population in the $S_{1/2} |F=0, m_F=0\rangle$ state, then the transitions to the $P_{1/2}, F=1$ manifold are possible, and they are detuned relevant to the 493 nm photons from $^{138}\text{Ba}^+$ by $\Delta_0 = -7.53$ GHz. The resulting

factor that contributes to the crosstalk probability equals $\left(\frac{\gamma/2\pi}{\Delta_0}\right)^2 \approx 4 \times 10^{-6}$.

- If the $^{133}\text{Ba}^+$ qubit has population in the $S_{1/2}, |F = 1, m_F = 0\rangle$ state, then:
 - One of the possible transitions is to the $P_{1/2}, |F = 0, m_F = 0\rangle$ state, and the relevant detuning is $\Delta'_1 = 4.22$ GHz. The corresponding factor contributing to the crosstalk probability is calculated as: $\left(\frac{\gamma/2\pi}{\Delta'_1}\right)^2 \approx 1.3 \times 10^{-5}$. Since this transition can only be driven by photons with π polarization, an additional factor should be introduced and the final crosstalk probability turns out to be $\approx 6 \times 10^{-6}$.
 - The other possible transitions are to the $P_{1/2}, |F = 1, m_F = \pm 1\rangle$ states, and the relevant detuning is $\Delta''_1 = 2.38$ GHz. The corresponding factor contributing to the crosstalk probability is found to be: $\left(\frac{\gamma/2\pi}{\Delta''_1}\right)^2 \approx 4 \times 10^{-5}$. Since this transition can only be driven by photons with σ^\pm polarizations, an additional factor should be introduced, and the final crosstalk probability is $\approx 2 \times 10^{-5}$.

Moreover, there is an additional factor ($\lesssim 1$) [197] that accounts for the mismatch in the temporal profiles of the emitted and absorbed 493 nm photons. Taking into account all the channels together, we arrive to the total probability of excitation of the memory qubit of $\approx 2 \times 10^{-8}$. If we assume that the remote entanglement success probability is about 10^{-4} , then we still expect to achieve the fidelity of $\approx 99.98\%$ which is far greater than a value that would be a limiting factor at this point.

5.2.2 Crosstalk during optical pumping

Another source where crosstalk errors come from is CW 493 nm beams required for the communication qubit addressing [196]. We assume that information is stored in a $^{133}\text{Ba}^+$ memory qubit, while we perform optical pumping to the edge state in the $D_{3/2}$ manifold in the $^{138}\text{Ba}^+$ communication qubit using all the polarizations of 493 nm laser light. We assume Gaussian beam profile, so that the intensity of the light I at a distance r from the beam center is given by:

$$I(r) = I_0 \exp\left(-\frac{2r^2}{w_0^2}\right), \quad (5.3)$$

where I_0 is a peak intensity and w_0 is a beam waist.

The crosstalk probability can be calculated as the ratio of the photon scattering rate at the origin (the position of the communication qubit) and at a distance r (the position of the memory qubit):

$$P_{\text{cross}} = \frac{\Gamma_{\text{sc}}(r)}{\Gamma_{\text{sc}}(r=0)}, \quad (5.4)$$

where the scattering rate $\Gamma_{\text{sc}}(r)$ is described by:

$$\Gamma_{\text{sc}}(r) = \frac{\gamma}{2} \left(\frac{\frac{I}{I_{\text{sat}}}}{1 + \frac{I}{I_{\text{sat}}} + 4\frac{\Delta^2}{\gamma^2}} \right), \quad (5.5)$$

with the natural linewidth γ , detuning Δ , and the saturation intensity I_{sat} defined

in Appendix C, Eq. (C.2). Taking into account that the laser beam is in resonance with the $S_{1/2} \leftrightarrow P_{1/2}$ transition in $^{138}\text{Ba}^+$ and has a detuning Δ with respect to the one in $^{133}\text{Ba}^+$, we obtain the probability of crosstalk as:

$$P_{\text{cross}} = \frac{2 \exp\left(-\frac{2r^2}{w_0^2}\right)}{1 + \exp\left(-\frac{2r^2}{w_0^2}\right) + 4\frac{\Delta^2}{\gamma^2}}, \quad (5.6)$$

where we assume that $I_0 = I_{\text{sat}}$. In this case, we also find several crosstalk channels:

- If the $^{133}\text{Ba}^+$ qubit has population in the $S_{1/2} |F = 0, m_F = 0\rangle$ state, then the possible transitions are to the $P_{1/2}, F = 1$ manifold, and the relevant detuning is $\Delta_0 = -7.53$ GHz.
- If the $^{133}\text{Ba}^+$ qubit has population in the $S_{1/2} |F = 1, m_F = 0\rangle$ state, then
 - one of the possible transitions is to the $P_{1/2}, |F = 0, m_F = 0\rangle$ state, and the relevant detuning is $\Delta'_1 = 4.22$ GHz.
 - the other possible transitions are to the $P_{1/2}, |F = 1, m_F = \pm 1\rangle$ states, and the relevant detuning is $\Delta''_1 = 2.38$ GHz.

In Fig. 5.8, we plot the probability of crosstalk for both $|F = 0\rangle$ and $|F = 1\rangle$ states as a function of the 493 nm beam waist and assume the inter-ionic distance of $r = 5 \mu\text{m}$. In order to reach an achievable remote entanglement probability of 10^{-4} and infidelity from the optical pumping of 10^{-4} , we would need a crosstalk probability of pumping to be around 10^{-8} , which leads to the requirement for the 493 nm pumping beam waist to be about $2.1 \mu\text{m}$. This is challenging, but definitely

not impossible to achieve in the experiment.

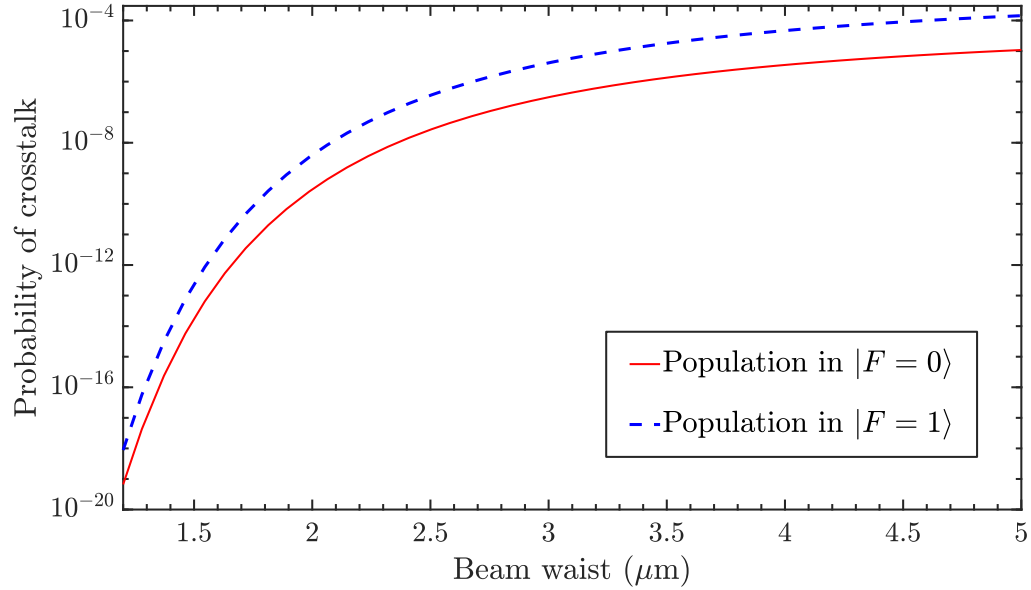


Figure 5.8: Crosstalk probability as a function of beam waist. The red solid curve represents the crosstalk probability in the case where the $^{133}\text{Ba}^+$ qubit has population in the $S_{1/2} |F = 0\rangle$ state; the blue dashed line represents the crosstalk probability in the case where the $^{133}\text{Ba}^+$ qubit has population in the $S_{1/2} |F = 1\rangle$ state.

We need to address one more crosstalk channel that is active during the optical pumping. When $^{138}\text{Ba}^+$ is being initialized in the $D_{3/2}$ manifold, it emits a number of 493 nm photons of the order of 10. Similarly to the crosstalk mechanism discussed in Chapter 5.2.1, a photon scattered by a communication ion can be absorbed by a memory ion. Since for a single photon generation we obtained the crosstalk probability of 2×10^{-8} , then in the case of 10 scattered photons the crosstalk probability is about 2×10^{-7} . As a result, remote entanglement probability of 10^{-4} that we assumed would give us the infidelity of the order of $\gtrsim 10^{-3}$.

5.2.3 Sympathetic cooling

Another important application of the mixed-species ion chains is sympathetic cooling. In this case, communication ions act as “coolant” ions and can perform sympathetic cooling on memory ions. As we discussed in Section 3.2.4, due to the high mass ratio between a $^{171}\text{Yb}^+$ memory ion and a $^{138}\text{Ba}^+$ communication ion, we observe a strong amplitude mismatch in the radial modes, leading to inefficient sympathetic cooling via the radial modes.

In the case where $^{133}\text{Ba}^+$ ions act as memory qubits, $^{138}\text{Ba}^+$ ions would be well suited to act as “coolant” ions. The mass difference between $^{133}\text{Ba}^+$ and $^{138}\text{Ba}^+$ is almost negligible, which results in an efficient cooling of both axial and radial modes. In fact, $^{136}\text{Ba}^+$ can be utilized as “coolant” ions instead, resulting in an even more efficient sympathetic cooling due to the mass ratio closer to 1.

Due to background collisions, the ion chain might get decrystallized, and when cooled down again, the ions are rearranged randomly. In order to perform MS gates, we need to know the ion chain configuration and the frequencies of the normal modes. According to our calculations performed for a 13-ion $^{133}\text{Ba}^+ / ^{138}\text{Ba}^+$ chain with 4 $^{138}\text{Ba}^+$ ions acting as “coolant” ions, the largest frequency shift of the radial modes is about 5 kHz, which is too large – the maximally tolerable frequency shift necessary to preserve an acceptable MS gate fidelity is of the order of 0.5 kHz. As a result, we might still need to perform re-ordering of the ion chain.

Appendix A: Remote entanglement

A.1 Hong-Ou-Mandel effect

In 1987, Hong, Ou, and Mandel demonstrated interference between two identical photons on a beamsplitter [198]. In this experiment, two identical photons are coming to two different input ports of the 50/50 beamsplitter, and both photons exit the same output port, indicating photon “bunching”. This effect in quantum optics is called Hong-Ou-Mandel (HOM) effect.

We can present the operation of a 50/50 beamsplitter in terms of creation operators a_k^\dagger , where index k indicates k -th beamsplitter port. Creation of a single photon can be expressed as: $|1_k\rangle = a_k^\dagger|0\rangle$. We use the following notations: two inputs get a_1^\dagger and a_2^\dagger , and two outputs produce a_3^\dagger and a_4^\dagger . The operation of a 50/50 beamsplitter can be expressed via a matrix U :

$$\begin{pmatrix} a_3^\dagger \\ a_4^\dagger \end{pmatrix} = U \begin{pmatrix} a_1^\dagger \\ a_2^\dagger \end{pmatrix}, \quad (\text{A.1})$$

where U is an unitary matrix that describes the physical process in the beamsplitter [199]. Additionally, we set the constraint that the beamsplitter is indeed a 50/50

one, which leads to the absolute value of each one of the four matrix elements being equal to $\frac{1}{\sqrt{2}}$. With these conditions, the matrix depends on just two real parameters – the phases Φ and Ψ (given that we ignore the global phase):

$$U = \frac{1}{\sqrt{2}} \begin{pmatrix} e^{-i\Phi} & e^{i\Psi} \\ e^{-i\Psi} & -e^{i\Phi} \end{pmatrix}. \quad (\text{A.2})$$

This form is general for any kind of 50/50 beamsplitter, including free-space and in-fiber ones. Then for the operators a_1^\dagger and a_2^\dagger , Eq. (A.1) results in the following expressions:

$$\begin{aligned} a_1^\dagger &= \frac{1}{\sqrt{2}} \left(e^{i\Phi} a_3^\dagger + e^{i\Psi} a_4^\dagger \right), \\ a_2^\dagger &= \frac{1}{\sqrt{2}} \left(e^{-i\Psi} a_3^\dagger - e^{-i\Phi} a_4^\dagger \right). \end{aligned} \quad (\text{A.3})$$

Let two identical particles enter both ports 1 and 2 of a 50/50 beamsplitter in the following way:

$$\begin{aligned} |1_1 1_2\rangle &= a_1^\dagger a_2^\dagger |0\rangle \\ &= \frac{1}{2} \left(e^{i(\Phi-\Psi)} a_3^\dagger a_3^\dagger - e^{-i(\Phi-\Psi)} a_4^\dagger a_4^\dagger - a_3^\dagger a_4^\dagger + a_4^\dagger a_3^\dagger \right) |0\rangle. \end{aligned} \quad (\text{A.4})$$

For bosons, $[a_i^\dagger, a_j^\dagger] = 0$, $\forall i, j$. Then, this can be applied to photons where the cross terms cancel out, and we obtain

$$|1_1 1_2\rangle = e^{i(\Phi-\Psi)} |2_3 0_4\rangle - e^{-i(\Phi-\Psi)} |0_3 2_4\rangle. \quad (\text{A.5})$$

We can see that photons exit the same output port, and they never can be detected on the opposite sides of a 50/50 beamsplitter.

For fermionic particles, $\{a_i^\dagger, a_j^\dagger\} = 0, \quad \forall i, j$. That leads to $a_j^\dagger a_j^\dagger |0\rangle = 0$, and

$$|1_1 1_2\rangle = a_4^\dagger a_3^\dagger |0\rangle = |1_3 1_4\rangle, \quad (\text{A.6})$$

indicating that fermionic particles antibunch and always exit different output ports of a 50/50 beamsplitter.

For simplicity in the following calculations, the phases Φ and Ψ can be chosen in such a way that

$$\begin{aligned} a_1^\dagger &= \frac{1}{\sqrt{2}} (a_3^\dagger + a_4^\dagger), \\ a_2^\dagger &= \frac{1}{\sqrt{2}} (a_3^\dagger - a_4^\dagger). \end{aligned} \quad (\text{A.7})$$

This form is used below in the discussion of entanglement of remote qubits.

A.2 Entanglement of remote qubits

Now let the two photons sent to a 50/50 beamsplitter be previously entangled with their atomic emitters, and the joint atom-photon state is given by:

$$|\psi\rangle = |\downarrow H\rangle + |\uparrow V\rangle, \quad (\text{A.8})$$

where $\{\uparrow, \downarrow\}$ are the atomic qubit states and $\{H, V\}$ are the photonic polarization states. We discuss the process of generating this ion-photon entanglement and the corresponding experimental results in Section 4.2.1 in detail. Let us introduce creation operators a^\dagger and b^\dagger for horizontal and vertical polarization photonic states, respectively: $|H\rangle = a^\dagger |0\rangle$ and $|V\rangle = b^\dagger |0\rangle$.

The joint state of a pair of ion-photon entangled states is demonstrated by the following expression:

$$|\psi_1\rangle \otimes |\psi_1\rangle = (|\downarrow H\rangle + |\uparrow V\rangle)_1 \otimes (|\downarrow H\rangle + |\uparrow V\rangle)_2. \quad (\text{A.9})$$

We can rewrite Eq. (A.9) in terms of the Bell states of photons and atoms:

$$|\psi_1\rangle \otimes |\psi_1\rangle = |\psi^+\rangle_a |\psi^+\rangle_p + |\psi^-\rangle_a |\psi^-\rangle_p + |\phi^+\rangle_a |\phi^+\rangle_p + |\phi^-\rangle_a |\phi^-\rangle_p, \quad (\text{A.10})$$

where the atomic Bell states are:

$$\begin{aligned} |\psi^+\rangle_a &= |\downarrow\uparrow\rangle + |\uparrow\downarrow\rangle, \\ |\psi^-\rangle_a &= |\downarrow\uparrow\rangle - |\uparrow\downarrow\rangle, \\ |\phi^+\rangle_a &= |\downarrow\downarrow\rangle + |\uparrow\uparrow\rangle, \\ |\phi^-\rangle_a &= |\downarrow\downarrow\rangle - |\uparrow\uparrow\rangle, \end{aligned} \quad (\text{A.11})$$

and the photonic Bell states have the same form:

$$\begin{aligned}
|\psi^+\rangle_p &= |HV\rangle + |VH\rangle, \\
|\psi^-\rangle_p &= |HV\rangle - |VH\rangle, \\
|\phi^+\rangle_p &= |HH\rangle + |VV\rangle, \\
|\phi^-\rangle_p &= |HH\rangle - |VV\rangle.
\end{aligned} \tag{A.12}$$

Using Eqs. (A.7), we can express the photonic Bell states in terms of the output modes of the 50/50 beamsplitter. We start with the $|\phi^+\rangle_p$ and $|\phi^-\rangle_p$ states:

$$\begin{aligned}
|\phi^\pm\rangle_p &= \left(a_1^\dagger a_2^\dagger \pm b_1^\dagger b_2^\dagger \right) |0\rangle \\
&= \left(a_4^\dagger a_4^\dagger - a_3^\dagger a_3^\dagger \pm b_4^\dagger b_4^\dagger \mp b_3^\dagger b_3^\dagger \right) |0\rangle \\
&= |0_3(HH)_4\rangle - |(HH)_3 0_4\rangle \pm |0_3(VV)_4\rangle \mp |(VV)_3 0_4\rangle.
\end{aligned} \tag{A.13}$$

Since the $|\phi^+\rangle_p$ and $|\phi^-\rangle_p$ states differ only by a phase factor, we cannot distinguish them from each other in experiment, and therefore we ignore the corresponding events.

If we consider the $|\psi^+\rangle_p$ state, we see photon bunching:

$$\begin{aligned}
|\psi^+\rangle_p &= \left(a_1^\dagger b_2^\dagger + b_1^\dagger a_2^\dagger \right) |0\rangle \\
&= \left(a_4^\dagger b_4^\dagger - a_3^\dagger b_3^\dagger \right) |0\rangle = |0_3(HV)_4\rangle - |(HV)_3 0_4\rangle,
\end{aligned} \tag{A.14}$$

while the $|\psi^-\rangle_p$ state results in photon antibunching:

$$\begin{aligned} |\psi^-\rangle_p &= \left(a_1^\dagger b_2^\dagger - b_1^\dagger a_2^\dagger\right) |0\rangle \\ &= \left(a_3^\dagger b_4^\dagger - b_3^\dagger a_4^\dagger\right) |0\rangle = |H_3 V_4\rangle - |V_3 H_4\rangle. \end{aligned} \tag{A.15}$$

It is easy to detect the $|\psi^+\rangle_p$ and $|\psi^-\rangle_p$ photonic Bell states by having polarizing beamsplitters after both output ports of the 50/50 beamsplitter. By getting coincident clicks on the corresponding pair of detectors [83], we determine the initial photonic Bell state at the input of the 50/50 beamsplitter, thus projecting the remote atoms into the corresponding Bell state, as well.

Appendix B: 355nm/532nm Optical-Frequency Combs Shifted in Time

B.1 Infinite-pulse trains

Direct realization of the Raman transitions is not always feasible due to a limited range of control over the laser frequency. We utilize the large-bandwidth ultrafast laser-pulse combs [120] to implement the Mølmer-Sørensen gate.

Consider two trains of N pulses, each acting on one of two species – indices a and b correspond to different species:

$$E_a(t) = \sum_{n=0}^{N-1} \mathcal{F}_a(t - nT) e^{i\omega_a^c t}, \quad (\text{B.1})$$

$$E_b(t) = \sum_{n=0}^{N-1} \mathcal{F}_b(t - (n + f)T) e^{i\omega_b^c t}, \quad (\text{B.2})$$

where $\mathcal{F}_{a,b}$ are envelopes and $\omega_{a,b}^c$ are carrier frequencies of combs a and b , respectively. T is a common period of the both combs, and fT is the shift in time between the combs.

Performing the Fourier transform and going to the limit of the infinite number

of pulses within the frequency domain ($N \rightarrow \infty$), we get:

$$\tilde{E}_a^{(0)}(\omega) = \tilde{\mathcal{F}}_a(\omega - \omega_a^c) \omega_R \sum_{k=-\infty}^{\infty} \delta(\omega - \omega_a^c - k\omega_R), \quad (\text{B.3})$$

$$\tilde{E}_b^{(0)}(\omega) = \tilde{\mathcal{F}}_b(\omega - \omega_b^c) \omega_R e^{-i(\omega - \omega_b^c)fT} \sum_{k=-\infty}^{\infty} \delta(\omega - \omega_b^c - k\omega_R), \quad (\text{B.4})$$

where $\omega_R = 2\pi/T$ is the repetition frequency of the lasers and $\tilde{\mathcal{F}}_{a,b}(\omega)$ are the Fourier transforms of $\mathcal{F}_{a,b}(t)$. After the inverse Fourier transformation, both of the infinite pulse trains acquire a form of Fourier series:

$$E_a^{(\infty)}(t) = \sum_{k=-\infty}^{\infty} E_k^a e^{i\omega_{ak}t}, \quad (\text{B.5})$$

$$E_b^{(\infty)}(t) = \sum_{k=-\infty}^{\infty} E_k^b e^{i\omega_{bk}t} e^{-ik\omega_R fT}, \quad (\text{B.6})$$

where

$$E_k^i = \frac{\omega_R}{2\pi} \tilde{\mathcal{F}}_i(\omega_{ik} - \omega_i^c),$$

$$\omega_{ik} = \omega_i^c + k\omega_R, \quad i = a, b. \quad (\text{B.7})$$

Now, starting with a Λ -type 3-level system subject to the comb of form Eq. (B.5), we apply rotating wave approximation and adiabatic elimination of the upper level to get the following equations of motion for the wave-function basis-expansion coefficients (for the details of the derivation, see Ref. [122], Appendix

B):

$$\begin{aligned}\dot{c}_1 &= -\frac{\hbar|\mu_{eg}|^2}{2\Delta} \left(\sum_k |E_k|^2 c_1 + \sum_k E_k (E_{k-q})^* c_2 \right), \\ \dot{c}_2 &= -\frac{\hbar|\mu_{eg}|^2}{2\Delta} \left(\sum_k E_k (E_{k-q})^* c_1 + \sum_k |E_k|^2 c_2 \right),\end{aligned}\quad (\text{B.8})$$

where $q = \omega^{(0)}/\omega_R$, $\Delta = \omega^{(3)} - \omega^c$. $\hbar\omega^{(3)}$ is the energy of the upper level of the 3-level ion.

The comb of form Eq. (B.6) generates an additional phase in the off-diagonal terms:

$$\sum_k E_k (E_{k-q})^* \rightarrow \sum_k E_k e^{-ik\omega_R fT} (E_{k-q})^* e^{i(k-q)\omega_R fT} = \sum_k E_k (E_{k-q})^* e^{-i\omega^{(0)} fT}.$$

(B.9)

Therefore, we obtain the following effective Hamiltonians for each 3-level system subject to the combs described in Eqs. (B.5) and (B.6):

$$\hat{H}_{\text{eff}}^a = -\frac{\hbar|\mu_{eg}^a|^2}{2\Delta_a} \begin{pmatrix} \sum_k |E_k^a|^2 & \sum_k E_k^a (E_{k-q_a}^a)^* \\ \sum_k E_k^a (E_{k+q_a}^a)^* & \sum_k |E_k^a|^2 \end{pmatrix}, \quad (\text{B.10})$$

$$\hat{H}_{\text{eff}}^b = -\frac{\hbar|\mu_{eg}^b|^2}{2\Delta_b} \begin{pmatrix} \sum_k |E_k^b|^2 & \sum_k E_k^b (E_{k-q_b}^b)^* e^{-i\xi} \\ \sum_k E_k^b (E_{k+q_b}^b)^* e^{i\xi} & \sum_k |E_k^b|^2 \end{pmatrix}, \quad (\text{B.11})$$

where the additional phase $\xi = \omega_b^{(0)} fT$ is only acquired by the interaction part of the Hamiltonian of one of the ions.

In the Mølmer-Sørensen scheme, this additional phase ξ enters as $\phi_s^{(2)} \rightarrow \phi_s^{(2)} + \xi$, which leads to the following modified truth table:

$$\begin{aligned}
|\uparrow\uparrow\rangle &\rightarrow |\uparrow\uparrow\rangle - ie^{i(\phi_s^{(1)} + \phi_s^{(2)} + \xi)} |\downarrow\downarrow\rangle, \\
|\downarrow\downarrow\rangle &\rightarrow |\downarrow\downarrow\rangle - ie^{-i(\phi_s^{(1)} + \phi_s^{(2)} + \xi)} |\uparrow\uparrow\rangle, \\
|\uparrow\downarrow\rangle &\rightarrow |\uparrow\downarrow\rangle - ie^{-i(\phi_s^{(2)} - \phi_s^{(1)} + \xi)} |\downarrow\uparrow\rangle, \\
|\downarrow\uparrow\rangle &\rightarrow |\downarrow\uparrow\rangle - ie^{i(\phi_s^{(2)} - \phi_s^{(1)} + \xi)} |\uparrow\downarrow\rangle.
\end{aligned} \tag{B.12}$$

The obtained additional phase ξ can be compensated by the adjustment of other phases. Consequently, after phase tuning, the Mølmer-Sørensen gate works the same way independent on the time shift between the combs acting on different ions.

B.2 Finite N-pulse trains

In section [B.1](#), we considered a formalism that only works for infinite number of pulses in a train. Here, we use a different technique to discuss finite N -pulse trains.

We start with the following Hamiltonian for two ions within a single mode of harmonic motion subject to two Raman pulse trains:

$$\begin{aligned}
\hat{H}_{\text{eff}} = \omega_t a^\dagger a &+ \frac{\omega_a}{2} \sigma_z^a + \frac{\omega_b}{2} \sigma_z^b + \frac{\theta_a}{2} \sum_{n=0}^{N-1} \delta(t - nT) (\sigma_+^a e^{i(k\hat{x} + \Delta\omega_a t)} + \sigma_-^a e^{-i(k\hat{x} + \Delta\omega_a t)}) \\
&+ \frac{\theta_b}{2} \sum_{n=0}^{N-1} \delta(t - (n + f)T) (\sigma_+^b e^{i(k\hat{x} + \Delta\omega_b t)} + \sigma_-^b e^{-i(k\hat{x} + \Delta\omega_b t)}), \tag{B.13}
\end{aligned}$$

where $\theta_i = \Omega_i T$, $\Delta\omega_i/2\pi$ is a net offset frequency between the combs, and pulse train b is shifted by fT in time relative to pulse train a .

In the rotating wave approximation, the single-period evolution operator is given by:

$$U = \exp(-iH_0(1-f)T) \exp\left[\frac{-i\theta_b}{2} (\sigma_+^b e^{ik\hat{x}} + \sigma_-^b e^{-ik\hat{x}})\right] \\ \times \exp(-iH_0fT) \exp\left[\frac{-i\theta_a}{2} (\sigma_+^a e^{ik\hat{x}} + \sigma_-^a e^{-ik\hat{x}})\right], \quad (\text{B.14})$$

where $H_0 = \omega_t a^\dagger a + \frac{(\omega_a + \Delta\omega_a)}{2} \sigma_z + \frac{(\omega_b + \Delta\omega_b)}{2} \sigma_z$.

Using Taylor expansion and expressing the coordinate operator in terms of creation and annihilation operators, we get:

$$U = \exp(-iH_0(1-f)T) \left[1 - \frac{i\theta_b}{2} (\sigma_+^b e^{i\eta(a+a^\dagger)} + \sigma_-^b e^{-i\eta(a+a^\dagger)})\right] \\ \times \exp(-iH_0fT) \left[1 - \frac{i\theta_a}{2} (\sigma_+^a e^{i\eta(a+a^\dagger)} + \sigma_-^a e^{-i\eta(a+a^\dagger)})\right], \quad (\text{B.15})$$

where $\eta = k\sqrt{\frac{\hbar}{2m\omega_t}}$ is the Lamb-Dicke parameter, and we keep track only of terms linear in θ :

$$U \approx \exp(-iH_0T) - \exp(-iH_0(1-f)T) \exp(-iH_0fT) \frac{i\theta_a}{2} (\sigma_+^a e^{i\eta(a+a^\dagger)} + \sigma_-^a e^{-i\eta(a+a^\dagger)}) \\ - \exp(-iH_0(1-f)T) \frac{i\theta_b}{2} (\sigma_+^b e^{i\eta(a+a^\dagger)} + \sigma_-^b e^{-i\eta(a+a^\dagger)}) \exp(-iH_0fT). \quad (\text{B.16})$$

The following expressions are useful for further calculations:

$$\exp\left(\frac{i\omega t}{2}\sigma_z\right)\sigma_{\pm}\exp\left(-\frac{i\omega t}{2}\sigma_z\right)=\exp(-i\omega t)\sigma_{\pm}, \quad (\text{B.17})$$

$$\exp(i\omega t a^\dagger a)\exp[i\eta(a+a^\dagger)]\exp(i\omega t a^\dagger a)=\exp[i\eta(ae^{-i\omega t}+a^\dagger e^{i\omega t})]. \quad (\text{B.18})$$

We will only keep linear in θ terms in the N -period evolution operator U^N . Therefore, we will have up to one non-trivial operator in each term. First, let us start with working with part (a) – second term in the RHS of Eq. (B.16) – as the non-trivial evolution operator:

$$U_a=\exp(-iH_0T)\left(-\frac{i\theta_a}{2}\right)\left(\sigma_+^a e^{i\eta(a+a^\dagger)}+\sigma_-^a e^{-i\eta(a+a^\dagger)}\right), \quad (\text{B.19})$$

while other evolution operators in that product are just $\exp(-iH_0T)$.

Then the corresponding partial N -period evolution due to this term is given by:

$$\begin{aligned} U_{aN} &= \left(-\frac{i\theta_a}{2}\right)\sum_{m=0}^{N-1}e^{-iH_0(N-m)T}\left(\sigma_+^a e^{i\eta(a+a^\dagger)}+\text{h.c.}\right)e^{-iH_0mT} \\ &= e^{-iH_0NT}\left(-\frac{i\theta_a}{2}\right)\left[\sum_{m=0}^{N-1}\sigma_+^a \exp(i(\omega_a+\Delta\omega_a)mT)D(i\eta e^{i\omega_t mT})+\text{h.c.}\right], \end{aligned} \quad (\text{B.20})$$

here we use expressions from Eqs. (B.17) and (B.18), and $D(\alpha)=\exp(\alpha a^\dagger-\alpha^*a)$ is the harmonic-oscillator displacement operator in phase space.

The term containing a non-trivial contribution from part (b) is:

$$U_b = \exp(-iH_0(1-f)T) \left(-\frac{i\theta_b}{2}\right) \left(\sigma_+^b e^{i\eta(a+a^\dagger)} + \sigma_-^b e^{-i\eta(a+a^\dagger)}\right) \exp(-iH_0 fT), \quad (\text{B.21})$$

while other evolution operators in this term are just $\exp(-iH_0T)$.

Then the corresponding partial N -period evolution due to this term is given by:

$$\begin{aligned} U_{bN} &= \left(-\frac{i\theta_b}{2}\right) \sum_{m=0}^{N-1} e^{-iH_0 mT} e^{-iH_0(1-f)T} \left(\sigma_+^b e^{i\eta(a+a^\dagger)} + \text{h.c.}\right) e^{-iH_0 fT} e^{-iH_0(N-m-1)T} \\ &= e^{-iH_0 NT} \left(-\frac{i\theta_b}{2}\right) \left[\sum_{m=0}^{N-1} \sigma_+^b \exp(i(\omega_b + \Delta\omega_b)(m+f)T) D(i\eta e^{i\omega_t(m+f)T}) + \text{h.c.} \right], \quad (\text{B.22}) \end{aligned}$$

where expressions from Eqs. (B.17) and (B.18) are used again.

Combining all together, we get the full time evolution operator U^N in the following form:

$$U^N = e^{-iH_0 NT} \left(\mathbb{I} - \frac{i\theta_a}{2} \sum_{m=0}^{N-1} Q_m^a - \frac{i\theta_b}{2} \sum_{m=0}^{N-1} Q_m^b \cdot e^{i\xi} + \text{h.c.} \right), \quad (\text{B.23})$$

with

$$\begin{aligned} Q_m^a &= \sigma_+^a \exp[i(\omega_a + \Delta\omega_a)mT] D(i\eta e^{i\omega_t mT}), \\ Q_m^b &= \sigma_+^b \exp[i(\omega_b + \Delta\omega_b)mT] D(i\eta e^{i\omega_t(m+f)T}), \\ \xi &= (\omega_b + \Delta\omega_b)fT. \end{aligned}$$

Comparing this result to the result from Section [B.1](#), we see that in both approaches system (a) stays unchanged, while system (b) accumulates the additional phase ξ that can be compensated.

Appendix C: Coherent operations with 532 nm light

Here we investigate stimulated Raman transitions in the $D_{3/2}$ manifold in $^{138}\text{Ba}^+$. First, we focus on the calculations of the two-photon Rabi frequency in both of the effective $\Delta m_j = \pm 1$ and $\Delta m_j = \pm 2$ microwave rotations discussed in Section 2.3.2.2 to estimate the stimulated Raman transition rate. Then, we look at the two-photon AC Stark shifts, and try to minimize them by choosing the appropriate polarization of 532 nm laser beams.

C.1 The Rabi Frequencies

In this section, in $D_{3/2}$ manifold, we investigate how good the coupling is when using the 532 nm laser beams, or in other words, how high the Rabi frequencies are.

There are multiple excited states i involved in the stimulated Raman transitions. Therefore, the two-photon Rabi frequency can be easily derived [103] and has the following form:

$$\Omega = \sum_i \frac{g_{0,i}^* g_{1,i}}{2\Delta_i}, \quad (\text{C.1})$$

where Δ_i is the detuning from the excited state i , and the expression for the single-

photon Rabi frequency is given by

$$g_{i,j} = C\gamma\sqrt{\frac{I}{2I_{sat}}}, \quad I_{sat} = \frac{\hbar\gamma\omega_e^3}{12\pi c^2}. \quad (\text{C.2})$$

Here, C is the Clebsch-Gordan coefficient, $\gamma/2\pi$ is a natural linewidth, I is the intensity of the laser, and ω_e is the resonant transition frequency from the ground state.

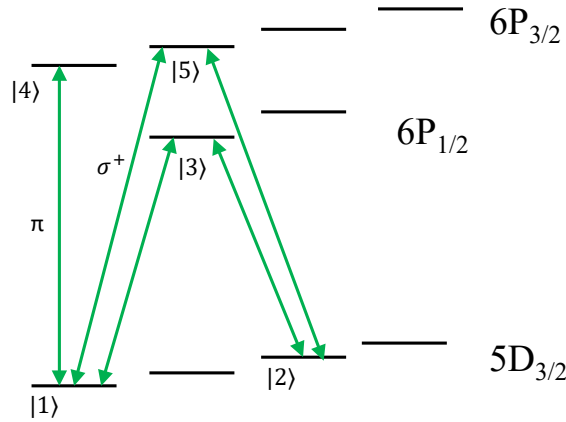


Figure C.1: Off-resonant coupling of 532 nm laser beams – represented by the green arrows – to $P_{1/2}$ and $P_{3/2}$ manifolds in $^{138}\text{Ba}^+$ in the case of the $\Delta m_j = \pm 2$ rotations between the states $|1\rangle$ and $|2\rangle$.

We perform calculations of the two-photon Rabi frequency in both of the effective $\Delta m_j = \pm 1$ and $\Delta m_j = \pm 2$ microwave rotations discussed in Section 2.3.2.2. For example, in Fig. C.1, we show the $\Delta m_j = \pm 2$ coherent rotations between the states $|1\rangle$ and $|2\rangle$ in the presence of the pair of 532 nm Raman beams off-resonantly coupled to both $P_{1/2}$ and $P_{3/2}$ states. In this case, the two-photon Rabi frequency is given by:

$$\Omega_{12} = \frac{g_{13}^* g_{23}}{2\Delta_{P_{1/2}}} + \frac{g_{15}^* g_{25}}{2\Delta_{P_{3/2}}}. \quad (\text{C.3})$$

When plugging in all the necessary parameters, we get: $\Omega_{12} = I \times \left(0.003 \frac{\text{Hz}}{\text{mW}/\text{cm}^2} \right)$,

where I is the laser intensity. Below we present Table C.1 with the corresponding atomic parameters and the final calculated values of the two-photon Rabi frequencies. We compare them for different manifolds: for $^{138}\text{Ba}^+$ $S_{1/2}$ manifold, for the $\Delta m_j = \pm 1$ rotations in the $D_{3/2}$ manifold in Ba, for the $\Delta m_j = \pm 2$ rotations in the $D_{3/2}$ manifold, and for $^{171}\text{Yb}^+$.

	Ba $S_{1/2}$ manifold	Ba $D_{3/2}$ $\Delta m_j = \pm 1$ rotations	Ba $D_{3/2}$ $\Delta m_j = \pm 2$ rotations	Yb
$\Delta_{P_{1/2}}$ (THz)	-44	102	102	34
$\Delta_{P_{3/2}}$ (THz)	-94	51.5	51.5	-66
$\gamma_{P_{1/2}}$ (MHz)	15.2	5.1	5.1	19.7
$\gamma_{P_{3/2}}$ (MHz)	19	0.7	0.7	25.8
Rabi frequency (Hz)	$0.026 I$	$-0.008 I$	$0.003 I$	$-0.028 I$

Table C.1: Atomic parameters such as the natural linewidth and detuning from the excited states $P_{1/2}$ and $P_{3/2}$ as well as the calculated Rabi frequency for different manifolds.

As mentioned in Ref. [83] and presented in Table C.1, the stimulated Raman transition rate for $^{171}\text{Yb}^+$ and $S_{1/2}$ manifold in $^{138}\text{Ba}^+$ are similar assuming equal 355 nm and 532 nm optical intensities are applied. However, the Rabi frequency calculated for $D_{3/2}$ manifold and $\Delta m_j = \pm 2$ rotations is about an order of magnitude smaller that leads to lower rates. Much higher 532 nm power is required to be able to drive the 532 nm rotations in the $D_{3/2}$ manifold in $^{138}\text{Ba}^+$ than in the the $S_{1/2}$ one.

C.2 Differential Stark Shifts

When the driving Raman fields are applied, they introduce two-photon AC Stark shifts to the energy levels. We can account for it by changing the frequencies of the corresponding Raman AOMs. However, if there are uncompensated fluctuations of the laser intensity, then we end up with detuning errors, so to prevent these types of errors AC Stark shift have to be canceled if possible.

Including multiple excited states j involved in the stimulated Raman transitions, we write the two-photon AC Stark shift as:

$$\chi_i = \sum_j \frac{|g_{ij}|^2}{4\Delta_{ij}}. \quad (\text{C.4})$$

Similarly to the previous section, for simplicity, we characterize the case of the $\Delta m_j = \pm 2$ coherent rotations between the states $|1\rangle$ and $|2\rangle$ in the presence of the pair of 532 nm Raman beams off-resonantly coupled to both $P_{1/2}$ and $P_{3/2}$ states – see Fig. C.1. We present the expression for the second-order Stark shift of the state $|1\rangle$ which is coupled to three other states – $|3\rangle$, $|4\rangle$, and $|5\rangle$ – since we have all the polarizations of the 532 nm laser fields:

$$\chi_1 = \frac{|g_{13}|^2}{4\Delta_{P_{1/2}}} + \frac{|g_{14}|^2}{4\Delta_{P_{3/2}}} + \frac{|g_{15}|^2}{4\Delta_{P_{3/2}}}. \quad (\text{C.5})$$

We perform the calculation of all four second-order AC Stark shift of the levels in the $D_{3/2}$ manifold. As discussed in Section 2.3.2.2, in order to minimize differential two-photon AC Stark shifts, we adjust the polarizations of our 532 nm

Raman beams so that the intensities of each polarization (σ^+ , σ^- , and π) are all equal.

Bibliography

- [1] Rodney Van Meter and Mark Oskin. Architectural implications of quantum computing technologies. *J. Emerg. Technol. Comput. Syst.*, 2(1):31–63, January 2006.
- [2] M. A. Nielsen and I. L. Chuang. *Quantum Computation and Quantum Information*. Cambridge Univ. Press, 2000.
- [3] T. D. Ladd, F. Jelezko, R. Laflamme, Y. Nakamura, C. Monroe, and J. L. O’Brien. Quantum computers. *Nature*, 464(7285):45–53, 2010.
- [4] Yuri Manin. *Vychislimoe i nevychislimoe (Computable and Noncomputable) [in Russian]*. Sov. Radio, 1980.
- [5] Paul Benioff. Quantum mechanical hamiltonian models of turing machines. *Journal of Statistical Physics*, 29(3):515–546, 1982.
- [6] Richard P. Feynman. Simulating physics with computers. *International Journal of Theoretical Physics*, 21(6):467–488, 1982.
- [7] David Deutsch and Roger Penrose. Quantum theory, the church-turing principle and the universal quantum computer. *Proceedings of the Royal Society of London. A. Mathematical and Physical Sciences*, 400(1818):97–117, 1985.
- [8] David Deutsch and Richard Jozsa. Rapid solution of problems by quantum computation. *Proceedings of the Royal Society of London. Series A: Mathematical and Physical Sciences*, 439(1907):553–558, 1992.
- [9] P. W. Shor. Algorithms for quantum computation: discrete logarithms and factoring. In *Proceedings 35th Annual Symposium on Foundations of Computer Science*, pages 124–134, Nov 1994.
- [10] J. I. Cirac and P. Zoller. Quantum computations with cold trapped ions. *Phys. Rev. Lett.*, 74:4091–4094, May 1995.
- [11] C. Monroe, D. M. Meekhof, B. E. King, W. M. Itano, and D. J. Wineland. Demonstration of a fundamental quantum logic gate. *Phys. Rev. Lett.*, 75:4714–4717, Dec 1995.

- [12] Peter W. Shor. Scheme for reducing decoherence in quantum computer memory. *Phys. Rev. A*, 52:R2493–R2496, Oct 1995.
- [13] A. M. Steane. Error correcting codes in quantum theory. *Phys. Rev. Lett.*, 77:793–797, Jul 1996.
- [14] Lov K. Grover. A fast quantum mechanical algorithm for database search. In *Proceedings of the Twenty-eighth Annual ACM Symposium on Theory of Computing*, STOC '96, pages 212–219, New York, NY, USA, 1996. ACM.
- [15] Colin D. Bruzewicz, John Chiaverini, Robert McConnell, and Jeremy M. Sage. Trapped-ion quantum computing: Progress and challenges. *Applied Physics Reviews*, 6(2):021314, 2019.
- [16] David S. Weiss and Mark Saffman. Quantum computing with neutral atoms. *Physics Today*, 70(7):44–50, 2017.
- [17] Lilian Childress and Ronald Hanson. Diamond nv centers for quantum computing and quantum networks. *MRS Bulletin*, 38(2):134138, 2013.
- [18] P. Krantz, M. Kjaergaard, F. Yan, T. P. Orlando, S. Gustavsson, and W. D. Oliver. A quantum engineer’s guide to superconducting qubits. *Applied Physics Reviews*, 6(2):021318, 2019.
- [19] Christoph Kloeffer and Daniel Loss. Prospects for spin-based quantum computing in quantum dots. *Annual Review of Condensed Matter Physics*, 4(1):51–81, 2013.
- [20] David P. DiVincenzo. The physical implementation of quantum computation. *Fortschritte der Physik*, 48(911):771–783, 2000.
- [21] Andreas V. Kuhlmann, Julien Houel, Arne Ludwig, Lukas Greuter, Dirk Reuter, Andreas D. Wieck, Martino Poggio, and Richard J. Warburton. Charge noise and spin noise in a semiconductor quantum device. *Nature Physics*, 9(9):570–575, 2013.
- [22] N. Somaschi, V. Giesz, L. De Santis, J. C. Lored, M. P. Almeida, G. Hornecker, S. L. Portalupi, T. Grange, C. Antón, J. Demory, C. Gómez, I. Sagnes, N. D. Lanzillotti-Kimura, A. Lemaître, A. Auffeves, A. G. White, L. Lanco, and P. Senellart. Near-optimal single-photon sources in the solid state. *Nature Photonics*, 10(5):340–345, 2016.
- [23] P. V. Klimov, J. Kelly, Z. Chen, M. Neeley, A. Megrant, B. Burkett, R. Barends, K. Arya, B. Chiaro, Yu Chen, A. Dunsworth, A. Fowler, B. Foxen, C. Gidney, M. Giustina, R. Graff, T. Huang, E. Jeffrey, Erik Lucero, J. Y. Mutus, O. Naaman, C. Neill, C. Quintana, P. Roushan, Daniel Sank, A. Vainsencher, J. Wenner, T. C. White, S. Boixo, R. Babbush, V. N. Smelyanskiy, H. Neven, and John M. Martinis. Fluctuations of energy-relaxation times in superconducting qubits. *Phys. Rev. Lett.*, 121:090502, Aug 2018.

- [24] Wolfgang Paul. Electromagnetic traps for charged and neutral particles. *Rev. Mod. Phys.*, 62:531–540, Jul 1990.
- [25] C. Langer, R. Ozeri, J. D. Jost, J. Chiaverini, B. DeMarco, A. Ben-Kish, R. B. Blakestad, J. Britton, D. B. Hume, W. M. Itano, D. Leibfried, R. Reichle, T. Rosenband, T. Schaetz, P. O. Schmidt, and D. J. Wineland. Long-lived qubit memory using atomic ions. *Phys. Rev. Lett.*, 95:060502, Aug 2005.
- [26] S. Olmschenk, K. C. Younge, D. L. Moehring, D. N. Matsukevich, P. Maunz, and C. Monroe. Manipulation and detection of a trapped Yb^+ hyperfine qubit. *Phys. Rev. A*, 76:052314, Nov 2007.
- [27] Ye Wang, Mark Um, Junhua Zhang, Shuoming An, Ming Lyu, Jing-Ning Zhang, L.-M. Duan, Dahyun Yum, and Kihwan Kim. Single-qubit quantum memory exceeding ten-minute coherence time. *Nat. Photonics*, 11(10):646–650, 2017.
- [28] V. M. Schäfer, C. J. Ballance, K. Thirumalai, L. J. Stephenson, T. G. Ballance, A. M. Steane, and D. M. Lucas. Fast quantum logic gates with trapped-ion qubits. *Nature*, 555(7694):75–78, 2018.
- [29] R. Barends, J. Kelly, A. Megrant, A. Veitia, D. Sank, E. Jeffrey, T. C. White, J. Mutus, A. G. Fowler, B. Campbell, Y. Chen, Z. Chen, B. Chiaro, A. Dunsworth, C. Neill, P. O’Malley, P. Roushan, A. Vainsencher, J. Wenner, A. N. Korotkov, A. N. Cleland, and John M. Martinis. Superconducting quantum circuits at the surface code threshold for fault tolerance. *Nature*, 508(7497):500–503, 2014.
- [30] W. Pfaff, B. J. Hensen, H. Bernien, S. B. van Dam, M. S. Blok, T. H. Taminiau, M. J. Tiggelman, R. N. Schouten, M. Markham, D. J. Twitchen, and R. Hanson. Unconditional quantum teleportation between distant solid-state quantum bits. *Science*, 345(6196):532–535, 2014.
- [31] Yang Wu, Ya Wang, Xi Qin, Xing Rong, and Jiangfeng Du. A programmable two-qubit solid-state quantum processor under ambient conditions. *npj Quantum Information*, 5(1):9, 2019.
- [32] Harry Levine, Alexander Keesling, Ahmed Omran, Hannes Bernien, Sylvain Schwartz, Alexander S. Zibrov, Manuel Endres, Markus Greiner, Vladan Vuletić, and Mikhail D. Lukin. High-fidelity control and entanglement of rydberg-atom qubits. *Phys. Rev. Lett.*, 121:123603, Sep 2018.
- [33] T. P. Harty, D. T. C. Allcock, C. J. Ballance, L. Guidoni, H. A. Janacek, N. M. Linke, D. N. Stacey, and D. M. Lucas. High-fidelity preparation, gates, memory, and readout of a trapped-ion quantum bit. *Phys. Rev. Lett.*, 113:220501, Nov 2014.

- [34] Justin E. Christensen, David Hucul, Wesley C. Campbell, and Eric R. Hudson. High fidelity manipulation of a qubit built from a synthetic nucleus. *Arxiv*: 1907.13331, 2019.
- [35] A. H. Myerson, D. J. Szwer, S. C. Webster, D. T. C. Allcock, M. J. Curtis, G. Imreh, J. A. Sherman, D. N. Stacey, A. M. Steane, and D. M. Lucas. High-fidelity readout of trapped-ion qubits. *Phys. Rev. Lett.*, 100:200502, May 2008.
- [36] Stephen Crain, Clinton Cahall, Geert Vrijsen, Emma E. Wollman, Matthew D. Shaw, Varun B. Verma, Sae Woo Nam, and Jungsang Kim. High-speed low-crosstalk detection of a $^{171}\text{Yb}^+$ qubit using superconducting nanowire single photon detectors. *arXiv*:1902.04059, 2019.
- [37] Gang-Qin Liu, Jian Xing, Wen-Long Ma, Ping Wang, Chang-Hao Li, Hoi Chun Po, Yu-Ran Zhang, Heng Fan, Ren-Bao Liu, and Xin-Yu Pan. Single-shot readout of a nuclear spin weakly coupled to a nitrogen-vacancy center at room temperature. *Phys. Rev. Lett.*, 118:150504, Apr 2017.
- [38] Easwar Magesan, Jay M. Gambetta, A. D. Córcoles, and Jerry M. Chow. Machine learning for discriminating quantum measurement trajectories and improving readout. *Phys. Rev. Lett.*, 114:200501, May 2015.
- [39] Minho Kwon, Matthew F. Ebert, Thad G. Walker, and M. Saffman. Parallel low-loss measurement of multiple atomic qubits. *Phys. Rev. Lett.*, 119:180504, Oct 2017.
- [40] Xing Rong, Jianpei Geng, Fazhan Shi, Ying Liu, Kebiao Xu, Wenchao Ma, Fei Kong, Zhen Jiang, Yang Wu, and Jiangfeng Du. Experimental fault-tolerant universal quantum gates with solid-state spins under ambient conditions. *Nature Communications*, 6(1):8748, 2015.
- [41] Matthew Reagor, Christopher B. Osborn, Nikolas Tezak, Alexa Staley, Guenivere Prawiroatmodjo, Michael Scheer, Nasser Alidoust, Eyob A. Sete, Nicolas Didier, Marcus P. da Silva, Ezer Acala, Joel Angeles, Andrew Bestwick, Maxwell Block, Benjamin Bloom, Adam Bradley, Catvu Bui, Shane Caldwell, Lauren Capelluto, Rick Chilcott, Jeff Cordova, Genya Crossman, Michael Curtis, Saniya Deshpande, Tristan El Bouayadi, Daniel Girshovich, Sabrina Hong, Alex Hudson, Peter Karalekas, Kat Kuang, Michael Lenihan, Riccardo Marianti, Thomas Manning, Jayss Marshall, Yuvraj Mohan, William O’Brien, Johannes Otterbach, Alexander Papageorge, Jean-Philip Paquette, Michael Pelstring, Anthony Polloreno, Vijay Rawat, Colm A. Ryan, Russ Renzas, Nick Rubin, Damon Russel, Michael Rust, Diego Scarabelli, Michael Selvanayagam, Rodney Sinclair, Robert Smith, Mark Suska, Ting-Wai To, Mehrnoosh Vahidpour, Nagesh Vodrahalli, Tyler Whyland, Kamal Yadav, William Zeng, and Chad T. Rigetti. Demonstration of universal parametric entangling gates on a multi-qubit lattice. *Science Advances*, 4(2), 2018.

- [42] Yang Wang, Aishwarya Kumar, Tsung-Yao Wu, and David S. Weiss. Single-qubit gates based on targeted phase shifts in a 3d neutral atom array. *Science*, 352(6293):1562–1565, 2016.
- [43] J. P. Gaebler, T. R. Tan, Y. Lin, Y. Wan, R. Bowler, A. C. Keith, S. Glancy, K. Coakley, E. Knill, D. Leibfried, and D. J. Wineland. High-fidelity universal gate set for $^9\text{Be}^+$ ion qubits. *Phys. Rev. Lett.*, 117:060505, Aug 2016.
- [44] C. J. Ballance, T. P. Harty, N. M. Linke, M. A. Sepiol, and D. M. Lucas. High-fidelity quantum logic gates using trapped-ion hyperfine qubits. *Phys. Rev. Lett.*, 117:060504, Aug 2016.
- [45] S. Crain, E. Mount, S. Baek, and J. Kim. Individual addressing of trapped $^{171}\text{Yb}^+$ ion qubits using a microelectromechanical systems-based beam steering system. *Applied Physics Letters*, 105(18):181115, 2014.
- [46] D. Kielpinski, C. Monroe, and D. J. Wineland. Architecture for a large-scale ion-trap quantum computer. *Nature*, 417(6890):709–711, 2002.
- [47] W. K. Hensinger, S. Olmschenk, D. Stick, D. Hucul, M. Yeo, M. Acton, L. Deslauriers, C. Monroe, and J. Rabchuk. T-junction ion trap array for two-dimensional ion shuttling, storage, and manipulation. *Applied Physics Letters*, 88(3):034101, 2006.
- [48] R. Bowler, J. Gaebler, Y. Lin, T. R. Tan, D. Hanneke, J. D. Jost, J. P. Home, D. Leibfried, and D. J. Wineland. Coherent diabatic ion transport and separation in a multizone trap array. *Phys. Rev. Lett.*, 109:080502, Aug 2012.
- [49] A. Walther, F. Ziesel, T. Ruster, S. T. Dawkins, K. Ott, M. Hettrich, K. Singer, F. Schmidt-Kaler, and U. Poschinger. Controlling fast transport of cold trapped ions. *Phys. Rev. Lett.*, 109:080501, Aug 2012.
- [50] C. Monroe and J. Kim. Scaling the ion trap quantum processor. *Science*, 339(6124):1164–1169, 2013.
- [51] C. Monroe, R. Raussendorf, A. Ruthven, K. R. Brown, P. Maunz, L.-M. Duan, and J. Kim. Large-scale modular quantum-computer architecture with atomic memory and photonic interconnects. *Phys. Rev. A*, 89:022317, Feb 2014.
- [52] V. A. Aksyuk, S. Arney, N. R. Basavanahally, D. J. Bishop, C. A. Bolle, C. C. Chang, R. Frahm, A. Gasparyan, J. V. Gates, R. George, C. R. Giles, J. Kim, P. R. Kolodner, T. M. Lee, D. T. Neilson, C. Nijander, C. J. Nuzman, M. Paczkowski, A. R. Papazian, F. Pardo, D. A. Ramsey, R. Ryf, R. E. Scotti, H. Shea, and M. E. Simon. 238 x 238 micromechanical optical cross connect. *IEEE Photonics Technology Letters*, 15(4):587–589, April 2003.
- [53] C. Monroe. Quantum information processing with atoms and photons. *Nature*, 416(6877):238–246, 2002.

- [54] L. Slodička, G. Hétet, N. Röck, P. Schindler, M. Hennrich, and R. Blatt. Atom-atom entanglement by single-photon detection. *Phys. Rev. Lett.*, 110:083603, Feb 2013.
- [55] S. Olmschenk, D. N. Matsukevich, P. Maunz, D. Hayes, L.-M. Duan, and C. Monroe. Quantum teleportation between distant matter qubits. *Science*, 323(5913):486–489, 2009.
- [56] Nicolas Sangouard, Romain Dubessy, and Christoph Simon. Quantum repeaters based on single trapped ions. *Phys. Rev. A*, 79:042340, Apr 2009.
- [57] Saikat Guha, Hari Krovi, Christopher A. Fuchs, Zachary Dutton, Joshua A. Slater, Christoph Simon, and Wolfgang Tittel. Rate-loss analysis of an efficient quantum repeater architecture. *Phys. Rev. A*, 92:022357, Aug 2015.
- [58] Koji Azuma, Kiyoshi Tamaki, and Hoi-Kwong Lo. All-photonic quantum repeaters. *Nature Communications*, 6(1):6787, 2015.
- [59] Siddhartha Santra, Sreraman Muralidharan, Martin Lichtman, Liang Jiang, Christopher Monroe, and Vladimir S Malinovsky. Quantum repeaters based on two species trapped ions. *New Journal of Physics*, 21(7):073002, jul 2019.
- [60] H. Inamori, N. Lütkenhaus, and D. Mayers. Unconditional security of practical quantum key distribution. *The European Physical Journal D*, 41(3):599, Jan 2007.
- [61] Koji Azuma, Kiyoshi Tamaki, and William J. Munro. All-photonic intercity quantum key distribution. *Nature Communications*, 6(1):10171, 2015.
- [62] Aeysha Khaliq and Barry C. Sanders. Practical long-distance quantum key distribution through concatenated entanglement swapping with parametric down-conversion sources. *J. Opt. Soc. Am. B*, 32(11):2382–2390, Nov 2015.
- [63] André Stefanov, Nicolas Gisin, Olivier Guinnard, Laurent Guinnard, and Hugo Zbinden. Optical quantum random number generator. *Journal of Modern Optics*, 47(4):595–598, 2000.
- [64] Xiongfeng Ma, Xiao Yuan, Zhu Cao, Bing Qi, and Zhen Zhang. Quantum random number generation. *npj Quantum Information*, 2(1):16021, 2016.
- [65] Miguel Herrero-Collantes and Juan Carlos Garcia-Escartin. Quantum random number generators. *Rev. Mod. Phys.*, 89:015004, Feb 2017.
- [66] Michael A. Nielsen. Cluster-state quantum computation. *Reports on Mathematical Physics*, 57(1):147 – 161, 2006.
- [67] Atul Mantri, Tommaso F. Demarie, and Joseph F. Fitzsimons. Universality of quantum computation with cluster states and (x, y)-plane measurements. *Scientific Reports*, 7(1):42861, 2017.

- [68] FangXing Xu, Wei Chen, Shuang Wang, ZhenQiang Yin, Yang Zhang, Yun Liu, Zheng Zhou, YiBo Zhao, HongWei Li, Dong Liu, ZhengFu Han, and GuangCan Guo. Field experiment on a robust hierarchical metropolitan quantum cryptography network. *Chinese Science Bulletin*, 54(17):2991–2997, 2009.
- [69] Thomas Walker, Koichiro Miyanishi, Rikizo Ikuta, Hiroki Takahashi, Samir Vartabi Kashanian, Yoshiaki Tsujimoto, Kazuhiro Hayasaka, Takashi Yamamoto, Nobuyuki Imoto, and Matthias Keller. Long-distance single photon transmission from a trapped ion via quantum frequency conversion. *Phys. Rev. Lett.*, 120:203601, May 2018.
- [70] V. Krutyanskiy, M. Meraner, J. Schupp, V. Krcmarsky, H. Hainzer, and B. P. Lanyon. Light-matter entanglement over 50 km of optical fibre. *npj Quantum Information*, 5(1):72, 2019.
- [71] R. Ursin, F. Tiefenbacher, T. Schmitt-Manderbach, H. Weier, T. Scheidl, M. Lindenthal, B. Blauensteiner, T. Jennewein, J. Perdigues, P. Trojek, B. Ömer, M. Fürst, M. Meyenburg, J. Rarity, Z. Sodnik, C. Barbieri, H. Weinfurter, and A. Zeilinger. Entanglement-based quantum communication over 144 km. *Nature Physics*, 3(7):481–486, 2007.
- [72] Juan Yin, Yuan Cao, Yu-Huai Li, Sheng-Kai Liao, Liang Zhang, Ji-Gang Ren, Wen-Qi Cai, Wei-Yue Liu, Bo Li, Hui Dai, Guang-Bing Li, Qi-Ming Lu, Yun-Hong Gong, Yu Xu, Shuang-Lin Li, Feng-Zhi Li, Ya-Yun Yin, Zi-Qing Jiang, Ming Li, Jian-Jun Jia, Ge Ren, Dong He, Yi-Lin Zhou, Xiao-Xiang Zhang, Na Wang, Xiang Chang, Zhen-Cai Zhu, Nai-Le Liu, Yu-Ao Chen, Chao-Yang Lu, Rong Shu, Cheng-Zhi Peng, Jian-Yu Wang, and Jian-Wei Pan. Satellite-based entanglement distribution over 1200 kilometers. *Science*, 356(6343):1140–1144, 2017.
- [73] L. Luo, D. Hayes, T.A. Manning, D.N. Matsukevich, P. Maunz, S. Olmschenk, J.D. Sterk, and C. Monroe. Protocols and techniques for a scalable atom-photon quantum network. *Fortschritte der Physik*, 57(11-12):1133–1152, 2009.
- [74] Connor Kupchak, Philip J. Bustard, Khabat Heshami, Jennifer Erskine, Michael Spanner, Duncan G. England, and Benjamin J. Sussman. Time-bin-to-polarization conversion of ultrafast photonic qubits. *Phys. Rev. A*, 96:053812, Nov 2017.
- [75] B. B. Blinov, D. L. Moehring, L.-M. Duan, and C. Monroe. Observation of entanglement between a single trapped atom and a single photon. *Nature*, 428(6979):153–157, 2004.
- [76] Immanuel Bloch. Quantum coherence and entanglement with ultracold atoms in optical lattices. *Nature*, 453(7198):1016–1022, 2008.

- [77] W. B. Gao, P. Fallahi, E. Togan, J. Miguel-Sanchez, and A. Imamoglu. Observation of entanglement between a quantum dot spin and a single photon. *Nature*, 491(7424):426–430, 2012.
- [78] E. Togan, Y. Chu, A. S. Trifonov, L. Jiang, J. Maze, L. Childress, M. V. G. Dutt, A. S. Sørensen, P. R. Hemmer, A. S. Zibrov, and M. D. Lukin. Quantum entanglement between an optical photon and a solid-state spin qubit. *Nature*, 466(7307):730–734, 2010.
- [79] D. Hucul, I. V. Inlek, G. Vittorini, C. Crocker, S. Debnath, S. M. Clark, and C. Monroe. Modular entanglement of atomic qubits using photons and phonons. *Nature Physics*, 11(1):37–42, 2015.
- [80] Christian Nölleke, Andreas Neuzner, Andreas Reiserer, Carolin Hahn, Gerhard Rempe, and Stephan Ritter. Efficient teleportation between remote single-atom quantum memories. *Phys. Rev. Lett.*, 110:140403, Apr 2013.
- [81] A. Narla, S. Shankar, M. Hatridge, Z. Leghtas, K. M. Sliwa, E. Zalus-Geller, S. O. Mundhada, W. Pfaff, L. Frunzio, R. J. Schoelkopf, and M. H. Devoret. Robust concurrent remote entanglement between two superconducting qubits. *Phys. Rev. X*, 6:031036, Sep 2016.
- [82] David A. Hucul. A modular quantum system of trapped atomic ions. *PhD Thesis*, 2015.
- [83] Ismail Volkan Inlek. Multi-species trapped atomic ion modules for quantum networks. *PhD Thesis*, 2016.
- [84] Carolyn Auchter, Chen-Kuan Chou, Thomas W. Noel, and Boris B. Blinov. Ion-photon entanglement and bell inequality violation with $^{138}\text{Ba}^+$. *J. Opt. Soc. Am. B*, 31(7):1568–1572, Jul 2014.
- [85] Dahyun Yum, Debashis De Munshi, Tarun Dutta, and Manas Mukherjee. Optical barium ion qubit. *J. Opt. Soc. Am. B*, 34(8):1632–1636, Aug 2017.
- [86] G. Araneda, D. B. Higginbottom, L. Slodička, Y. Colombe, and R. Blatt. Interference of single photons emitted by entangled atoms in free space. *Phys. Rev. Lett.*, 120:193603, May 2018.
- [87] C. Crocker, M. Lichtman, K. Sosnova, A. Carter, S. Scarano, and C. Monroe. High purity single photons entangled with an atomic qubit. *Opt. Express*, 27(20):28143–28149, Sep 2019.
- [88] D. J. Larson, J. C. Bergquist, J. J. Bollinger, Wayne M. Itano, and D. J. Wineland. Sympathetic cooling of trapped ions: A laser-cooled two-species nonneutral ion plasma. *Phys. Rev. Lett.*, 57:70–73, Jul 1986.

- [89] G. Morigi and H. Walther. Two-species coulomb chains for quantum information. *The European Physical Journal D - Atomic, Molecular, Optical and Plasma Physics*, 13(2):261–269, Jan 2001.
- [90] M. D. Barrett, B. DeMarco, T. Schaetz, V. Meyer, D. Leibfried, J. Britton, J. Chiaverini, W. M. Itano, B. Jelenković, J. D. Jost, C. Langer, T. Rosenband, and D. J. Wineland. Sympathetic cooling of $^9\text{Be}^+$ and $^{24}\text{Mg}^+$ for quantum logic. *Phys. Rev. A*, 68:042302, Oct 2003.
- [91] J. P. Home, M. J. McDonnell, D. J. Szwer, B. C. Keitch, D. M. Lucas, D. N. Stacey, and A. M. Steane. Memory coherence of a sympathetically cooled trapped-ion qubit. *Phys. Rev. A*, 79:050305, May 2009.
- [92] J. D. Jost, J. P. Home, J. M. Amini, D. Hanneke, R. Ozeri, C. Langer, J. J. Bollinger, D. Leibfried, and D. J. Wineland. Entangled mechanical oscillators. *Nature*, 459(7247):683–685, 2009.
- [93] Q. A. Turchette, Kielpinski, B. E. King, D. Leibfried, D. M. Meekhof, C. J. Myatt, M. A. Rowe, C. A. Sackett, C. S. Wood, W. M. Itano, C. Monroe, and D. J. Wineland. Heating of trapped ions from the quantum ground state. *Phys. Rev. A*, 61:063418, May 2000.
- [94] L. Deslauriers, S. Olmschenk, D. Stick, W. K. Hensinger, J. Sterk, and C. Monroe. Scaling and suppression of anomalous heating in ion traps. *Phys. Rev. Lett.*, 97:103007, Sep 2006.
- [95] R. B. Blakestad, C. Ospelkaus, A. P. VanDevender, J. M. Amini, J. Britton, D. Leibfried, and D. J. Wineland. High-fidelity transport of trapped-ion qubits through an **X**-junction trap array. *Phys. Rev. Lett.*, 102:153002, Apr 2009.
- [96] G. Shu, G. Vittorini, A. Buikema, C. S. Nichols, C. Volin, D. Stick, and Kenneth R. Brown. Heating rates and ion-motion control in a **Y**-junction surface-electrode trap. *Phys. Rev. A*, 89:062308, Jun 2014.
- [97] P. O. Schmidt, T. Rosenband, C. Langer, W. M. Itano, J. C. Bergquist, and D. J. Wineland. Spectroscopy using quantum logic. *Science*, 309(5735):749–752, 2005.
- [98] J. I. Cirac, P. Zoller, H. J. Kimble, and H. Mabuchi. Quantum state transfer and entanglement distribution among distant nodes in a quantum network. *Phys. Rev. Lett.*, 78:3221–3224, Apr 1997.
- [99] H.-J. Briegel, W. Dür, J. I. Cirac, and P. Zoller. Quantum repeaters: The role of imperfect local operations in quantum communication. *Phys. Rev. Lett.*, 81:5932–5935, Dec 1998.
- [100] H. J. Kimble. The quantum internet. *Nature*, 453:1023, Jun 2008.

- [101] P. Kómár, E. M. Kessler, M. Bishof, L. Jiang, A. S. Sørensen, J. Ye, and M. D. Lukin. A quantum network of clocks. *Nature Physics*, 10:582, Jun 2014.
- [102] L.-M. Duan and C. Monroe. Colloquium: Quantum networks with trapped ions. *Rev. Mod. Phys.*, 82:1209–1224, Apr 2010.
- [103] Jonathan Albert Mizrahi. Ultrafast control of spin and motion in trapped ions. *PhD Thesis*, 2013.
- [104] Kenneth Earl Wright II. Manipulation of the quantum motion of trapped atomic ions via stimulated raman transitions. *PhD Thesis*, 2017.
- [105] L. D. Landau and E. M. Lifshitz. *Course of Theoretical Physics, Vol. 3*. Pergamon Press, 2 edition, 1965.
- [106] D. A. Varshalovich and A. N. Moskalev. *Quantum Theory of Angular Momentum*. World Scientific Pub., 1988.
- [107] D. J. Berkeland and M. G. Boshier. Destabilization of dark states and optical spectroscopy in zeeman-degenerate atomic systems. *Phys. Rev. A*, 65:033413, Feb 2002.
- [108] H. Orbest. Resonance fluorescence of single barium ions. *Diplomarbeit*, 1999.
- [109] M. D. Rotter. Quantum feedback and quantum correlation measurements with a single barium ion. *PhD Thesis*, 2008.
- [110] E Biémont, J-F Dutrieux, I Martin, and P Quinet. Lifetime calculations in Yb II. *Journal of Physics B: Atomic, Molecular and Optical Physics*, 31(15):3321–3333, aug 1998.
- [111] A. S. Bell, P. Gill, H. A. Klein, A. P. Levick, Chr. Tamm, and D. Schnier. Laser cooling of trapped ytterbium ions using a four-level optical-excitation scheme. *Phys. Rev. A*, 44:R20–R23, Jul 1991.
- [112] William D. Phillips and Harold Metcalf. Laser deceleration of an atomic beam. *Phys. Rev. Lett.*, 48:596–599, Mar 1982.
- [113] Wayne M. Itano and D. J. Wineland. Laser cooling of ions stored in harmonic and penning traps. *Phys. Rev. A*, 25:35–54, Jan 1982.
- [114] D. J. Wineland, C. Monroe, W. M. Itano, D. Leibfried, B. E. King, and D. M. Meekhof. Experimental issues in coherent quantum-state manipulation of trapped atomic ions. *Journal of research of the National Institute of Standards and Technology*, 103(3):259–328, 1998.
- [115] B. B. Blinov, D. Leibfried, C. Monroe, and D. J. Wineland. Quantum computing with trapped ion hyperfine qubits. *Quantum Information Processing*, 3(1):45–59, Oct 2004.

- [116] Rachel Noek, Geert Vrijsen, Daniel Gaultney, Emily Mount, Taehyun Kim, Peter Maunz, and Jungsang Kim. High speed, high fidelity detection of an atomic hyperfine qubit. *Opt. Lett.*, 38(22):4735–4738, Nov 2013.
- [117] M Acton, K.-A. Brickman, P. C. Haljan, P. J. Lee, L. Deslauriers, and C. Monroe. Near-perfect simultaneous measurement of a qubit register. *Quantum Info. Comput.*, 6(6):465–482, September 2006.
- [118] Steven Matthew Olmschenk. Quantum teleportation between distant matter qubits. *PhD Thesis*, 2009.
- [119] David J. Jones, Scott A. Diddams, Jinendra K. Ranka, Andrew Stentz, Robert S. Windeler, John L. Hall, and Steven T. Cundiff. Carrier-envelope phase control of femtosecond mode-locked lasers and direct optical frequency synthesis. *Science*, 288(5466):635–639, 2000.
- [120] D. Hayes, D. N. Matsukevich, P. Maunz, D. Hucul, Q. Quraishi, S. Olmschenk, W. Campbell, J. Mizrahi, C. Senko, and C. Monroe. Entanglement of atomic qubits using an optical frequency comb. *Phys. Rev. Lett.*, 104:140501, Apr 2010.
- [121] R. Islam, W. C. Campbell, T. Choi, S. M. Clark, C. W. S. Conover, S. Debnath, E. E. Edwards, B. Fields, D. Hayes, D. Hucul, I. V. Inlek, K. G. Johnson, S. Korenblit, A. Lee, K. W. Lee, T. A. Manning, D. N. Matsukevich, J. Mizrahi, Q. Quraishi, C. Senko, J. Smith, and C. Monroe. Beat note stabilization of mode-locked lasers for quantum information processing. *Opt. Lett.*, 39(11):3238–3241, Jun 2014.
- [122] D. L. Hayes. Remote and local entanglement of ions using photons and phonons. *PhD Thesis*, 2012.
- [123] I. V. Inlek, C. Crocker, M. Lichtman, K. Sosnova, and C. Monroe. Multispecies trapped-ion node for quantum networking. *Phys. Rev. Lett.*, 118:250502, Jun 2017.
- [124] M. R. Dietrich, N. Kurz, T. Noel, G. Shu, and B. B. Blinov. Hyperfine and optical barium ion qubits. *Phys. Rev. A*, 81:052328, May 2010.
- [125] A Keselman, Y Glickman, N Akerman, S Kotler, and R Ozeri. High-fidelity state detection and tomography of a single-ion zeeman qubit. *New J. Phys.*, 13(7):073027, jul 2011.
- [126] Vera M. Schäfer. Fast gates and mixed-species entanglement with trapped ions. *PhD Thesis*, 2018.
- [127] J. A. Sherman, M. J. Curtis, D. J. Szwer, D. T. C. Allcock, G. Imreh, D. M. Lucas, and A. M. Steane. Experimental recovery of a qubit from partial collapse. *Phys. Rev. Lett.*, 111:180501, Oct 2013.

- [128] T. R. Tan, J. P. Gaebler, Y. Lin, Y. Wan, R. Bowler, D. Leibfried, and D. J. Wineland. Multi-element logic gates for trapped-ion qubits. *Nature*, 528:380 EP –, Dec 2015.
- [129] T. Ruster, C. T. Schmiegelow, H. Kaufmann, C. Warschburger, F. Schmidt-Kaler, and U. G. Poschinger. A long-lived zeeman trapped-ion qubit. *Applied Physics B*, 122(10):254, Sep 2016.
- [130] N. Yu, W. Nagourney, and H. Dehmelt. Radiative lifetime measurement of the Ba^+ metastable $D_{3/2}$ state. *Phys. Rev. Lett.*, 78:4898–4901, Jun 1997.
- [131] N. Aharon, M. Drewsen, and A. Retzker. General scheme for the construction of a protected qubit subspace. *Phys. Rev. Lett.*, 111:230507, Dec 2013.
- [132] N Aharon, M Drewsen, and A Retzker. Enhanced quantum sensing with multi-level structures of trapped ions. *Quant. Sci. Tech.*, 2(3):034006, jul 2017.
- [133] N Aharon, I Cohen, F Jelezko, and A Retzker. Fully robust qubit in atomic and molecular three-level systems. *New Journal of Physics*, 18(12):123012, dec 2016.
- [134] M. Chwalla, J. Benhelm, K. Kim, G. Kirchmair, T. Monz, M. Riebe, P. Schindler, A. S. Villar, W. Hänsel, C. F. Roos, R. Blatt, M. Abgrall, G. Santarelli, G. D. Rovera, and Ph. Laurent. Absolute frequency measurement of the $^{40}\text{Ca}^+ 4s\ ^2\text{S}_{1/2} - 3d\ ^2\text{D}_{5/2}$ clock transition. *Phys. Rev. Lett.*, 102:023002, Jan 2009.
- [135] Qu Liu, Yao Huang, Jian Cao, Bao-Quan Ou, Bin Guo, Hua Guan, Xue-Ren Huang, and Ke-Lin Gao. Frequency measurement of the electric quadrupole transition in a single laser-cooled $^{40}\text{Ca}^+$. *Chinese Physics Letters*, 28(1):013201, jan 2011.
- [136] N. Akerman, Y. Glickman, S. Kotler, A. Keselman, and R. Ozeri. Quantum control of $^{88}\text{Sr}^+$ in a miniature linear paul trap. *Applied Physics B*, 107(4):1167–1174, Jun 2012.
- [137] V. Letchumanan, G. Wilpers, M. Brownnutt, P. Gill, and A. G. Sinclair. Zero-point cooling and heating-rate measurements of a single $^{88}\text{Sr}^+$ ion. *Phys. Rev. A*, 75:063425, Jun 2007.
- [138] Clayton Crocker. High purity single photons entangled with Ba ions for quantum networking. *PhD Thesis*, 2019.
- [139] B. Merkel, K. Thirumalai, J. E. Tarlton, V. M. Schäfer, C. J. Ballance, T. P. Harty, and D. M. Lucas. Magnetic field stabilization system for atomic physics experiments. *Review of Scientific Instruments*, 90(4):044702, 2019.

- [140] C. J. Dedman, R. G. Dall, L. J. Byron, and A. G. Truscott. Active cancellation of stray magnetic fields in a bose-einstein condensation experiment. *Review of Scientific Instruments*, 78(2):024703, 2007.
- [141] David Hucul, Justin E. Christensen, Eric R. Hudson, and Wesley C. Campbell. Spectroscopy of a synthetic trapped ion qubit. *Phys. Rev. Lett.*, 119:100501, Sep 2017.
- [142] G.J. Milburn, S. Schneider, and D.F.V. James. Ion trap quantum computing with warm ions. *Fortschritte der Physik*, 48(9-11):801–810, 2000.
- [143] Klaus Mølmer and Anders Sørensen. Multiparticle entanglement of hot trapped ions. *Phys. Rev. Lett.*, 82:1835–1838, Mar 1999.
- [144] Anders Sørensen and Klaus Mølmer. Entanglement and quantum computation with ions in thermal motion. *Phys. Rev. A*, 62:022311, Jul 2000.
- [145] V. Negnevitsky, M. Marinelli, K. K. Mehta, H.-Y. Lo, C. Flühmann, and J. P. Home. Repeated multi-qubit readout and feedback with a mixed-species trapped-ion register. *Nature*, 563(7732):527–531, 2018.
- [146] C. D. Bruzewicz, R. McConnell, J. Stuart, J. M. Sage, and J. Chiaverini. Dual-species, multi-qubit logic primitives for Ca^+/Sr^+ trapped-ion crystals. [arXiv:1905.13122v1](https://arxiv.org/abs/1905.13122v1), 2019.
- [147] C. J. Ballance, V. M. Schäfer, J. P. Home, D. J. Szwer, S. C. Webster, D. T. C. Allcock, N. M. Linke, T. P. Harty, D. P. L. Aude Craik, D. N. Stacey, A. M. Steane, and D. M. Lucas. Hybrid quantum logic and a test of bell’s inequality using two different atomic isotopes. *Nature*, 528:384 EP –, Dec 2015.
- [148] Shi-Liang Zhu, C Monroe, and L.-M Duan. Arbitrary-speed quantum gates within large ion crystals through minimum control of laser beams. *Europhysics Letters (EPL)*, 73(4):485–491, feb 2006.
- [149] Shi-Liang Zhu, C. Monroe, and L.-M. Duan. Trapped ion quantum computation with transverse phonon modes. *Phys. Rev. Lett.*, 97:050505, Aug 2006.
- [150] Christian F Roos. Ion trap quantum gates with amplitude-modulated laser beams. *New Journal of Physics*, 10(1):013002, jan 2008.
- [151] T. Choi, S. Debnath, T. A. Manning, C. Figgatt, Z.-X. Gong, L.-M. Duan, and C. Monroe. Optimal quantum control of multimode couplings between trapped ion qubits for scalable entanglement. *Phys. Rev. Lett.*, 112:190502, May 2014.
- [152] A M Steane, G Imreh, J P Home, and D Leibfried. Pulsed force sequences for fast phase-insensitive quantum gates in trapped ions. *New Journal of Physics*, 16(5):053049, may 2014.

- [153] Pak Hong Leung, Kevin A. Landsman, Caroline Figgatt, Norbert M. Linke, Christopher Monroe, and Kenneth R. Brown. Robust 2-qubit gates in a linear ion crystal using a frequency-modulated driving force. *Phys. Rev. Lett.*, 120:020501, Jan 2018.
- [154] Pak Hong Leung and Kenneth R. Brown. Entangling an arbitrary pair of qubits in a long ion crystal. *Phys. Rev. A*, 98:032318, Sep 2018.
- [155] K. A. Landsman, Y. Wu, P. H. Leung, D. Zhu, N. M. Linke, K. R. Brown, L. Duan, and C. Monroe. Two-qubit entangling gates within arbitrarily long chains of trapped ions. *Phys. Rev. A*, 100:022332, Aug 2019.
- [156] Todd J. Green and Michael J. Biercuk. Phase-modulated decoupling and error suppression in qubit-oscillator systems. *Phys. Rev. Lett.*, 114:120502, Mar 2015.
- [157] Alistair R. Milne, Claire L. Edmunds, Cornelius Hempel, Federico Roy, Sandeep Mavadia, and Michael J. Biercuk. Phase-modulated entangling gates robust to static and time-varying errors. [arXiv:1808.10462](https://arxiv.org/abs/1808.10462), 2018.
- [158] Yao Lu, Shuaining Zhang, Kuan Zhang, Wentao Chen, Yangchao Shen, Jialiang Zhang, Jing-Ning Zhang, and Kihwan Kim. Global entangling gates on arbitrary ion qubits. *Nature*, 572(7769):363–367, 2019.
- [159] Yotam Shapira, Ravid Shaniv, Tom Manovitz, Nitzan Akerman, and Roei Ozeri. Robust entanglement gates for trapped-ion qubits. *Phys. Rev. Lett.*, 121:180502, Nov 2018.
- [160] A. E. Webb, S. C. Webster, S. Collingbourne, D. Bretaude, A. M. Lawrence, S. Weidt, F. Mintert, and W. K. Hensinger. Resilient entangling gates for trapped ions. *Phys. Rev. Lett.*, 121:180501, Nov 2018.
- [161] Farhang Haddadfarshi and Florian Mintert. High fidelity quantum gates of trapped ions in the presence of motional heating. *New Journal of Physics*, 18(12):123007, dec 2016.
- [162] D.F.V. James. Quantum dynamics of cold trapped ions with application to quantum computation. *Applied Physics B*, 66(2):181–190, Feb 1998.
- [163] J.P. Home. Quantum science and metrology with mixed-species ion chains. *Adv. At. Mol. Opt. Phys.*, 62:231, 2013.
- [164] P J Lee, K-A Brickman, L Deslauriers, P C Haljan, L-M Duan, and C Monroe. Phase control of trapped ion quantum gates. *Journal of Optics B: Quantum and Semiclassical Optics*, 7(10):S371–S383, sep 2005.
- [165] Patricia J. Lee. Quantum information processing with two trapped cadmium ions. *PhD Thesis*, 2006.

- [166] Giovanna Morigi, Jürgen Eschner, and Christoph H. Keitel. Ground state laser cooling using electromagnetically induced transparency. *Phys. Rev. Lett.*, 85:4458–4461, Nov 2000.
- [167] F. Schmidt-Kaler, J. Eschner, G. Morigi, C.F. Roos, D. Leibfried, A. Mundt, and R. Blatt. Laser cooling with electromagnetically induced transparency: application to trapped samples of ions or neutral atoms. *Applied Physics B*, 73(8):807–814, Dec 2001.
- [168] Regina Lechner, Christine Maier, Cornelius Hempel, Petar Jurcevic, Ben P. Lanyon, Thomas Monz, Michael Brownnutt, Rainer Blatt, and Christian F. Roos. Electromagnetically-induced-transparency ground-state cooling of long ion strings. *Phys. Rev. A*, 93:053401, May 2016.
- [169] C. Monroe, D. M. Meekhof, B. E. King, S. R. Jefferts, W. M. Itano, D. J. Wineland, and P. Gould. Resolved-sideband raman cooling of a bound atom to the 3d zero-point energy. *Phys. Rev. Lett.*, 75:4011–4014, Nov 1995.
- [170] Shi-Liang Zhu and Z. D. Wang. Unconventional geometric quantum computation. *Phys. Rev. Lett.*, 91:187902, Oct 2003.
- [171] S. Debnath, N. M. Linke, C. Figgatt, K. A. Landsman, K. Wright, and C. Monroe. Demonstration of a small programmable quantum computer with atomic qubits. *Nature*, 536:63 EP –, Aug 2016.
- [172] Timothy Andrew Manning. Quantum information processing with trapped ion chains. *PhD Thesis*, 2014.
- [173] Yukai Wu, Sheng-Tao Wang, and L.-M. Duan. Noise analysis for high-fidelity quantum entangling gates in an anharmonic linear paul trap. *Phys. Rev. A*, 97:062325, Jun 2018.
- [174] Guin-Dar Lin and L.-M. Duan. Sympathetic cooling in a large ion crystal. *Quantum Information Processing*, 15(12):5299–5313, Dec 2016.
- [175] D. Kielpinski, C. Volin, E. W. Streed, F. Lenzini, and M. Lobino. Integrated optics architecture for trapped-ion quantum information processing. *Quantum Information Processing*, 15(12):5315–5338, Dec 2016.
- [176] Karan K. Mehta, Colin D. Bruzewicz, Robert McConnell, Rajeev J. Ram, Jeremy M. Sage, and John Chiaverini. Integrated optical addressing of an ion qubit. *Nature Nanotechnology*, 11(12):1066–1070, 2016.
- [177] Robert J. Niffenegger, Jules Stuart, Cheryl Sorace-Agaskar, Dave Kharas, Suraj Bramhavar, Colin D. Bruzewicz, William Loh, Robert McConnell, David Reens, Gavin N. West, Jeremy M. Sage, and John Chiaverini. Integrated optical control and enhanced coherence of ion qubits via multi-wavelength photonics. *arXiv:2001.05052*, 2020.

- [178] David B. Hume. Two-species ion arrays for quantum logic spectroscopy and entanglement generation. *PhD Thesis*, 2010.
- [179] F Splatt, M Harlander, M Brownnutt, F Zähringer, R Blatt, and W Hänsel. Deterministic reordering of $^{40}\text{Ca}^+$ ions in a linear segmented paul trap. *New Journal of Physics*, 11(10):103008, oct 2009.
- [180] P. Maunz, D. L. Moehring, S. Olmschenk, K. C. Younge, D. N. Matsukevich, and C. Monroe. Quantum interference of photon pairs from two remote trapped atomic ions. *Nature Physics*, 3:538, Jun 2007.
- [181] R. Hanbury Brown and R. Q. Twiss. Correlation between photons in two coherent beams of light. *Nature*, 177(4497):27–29, 1956.
- [182] M. Schubert. Intensitätskorrelation in der resonanzfluoreszenz eines einzelnen gespeicherten ions. *PhD Thesis, Universität Hamburg*, 1991.
- [183] D. J. Berkeland, J. D. Miller, J. C. Bergquist, W. M. Itano, and D. J. Wineland. Minimization of ion micromotion in a paul trap. *Journal of Applied Physics*, 83(10):5025–5033, 1998.
- [184] J. D. Sivers, X. Li, and Q. Quraishi. Ion-photon entanglement and quantum frequency conversion with trapped Ba^+ ions. *Appl. Opt.*, 56(3):B222–B230, Jan 2017.
- [185] D B Higginbottom, L Slodička, G Araneda, L Lachman, R Filip, M Hennrich, and R Blatt. Pure single photons from a trapped atom source. *New Journal of Physics*, 18(9):093038, sep 2016.
- [186] K. Sosnova, C. Crocker, M. Lichtman, A. Carter, S. Scarano, and C. Monroe. Trapped ion single-photon emitter for quantum networking. In *Frontiers in Optics / Laser Science*, page FW7A.5. Optical Society of America, 2018.
- [187] Lucas Schweickert, Klaus D. Jöns, Katharina D. Zeuner, Saimon Filipe Covre da Silva, Huiying Huang, Thomas Lettner, Marcus Reindl, Julien Zichi, Rinaldo Trotta, Armando Rastelli, and Val Zwiller. On-demand generation of background-free single photons from a solid-state source. *Applied Physics Letters*, 112(9):093106, 2018.
- [188] Martin Madsen. Advanced ion trap development and ultrafast laser-ion interactions. *PhD Thesis*, 2006.
- [189] Sreraman Muralidharan, Linshu Li, Jungsang Kim, Norbert Lütkenhaus, Mikhail D. Lukin, and Liang Jiang. Optimal architectures for long distance quantum communication. *Scientific Reports*, 6(1):20463, 2016.
- [190] Prem Kumar. Quantum frequency conversion. *Opt. Lett.*, 15(24):1476–1478, Dec 1990.

- [191] S. Tanzilli, W. Tittel, M. Halder, O. Alibart, P. Baldi, N. Gisin, and H. Zbinden. A photonic quantum information interface. *Nature*, 437(7055):116–120, 2005.
- [192] Taehyun Kim, Peter Maunz, and Jungsang Kim. Efficient collection of single photons emitted from a trapped ion into a single-mode fiber for scalable quantum-information processing. *Phys. Rev. A*, 84:063423, Dec 2011.
- [193] L J Stephenson, D P Nadlinger, B C Nichol, S An, P Drmota, T G Ballance, K Thirumalai, J F Goodwin, D M Lucas, and C J Ballance. High-rate, high-fidelity entanglement of qubits across an elementary quantum network. *Arxiv: 1911.10841*, 2019.
- [194] Daniel M. Greenberger, Michael Horne, and Anton Zeilinger. Similarities and differences between two-particle and three-particle interference. *Fortschritte der Physik*, 48(4):243–252, 2000.
- [195] Matthias Fitzi, Nicolas Gisin, and Ueli Maurer. Quantum solution to the byzantine agreement problem. *Phys. Rev. Lett.*, 87:217901, Nov 2001.
- [196] Allison Carter. (private communication).
- [197] Yimin Wang, Ji ří Minář, Lana Sheridan, and Valerio Scarani. Efficient excitation of a two-level atom by a single photon in a propagating mode. *Phys. Rev. A*, 83:063842, Jun 2011.
- [198] C. K. Hong, Z. Y. Ou, and L. Mandel. Measurement of subpicosecond time intervals between two photons by interference. *Phys. Rev. Lett.*, 59:2044–2046, Nov 1987.
- [199] Yuan Liang Lim and Almut Beige. Generalized Hong-Ou-Mandel experiments with bosons and fermions. *New Journal of Physics*, 7:155–155, jul 2005.